PHYSIK-DEPARTMENT

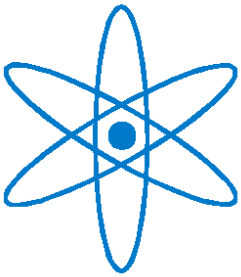

Study of the Higgs Boson Discovery Potential in the Process $pp \to H/A \to \mu^+\mu^-/\tau^+\tau^-$ with the ATLAS Detector

Dissertation

von

Georgios Dedes

TECHNISCHE UNIVERSITÄT
MÜNCHEN

Technische Universität München

Max-Planck-Institut für Physik
(Werner-Heisenberg-Institut)

Study of the Higgs Boson Discovery Potential in the Process $pp \to H/A \to \mu^+\mu^-/\tau^+\tau^-$ with the ATLAS Detector

Georgios Dedes

Vollständiger Abdruck von der Fakultät für Physik der Technischen Universität München zur Erlangung des akademischen Grades eines
Doktors der Naturwissenschaften
genehmigten Dissertation.

Vorsitzender: Univ.-Prof. Dr. A. J. Buras
Prüfer der Dissertation:
1. Priv.-Doz. Dr. H. Kroha
2. Univ.-Prof. Dr. L. Oberauer

Die Dissertation wurde am 04.02.2008 bei der Technischen Universität München eingereicht und durch die Fakultät für Physik am 22.04.2008 angenommen.

This dissertation is made at the
Physics Department of the Technical University in Munich ,
and at the Max-Planck-Institute for Physics in Munich.

Supervisor:
PD Dr. Hubert Kroha

«Καὶ πολλὰ τὰ λιόδεντρα
    ποὺ νὰ κρησάρουν στὰ χέρια τους τὸ φῶς
    κι ἐλαφρὸ ν' ἁπλώνεται στὸν ὕπνο σου
καὶ πολλὰ τα τζιτζίκια
    πού νὰ μὴν τὰ νιώθεις
    ὅπως δὲ νιώθεις τὸ σφυγμό στὸ χέρι σου
ἀλλὰ λίγο τὸ νερό
    γιὰ νὰ τὸ χεις Θεὸ
    καὶ να κατέχεις τὶ σημαίνει ὁ λόγος του
καὶ τὸ δέντρο μονάχο του
    χωρὶς κοπάδι
    γιὰ νὰ τὸ κάνεις φίλο σου
    καὶ νὰ γνωρίζεις τ' ἀκριβό του τ' ὄνομα
φτενό στὰ πόδια σου τὸ χῶμα
    γιὰ νὰ μὴν ἔχεις ποῦ ν' ἁπλώσεις ρίζα
    καὶ νὰ τραβᾶς τοῦ βάθους ὁλοένα
καὶ πλατὺς ἐπάνου ὁ οὐρανός
    γιὰ νὰ διαβάζεις μόνος σου τὴν ἀπεραντοσύνη»

Στη μνήμη του θείου μου.

Abstract

In this thesis, the discovery potential of the ATLAS experiment at the Large Hadron Collider (LHC) at CERN for the heavy neutral Higgs bosons H/A of the Minimal Supersymmetric extension of the Standard Model of particle physics (MSSM) in the decay channels $H/A \rightarrow \tau^+\tau^- \rightarrow e/\mu + X$ and $H/A \rightarrow \mu^+\mu^-$ has been studied. The ATLAS detector is designed to study the full spectrum of the physics phenomena occuring in the proton-proton collisions at 14 TeV center-of-mass energy and to provide answers to the question of the origin of particle masses and of electroweak symmetry breaking. For the studies, the ATLAS muon spectrometer plays an important role. The spectrometer allows for a precise muon momentum measurement independently of other ATLAS subdetectors. The performance of the muon spectrometer depends strongly on the performance of the muon tracking detectors, the Monitored Drift Tube Chambers (MDT).

Computer programs have been developed in order to test and verify the ATLAS muon spectrometer simulation, an essential ingredient for data analysis. In addition, dedicated programs for the monitoring of the quality of the data collected by the muon spectrometer have been developed and tested with data from cosmic ray muons. High-quality cosmic ray muon data have been used for the calibration of the MDT-chambers. A new calibration method, called analytical autocalibration, has been tested. The proposed method achieved the required accuracy of 20 μm in the determination of the space-to-drift-time relationship of the drift tubes of the MDT chambers with only 2000 muon tracks per chamber.

Reliable muon detector simulation and calibration are essential for the study of the MSSM Higgs boson decays $H/A \rightarrow \tau^+\tau^- \rightarrow e/\mu + X$ and $H/A \rightarrow \mu^+\mu^-$ and of the corresponding background processes. The signal selection and background rejection requirements have been optimized for maximum signal significance. The following results have been obtained for different assumptions on the MSSM Higgs boson mass m_A and on the ratio $\tan\beta$ of the vacuum expectation values of the two MSSM Higgs boson doublets: For the decay into τ-pairs, 5σ signal significance is obtained for $\tan\beta \gtrsim 5$ and $m_A = 150$ GeV/c^2 or for $\tan\beta \gtrsim 25$ and $m_A = 600$ GeV/c^2 for an integrated luminosity of 30 fb^{-1}. For the decay into muon pairs, 5σ signal significance is achieved for $\tan\beta \gtrsim 20$ and $m_A = 200$ GeV/c^2 or for $\tan\beta \gtrsim 60$ and $m_A = 450$ GeV/c^2 for an integrated luminosity of 30 fb^{-1}. In addition, the mass of the Higgs boson H/A can be measured in the decay $H/A \rightarrow \mu^+\mu^-$ exploiting the high muon momentum resolution of the ATLAS detector. The measurement accuracy degrades with increasing mass. A Higgs boson mass of 200 GeV/c^2 can be etermined with an accuracy of 2%.

Zusammenfassung

In dieser Arbeit wurde das Entdeckungspotential des ATLAS Experiments am Large Hadron Collider (LHC) am CERN für schwere neutrale Higgsbosonen H/A in der minimalen supersymmetrischen Erweiterung des Standardmodells der Teilchenphysik (MSSM) in den Zerfallskanälen $H/A \to \tau^+\tau^- \to \mathrm{e}/\mu + X$ und $H/A \to \mu^+\mu^-$ untersucht. Das Design des ATLAS Detektors erlaubt die Erforschung des gesamten Spektrums physikalischer Phänomene, die bei Proton-Proton-Kollisionen mit einer Schwerpunktsenergie von 14 TeV auftreten können, sowie die Beantwortung der Frage nach dem Ursprung der Teilchenmassen und der elektroschwachen Symmetriebrechung. Das ATLAS-Myonspektrometer spielt dabei eine wichtige Rolle. Mit diesem Spektrometer ist eine präzise Messung der Myonimpulse, unabhängig von anderen Subdetektoren, möglich. Die Leistungsfähigkeit des Myonspektrometers hängt stark von der Effizienz der und der Ortsauflösung Myon-Spurdetektoren, der Monitored Drift Tube (MDT)-Kammern, ab.

Im Rahmen dieser Arbeit wurden Computerprogramme entwickelt, um die Simulation des ATLAS-Myonspektrometers zu überprüfen. Simulationsrechnungen stellen für physikalische Prozesse im Detektor eine wichtige Komponente der Datenanalyse dar. Weiterhin wurden spezielle Programme zur Überwertung der Datenqualität des Myonspektrometers entwickelt und mit Hilfe von Daten kosmischer Myonen getestet. Daten guter Qualität von kosmischen Myonen im Myon-Detektor wurden daraufhin zur Kalibrierung der MDT-Kammern verwendet. Dabei wurde eine neue Kalibrationsmethode, die so genannte analytische Autokalibration, verwendet. Diese Methode erreicht bei der Bestimmung der Orts-Driftzeit-Beziehung der Driftrohre der MDT-Kammern die erforderliche Genauigkeit von 20 μm mit lediglich 2000 Myonen pro Kammer.

Um die Zerfälle des MSSM-Higgsboson Zerfälle $H/A \to \tau^+\tau^- \to \mathrm{e}/\mu + X$ und $H/A \to \mu^+\mu^-$ und die jeweiligen Untergrundprozesse zu untersuchen, ist eine zuverlässige Simulation und Kalibration des Myonspektrometers unverzichtbar. Die Kriterien für die Selektion des Signals und die Unterdrückung des Untergrunds wurden optimiert, um eine maximale Signalsignifikanz zu erhalten. Folgende Ergebnisse wurden unter verschiedenen Annahmen für die Higgsbosonmasse m_A und das Verhältnis tanβ der Vakuumerwartungswerte der beiden MSSM-Higgsbosondupletts erzielt: Für den Zerfall in ein τ-lepton-paar wird eine Signalsignifikanz von 5σ für $\tan\beta \gtrsim 5$ und $\mathrm{m}_A = 150$ GeV/c^2 oder für $\tan\beta \gtrsim 25$ und $\mathrm{m}_A = 600$ GeV/c^2 bei einer integrierten Luminosität von 30 fb^{-1} erreicht. Beim Zerfall in ein Myon-paar wird für $\tan\beta \gtrsim 20$ und $\mathrm{m}_A = 200$ GeV/c^2 oder für $\tan\beta \gtrsim 60$ und $\mathrm{m}_A = 450$ GeV/c^2 eine Signalsignifikanz von 5σ bei einer integrierten Luminosität von 30 fb^{-1} erreicht. Zusätzlich kann im Zerfall $H/A \to \mu^+\mu^-$ die Higgsbosonmasse unter Ausnutzung der hohen der Myonimpulsauflösung des ATLAS-Detektos gemessen werden, wobei die Meßgenauigkeit mit zunehmender Masse abnimmt. Eine Higgsbosonmasse von 200 GeV/c^2 kann mit einer Genauigkeit von 2% bestimmt werden.

Acknowledgements

I am grateful to my supervisor Hubert Kroha for accepting me nearly four years ago at the Max-Planck-Institut für Physik in Munich and in the MDT group. He provided me all the necessary means and motivation to complete my doctoral thesis in the ATLAS collaboration and gave me the privilege to work in such a stimulating environment as CERN.

I want to thank Sandra Horvat and Oliver Kortner for introducing me to the full range of aspects of a large scale particle physics experiment such as ATLAS, both at MPI and at CERN. Through their guidance and experience, I managed to get familiar with our experiment and aqcuire all the necessary skills which led me to the completion of this work.

I am thankfull to the rest of the members of the MPI MDT group: My officemate Sergey Kotov for our exciting discussions during the last three years, varying from a quantum theory of gravity to computer games. Susanne Mohrdieck-Möck for her instructions, always with patience and understanding during the last difficult months. Chrysostomos Valderanis for his company and his advice. Federica Legger Vadym Zuravlov, Jianming Yuan and Igor Potrap for helping me in so many different ways and for simply putting up with me.

I would also like to thank Nectarios Benekos and Rosy Nikolaidou for their guidance and their important scientific contribution to this thesis during my staying at CERN, but above all, for being true friends to me all this time.

My thanks to the students of the group, who I initially met as colleagues but I leave considering them as invaluable friends: Manfred Groh, I would need many pages to thank him for all his help and support during the past years. Jörg von Loeben for making me familiar with the rich Bavarian culture. Jens Schmaller, Steffen Kaiser and Thies Ehrich for the cheerfull atmosphaire they brought to the group along with their scientific knowledge.

For their help and interest in my work I am indebted to Steve Goldfarb, Daniela Rebuzzi, Matthias Schott, Nabil Ghodbane, Laurent Chevalier, Marcus Warsinsky, Gabriele Chiodini, Masaya Ishino, Tony Liss and Maria Smizanska.

Ευχαριστώ τους Έλληνες φίλους μου στο Μόναχο: Άγι Κιτσίκη, Τηλέμαχο Ματιάκη, Μάκη Τσιπουρίδη, Γιώργο Λιδώρη. Ήταν ο ελληνικός μου μικρόκοσμος τόσο στις δύσκολες όσο και στις ευχάριστες στιγμές. Τα ξενύχτια, οι εκδρομές και τα συμπόσια μας θα μου μείνουν αξέχαστα.

Ένα μεγάλο ευχαριστώ στη Λένα. Δύσκολο να το συνοψίσω σε μιά γραμμή, γιατί επτά χρόνια υπομονής και υποστήριξης δεν είναι ούτε εύκολα ούτε αυτονόητα.

Ευχαριστώ την οικογένεια μου: Τον πατέρα μου Προκόπη, τη μητέρα μου Καίτη και την αδερφή μου Ναστάζια. Πάντα με παρότρυναν να ακολουθήσω το δρόμο μου, χώρις ποτέ να υπολογίσουν κόστος ή κόπο. Αυτό το διδακτορικό είναι το αποτέλεσμα της πίστης τους και της αγάπης τους σε μένα.

Contents

Curriculum Vitae

Born on April 23^{th}, 1980 in Athens, Greece.

Education

Since September 2004 I participate in the ATLAS experiment at CERN by working within the ATLAS Muon Group at the Max-Planck-Institut für Physik in Munich.

1999 - 2004 studied in the Physics Department of the Natural Sciences Faculty of the Aristotle University of Thessaloniki (AUTH), Greece.

1992-1998: Gymnasium and High School in Salamis, Greece.

1986-1992: Primary School in Salamis, Greece.

Lebenslauf

23.April 1980 in Athen, Griechenland geboren

Ausbildungsweg

Seit 2004 Mitarbeit am ATLAS Experiment (CERN) bei der ATLAS Myon Gruppe des Max-Planck-Instituts für Physik in München.

1999 - 2004 Studium der Physik an der Aristotles Universität in Thessaloniki, Griechenland
Abschluss: 21. Juli 2004, Diplomarbeit: "Tests on the ATLAS Monitored Drift Tube BIS prototype chamber ARTEMIS with cosmic ray muons" unter Betreuung von Dr. Hariclea Petridou.

1992-1998: Besuch des Gymnasiums in Salamis, Griechenland. Abschluss: Abitur

1986-1992: Besuch des Grundschule in Salamis, Griechenland.

München, den Unterschrift

....

1

Introduction

The understanding of the structure of matter around us and the forces that bind together its elementary building blocks is a long lasting effort, occupying human minds for more than 2000 years. During the second half of the 20th century, a set of theories has emerged, discribing all the known elementary particles and their interactions, except for gravity. The common frame of these theories is a quantum field theory called the Standard Model. It incorporates the Glashow-Weinberg-Salam theory of the electroweak processes and quantum chromodynamics (QCD), the theory of strong interactions. The constituents of matter are described by fermions wih spin 1/2, while the forces are carried by bosons with spin 1.

Despite the outstanding success of the Standard Model, a corner stone of this theory still remains untested: the mechanism of spontaneous electroweak symmetry breaking, which is responsible for the particle masses. The Higgs mechanism provides an elegant solution to this problem by introducing one additional particle, the Higgs boson. The discovery of the Higgs particle and the determination of its mass is one of the most active fields of modern particle physics.

Even if the spontaneous electroweak symmetry breaking mechanism is revealed through the discovery of the Higgs particle, the Standard Model still leaves unanswered questions, like the origin of the dark matter in the universe, or the large difference between the electroweak scale and the Planck scale. These open questions lead physicists to believe that the Standard Model is not the final theory of elementary particles and their interactions, but only a low energy approximation of a more general theory describing nature.

Many of these questions find answers in the context of supersymmetic extensions of the Standard Model. Supersymmetry is a new symmetry between fermions and bosons. Due to the new symmetry, for each Standard Model particle a new supersymmetric partner is introduced, with all the quantum numbers unchanged except for the spin which differs by one half. A further consequence is the prediction of five Higgs bosons in the Minimal Supersymmetric extension of the Standard Model (MSSM), three of them neutral and two charged.

The Large Hadron Collider (LHC) at the European Center for Particle Physics (CERN) will start its operation in the year 2008. The LHC is a proton-proton collider with a center-of-mass energy of 14 TeV and a design luminosity of 10^{34} cm^2 s^{-1}. The main motivation for this experiment is the search for the Higgs boson in either the Standard Model or in possible extensions, or the exclusion of the Higgs mech-

anism as a solution to the spontaneous electroweak symmetry breaking. The two general purpose experiments, ATLAS and CMS, will explore the TeV-energy regime where at least one Higgs particle can be discovered.

During the past years, the ATLAS detector has been constructed and finally installed at CERN. This thesis explores the discovery potential of the ATLAS experiment for heavy neutral Higgs bosons predicted by the Minimal Supersymmetric Standard Model (MSSM). The searches are focused on the Higgs mass range of 150 to 600 GeV/c^2 and tanβ values between 10 and 60, where tanβ is the ratio of the vacuum expectation values of the two Higgs boson doublets in this model. The dominant leptonic decay modes are into a τ-lepton pair and into a muon pair. They have been investigated in two separate analyses using the ATLAS detector simulation.

Preparation for physics studies involves detailed simulation of the expected physics processes and the detector response. In this thesis, a dedicated software package for the validation of the description and performance of the ATLAS muon spectrometer simulation, was developed. Its purpose is to confirm that the simulation of the muon spectrometer meets the requirements and to identify problems and discrepancies. In addition, a data quality package was developed for the needs of the ATLAS muon spectrometer data taking using cosmic ray muons. This package provides offline monitoring capabilities and is designed use during the data taking with proton-proton collisions. For the largest part of the ATLAS detector, the precision measurement on the muon tracks is provided from the muon drift-tube chambers. The calibration of the muon drift-tube chambers has a vital contribution to the achieved accuracy of the ATLAS muon spectrometer. Therefore, the study of the calibration methods and their testing with the cosmic muon data collected with the ATLAS detector is an important step towards physics studies involving muons in the final state.

The thesis is structured in the following way:

First we describe the LHC experiment with focus on the ATLAS detector (Chapter 2). Before the description of the physics analysis, the verification of the ATLAS muon spectrometer simulation and the ATLAS muon data quality evaluation are explained (Chapters 3 and 4). The latter methods have been applied to data from cosmic muons. Methods for the calibration of the space - drift-time relationship of the muon drift-tube chambers have been tested with cosmic muon data and compared (Chapter 5). Chapter 6 discusses the theoretical framework for the MSSM Higgs boson searches, including elements of the Standard Model, motivation for Supersymmetry and the Minimal Supersymmetric Standard Model focusing on the Higgs sector. Finally, the search for the heavy neutral Higgs bosons predicted by the MSSM in simulated data is described using the decays channels in muon and τ-lepton pairs (Chapters 7 and 8).

2

The Large Hadron Collider and the ATLAS Detector

This chapter presents an overview of the LHC accelerator and its experiments. A general description of the accelerator will be given in section 2.1. Then the focus will be on the ATLAS detector in section 2.2 including physics goals and design criteria. Description of the ATLAS detector components follows, with special interest in the muon spectrometer which plays an important role for the physics studies. Finally, a brief summary of the trigger system is given.

2.1 The Large Hadron Collider

The Large Hadron Collider (LHC) [1] is a proton-proton collider at CERN operating at 14 TeV center-of-mass energy, the highest ever achieved. It will be operational in the year 2008.

The two counter rotating proton beams will collide in four interaction points, where four detectors will be located, ATLAS, CMS, ALICE and LHCb. ATLAS [2] and CMS [3] are the two large general purpose experiments which will probe the full range of physics phenomena up to the TeV energy scale. ALICE [4] will focus on quark - gluon plasma physics by exploiting heavy ion (Pb-Pb) collisions, while LHCb [5] is a dedicated B-Physics experiment that will study CP violation in the B-system. In addition to the four detectors located directly at the collision points, there are two other LHC experiments, TOTEM [6] designed to measure the total pp cross section and study elastic scattering and diffraction, and LHCf [7] designed to investigate the particle spectrum produced in pp collisions in the very forward direction with respect to the beams.

The LHC is located in the tunnel of the previous LEP experiments in a depth of approximately 100 m (see Figure 2.1). The accelerator circumference is 26.7 km.

A total of 1232 superconducting dipole magnets keep the proton beams on their circular path, posing one of the biggest technological challenges for LHC. The dipole magnets are made of Niobium-Titanium (NbTi) cables that become superconducting at an operating temperature of 1.9 K and incorporate two separated vacuum beam pipes. The strength of the magnetic field produced by the dipoles reaches up to 8.4 T.

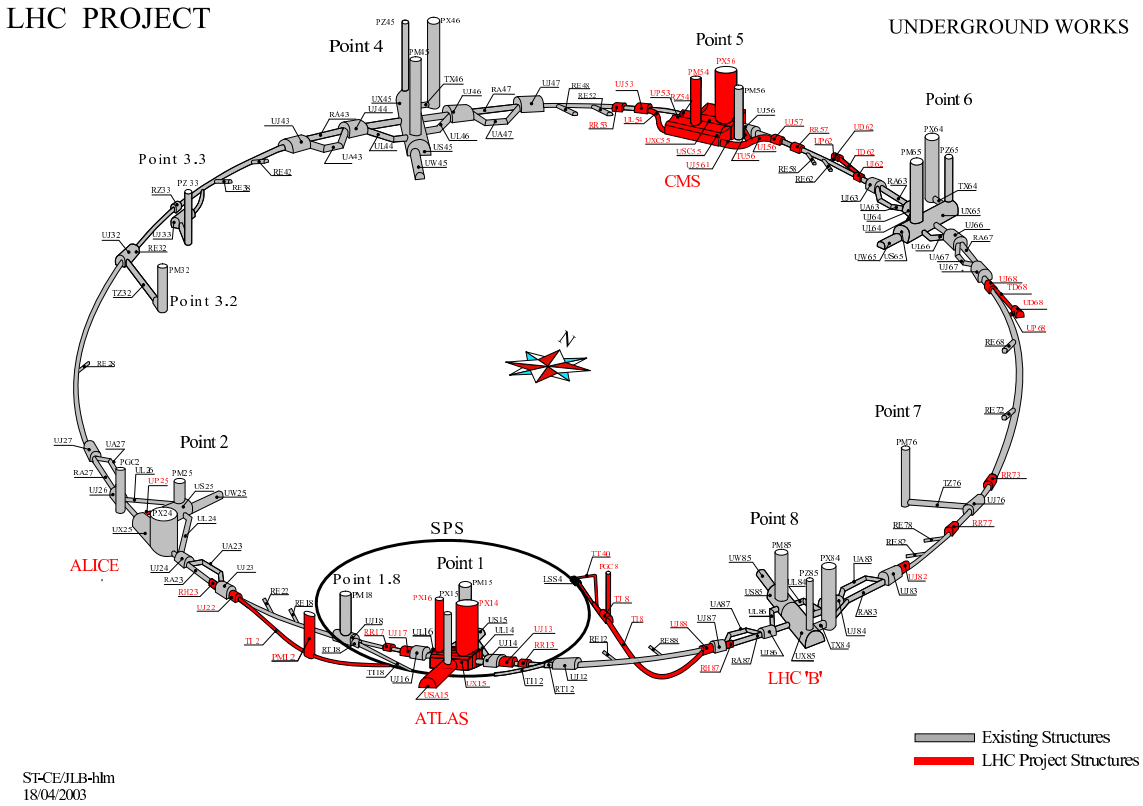

Fig. 2.1: The LHC underground complex.

Superconducting cavities deliver the radiofrequency (RF) power needed for the proton acceleration of up to 7 TeV. The cavities will be operated at a temperature of 4.5 K.

Each proton beam will consist of 2808 proton bunches, with 10^{11} protons per bunch and a bunch size of approximately 10 cm in length and 16.7 μm in the transverse plane close to the interaction points. The time interval between two consecutive bunches will be 25 ns. On average 23 inelastic pp collisions take place per bunch crossing at the design luminosity of 10^{34} cm^{-2} s^{-1}. This means that for every interesting event in the detectors, products from another 22 collisions on average will overlap (called minimum bias or pile-up events).

Initially the accelerator will be operated at the lower luminosity of $2 \cdot 10^{33}$ cm^{-2} s^{-1}, reaching the nominal luminosity of 10^{34} cm^{-2} s^{-1} after about three years. Assuming an operating time of 10^7 s per year, LHC will collect 10 fb^{-1} per year in the low luminosity phase and 100 fb^{-1} per year while running at nominal luminosity.

2.2 The ATLAS Detector

The ATLAS detector (see Figure 2.2), one of the two general purpose experiments at LHC, has been designed to exploit the full physics potential offered by the accel-

erator. In this section, the physics goals of the ATLAS experiment will be briefly discussed. Subsequently the main detector parts with emphasis on the muon detector, will be described.

ATLAS is a detector optimized to provide insight into the origin of the Electroweak Symmetry Breaking by answering the question of the existence of the Higgs boson. The search for the Higgs boson poses some of the strictest requirements on the detector performance such as high-resolution electron, photon and muon energy and momentum measurements, excellent secondary vertex detection for b-quarks, and high-resolution calorimetry for jet energy and missing transverse energy measurements. All these aspects are essential for accessing the full range of Higgs boson decays.

Especially during the first years of the lower luminosity phase, further precision measurements on other well established Standard Model parameters will be of great importance. LHC can be considered a top quark and W boson factory. Several millions of $t\bar{t}$ pairs and single $W^{\pm}$ events are expected within one year of data taking. Top quark and W boson masses can be measured with even higher accuracy than at LEP and Tevatron, due to the high statistics available at the LHC.

In addition to the Higgs boson searches and the precision measurements of the Standard Model parameters, ATLAS will have a handle on a rich variety of possible physics phenomena beyond the Standard Model which include searches for new heavy gauge bosons, indications of quark compositeness and the rich particle spectrum predicted by Supersymmetry (SUSY).

The ATLAS detector (see Figure 2.2) has a cylindrical shape with a radius of 11 m and length of 44 m. The coordinate system for the detector is defined as follows (see Figure 2.3): The beam direction defines the z-axis and the x-y plane is the plane transverse to the beam direction. The positive x-axis is pointing to the center of the accelerator ring, while the postitive y-axis is pointing upwards. In this system two angles are defined: The azimuthal angle ϕ around the beam axis in the x-y plane and the polar angle θ with respect to the beam axis. The pseudorapidity is defined as $\eta = -\ln\tan(\theta/2)$ and the distance in the pseudorapidity-azimuthal angle space is given by $\Delta\mathrm{R} = \sqrt{(\Delta\eta)^2 + (\Delta\phi)^2}$.

The innermost detector layer (Inner Detector) is the tracking detector, a cylinder of 1.2 m radius and 7 m length. It is located inside a superconducting solenoid which creates a magnetic field of 2 T. Charged particle pattern recognition, momentum and vertex measurements are achieved with a combination of high spatial resolution silicon pixel and strip detectors in the inner part of the volume, and straw tube detectors sensitive to transition radiation in the outer part.

The middle layer of the ATLAS detector, directly outside the solenoid magnet, is the calorimeter. It extends to a radius of 4.25 m and has a length of 13.3 m. In the barrel region, a highly granular liquid-argon (LAr) calorimeter is used for shower detection and a scintillator-tile technology for hadron calorimetry. In the endcap regions the (LAr) technology is used for both electromagnetic and hadronic calorimetry. The overall system provides high-resolution measurement of energy

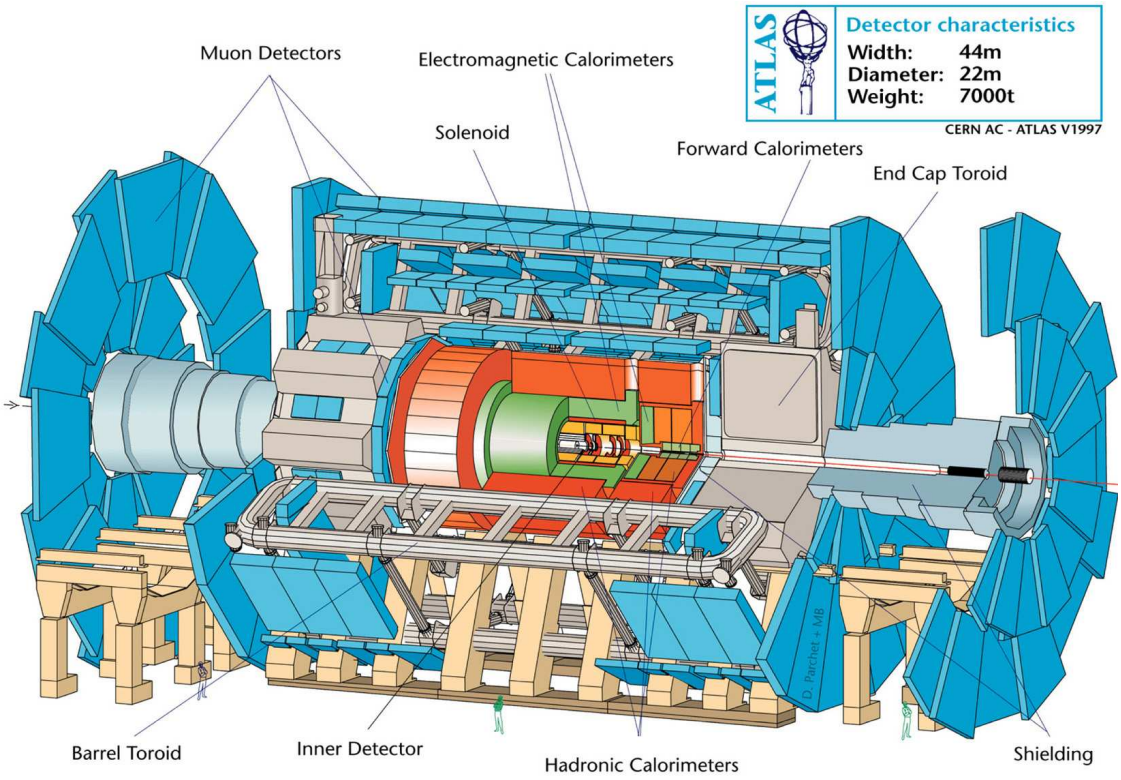

Fig. 2.2: Schematic view of the ATLAS Detector.

deposits of neutral and charged particles.

Finally the outermost layer of the detector consist of the muon spectrometer with an air-core toroid magnet system, which is divided into a long barrel section and two end-cap sections. It generates an average magnetic field of 0.4 T within an open structure. This design was choosen in order to minimize multiple scattering which would degrade the muon momentum resolution. The muon spectrometer is instrumented with different technologies for trigger and tracking chambers, which provide high spatial resolution in order to achieve the high momentum resolution required for the study of many important physics proccesses with muons in the final state.

2.2.1 The Magnet System

The magnet system of ATLAS [9] (see Figure 2.4) has an overall length of 26 m and a total volume of about 8000 m^3 within a radius of 10 m. It consists of four seperate superconducting magnets: A Central Solenoid (CS), a Barrel Toroid (BT) and two End-Cap Toroids (ECT).

The central solenoid magnet with an outer radius of 1.3 m and an axial length 5.3 m consists of of a single-layer Nb-Ti coil. Because of its location before the

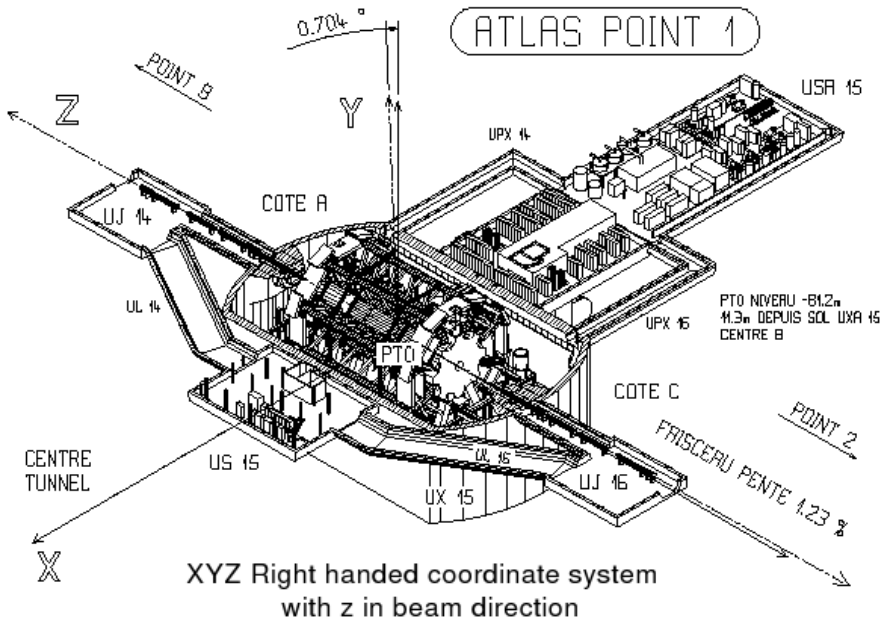

Fig. 2.3: Global coordinates system for the ATLAS detector.

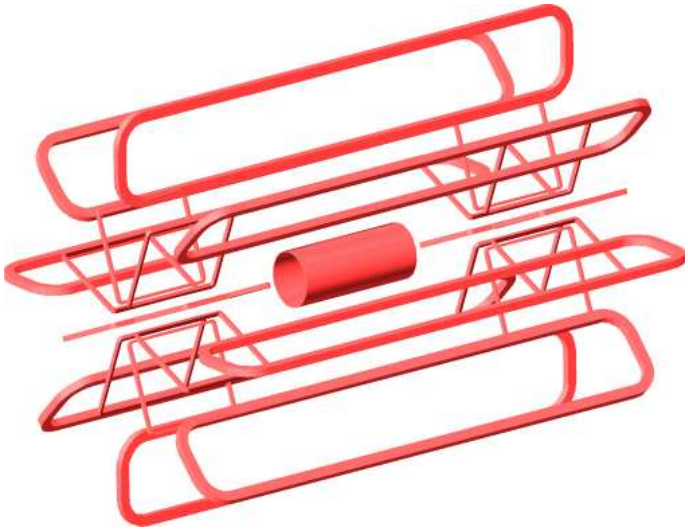

Fig. 2.4: The magnet system for the ATLAS detector.

electromagnetic calorimeter, the minimization of material is vital. As a consequence, the vacuum vessels of the central solenoid and the electromagnetic calorimeter are combined. In addition, as return yoke the iron absorber of the tile calorimeter is used. It will be operated at a temperature of 4.5 K delivering an average axial magnetic field of 2 T in the Inner Detector region.

The Barrel Toroid is the largest component of the ATLAS magnet system with an outer radius of 10 m and an axial length of 26 m. It consists of eight Nb-Ti racetrack shaped coils with individual cryostats, assembled symmetrically around the beam axis. The Barrel Toroid is operated at a temperature of 4.5 K providing an average toroidal magnetic field of 0.4 T. The magnetic field lines are perpenticular to the x-y plane.

For the end-cap regions, two additional toroid magnets are used. Each of the Endcap Toroids has an outer radius of 10.7 m and an axial length of 5 m. Eight Nb-Ti coils are housed in one large cryostat for each Endcap Toroid. The Endcap Torroids coils are rotated by 22.5^o with respect to the Barrel Toroid coils.

2.2.2 The Inner Detector

The Inner Detector [10], [11] (see Figure 2.5) is designed to accurately reconstruct trajectories of charged particles in the very high track multiplicity events at the LHC. A fast, high-granularity and radiation hard detector is required in order to achieve the ATLAS physics requirements.

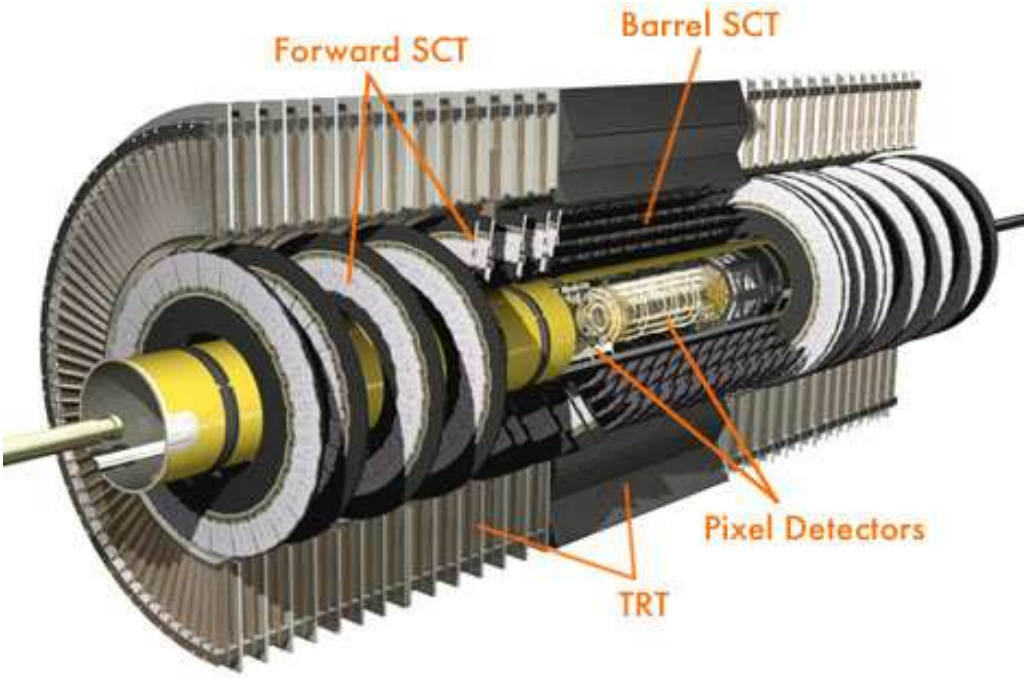

Fig. 2.5: The ATLAS Inner Detector.

A combination of three different technologies provides momentum measurement with a resolution of $\sigma(1/p_T) \simeq 0.56 \oplus 22/(p_T \cdot \sqrt{sin\theta})$ (TeV^{-1}) over a solid angle range of $|\eta| < 2.5$.

Closest to the interaction point, the pixel detector provides three high precision track point measurements. 1500 barrel and 700 end-cap pixel detector modules, are arranged in three layers in the barrel region (radii of 5.05 cm, 8.85 cm and 12.25 cm) and in three end-cap disks on each side, covering pseudorapidity up to ±2.5. The 80 million pixels offer an excellent impact parameter resolution, crucial for b-jet tagging.

The next layer of the Inner Detector is the Semiconductor Tracker (SCT) consisting of silicon strip detector modules, 2112 in the barrel and 1976 in the endcaps part. The modules are arranged in four layers at radii from 29.9 cm to 51.4 cm in the barrel and in nine wheels at $|z|$ positions from 83.5 cm to 272.8 cm in the endcaps. The tracking detector provides eight precision measurements per track in the x-y plane and also a measurement of the z position.

The outermost part of the Inner Detector is the Transition Radiation Tracker (TRT). It is based on straw drift-tube detectors. Each straw is 4 mm in diameter, equipped with a 85 μm diameter wire and filled with a gas mixture of $Xe/CO_2/O_2$ (70%/27%/3%). 36 measurements per track are provided by 73 layers of straws in the barrel region (in the vertical range from 56 cm to 107 cm) and 18 wheels in each endcap (ranging in $|z|$ from 83 cm to 277 cm). This detector covers pseudorapidity up to $\eta = \pm 2.5$. In addition, the use of Xe gas allows for the detection the transition radiation photons produced in radiators interleaved between the straws, thus adding to the electron identification capability of the detector.

2.2.3 The Calorimeter System

The ATLAS calorimeter system [12], [13] (see Figure 2.6) provides measurement of the energy (and θ-ϕ direction) of particles and jets produced in the collision. Energy measurement is based on the formation of a shower produced when relativistic particles traverse dense matter. For electrons, positrons and photons, electromagnetic showers are created through Bremsstrahlung ($e^{\pm} \rightarrow e^{\pm}\gamma$) and pair production ($\gamma \rightarrow e^+e^-$) in the electric field of nuclei. In the case of hadrons, hadronic showers are produced by a cascade of hadron-nucleus interactions. The hadronic interactions in matter are characterized by the interaction length of the material. Typically, the interaction length is up to an order of magnitute longer than the radiation length characterizing the absorbtion of electromagnetically interacting particles in matter. This effect is employed in the calorimeter system for the separation of electromagnetic showers detected in the electromagnetic calorimeter (ECAL) and the hadronic showers measured by the hadron calorimeter (HCAL).

The calorimeter system, which is discussed in detail in the following, provides a pseudoroapidity coverage of $|\eta| < 4.9$ and energy resolution of $\sigma(\mathrm{E})/\mathrm{E} \simeq 10\ \%/\sqrt{E} \oplus 1\ \%$ for the electromagnetic showers and $\sigma(\mathrm{E})/\mathrm{E} \simeq 50\ \%/\sqrt{E} \oplus 3\ \%$ in $|\eta| < 3$ and $\sigma(\mathrm{E}_T)/E_T \simeq 100\ \%/\sqrt{E} \oplus 10\ \%$ in $3 < |\eta| < 5$ for the hadronic showers.

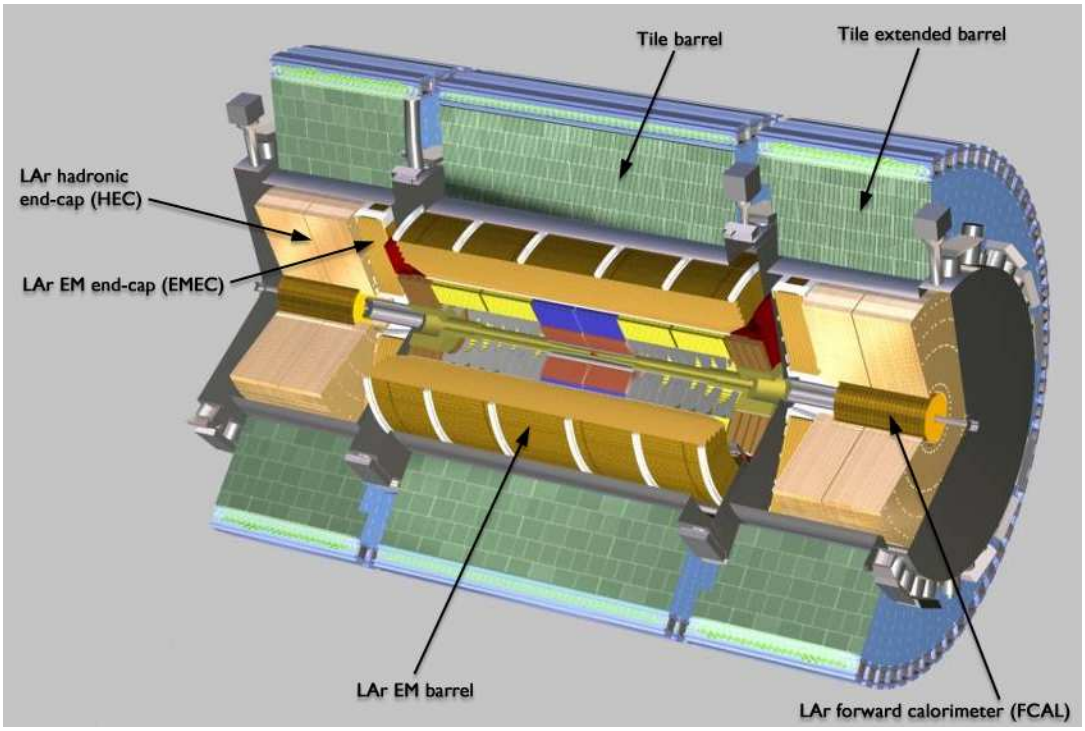

Fig. 2.6: The ATLAS calorimeter system.

The electromagnetic calorimeter is divided into a barrel part covering the pseudorapidity range $|\eta| < 1.475$ and two end-caps covering $1.375 < |\eta| < 3.2$. The barrel consist of two identical halfs separated at z=0, while each end-cap consists of two coaxial wheels: an outer wheel ($1.375 < |\eta| < 2.5$) and an inner wheel ($2.5 < |\eta| < 3.2$). The electromagnetic calorimeter is a LAr sampling calorimeter, with accordeon-shaped Kapton electrodes and lead absorber plates. The accordeon geometry provides a complete symmetry in ϕ without azimuthal cracks. The total material thickness (varying with pseudorapidity) is above 24 X_o for the barrel region and above 26 X_o for the endcaps. In the main acceptance region $|\eta| < 2.5$, the electromagnetic calorimeter is segmented into three longitudinal sections, while two segments exist in the inner wheel. The first longitudinal section with thickness of 6 X_o, segmented in $|\eta|$ with 4mm pitch contributes to particle identification and provides precise $|\eta|$ measurements. The second section is transversly segmented into cells of size $\Delta\eta \times \Delta\phi = 0.025 \times 0.025$. It increases the total calorimeter thickness to 24 X_o, allowing for precise energy measurements and electron-hadron(jet) separation by using efficient isolation cuts on the showers. The third section has a coarser granularity but adds a thickness of up to 12 X_o. In order to correct for the energy lost in the material in front of the calorimeter, an additional, independent sampling device is added,both in the barrel and the end-caps. The so called "presampler" is an active LAr calorimeter layer with coarser granularity than the rest of the electromagnetic calorimeter.

In the hadronic calorimeter, several technologies are used in order to cover the pseudorapidity range $|\eta| < 4.9$, consisting of the barrel ($|\eta| < 1.6$), two endcaps ($1.5 < |\eta| < 3.2$) and two forward regions ($3.1 < |\eta| < 4.9$). An important parameter of the hadronic calorimeter design is its thickness. A total thickness of 11 interaction lengths λ provides good containment for hadronic jets and minimizing leakage into the muon system. For $|\eta| < 1.6$ an iron-scintillating tile calorimeter is used, oriented perpenticular to the colliding beams, with 3 mm thick scintillating tiles (active material) and 14 mm thick iron absorber lates. There are one barrel and two extended barrel parts which are segmented in three layers with a granularity of $\Delta\eta \times \Delta\phi = 0.1 \times 0.1$ on the first two and 0.2×0.1 for the last layer. The extended barrel parts cover a pseudorapidity range of $0.8 < |\eta| < 1.7$.

In the range $1.5 < |\eta| < 4.9$, LAr technology is used for the hadronic calorimeter. Each endcap consists of two, equal diameter wheels. Both wheels are constructed out of copper plates with 25 mm and 50 mm thickness respectively and an 8.5 mm wide gap inbetween. The total thickness of the endcap hadron calorimeter is approximately 12 interaction lengths. Finally, the forward hadron calorimeter (FCAL) which is also using LAr as active material, covers the solid angle region very close to the beam. It is hosted in the same cryostat as the hadron and the electromagnetic endcap calorimeters. It improves the hermeticity of the detector and the missing energy measurement and plays an important role in the forward-jet tagging. The only 5 m distance of the FCAL front face to the interaction point call for a radiation hard and high-density detector. The forward calorimeter has a total thickness of 9 interaction lengths segmented into three longitudunal sectors, the first with copper and the second and the third with thungsten absorber plates.

2.2.4 The Muon Spectrometer

High momentum processes with muons in the final state are one of the cleanest signatures of interesting physics at the LHC. For that reason, the ATLAS detector will operate with a high-resolution muon spectrometer [8], [14] consisting of fast trigger chambers and high precision tracking chambers (see Figure 2.7).

The muon momentum measurement in the muon spectrometer is based on the magnetic deflection of muon trajectories in the magnetic field of the toroidal magnet system described in detail in sector 2.2.1. The toroidal magnet system offers high bending power over the whole pseudorapidity range up to $|\eta| < 2.7$, with a magnetic field mostly orthogonal to the muon trajectories (see Figure 2.8). In the barrel region ($|\eta| < 1$), tracks are measured in chambers arranged in three cylindrical layers (inner, medium and outer) at around the beam axis at radii of 5 m, 7.5 m and 10 m. In the so called transition region ($1 < |\eta| < 1.4$) and in the end-cap region ($1.4 < |\eta| < 2.7$), chambers are installed in vertical discs in three layer at distances of 7.4 m, 10 m, 13 m and 21 m from the interaction point. The ϕ symmetry of the toroid magnets is reflected in the symmetric stucture of the muon chamber system which consists of eight octants. Each octant is subdivided in two overlapping (so called small and large) sectors. Therefore, the main types of MDT chambers in the

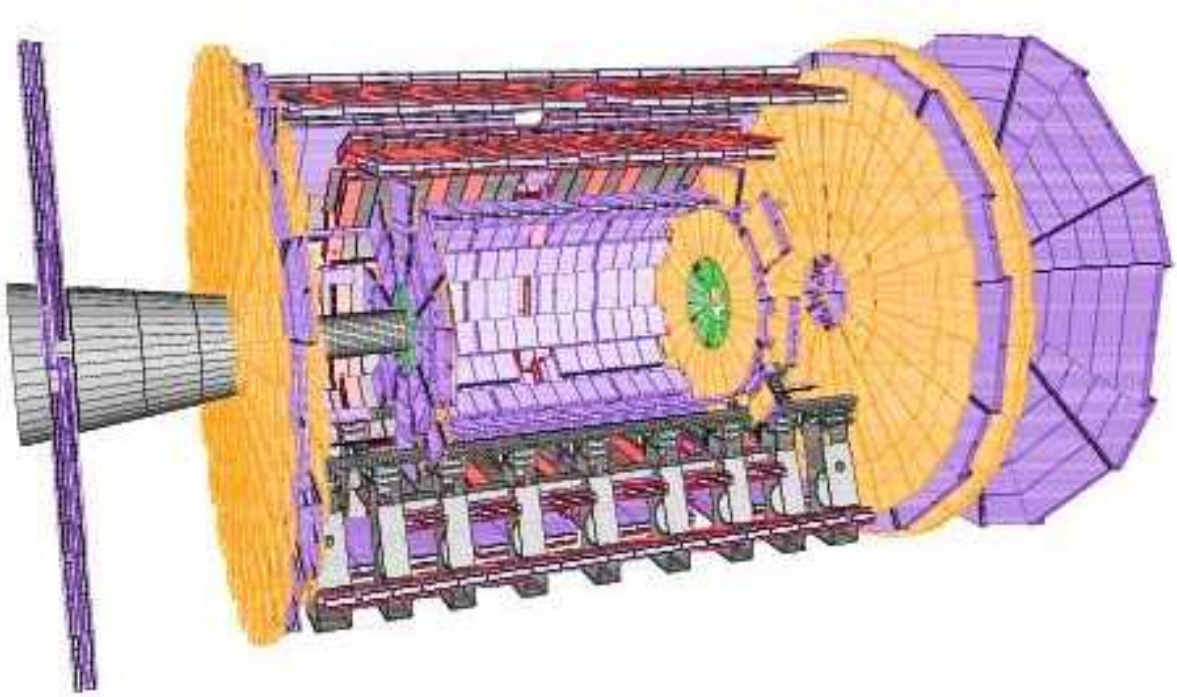

Fig. 2.7: The ATLAS muon spectrometer

barrel, according to their location in the layers and the ϕ-octants are the BIS/L (Barrel Inner Small/Large), BMS/L (Barrel Middle Small/Large), BOS/L (Barrel Outer Small/Large), together with some special chambers for the feet region, the rails and the transition region between barrel and end-cap. More details about the muon chamber layout can be found in Appendix A.

The momentum of the muons traversing the barrel region is determined from the track sagitta measurement, utilizing three space points measured in the inner layer at the inner boundary of the magnetic field, the outer layer at the outer boundary of the magnetic field and the middle layer inside the magnetic field volume. In the endcap region the magnet cryostats do not allow for the positioning of chambers inside the magnetic field volume, so the momentum is determined by a point(inner layer)-angle(middle and outer layer) measurement.

Over most of the pseudorapidity range, the precision measurement of the track coordinates in the bending direction of the magnetic field is provided by the **M**onitored **D**rift **T**ube (MDT) chambers. Close to the beam axis at high pseudorapidities, **C**athode **S**trip **C**hambers (CSC) are used in the inner layer. The muon spectrometer contains an independent trigger system, which also provides a measurement

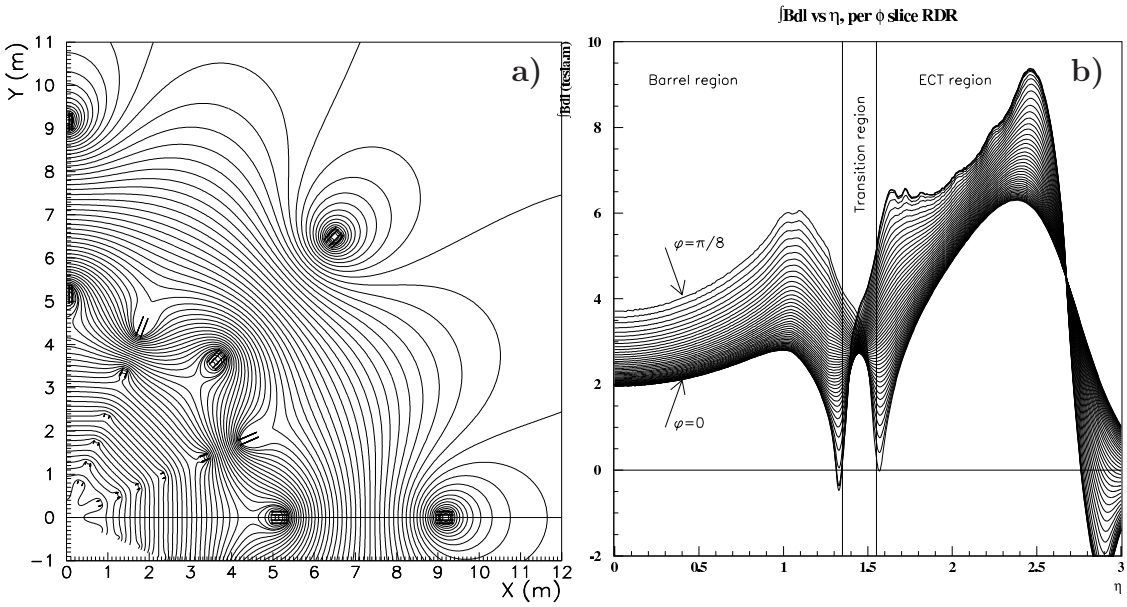

Fig. 2.8: The toroidal magnetic field of the ATLAS muon spectrometer: *a)* The field lines in a quadrant of the x-y plane. *b)*: The bending power as a function of pseudorapidity.

of the track coordinates orthogonal to the bending direction of the magnetic field. In the barrel region **R**esistive **P**late **C**hambers (*RPC*), while in the endcap regions **T**hin **G**ap **C**hambers (TGC) are used as trigger chambers.

Precision Tracking Detectors

The basic detection element of the MDT chambers are aluminium tubes of 30 mm diameter and 400 μm wall thickness with a 50 μm diameter gold-plated central wire made of W/Re (93%/7%). The tube is filled with a non flammable gas mixture of Ar/CO_2 (93%/7%) at 3 bar absolute pressure. The aluminium wall of the tubes is electrically grounded, while the wire is at a high-voltage of 3080-V. The tubes are closed at both sides with cylindrical elements (endplugs) designed to center the wire with an accuracy better than 10 μm.

MDT chambers vary in shape according to their location in the muon spectrometer, in order to optimize solid angle coverage. There are 1172 MDT chambers covering the pseudorapidity range of $|\eta| < 2$ with a total area of 5500 m^2. More details about the MDT chamber layout can be found in Appendix A. All regular MDT chambers (see Figure 2.9) consist of two triple or quadruple (called multilayers) seperated by a spacer structure. The multilayers consist of three layers of tubes in the chambers of the Middle and Outer stations and of four layers of tubes in the chambers of the Inner station. The MDT chambers combine high spatial resolution

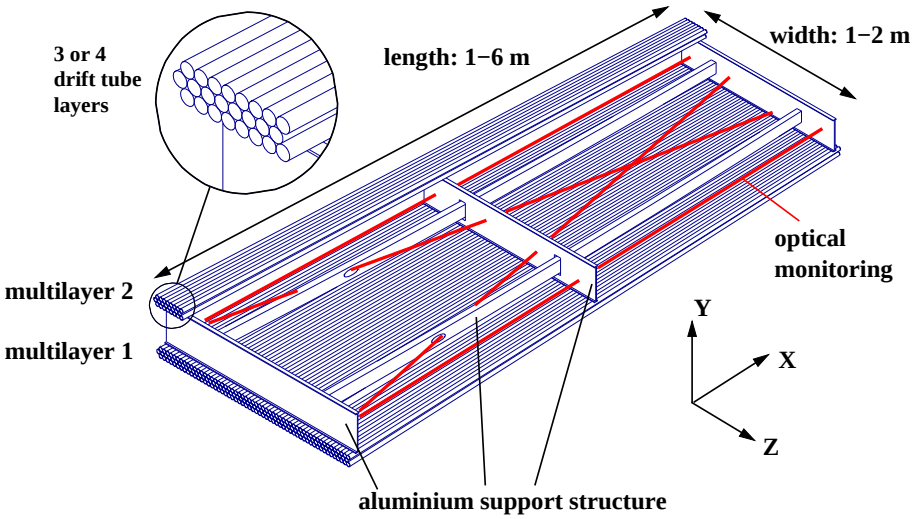

Fig. 2.9: Schematic representation of an MDT chamber. In detail the three or four layer of tubes that make each of the two multilayers are illustrated.

of individual drift tubes of 80 μm (rms) with high mechanical precision. The sense wires of the drift tubes are positioned within a chamber with an accuracy of better than 20 μm (rms) resulting in a chamber resolution of 30-40 μm.

Deformations of the chambers will occur in the various mounting positions in ATLAS and may change in time due to thermal gradients. Therefore, a chamber-internal optical alignment system is implemented, which continiously monitors the deformations. It consists of four optical alignment rays (two of them parallel to the tube direction and two in the diagonal directions between the corners of the chamber), comprising of an LED light source and a sensor of a CCD camera, and measuring relative muvements with an accuracy of a few μm. In addition each chamber carries a number of temperature and B-field sensors. In addition to the chamber-internal alignment system, an optical position measuring system monitors the relative positions of the MDT chambers in different layers of the muon spectrometer.

In the region of $|\eta| > 2$ in the inner layer, counting rates exceed the level for safe operation of the MDT chambers is exceeded. Therefore, in this region of the endcaps the MDT chambers are replaced by the CSC chambers (see Figure 2.10). CSC chambers are multiwire proportional chambers with both cathodes segmented into strips, one perpendicular and one parallel to the wires. The position of the tracks is obtained by interpolation between neighbouring cathode strips with induced currents. A CSC chamber consists of four wire planes. The operating voltage is 2600 V, the anode wire, made of gold-plated W/Re (97%/3%), has a diameter of 30 μm and the readout pitch in the bending direction is 5.08 mm. The gas mixture used is $\mathrm{Ar}/CO_2/CF_4$ (30%/50%/20%).

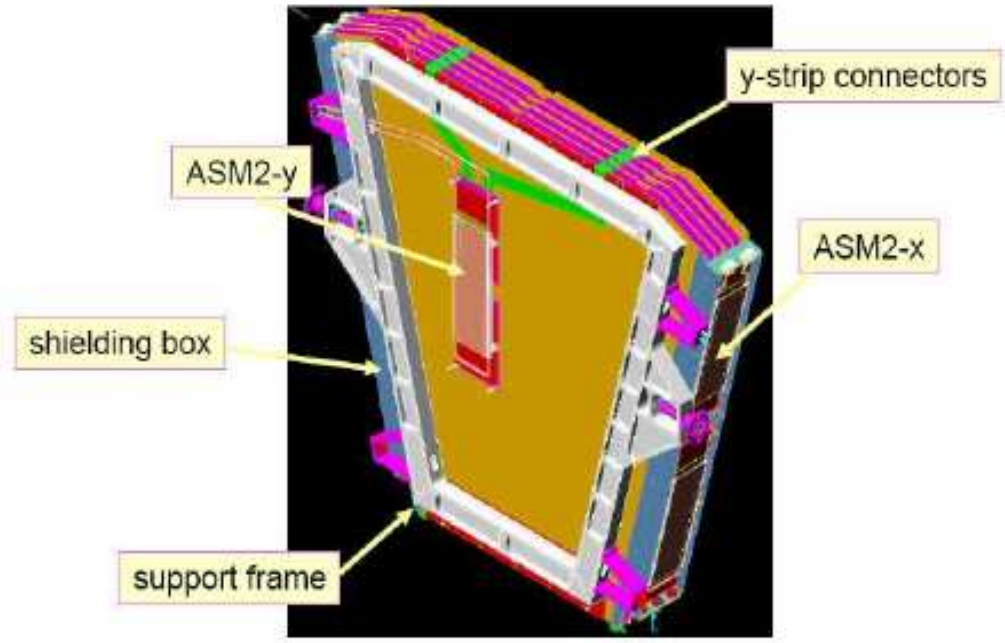

Fig. 2.10: Schematic representation of a CSC chamber. In the picture, the four wire layers, almost parallel to the x-y plane and the read out and support structures are indicated.

Fast Trigger Chambers

The trigger system in the barrel region uses RPC chambers (see Figure 2.11) consisting of two 2 mm wide gas volumes without wires between 2 mm thick resistive plates made of Bakelite. The correct distance of the plates is assured by insulating spacers. The gas mixture used is $C_2H_2F_4/Iso - C_4H_{10}/SF_6$. At the nominal operating conditions, the high voltage applied is 9.4 kV creating an electrical field of about 4.5 kV/mm. When a charged particle crosses the gas volume, avalanches are created along the tracks. The signal is read out via 25-35 mm wide aluminium strips placed on the outside of the bakelite plates. For each gas gap, strips oriented in η and ϕ measure the two transverse track coordinates. A minimum of three out of four possible signals in a chamber is required for a valid track. The signal width is of 5 ns (FWHM).

The RPC chambers are arranged in cylindrical layers around the beam axis following the layout of the MDT chambers. For each MDT chamber there are two RPC chambers in the middle layer (one above and one below the MDT chamber) and one RPC chamber in the outer layer (either above or below the MDT chamber). The large lever arm between the middle and the outer RPC layer provides for a high-p_T muon trigger with 10-30 GeV threshold, while the two middle chambers allow

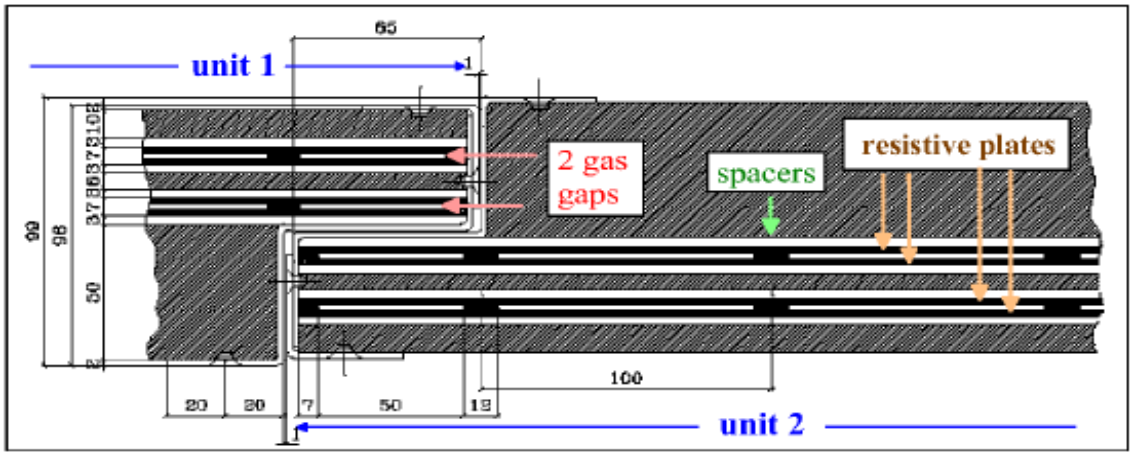

Fig. 2.11: Schematic representation of an RPC chamber. The cross section on the y-z plane shows the two units with an overlap in Z and the two gas gaps in each unit. In the perpenticular to the drawing direction (x), the units are also segmented in two DoubletPhi contigious parts.

for a low-p_T muon trigger with a 5-10 GeV threshold.

Finally, in the endcap region the muon trigger is provided by TGC chambers (see Figure 2.12). TGC chambers are multiwire propotional chambers filled with a highly quenching gas mixture of CO_2 and n-C_5H_{12} (n-pentane) 1.8 mm wire pitch and cathode readout strips in two or three gas volumes per chamber. Operating at a high-voltage of approximately 3 kV, the gas gain achieved is 10^6 with signal width of about 25 ns.

TGC chambers are mounted on independent wheels like the endcap MDT chambers. There are in total four TGC wheels on each side of the detector. An inner wheel just in front of the inner MDT/CSC chambers and three middle wheels, one in front and two behind the middle MDT chambers wheel. The signals from the inner TGC wheel are not used for the first level trigger, rather they are used in the higher level trigger and as an input for the reconstruction algorithms.

2.2.5 The Trigger System

The LHC bunch-crossing rate is 40 MHz yielding an interaction rate of approximatelly 10^9 Hz at the nominal luminosity of 10^{34} cm^{-2} s^{-1}. This high interaction rate makes it impossible for the LHC detectors to proccess and store the whole event from every bunch-crossing. A highly selective trigger system with an overall rejection factor of 10^7 is needed to reduce the event rate written to permament storage media to the required <100 Hz. The ATLAS trigger and data acquisition [15] is based on three levels of event selection (see Figure 2.13):

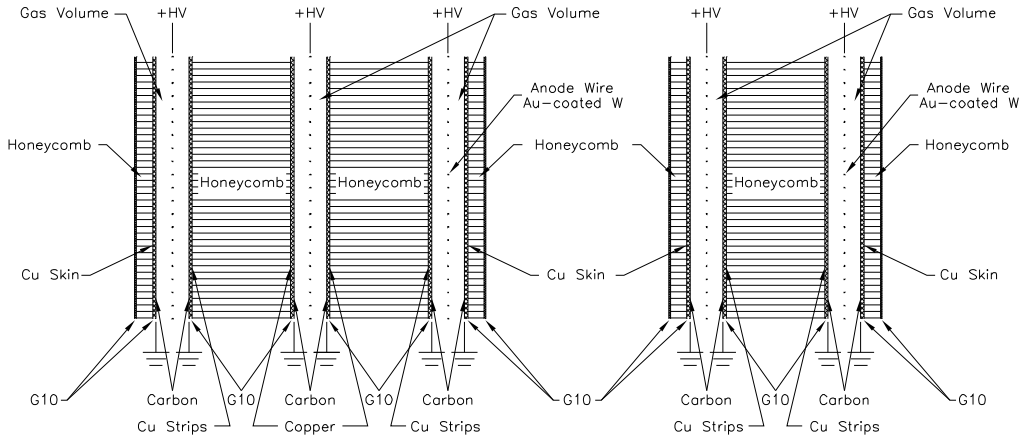

Fig. 2.12: A schematic representation of a TGC chamber. In the picture a cross section on the y-z plane is illustrated. In the two drawings the case of the triplet and the doublet with two and three gas volumes respectively is depicted.

- **First Level Trigger (LVL1)**: The LVL1 trigger makes an initial selection based on reduced granularity information from a subset of detectors. For the muon trigger high-p_T thresholds are required. Objects searched for by the calorimeters are high-p_T electrons, photons, jets and taus decaying hadronically. The goal is to reduce the event rate to 75 kHz. An essential requirement is the identification of the bunch-crossing to which the trigger signals belong. The time of flight to the muon spectrometer is comparable to the time interval between two consecutive bunch-crossings, while for the calorimeters signal pulses extend over many bunch-crossings. Therefore, information is stored temporarily for about ~ 2 μs) in pipeline memories for further proccessing. Events finally selected by the LVL1 trigger are stored into the Read Out Buffers (ROB).

- **Second Level Trigger (LVL2)**: The LVL2 trigger reads the ROB and also makes use of the region of interest (ROI) information provided by the LVL1 trigger. This includes information on the η and ϕ position as well as on the energy or momentum respectively. The event rate is reduced to $\sim$ 1 kHz. This decrease compared to LVL1 comes from track isolation requirements and sharpening of the p_T threshold for the muons, taking into account the more precise MDT chambers measurements. For the calorimeter, refinement of the higher level decision comes from the use of the full calorimetr granularity combined with the information from the inner detector.

- **Event Filter (EF)**: The last stage of selections is performed in the EF which is based in offline algorithms including the proccess of the event building from the information stored in the ROB. The event rate is reduced to $\sim$ 100 Hz for permament storage.

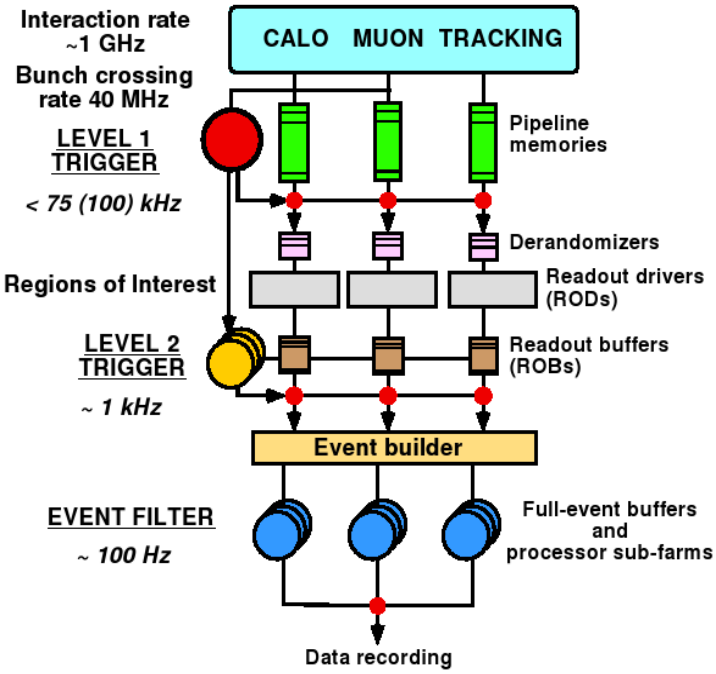

Fig. 2.13: The ATLAS trigger scheme.

3

Validation of the Muon Spectrometer Simulation

The study of the performance of the ATLAS detector and the analysis of the experimental data, require a detailed simulation of the response of the ATLAS detector to the particles in the final states of proton-proton collisions at the LHC. To achieve a realistic simulation, the material distribution in ATLAS, the interaction of particles with matter, and the response of the sensitive elements of the ATLAS detector to the traversing particles, must be implemented in the simulation programm.

The simulation program of the ATLAS detector [16] consists of independent modules for each subdetector (Inner Detector, Calorimeters, Muon Spectrometer and Magnet System). Dynamic loading and the organization of the detector simulation in the form of plug-in modules make the implementation simple, as no modification of the framework code is required. The reference simulation tool adopted by all the detector component applications is the GEANT4 package [17],[18].

In this chapter the validation algorithms developed for the muon spectrometer simulation are presented. The structure of the detector description and the algorithms for the geometry validation are described in Section 3.1. Section 3.2 introduces the concept and structure of the dedicated software developed for the simulation validation software. A summary of the results obtained with the program is shown in Section 3.3.

3.1 Muon Detector Simulation

The simulation program for the ATLAS Muon Spectrometer is currently in a full operational mode and integrated into the common analysis framework of ATLAS, called ATHENA [20].

3.1.1 Software Structure

The description of the ATLAS muon spectrometer relies on two main software components:

1. a relational database which implements a schema capable of hierarchical version control,

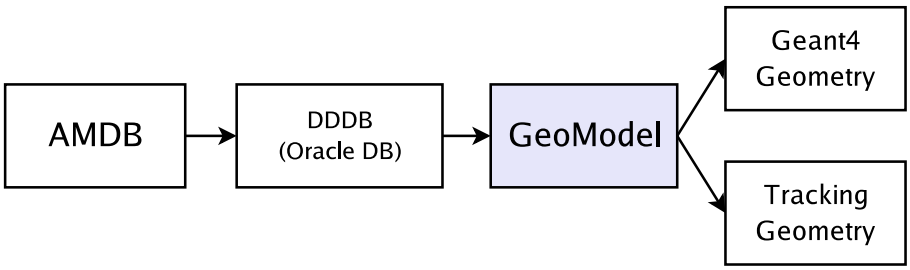

Fig. 3.1: Dataflow of GeoModel: The AMDB detector description file is converted into an Orcale Database (Detecor Description Database). GeoModel itself depends on this file and provides geometry information for track reconstruction and the full ATLAS Geant4 simulation

2. a set of geometrical primitives and classes providing a description of all volumes and materials of the detector.

All data related to the detector description reside in the AMDB (Atlas Muon DataBase) database. The AMDB detector description is developed in two independent branches: the description of active elements (sensitive detector components) and the description of passive elements (dead matter such as magnets and support structures).

In the current architecture, the geometrical description is decoupled from the simulation framework. An ATLAS-wide detector description software package, optimized for minimum memory consumption, GeoModel [19], issued as the single source of geometry information for both simulation and reconstruction.

Due to the complexity of the muon spectrometer and to the large number of parameters to control for its correct description, several debugging tools have been developed, to check the geometry and material consistency. A variety of methods have been and are currently employed, including visualization tools. In the following paragraphs, two of them are discussed in detail, the detection and the removal of conflicts among the volumes defining the components of muon spectrometer, and the check on the muon chamber positions.

3.1.2 Detection of Geometry Conflicts

The muon spectrometer detector description system has undergone specific visual debugging with respect to the detection of geometrical conflicts among volumes. The detection of volume overlaps is complicated because of the complexity of the geometry. However, their removal has been especially crucial to allow for tolerance between components in view of the simulation of the effects of chamber misalignment. Chamber conflicts can cause unpredictable behavior of the simulation process including subtle changes to particle multiplicity and physics observables.

The volume conflicts can be classified into three different types (see Figure 3.2):

	Layout 1	Layout 2	Layout 1	Layout 2
Overlappings	16852	266673	1358	1468
Overshootings	6450	5763	1772	1788

Tab. 3.1: Amount of conflicts in two geometrical layout versions at the time of the first check on the geometry (first two columns) and after the massive clash cleaning (second two columns).

- **Overshooting**: when a given volume (A in Figure 3.2) sticks outside its mother volume.
- **Overlapping**: when two daughter volumes overlap (A and B, or C and D).
- **Solid errors**: when a solid volume has one or more null dimension(s).

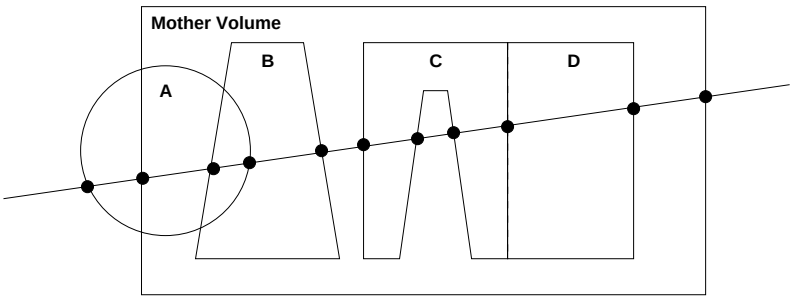

Fig. 3.2: Representation of the three different types of conflicts between volumes. Overshooting errors: between A and the mother volume. Overlaping errors: between the two daughter volumes A and B, or C and D. Solid errors are not represented here, they correspond to the situation when one or more dimension(s) defining the solid volumes happen to be null.

Geant4 has a dedicated tool which recursively loops over the full volume tree detecting the overlaps. The Geant4 visualization tools then help to identify the conflicts. A GeoModel specific tool for the conflict detection has been used [24].

By intensively applying this procedure, a substantial reduction of the conflicts has been achieved. Table 3.1 shows the amount of volume conflicts at the time of the first test and the current status.

3.2 Validation of the Muon Detector Simulation

The aim of the muon detector simulation validation is threefold:

- To ensure the compatibility and reproducibility of data samples produced at different computing centres of the ATLAS computing infrastructure.

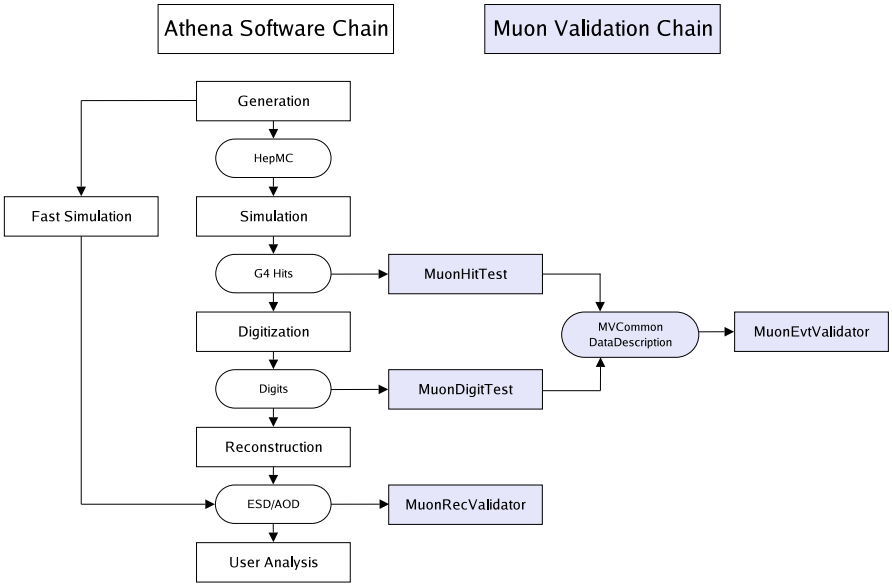

Fig. 3.3: Schematic representation of the muon detector simulation and validation software. The first step of the simulation chain is the generation which produces the momentum-vectors of the particles. The next step produses the G4 hits by simulating the interactions of the particles with the materials of the detector. Hits serve as an input for digitization which simulates the signals coming from the detector response to the particles. Finally, digits are the input to the reconstruction algorithms. Alternatively, fast simulation uses the generated particles appying to them a parametrized detector response. Validation of the muon spectrometer simulation is performed on the hits and digits level (present chapter) and on the reconstruction level.

- To monitor the changes and the improvements of the ATLAS detector geometry and simulation by means of a detailed check on an event-by-event basis for each step in the muon software chain.
- To verify the validity of the simulated physics processes.

Figure 3.3 shows a flow diagram for the muon simulation and validation software. There are two basic validation steps:

- Monitoring of the total number of hits/digits per chamber. This allows for identifying inefficiencies.
- Monitoring of the average number of hits/digits per chamber and per event. This allows for detecting inefficiencies independent of the number of events.

Details of the validation variables used are discussed in Appendix B.

3.3 Simulation Validation Results

The information coming from the interaction of the simulated tracks with the sensitive part of the detector is referred to as a hit. Muon hits are generated by Geant4 when charged particles cross the sensitive part of the muon chambers. Digit are the simulated digitized output signals of the detectors originating from the hits. Comparison of muon hit and digit distributions is important for the verification of the muon simulation chain.Control plots for the simulation and the digitization using a single muon sample are shown in Figures 3.4 to 3.7.

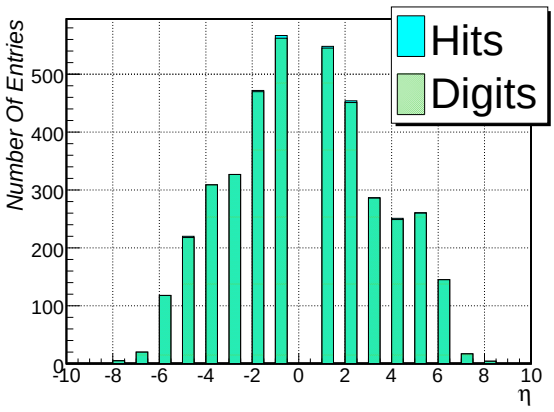

Fig. 3.4: Comparison of the overall number of MDT chamber hits and digits versus η position of the chamber.

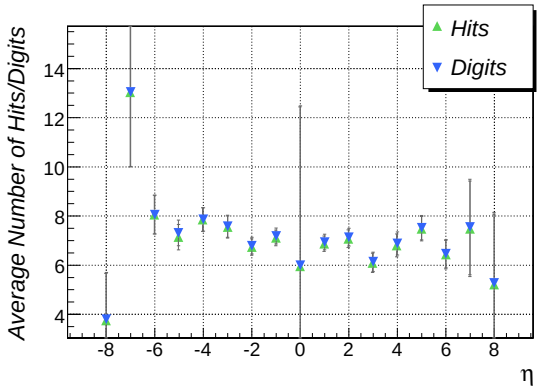

Fig. 3.5: Comparison of the average number of MDT chamber hits and digits per event versus η position of the chamber.

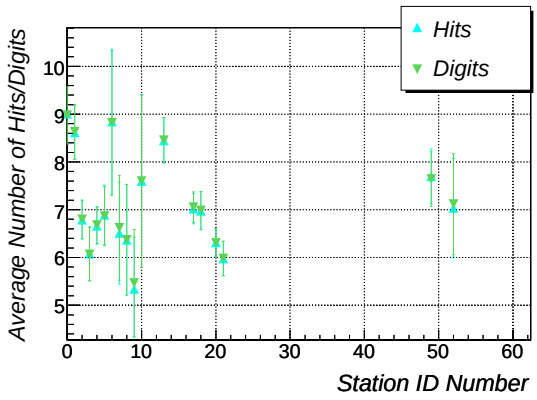

Fig. 3.6: Comparison of the average number of MDT chamber hits and digits per event for 1000 events versus chamber name.

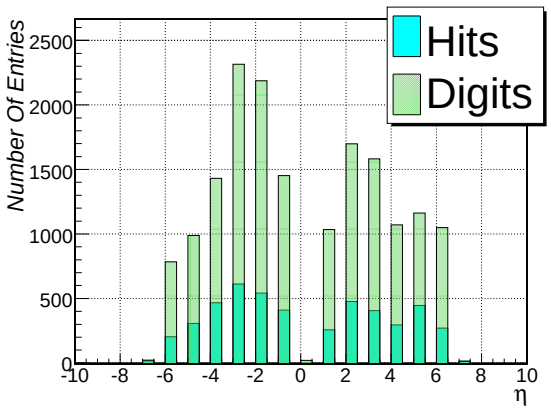

Fig. 3.7: Comparison of the overall number of RPC chamber hits and digits versus η position of the chamber.

In these figures, which refer to the ideal initial detector geometry, no significant differences in the overall and the average numbers of hits and digits can be seen for

the MDT chambers. More hits than digits are expected for MDT chambers, since in a single particle crossing the discriminator threshold of the tube read out can be passed several times. Therefore it was chosen that only one hit per tube and event is counted for the validation of MDT chamber simulation, secondary hits are neglected. These quantities are calculated for each chamber separately as well as for all chamber with the same η, ϕ and station name. The latter choice is done since the number of stations is too large to be compared one by one efficiently. Not only the overall hits and digits multiplicity comparison might be used for validation. The average number of hits/digits per event for a given chamber type is also of interest: Roughly six digits per muon passing through a six layer MDT chamber are expected, which is perfectly consistent with the average value shown in Figure 3.6.

The validation procedure of RPC, TGC and CSC chambers is more complicated, since their structure (more than one read-out strip or wire for one gas volume) implies that one hit in the simulation steps leads to several digits. This explains the large excess of digits shown in Figure 3.7.

With the variables defined so far, only inefficiencies in the simulation of the complete chamber but not on lower levels, e.g. on the tube level for MDT chambers, can be detected. If no inefficiencies at the MDT tube level are assumed, it is expected that each digit has a parent hit at simulation level. The inverse association is not so trivial since some hits might be not digitized. Figures 3.8 and 3.9 show the association probabilities for a hit to give a digit and for a digit to be associated with a parent hit for the above simulated event sample.

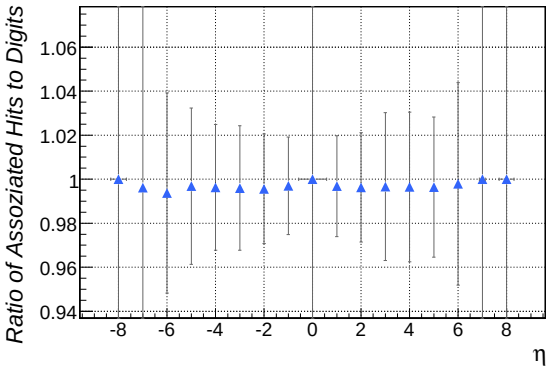

Fig. 3.8: Probability of MDT chamber hits to get digitized for 1000 events versus η position of the chambers.

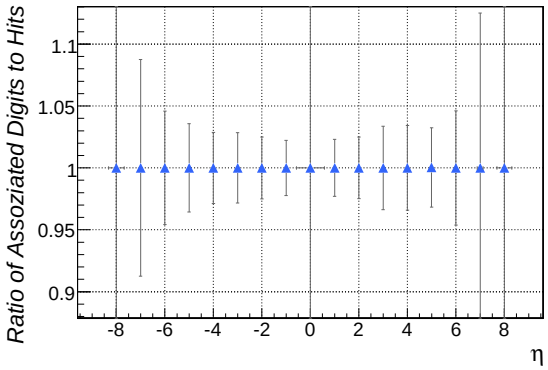

Fig. 3.9: Probability of MDT chamber digits to have a parent hit for 1000 events versus η position of the chambers.

The association probability for digits to hits is 100% as expected. The inverse association probability is less than 100%, which is an indication that not all hits have been digitized. This explains the small excess of hits seen in Figure 3.4.

In Figures 3.10 to 3.13 the comparison of the digit multiplicity for two different muon spectrometer geometries is shown. The first detector geometry layout (labeled

as *Ideal*) describes the ideal positioning of the chambers, while the second layout describes a misaligned muon spectrometer (labeled as *Misaligned*), in which the positions of the all chambers are shifted randomly by 1 mm in each direction and by 1 mrad for each angle on average.

A larger amount of MDT chamber digits is seen in the ideal compared to the misaligned layout (see Figures 3.10, 3.11), which could be explained by the overlapping of chambers in the latter case. No significant difference can be seen for RPC and TGC chambers (see Figures 3.12, 3.13).

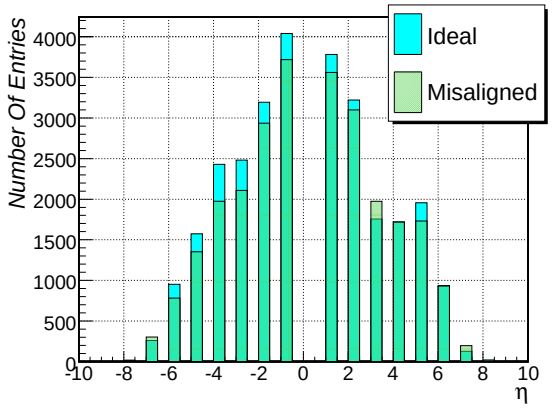

Fig. 3.10: Comparison of the overall number of MDT chamber digits for two different geometries versus η position of the chambers.

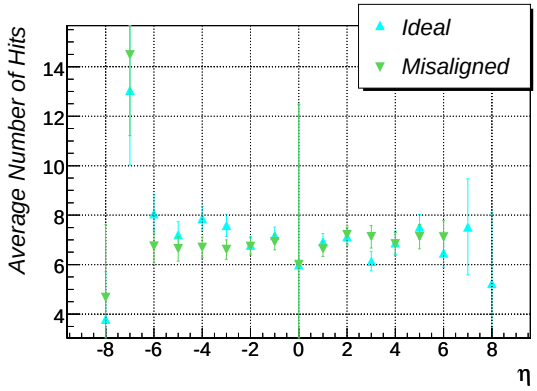

Fig. 3.11: Comparison of the average number of MDT chambers digits per event for two different detector geometries versus η position of the chambers.

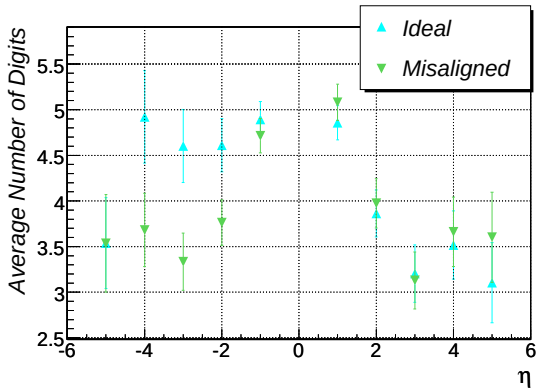

Fig. 3.12: Comparison of the average number of TGC chamber digits per event for two different detector geometries versus η position of the chambers.

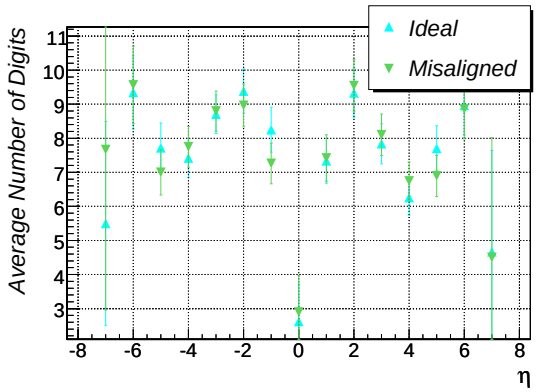

Fig. 3.13: Comparison of the average number of RPC chamber digits per event for two different detector geometries versus η position of the chambers.

4

Offline Muon Data Quality

In this chapter, tools monitoring the quality of experimental data acquired with the muon spectrometer are presented. An overview of the data quality monitoring framework and its scope is given in Section 4.1. In Section 4.2 a package for data quality monitoring in the muon spectrometer is described. Finally, examples of the monitoring process for MDT and RPC chambers are summarized in Section 4.3

4.1 Motivation and Overview

Data Quality Monitoring (DQM) is an important aspect of the data taking process of high energy physics experiments. For the ATLAS experiment, with about 140 million electronic channels and an event rate of 10^5 Hz, hardware status monitoring and data quality determination is vital. In the online environment, DQM signals the shift crew to take action in order to avoid collecting faulty data. In the offline enviroment one can perform more complex checks, using higher level information to determine the quality of the already collected data.

The ATLAS collaboration has developed a framework for data quality monitoring (DQMF) [31]. In the DQMF analysis algorithms are applied to the data from various subdetectors. The algorithms provide the relevant monitoring information in form of histograms which are compared to reference histograms. If the deviation from the reference histograms is too large, a warning is sent to the shifter and archived for later investigation.

4.2 Muon Data Quality Monitoring

The quality of data acquired by the muon spectrometer can be monitored by means of a few basic distribution related to the operation of the muon chambers. The following quantities are used to monitor the integrity and quality of data of MDT chambers:

- **Number of hits per chamber multilayer.** The mean number of hits in a multilayer of a chamber should be equal to the number of tubes crossed by a muon. A higher mean number of hits in a chamber is an indication for

accidental hits which can be caused by electronics noise. A lower mean number of hits in a chamber is an indication for inefficiencies.

- **Hit distribution in a chamber.** The distribution of hits in a chamber should reflect the illumination of the chamber with muons. It is therefore a smooth distributions. Holes or dips in the distribution show inefficient tubes. Spikes are used to spot tubes with a high rate of accidental hits.

- **Pulse height spectrum.** The heights of muon pulses have a Landau like shape. Very small pulses are due to electronics noise. The amount of small pulses indicates the level of electronics noise in a chamber.

- **Drift time spectrum.** Muons in a given event cause hits within the minimum and maximum drift time. Accidental hits can have smaller times than the minimum drift time and larger times than the maximum drift times. The amount of hits with unphysical times is a measure for the accidental hit rate of the tubes of a chamber.

The monitoring of the data from RPC trigger chambers is based on the number of hits, the hit profile, and the hit times. In order to assure that the RPC and MDT read-out is synchronized, the correlation of the positions of RPC and MDT hits is used.

4.3 Application to data from the commissioning with cosmic muons

Since the end of 2006, the muon spectrometer is successively taken into operation and commissioned with cosmic muons. The quality of the data was monitored in the way described above. Figure 4.1 shows the monitoring distribution of an 8-layer muon chamber in the top sector of the muon spectrometer barrel. The distribution of the number of hits in a multilayer (Figure 4.1 a) peaks at 4 as expected for a chamber with a quadruple layers. This shows that the chamber as a whole is not noisy. However, the distribution of hits in a layer (Figure 4.1 b) shows that one tube is noisy and has given hits many more times than the other tubes. The accidental hits in this tube lead to entries with unphysical drift times (see Figure 4.1 d). Most of the accidental hits have very small pulse heights. These lead to the spike at about 40 ADC counts in Fig. 4.1 c) while the muon hits lead to the Landau like pulse-height distribution. Almost all hits with unphysical drift times are removed from the drift-time spectrum in Figure 4.1 e) by rejecting hits with ADC counts below 50.

The positions of MDT hits are plotted versus the positions of RPC hits in Figure 4.2. The clear correlation between the two shows that the read-out of MDT and RPC chambers was synchronous.

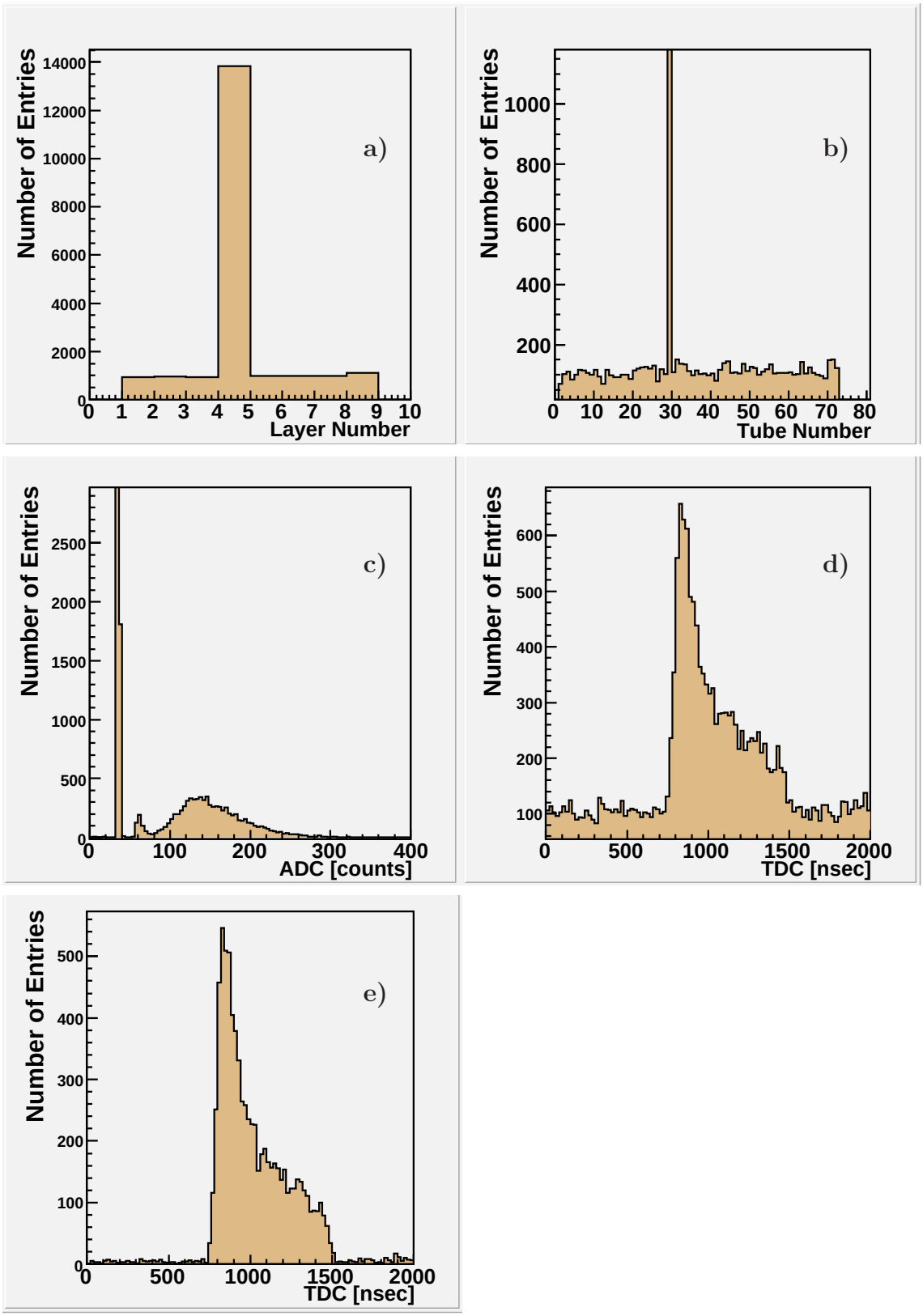

Fig. 4.1: Basic monitoring plots for MDT chamber BIL3C05: a) Mean hit per number per chamber multilayer. b) Hits per tube within a layer. c) Pulse height spectrum in ADC counts. d) Drift time TDC spectrum in nsec. e) Drift time TDC spectrum in nsec for hits with a pulse height ADC value above 50.

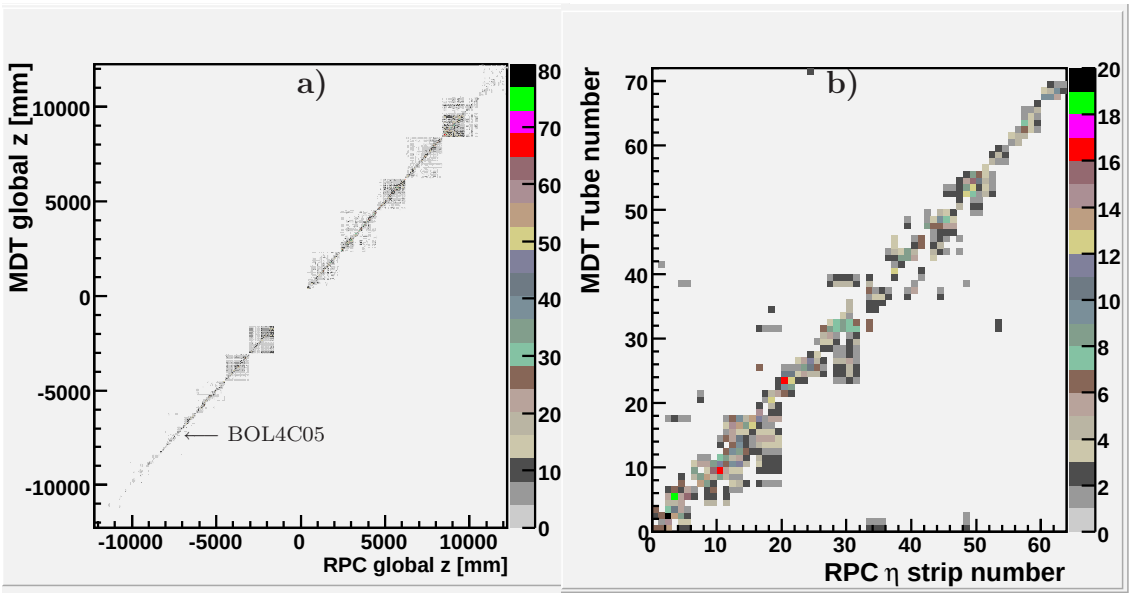

Fig. 4.2: MDT-RPC correlation plots for barrel sector 5. a) correlation between BOL MDT the unigue RPC layer in this station. For all three plots the vertical axis indicates the global hit position in z coordinate, as measured from MDTs, in mm. The horizontal axis indicates the global hit position in z coordinate, as measured from RPCs, in mm. Focusing in more detail in a specific chamber (BOL4C05 - Barrel large chamber of the outer layer located on the top of the detector), plot b) illustrates the same correlation within a chamber. The vertical axis indicated MDT tube number within a layer, while the horizontal RPC η strip within a Gas Gap.

Based on the histograms presented here a set of commissioning data of high quality was selected to study the performance of the autocalibration of the space-time relationship of MDT chambers. The results of this study are presented in the next chapter.

5

Calibration of the MDT Chambers with Cosmic Rays

In this chapter the calibration of the MDT chambers is discussed. A brief introduction of the calibration procedure is given in section 5.1. The calibration methods are described in Section 5.2. In section 5.3, we present tests performed on the new analytical autocalibration algorithm. Finally, we compare the conventional and the analytical autocalibration methods in Section 5.4.

5.1 Introduction

Calibration of the MDT chambers means determination of the range-to-drift-time or r(t)-relations of the drift tubes, where r is the radial drift distance and t the measured drift time. When a muon passes through the volume of the drift tube, it ionizes the argon atoms along its trajectory creating clusters of free electrons and positively charged ions. Both electrons and ions travel under the influence of the electric field inside the tube towards the sense wire (anode) and towards the tube wall (cathode) respectively. The r(t)-relation connects the drift time of the electrons to the drift radius. Autocalibration means, that reduntant information in the muon track reconstruction in an MDT chamber is used for calibration of the r(t)-relationship and no external reference is needed (see below).

The calibration methods have been tested with data from cosmic ray muons taken with the bottom sector of the ATLAS muon spectrometer after its installation.

5.2 Algorithms

5.2.1 Integration Method

The simplest method for determinating the r(t)-relation is based on the assumption of homogeneously illuminated drift tubes, i.e. the number of the incident tracks per drift radius interval can be taken as constant. Calculating the number of tracks per drift time interval one obtains:

$$\frac{dN}{dt} = \frac{dN}{dr} \cdot \frac{dr}{dt} = \frac{N}{r_{max}} \cdot \frac{dr}{dt} \quad , \tag{5.1}$$

where r_{max} denotes the maximum drift radius equal to the inner tube radius (14.6 mm). Solving Equation 5.1 for dr/dt and integrating over t, a first approximation of the r(t)-relation is obtained:

$$r(t) = \int_0^t \frac{r_{max}}{N} \frac{dN}{dt'} dt' \quad . \tag{5.2}$$

The accuracy of r(t)-relation determined with this method is about 200 μm, which is an order of magnitude higher than the required accuracy. The discrepancy is due to δ-electrons which are knocked out of the tube walls by the incident muons. δ-electrons ionize the gas fill like the muons and create hits. If the distance of the δ-electron from the anode wire of a tube is larger than the distance of the muon, the muon hit is masked by the earlier δ-electron hit. Therefore, short drift times appear more frequently than longer ones, meaning that the homogeneous irradiation of a drift tube is only at first approximation. The r(t)-relation obtained through integration is appropriate only as a starting value for a more accurate calibration process.

5.2.2 Conventional Autocalibration Method

Improvement can be achieved by the so called conventional autocalibration method. In this method, the r(t)-relation obtained from the integration method is further improved by using correlation among tubes crossed by a muon. In the case of three tube layers three drift radii r_1, r_2 and r_3 are considered. The three radii are used in a straight track fit. For each tube k=1,2,3 the residual $\Delta(t_k) = r(t_k) - d_k$ is calculated, where d_k is the shortest distance between the fitted trackand the k-th wire. The residuals are averaged over a large number of tracks and the r(t)-relation is iteratively replaced until $|\langle\Delta(t_k)\rangle| \leq 1\mu$m:

$$r(t)_{i+1} = r(t)_i - \langle\Delta(t)\rangle \quad , \tag{5.3}$$

where $\Delta(t)$ is the average over all muon tracks. The same r(t)-relation is assumed over three layers. Conventional autocalibration has the problem for tracks hitting a tube in an incident angle near 30^o, which result in tracks with the same drift radius in all tube layers. Therefore minimization of averaged residuals does not improve the r(t)-relation.

5.2.3 Analytical Autocalibration

The analytical autocalibration takes into account correlations between the residuals in individual drift tube layers and provides an improved r(t)-relation in the angular range atound 30^0 [35], [36]. It can be shown [35] that the residual is a linear combination of the (systematic) errors $\epsilon(t)$ of the r-t relationship for small $\epsilon(t)$:

$$\Delta(k) = \sum_{hits\ i} m_{ki}\epsilon(t_i); \tag{5.4}$$

the coefficient matrix can be calculated analytically and is derived in [Mario's PhD thesis].

It can be shown that Equation (5.4) has no unique solution for a single track in general. Only the combination of a set of tracks with different incident angles lead to a set of residual equations which have a unique solution. As Equation (5.4) is only exact in the limit of $\epsilon(t) \to 0$, iterations are needed until the analytic autocalibration leaves the input r-t relationship unaltered.

5.2.4 Methods

The performance of the conventional and the analytic autocalibration are studied with cosmic-muon data in this chapter. The focus of the study is on the speed of convergence of the two algorithms in terms of number of iterations and required number of tracks.

5.3 Tests with the Analytical Autocalibration

In the next pages, for all MDT chambers in sector 13 an r(t)-relation will be determined using the integration method. This r(t)-relation will be further used to perform the optimized calibration algorithms. The maximum available number of muon tracks will be used for all chambers. It is necessary to mention that, the MDT chambers in the inner station (BIL) have registered only around 7000 tracks and therefore, the results are expected to be worse than for other chambers. If not stated explicitly, the data used will be those from MDT chamber BML3A07.

5.3.1 Autocalibration using different number of tracks

Before moving further in this study, it would be interesting to determine how many muon tracks are needed in order to obtain a satisfactory r(t)-relation. For this reason, we compare the results using different numbers of tracks each time.

As illustrated in Figure 5.1 for the chamber BOL3A07, for less than 1000 tracks the required accuracy of 20 μm is not achieved. Using approximately 1500 tracks, the obtained accuracy is within the required limits and with 2000 tracks satisfactory results with an RMS of 14.2 μm are achieved. The results obtained by using other chambers are similar. In the next steps of the study, 2000 muon tracks will be used.

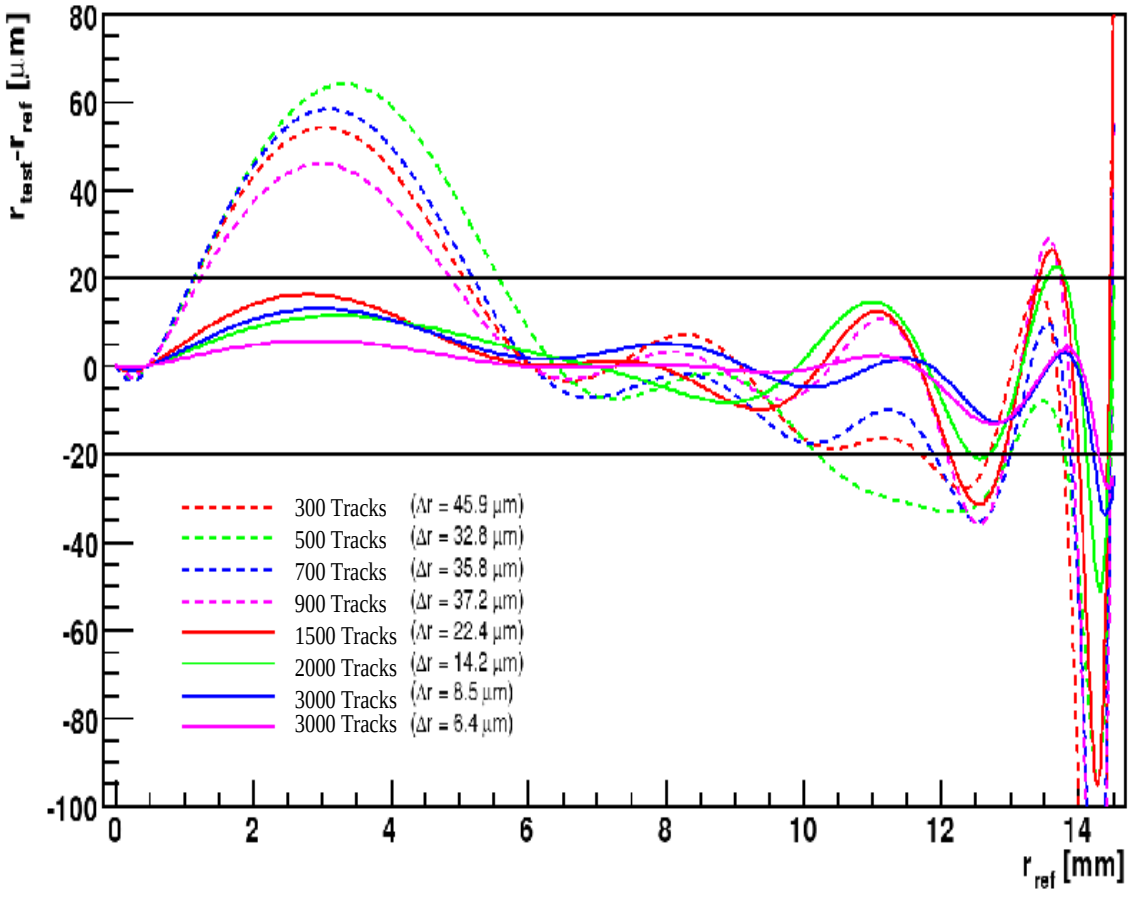

Fig. 5.1: Quality of the analytic autocalibration for different numbers of muon tracks used in chamber BOL3A07. The vertical axis indicates the difference between r(t)-relation using various number of tracks to the reference r(t)-relation, obtained by using the maximum number of tracks (10000). The horizontal axis indcates the drift radius. Δr corresponds to the mean value of $|r_{test}\text{-}r_{ref}|$.

An interesting effect is the large deviation for drift radii longer than 14 mm and it will be explained in detail in the following pages.

5.3.2 Comparison of the r(t)-relations from different stations

The fact that chambers in a specific station have the same structure and geometry setup, motivates us to compare the r(t)-relations from these chambers. If the differences were small enough, then the whole calibration process could be applied to only one of the chambers. This is not the case as will be shown here. In Figure 5.2 we

present the results for the BML station. The discrepancy from chamber to chamber is almost always larger than the 20 μm requirement. Therefore, it is obvious that the calibration process should be applied in each chamber separately.

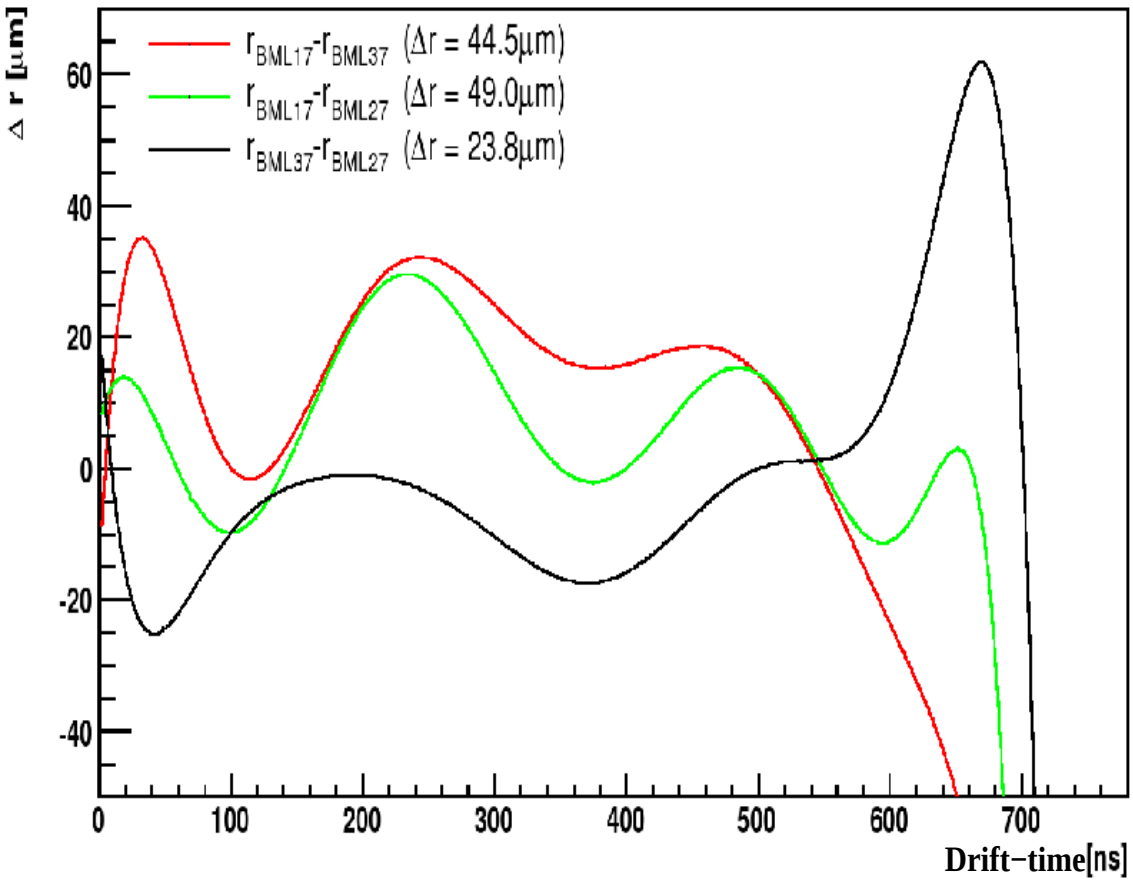

Fig. 5.2: Comparison of the r(t)-relations inside the BML station. The vertical axis indicates the difference of the r(t)-relations for a different pair of BML chambers each time. The horizontal axis indicates the drift time. Δr values correspond to mean discrepancies.

The chambers of the BIL station where not filled with the right gas mixture as the chambers of the BML and BOL stations. This fact is a motivation to investigate the discrepancy in the r(t)-relations for the different gas mixtures. Comparing the r(t)-relation differences in the three stations (see Figure 5.3), it is shown that the difference between BIL and BML or BOL chambers is smaller than the difference between BML and BOL. This is attributed to the temperature differences between the these chambers.

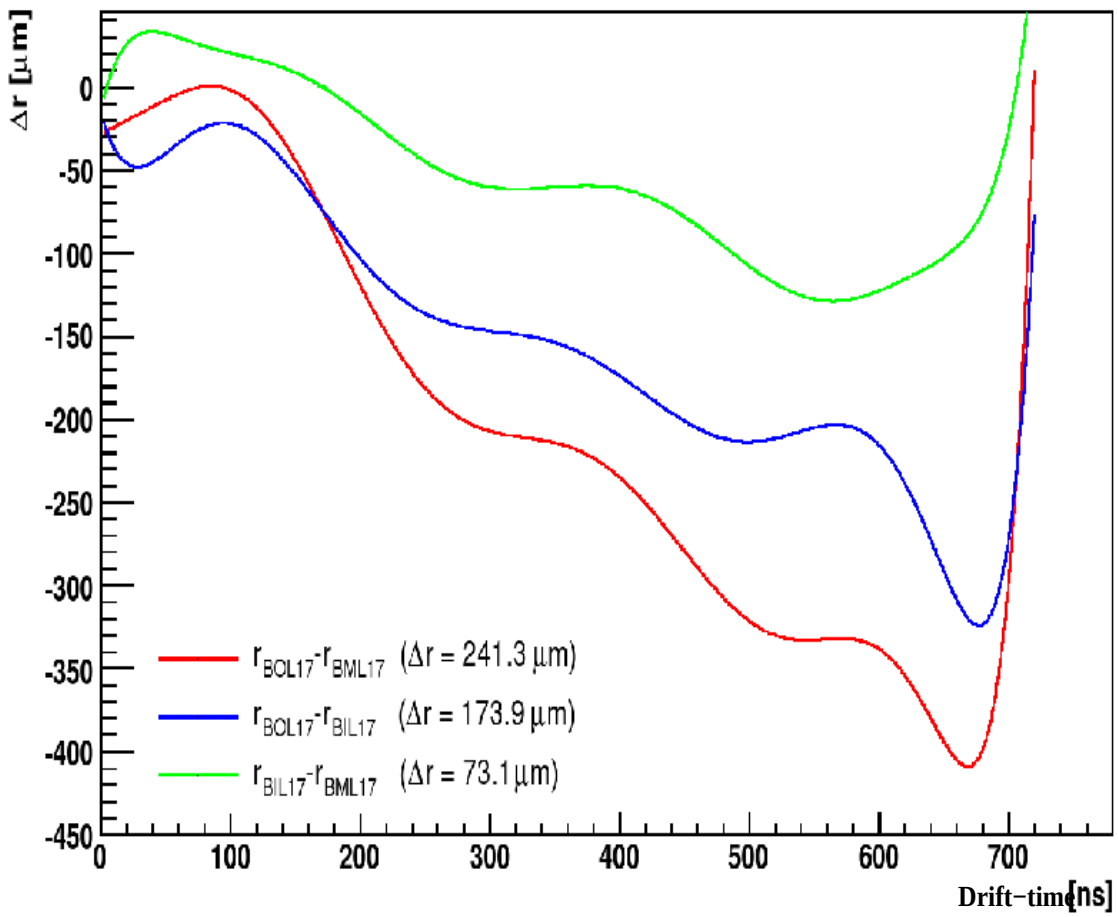

Fig. 5.3: Comparison of the r(t)-relations between different stations. The vertical axis indicates the difference of the r(t)-relations for a different pair of chambers each time. The horizontal axis indicates the drift time. Δr values correspond to mean discrepancies.

5.3.3 Comparison of the correction functions

In the calibration algorithm, three different kinds of correction functions were implemented: Legendre and Chebyshev polynomials and as a different approach, polygons. Comparing the two kind of polynomials, it is found that only a small diference in the coefficient exists. Due to this, the results from the two polynomial kinds are almost the same. In Figure 5.4, the comparison is illustrated. In the r(t)-relation graph one can note a steep rise and then a fall for large drift times. In the case of polygons this behaviour is even more prominent, which indcated that the use of polynoms is preferable.

Order	Chebyshev	Legendre
0	1	1
1	x	x
2	$2x^2-1$	$\frac{1}{2}(3x^2-1)$
3	$4x^3-3x$	$\frac{1}{2}(5x^3-3x)$
4	$8x^4-8x^2+1$	$\frac{1}{8}(35x^4-30x^2+3)$
5	$16x^5-20x^3+5x$	$\frac{1}{8}(63x^5-70x^3+15x)$

Tab. 5.1: Table indicating the Chebyshev- and Legendre-polynomial terms for various orders.

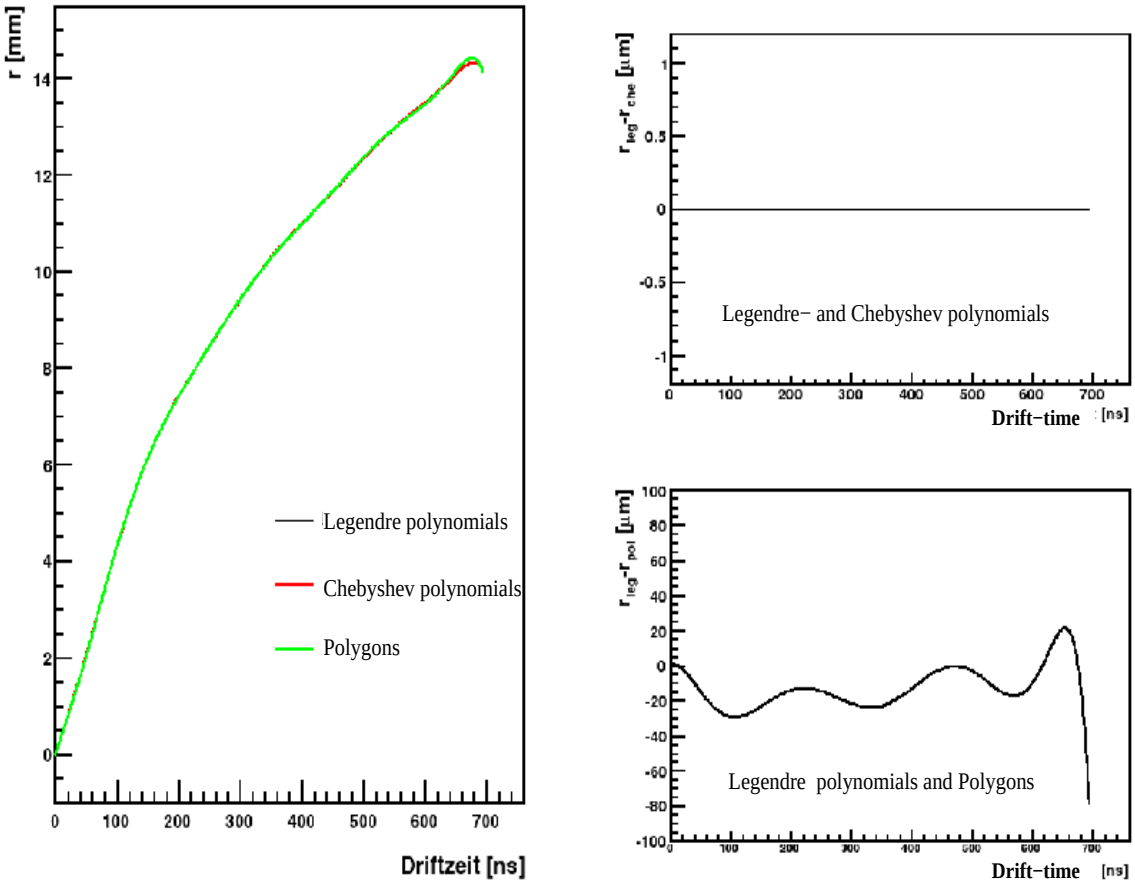

Fig. 5.4: Comparison of the results from different correction functions. The left graph illustrates the different r(t)-relations. The upper right plot shows the difference between the two kinds of polynomials, while the lower right plot shows the difference between the Legendre-polynomials and the polygone function.

5.3.4 Comparison for different orders of the correction polynomial

Usually polynomials of 15^{th} order were used in the calibration algorithm. The optimal order was found by studying the deviation of the results yielded by polynomials of various orders, when compared to the results of 22^{th} order. As shown in Figure 5.5 from the order of 16 and above no particular discrepancy exists. This behaviour is common in both Legendre and Chebyshev polynomials.

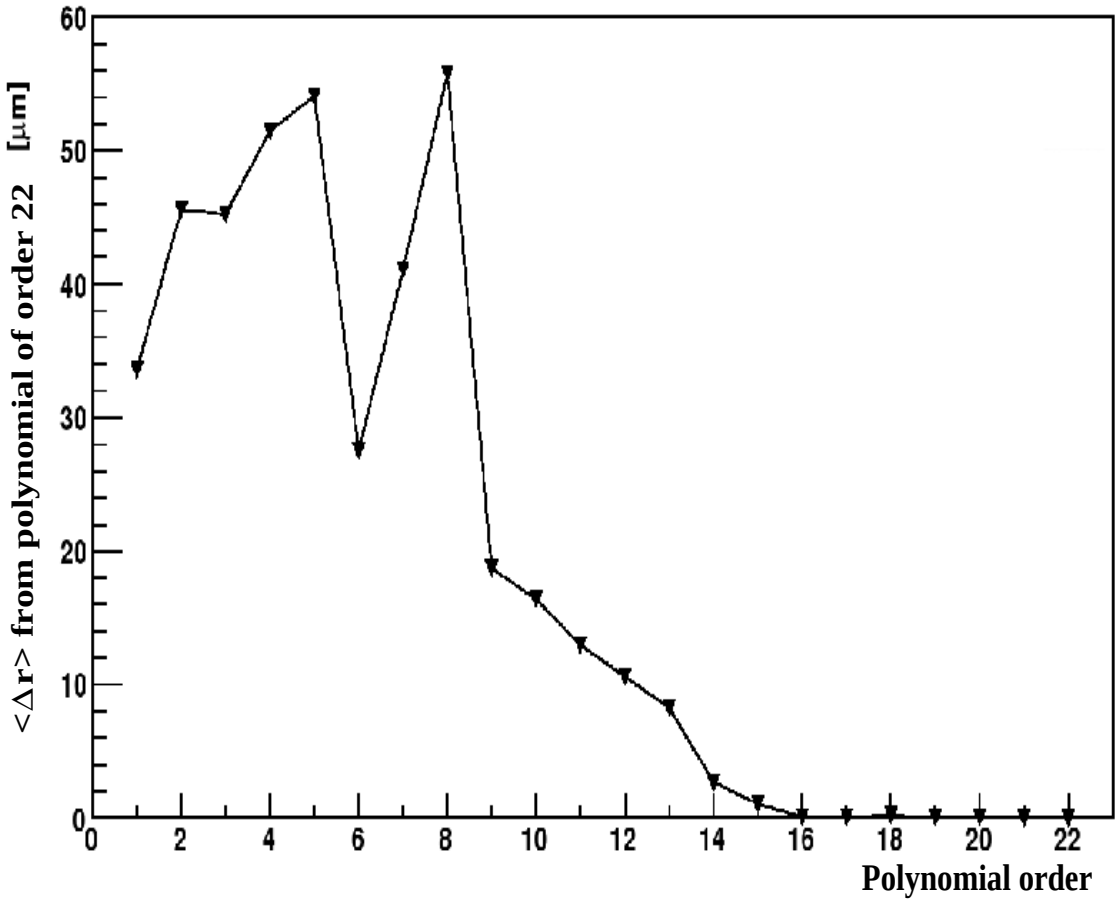

Fig. 5.5: Comparison of the results for different polynomial orders. The vertical axis indicates the r(t)-relation mean difference of various order polynomials to the 22^{th} order reference polynomial.

5.3.5 Behaviour for fixed start and end points

The algorithm offers the additional functionality, to constrain the r(t)-relation in the start and end-points r(0)=0 and $r_{max}(t_{max})$=14.6 mm. The r(t)-relation calculation

with fixed points yield an even more prominent rise of the curve for large drift times, while in the rest of the range the two curves are identical (see Figure 5.6). Therefore the option of fixed points in the calibration process is not appropriate.

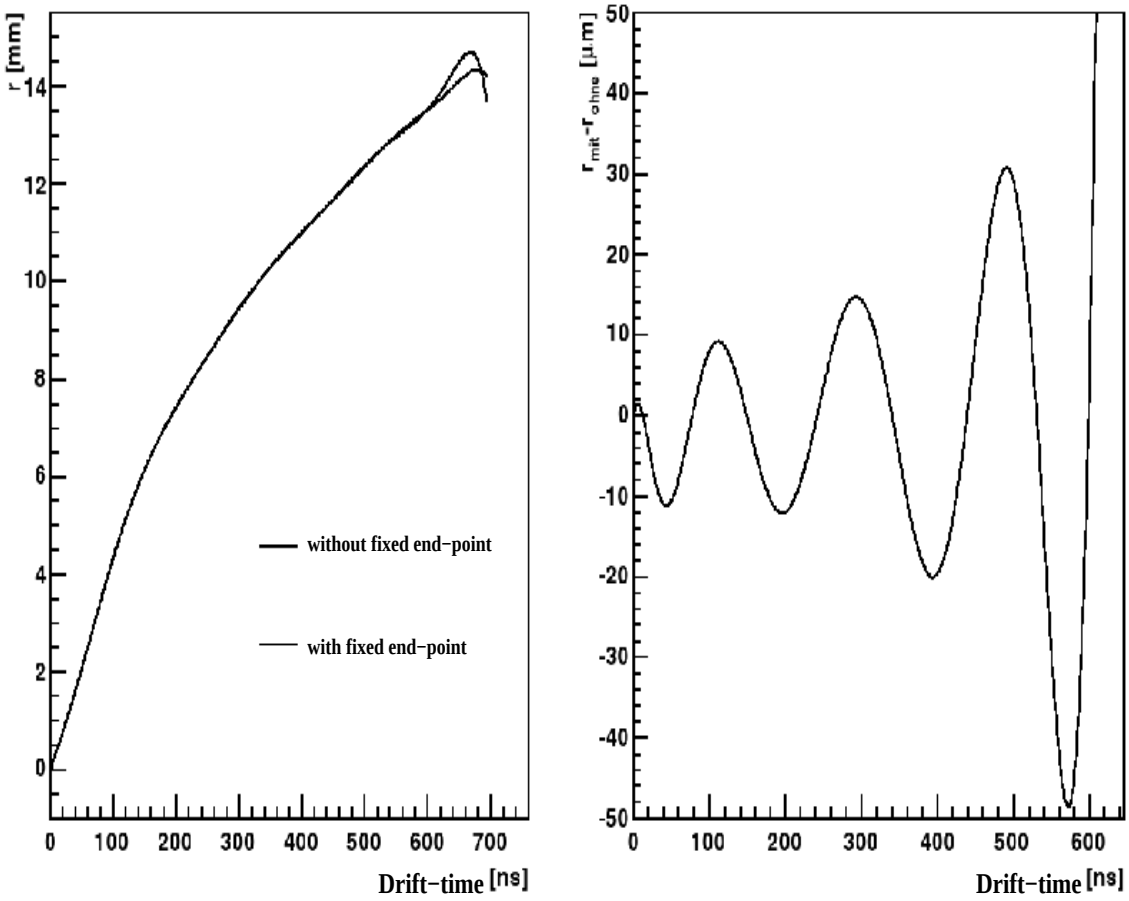

Fig. 5.6: Results for r(t)-relation with fixed end-point. The left graph shows the r(t)-relations with and without fixed end-points. The right graph illustrates the diffrence between the two r(t)-relations.

If both points are left unconstrained, then the artifact in the high drift times range disappears (see Figure 5.7). The deviation of the unconstrained to the constrained r(t)-relation reaches up to 210 μm. Simulation confirms that the most realistic description of data is obtained by using fixed start point and unconstrained end point [36].

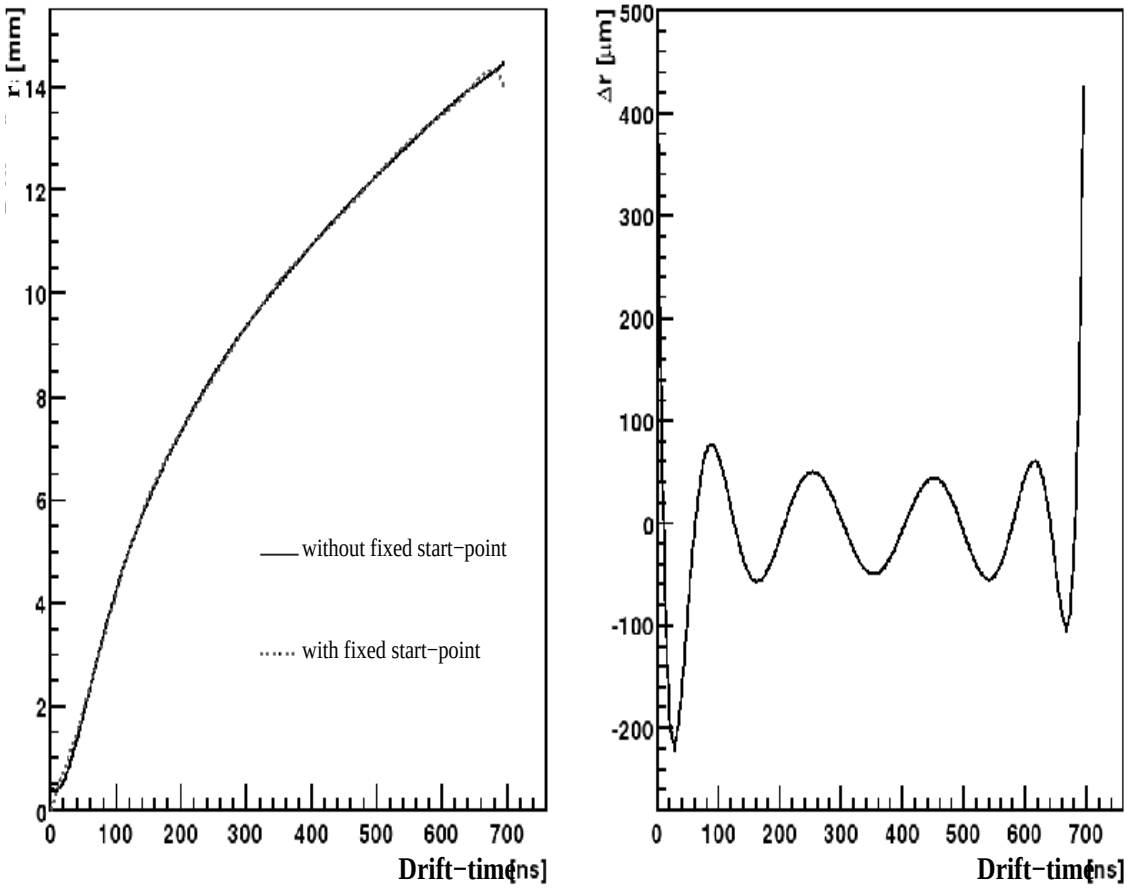

Fig. 5.7: r(t)-relation with fixed start-point. The left graph indicates the comparison between r(t)-relation with and without fixed start-point. The right graph shows the difference between the two.

5.4 Comparison between conventional and analytical method

In the following section, the performance of the conventional autocalibration will be compared with that obtained from the analytical. It will also be investigated whether it is better to restrict the autocalibration to a multilayer of the muon chamber, or to perform it with tracks reconstructed in the whole chamber.

5.4.1 Direct comparison with and without Multilayer-splitting

The comparison of the conventional and the analytical methods as a function of drift time (Figure 5.8), show that the two methods agree when no multilayer splitting is applied for the conventional autocalibration method. In that case the deviation between the two methods is less than the required 20 μm accuracy, in the whole drift times range.

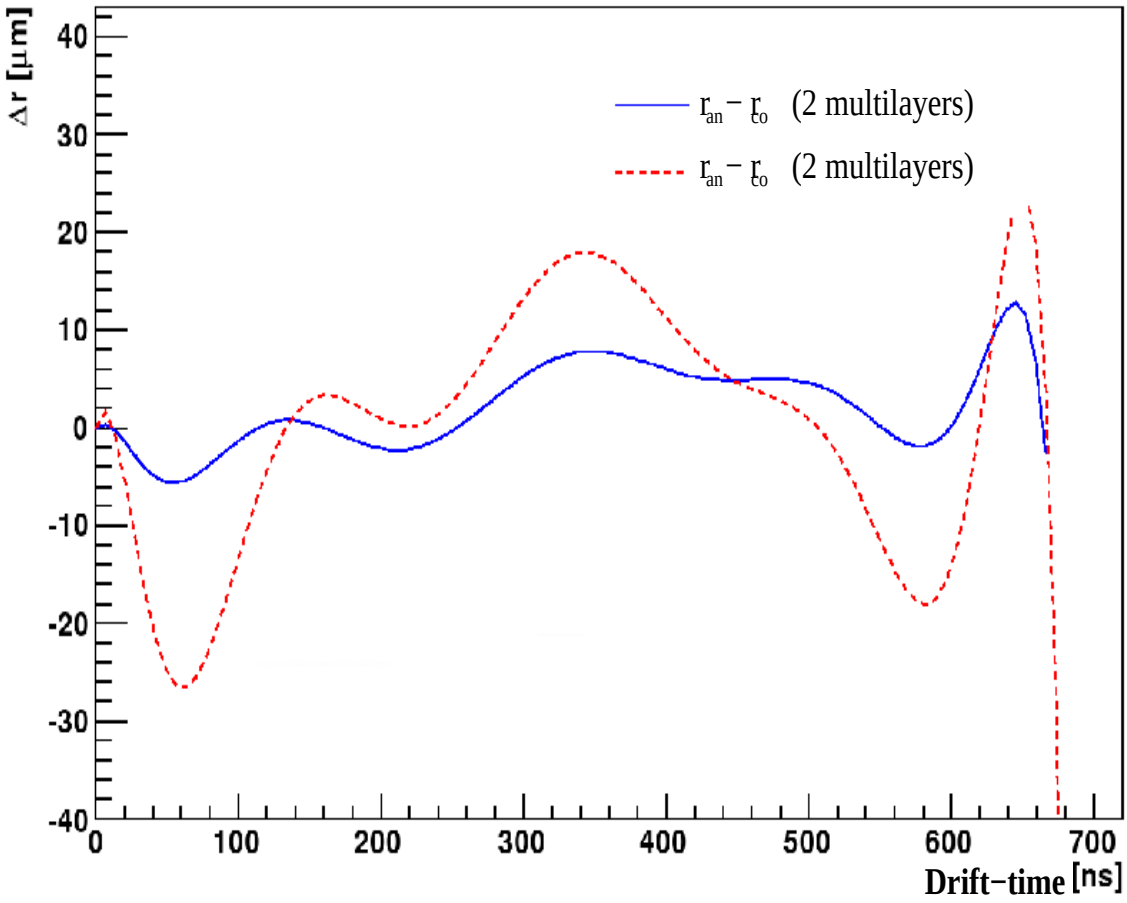

Fig. 5.8: Difference between the analytical and conventional autocalibration methods. Continuous line indicates the case without multilayer splitting (both multilayers) while the dashed line with multilayer splitting (one multilayer).

5.4.2 Comparison of the number of required iterations

As a further step, we investigate the required number of iterations for the conventional and the analytical autocalibration process, both with and without multilayer

splitting. For the cases of the analytical method with as well as without multilayer splitting and for the conventional method without multilayer splitting, the results are within the 20 μm accuracy limit after 5 iterations. The convetional method with multilayer splitting requires 7 iterations in order for the same accuracy to be achieved (see Figure 5.9). The conventional method using both multilayers and the analytical in only one multilayer show identical behaviour, while the analytical using both multilayers converges faster.

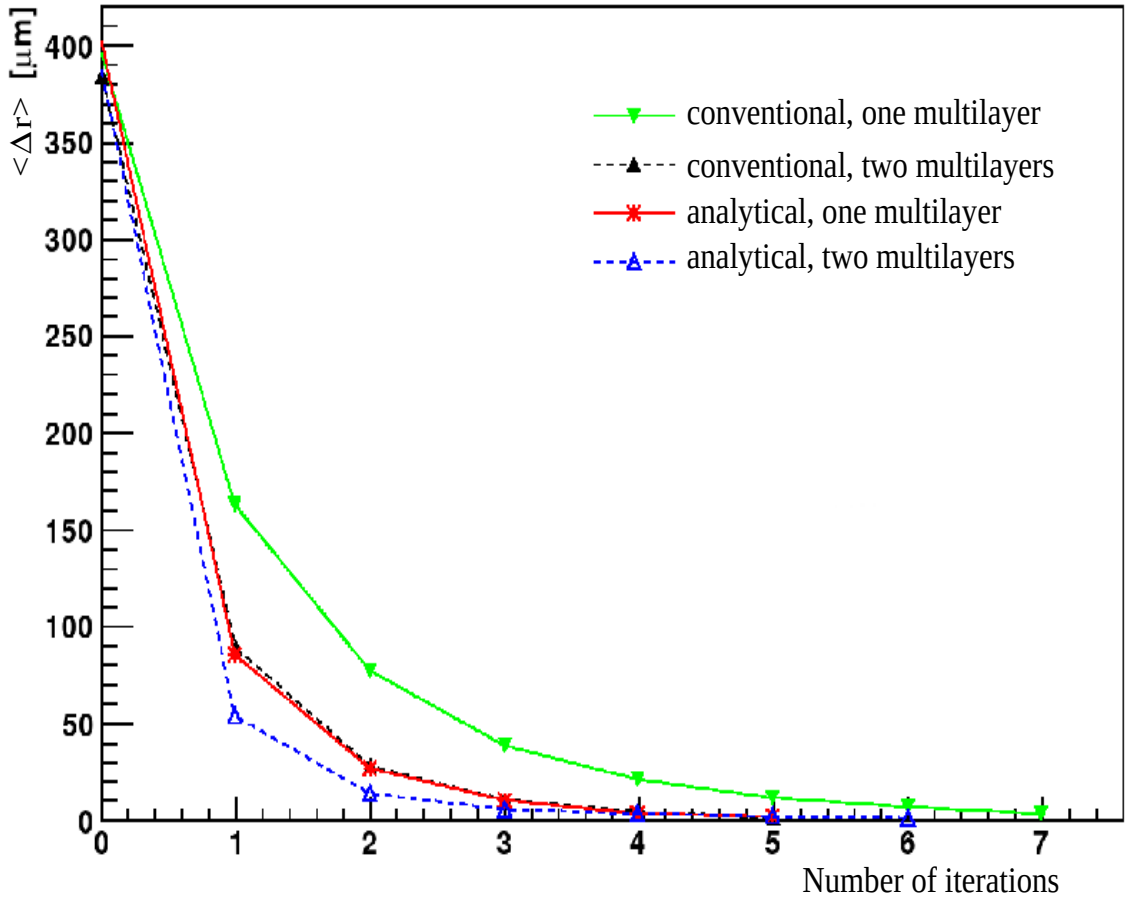

Fig. 5.9: Convergence of the two methods under different conditions as a function of the number of iterations. The vertical axis denotes the mean deviation from the case where the maximum number of iterations were used.

5.4.3 Comparison of the number of required muon tracks

Investigating further the differences between conventional and analytical method, we compare convergence of each method as a function of the number of used tracks. As showed in Figure 5.10, for both methods no significant discrepancy is observed. We

further note that there a difference for each method, depending if both or only one multilayer is used. Using two multilayers yields in both cases better convergence.

The advantage of the analytical autocalibration method is that, the full information for the residuals af the r(t)-relation is used. Also, when using two multilayers, due to the larger number of tubes, more fix points are available for the autocalibration process.

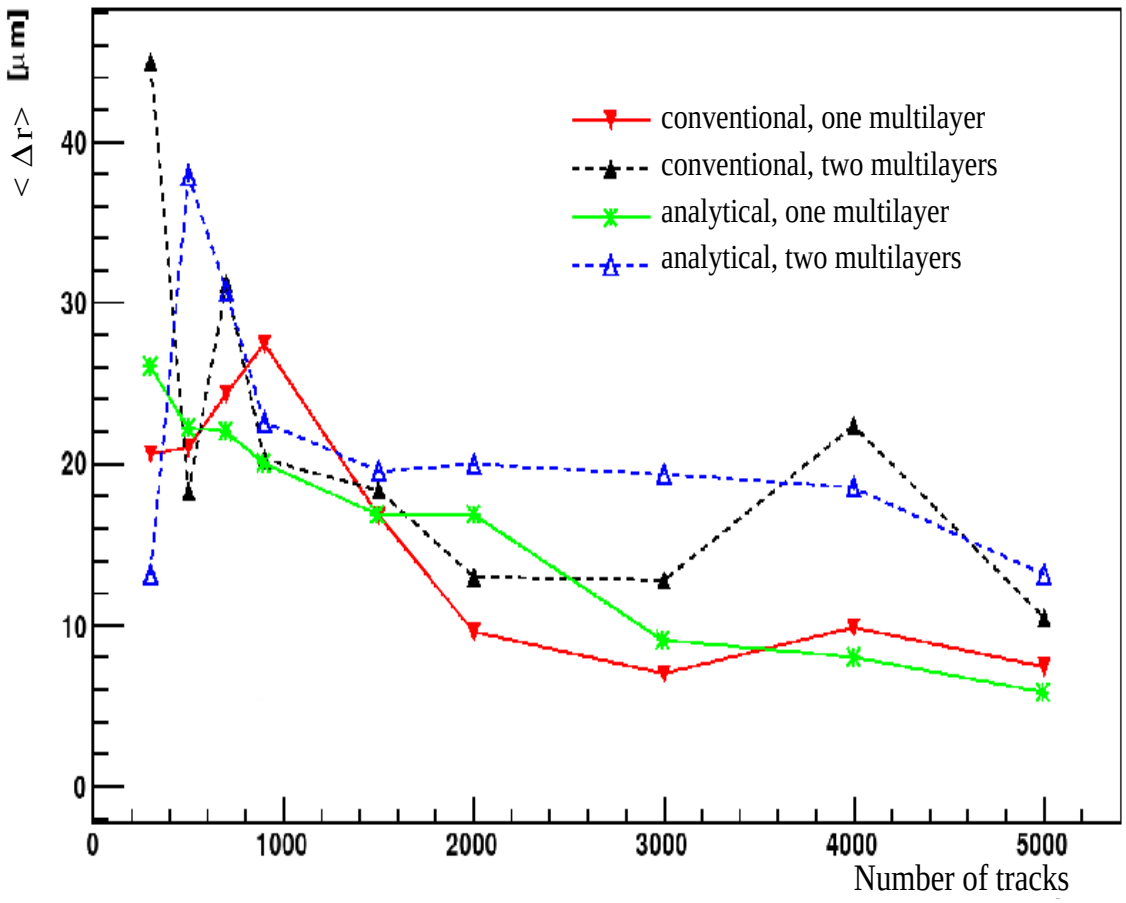

Fig. 5.10: Convergence of the two methods under different conditions as a function of the number of used tracks. The vertical axis denotes the mean deviation from the case where the maximum number of tracks were used.

5.5 Summary

In this chapter, the analytical autocalibration method was introduced. It is an iterative process in which the difference (residual) between the true and the experimental the r(t)-relation of MDT chambers, is parametrized with a Legendre or Chebysev

polynomial. The accuracy achieved is better than 20 μm by using approximately 2000 tracks per chamber and both chamber multilayers. The number of required iterations is less than 5 and as shown, the results are comparable with those obtained from the conventional autocalibration method, however the analytic approach guarantees faster convergence.

6

Higgs Mechanism in the Standard Model and Supersymmetric Extensions

This chapter gives a brief introduction to the physics aspects at LHC which are relevant for this thesis. A short description of the Standard Model is given in Section 6.1, introducing the lagrangian of the electroweak sector of the Standard model. The Higgs mechanism responsible for electroweak symmetry breaking is introduced in Section 6.2. Open questions in the Standard Model and motivation for supersymmetric extensions are presented in Section 6.3. In particular the Minimal Supersymmetric extension of the Standard Model (MSSM) is described in Section 6.4 and the MSSM Higgs sector in 6.5. Finally, the Higgs production mechanisms and decay modes are presented in Section 6.6. More detailed description can be found in [37], [38] and [39].

6.1 The Standard Model

The Standard Model (SM) of elementary particle physics is an elegant framework for the description of the phenomena of the sub-nuclear world. Its theoretical predictions have been verified with high accuracy by many experiments during the past decades.

The Standard Model describes three fundamental interactions of elementary particles in a uniform way:

- Quantum electrodynamics (QED) describes the interactions of electrically charged particles.
- The weak interaction, responsible for instance, for radioactive decays, is unified with QED in the Glashow-Salam-Weinberg theory.
- Quantum chromodynamics (QCD) describes the strong interaction between quarks and gluons.

In the Standard Model, two types of particles are distinguished according to their spin: particles with spin 1/2 called *fermions* are the matter constituents, and particles with spin 1 called *gauge bosons* are the force carriers.

QED is an Abelian gauge theory defined by the U(1) gauge group. It describes the interaction between electrically charged particles via the exchange of a massless gauge boson with spin 1, the photon (γ). The electromagnetic and the weak forces are unified in the Glashow-Salam-Weinberg theory with the $SU(2) \otimes U(1)$ gauge symmetry group. The weak interaction is mediated by three gauge bosons, W^+, W^- and Z^0. The three bosons are massive and have been observed experimentally by the UA1 and UA2 experiments at CERN [41], [42], [43], [44]. Their masses were found to be $m_W = 80.403 \pm 0.029$ GeV/c^2 and $m_Z = 91.1876 \pm 0.0021$ GeV/c^2 [40]. The strong interaction between quarks is described by QCD, a non-Abelian gauge theory based on the $SU(3)$ colour symmetry group. It is mediated by 8 gauge bosons called gluons.

Left-handed and right-handed fermions are grouped in the following way in doublets and singlets, respectively, of the weak isospin:

$$\ell_{A_L} = \begin{pmatrix} \nu_A \\ l_A \end{pmatrix}_L, \quad l_{A_R}, \quad q_{A_L} = \begin{pmatrix} p_A \\ n_A \end{pmatrix}_L, \quad p_{A_R} \quad , \quad n_{A_R} \tag{6.1}$$

$$\begin{aligned} \nu_A &= \nu_e, \nu_\mu, \nu_\tau \quad , && (6.2)\\ l_A &= e, \mu, \tau \quad , && (6.3)\\ p_A &= u, c, t \quad , && (6.4)\\ n_A &= d, s, b \quad . && (6.5) \end{aligned}$$

and A the generation index. The dynamics of the fermions and their interactions with the weak gauge fields are described by the following Lagrangian $\mathcal{L}_F$ (assuming massles neutrinos and getting $\hbar = c = 1$):

$$\mathcal{L}_F = i \sum_A (\bar{\ell}_{A_L} D_L \ell_{A_L} + \bar{l}_{A_R} D_R l_{A_R} + \bar{q}_{A_L} D_L q_{A_L} + \bar{p}_{A_R} D_R p_{A_R} + \bar{n}_{A_R} D_R n_{A_R}) \tag{6.6}$$

where $D_{L,R} = \gamma^\mu D_{L,R_\mu}$ and D_{L,R_μ} are the following covariant derivatives, with

$$D_{L_\mu} = \partial_\mu - i g_1 \vec{I} \cdot \vec{W}_\mu - i g_2 \frac{Y}{2} B_\mu \quad , \tag{6.7}$$

$$D_{R_\mu} = \partial_\mu - i g_2 \frac{Y}{2} B_\mu \quad . \tag{6.8}$$

$\vec{W}_\mu = (W_{\mu,1}, W_{\mu,2}, W_{\mu,3})$ and B_μ are the gauge fields of the SU(2) and U(1) gauge groups of the Standard Model. g_1 denotes the weak isospin gauge coupling and g_2 the weak hypercharge gauge coupling. $\vec{I}$ and Y are the weak isospin vector and the hypercharge, respectively. The fields W_μ couple only to the left-handed fermions.

Finally, the gauge fields and their self interactions are described by the following Lagrangian $\mathcal{L}_G$:

$$\mathcal{L}_G = -\frac{1}{4}F^a_{\mu\nu}F^{\mu\nu}_a - \frac{1}{4}F_{\mu\nu}F^{\mu\nu} \quad , \tag{6.9}$$

where

$$F^a_{\mu\nu} = \partial_\mu W^a_\nu - \partial_\nu W^a_\mu + g_1\epsilon^{abc}W^b_\mu W^c_\mu \quad , \tag{6.10}$$

$$F_{\mu\nu} = \partial_\mu B_\nu - \partial_\nu B_\mu \quad . \tag{6.11}$$

ϵ^{abc} are the elements of the Levi-Civita tensor, the structure constants of the group $SU(2)$.

6.2 The Higgs Mechanism

The fermions and weak gauge bosons described by the above Lagrangians are massless which is required by the local SU(2) gauge symmetry. Of course, this contradicts the experimental results.

An elegant solution to this problem is provided by the Higgs mechanism, which introduces spontaneous electroweak symmetry breaking into the original massless Lagrangian. The mechanism implies that the Lagrangian of the system retains its invariance under the the local SU(2) gauge symmetry group while the ground state (vacuum) is not invariant.

For this purpose, a complex SU(2) doublet scalar field ϕ is introduced, described by the Lagrangian $\mathcal{L}_H$:

$$\mathcal{L}_H = (D_{L\mu}\phi)^\dagger D^\mu_L\phi - V_\phi \quad , \tag{6.12}$$

with the potential:

$$V_\phi = \mu^2|\phi|^2 + \lambda|\phi|^4 \quad . \tag{6.13}$$

μ is the mass parameter and λ the self coupling of the scalar field. Two cases can be distinguished for the value of μ^2:

1. If $\mu^2 > 0$, the potential has only one minimum for $\phi = 0$ (Figure 6.1 a). It describes a massive scalar particle with mass μ and quartic coupling λ.

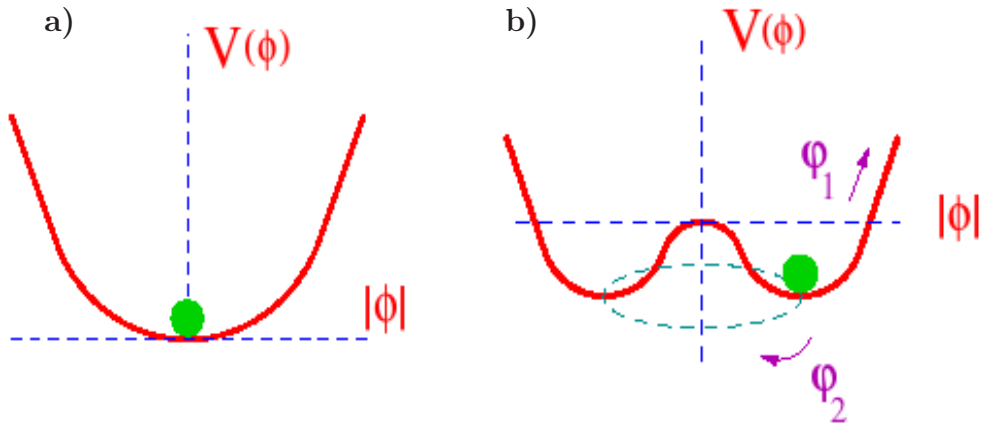

Fig. 6.1: Illustration of the Higgs potential: a) For $\mu^2 > 0$ the shape of the potential V_ϕ is a parabola and there is one minimum at ϕ=0. b) For $\mu^2 < 0$ there is a continuous set of degenerate vacuum states connected through massless field exitations [37]. In the Standard Model the potential is a function of four Higgs field components.

2. If $\mu^2 < 0$, the potential has the shape illustrated in Figure 6.1 b) with minimum for non-zero values of the scalar field:

$$|\phi_0| = \sqrt{\frac{-\mu^2}{2\lambda}} = \frac{\upsilon}{\sqrt{2}} \tag{6.14}$$

where υ is called the vacuum expectation value of the scalar field ϕ. It has been experimentaly determined from the lifetime of the μ-decay to be 246 GeV. There is a continuous set of degenerate vacuum states due to the electroweak gauge symmetry. One of those vacuum states is selected as the ground state of the system breaking the SU(2)×U(1) symmetry.

After electroweak symmetry breaking, the coupling terms between the Higgs field and the gauge fields W_μ and B_μ from the covariant derivatives 6.8 generate masses for the following fields:

$$W_\mu^\pm = \frac{1}{\sqrt{2}}(W_{\mu,1} \pm iW_{\mu,2}) \quad , \tag{6.15}$$

$$Z_\mu = -sin\theta_W \cdot B_\mu + cos\theta_W \cdot W_{\mu,3} \quad . \tag{6.16}$$

where θ_W is the weak mixing angle. The fields $W_\mu^\pm$ and Z_μ correspond to the weak gauge bosons $W^\pm$ and Z^o. Their masses are given by:

$$m_W^2 = \frac{g_1^2 v^2}{4} \quad , \quad m_Z^2 = (g_1^2 + g_2^2)\frac{v^2}{4} = \frac{m_W^2}{cos^2\theta_W} \quad . \tag{6.17}$$

There is still one vector field remaining massless, the photon field:

$$A_\mu = cos\theta_W \cdot B_\mu + sin\theta_W \cdot W_{\mu,3} \quad . \tag{6.18}$$

The fact that the photon has zero mass means that the Lagrangian is still invariant under U(1) transformations corresponding to the Abelian gauge symmetry of QED, while the $SU(2)_L \otimes U(1)_Y$ gauge symmetry is broken.
By introducing Yukawa couplings g_f between fermions f and the Higgs field, fermions acquire masses given by $m_f = g_f v/\sqrt{2}$. The mass of the Higgs particle is given by $m_H = \sqrt{-2\mu^2} = \sqrt{2\lambda} \cdot v$. The mass it is not predicted by the theory, but can be only experimentally determined.

6.3 Beyond the Standard Model - Motivation for Supersymmetry

Although the Standard Model (SM)is the most successful physical theory today, it still leaves a number of questions unanswered. These questions are a motivation for new theoretical models extending the Standard Model.

Supersymmetry (SUSY), a new symmetry relating bosons and fermions, is the most favoured candidate for an extension of the Standard Model. Supersymmetric extentions of the Standard Model share general characteristics. Each Standard Model particle has a supersymmetric partner (superpartner) with spin different by 1/2 and all other quantum numbers remaining the same. One cannot find superpartners among the existing Standard Model particles, since there are no particles fullfilling this requirement. Thus, the particle spectrum has to be doubled. Searches for indications of SUSY have been performed during the last three decades [39], but no direct observation of supersymmetric particles has been made so far.

SUSY can provide solutions to some of the problems of the Standard Model. In the following, the most important of ones are briefly explained (more details and discussion of the prospects for SUSY searches at the LHC can be found in [45]).

1. **Unification of gauge couplings**: In the framework of the Grand Unificated Theories (GUT), unification of the energy dependent gauge couplings of the Standard Model should occur at very high energy ($10^{15} - 10^{16}$ GeV). To verify if such a unification is possible, the running of couplings with energy has to be

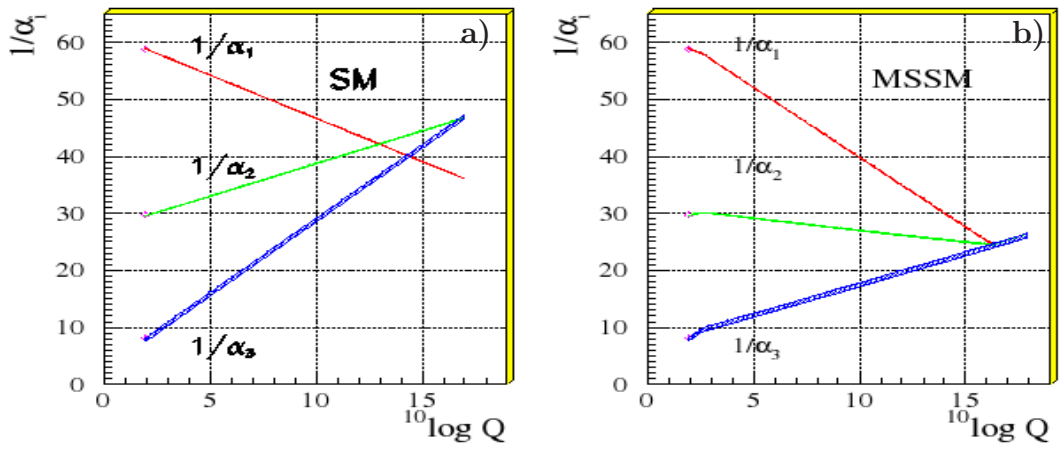

Fig. 6.2: Running of the inverse gauge couplings with energy. a) in the case of the Standard Model and b) in the case of MSSM. α_1, α_2, α_3 are the gauge couplings squared for the U(1), SU(2) and SU(3) gauge interactions respectively [45].

examined, which is described by the renormalization group (RG) equations. In leading order of perturbation theory they take the following form:

$$\frac{1}{\alpha_i(Q^2)} = \frac{1}{\alpha_i(\mu^2)} - \frac{b_i}{4\pi} \cdot log(\frac{Q^2}{\mu^2}) \tag{6.19}$$

where α_1, α_2, α_3 are the gauge couplings squared ($\alpha_i = g_i/4\pi$) for the U(1), SU(2) and SU(3) gauge interactions of the Standard Model, respectively, b_i the beta functions ($b_i = \frac{\partial \alpha_i}{\partial \mu}$) and Q and μ high and low energy scales, respectively. The Standard Model beta-functions do not yield a common unification point for all coupling constants (Figure 6.2 a), while in the Minimal Supersymmetric Extension of the Standard Model (MSSM; see below) this is possible (Figure 6.2 b).

2. **Solution of the hierarchy problem**:

   Radiative loop corrections to the Standard Model Higgs boson mass diverge linearly with the energy scale Λ up to which the Standard Model is supposed to be valid ($\delta m_H^2 \sim \Lambda^2$) which could be the GUT unification scale (10^{16} GeV) or even the Planck scale (10^{19} GeV). For the Standard Model to be consistent, the Higgs mass has to be smaller than 1 TeV, close to the electromagnetic symmetry breaking scale defined by the Higgs vacuum expectation value $v =$ 246 GeV. Due to the large difference (hierarchy) between the two energy scales, the large corrections to the Higgs mass have to be compensated by a large

uncorrected mass value with very precise fine-tunning which appears to be unnatural.

A more elegant way to eliminate the large radiative corrections to the Higgs mass is provided in supersymmetric extensions of the Standard Model where the fermion loop corrections of the SM are approximatelly cancelled by additional superpartner boson loop corrections which appear with opposite sign. The cancellation is not exact because Supersymmetry must be broken at a mass scale M_{SUSY} leading to mass differences between fermionic and bosonic superpartners on the order of M_{SUSY}.

Requiring that the remaining radiative corrections should not exceed the mass of the Higgs boson ($m_H \lesssim 1$ TeV), i.e.

$$\delta m_H^2 \sim g_t^2 M_{SUSY}^2 \lesssim m_H^2 \quad , \tag{6.20}$$

leads to a rough estimate of M_{SUSY} as $M_{SUSY} \lesssim m_H/g_t \approx 10^3$ GeV, with largest Yukawa coupling the one between the Higgs boson and the top-quark, $g_t = \sqrt{2}m_t/v \approx 1$.

6.4 The Minimal Supersymmetric Standard Model

The Minimal Supersymmetric extension of the Standard Model (MSSM) incorporates the Standard Model particles and their superpartners, together with two Higgs doublets, separate for the coupling to fermions with third component of the weak isospin +1/2 and -1/2, respectively. A brief discussion of the basic features of this model follows in this section. A comprehensive overview of the MSSM can be found in [46] and [47].

An important feature to be incorporated into the MSSM is the breaking of supersymmetry. If the symmetry would be retained at any energy, then the ordinary particles and their superpartners would be degenerate in mass. As a consequence, at least the lighter superpartners (e.g. selectrons) should already have been discovered. Due to SUSY breaking, superpartners acquire larger masses which explains that they have not been observed until now. In Table 6.1 the particle spectrum of the MSSM is summarized.

The MSSM Lagrangian consists of the supersymmetric generalization of the Standard Model Lagrangian including two Higgs doublets and their mixing and additional terms imposing SUSY breaking.

Additional interactions leading to the violation of lepton or baryon number become in principle possible in the MSSM Lagrangian. They can be avoided by requiring a new discrete symmetry, R-parity, defined as:

	SM particle	Spin	R-Parity	Superpartner	Spin	R-Parity
Gauge particles	Gluon g	1	+1	Gluino $\tilde{g}$	1/2	-1
	Weak bosons $(W^{\pm}, Z)$	1	+1	Wino, Zino $(\tilde{W}^{\pm}, \tilde{Z})$	1/2	-1
	Hypercharge B (γ)	1	+1	Bino (Photino) $\tilde{B}$ ($\tilde{\gamma}$)	1/2	-1
	Higgs bosons $(H_1^+, H_1^0, H_2^0, H_2^-)$	0	+1	Higgsinos $(\tilde{H}_u^+, \tilde{H}_u^0, \tilde{H}_d^0, \tilde{H}_d^-)$	1/2	-1
Matter particles	Quarks u, d, c, s, t, b	1/2	+1	Squarks $\tilde{u}$, $\tilde{d}$, $\tilde{c}$, $\tilde{s}$, $\tilde{t}$, $\tilde{b}$	0	-1
	Leptons $\nu_e, e, \nu_\mu, \mu, \nu_\tau, \tau$	1/2	+1	Sleptons $\tilde{\nu}_e$, $\tilde{e}$, $\tilde{\nu_\mu}$, $\tilde{\mu}$, $\tilde{\nu_\tau}$, $\tilde{\tau}$	0	-1

Tab. 6.1: The particle spectrum of the MSSM.

$$R = (-1)^{3(B-L)+2S} \quad . \tag{6.21}$$

with B denoting the baryon number, L the lepton number and S the spin of the particle. The consequence of R-parity conservation is that superparticles are created in pairs and that the lightest supersymmetric particle is stable.
The SUSY breaking terms in the Lagrangian lead to a vast number of new free parameters. The MSSM has in total 124 free parameters.

6.5 The MSSM Higgs Mechanism

In the MSSM, the description of electroweak symmetry breaking is more complicated compared to the SM. This is due to the fact that one needs two complex Higgs doublets in order to give masses to up- and down-type quarks and leptons via Yukawa couplings, which after spontaneous symmetry breaking can be parametrized as:

$$H_1 = \begin{pmatrix} H_1^0 \\ H_1^- \end{pmatrix} = \begin{pmatrix} \upsilon_1 + \frac{S_1 + iP_1}{\sqrt{2}} \\ H_1^- \end{pmatrix}, \quad H_2 = \begin{pmatrix} H_2^+ \\ H_2^0 \end{pmatrix} = \begin{pmatrix} H_2^+ \\ \upsilon_2 + \frac{S_2 + iP_2}{\sqrt{2}} \end{pmatrix} \tag{6.22}$$

where υ_i are the vacuum expectation values of the neutral components and S_i and P_i are real scalar fields.

The Higgs sector of the MSSM has eight degrees of freedom. In analogy to the Standard Model, three degrees of freedom are absorbed into the longitudinal polarization states of the weak bosons and the remaining five represent five physical

Higgs bosons: two CP-even neutral ones (h,H), one CP-odd neutral (A) and two charged ones ($H^{\pm}$).

The MSSM Higgs potential (at the tree level) is given by:

$$V(H_1,H_2) = m_1^2|H_1|^2 + m_2^2|H_2|^2 - m_3^2(H_1H_2 + h.c.) + \frac{g_1^2+g_2^2}{8}(|H_1|^2-|H_2|^2)^2 + \frac{g_1^2}{2}|H_1^\dagger H_2|^2 \quad . \tag{6.23}$$

where $m_{1,2}^2 = m_{H_{1,2}}^2 + \mu^2$ with μ denoting the Higgs mixing parameter. g_1 and g_2 are the SU(2) and U(1) gauge couplings, respectively. The mass eigenstates of the Higgs fields are given by:

$$\begin{aligned} G^0 &= -cos\beta \cdot P_1 + sin\beta \cdot P_2 \quad (Goldstone\ boson,\ absorbed\ by\ Z^o),\\ A &= sin\beta \cdot P_1 + cos\beta \cdot P_2 \quad (CP-odd\ neutral\ Higgs),\end{aligned}$$

$$\begin{aligned} G^+ &= -cos\beta \cdot (H_1^-)^* + sin\beta \cdot H_2^+ \quad (Goldstone\ boson\ absorbed\ by\ W^+),\\ H^+ &= sin\beta \cdot (H_1^-)^* + cos\beta \cdot H_2^+ \quad (charged\ Higgs\ boson),\end{aligned}$$

$$\begin{aligned} h &= -sin\alpha \cdot S_1 + cos\alpha \cdot S_2 \quad (SM-like\ CP-even\ neutral\ Higgs\ boson),\\ H &= cos\alpha \cdot S_1 + sin\alpha \cdot S_2 \quad (heavy\ CP-even\ neutral\ Higgs\ boson).\end{aligned}$$

The angle β is given by the relation $\tan\beta = v_2/v_1$, the ratio of the vacuum expectation values of the two Higgs doublets. The mixing angle α of the CP-even Higgs bosons is a function of the free parameters $\tan\beta$ and m_A the mass of the CP-odd Higgs boson A:

$$tan2\alpha = \left(\frac{m_A^2+m_Z^2}{m_A^2-m_Z^2}\right)\cdot tan2\beta \quad . \tag{6.24}$$

The mass eigenvalues of the Higgs bosons can be expressed (at tree level) as a function of these two free parameters. The five physical Higgs masses are given by:

$$\begin{aligned} m_A^2 &= m_1^2 + m_2^2 \quad ,\\ m_{H^\pm}^2 &= m_A^2 + m_W^2 \quad ,\\ m_{H,h}^2 &= \frac{1}{2}\left[m_A^2 + m_Z^2 \pm \sqrt{(m_A^2+m_Z^2)^2 - 4\, m_A^2 m_Z^2 cos^2 2\beta}\right] \quad ,\end{aligned} \tag{6.25}$$

leading to the following constraints on the Higgs masses.

$$\begin{aligned} m_{H^\pm} &\geq m_W \quad , \\ m_h \leq m_A &\leq m_H \quad , \\ m_h \leq m_Z|cos2\beta| &\leq m_Z \quad , \\ m_h^2 + m_H^2 &= m_A^2 + m_Z^2 \quad . \end{aligned} \tag{6.26}$$

Equations 6.26 show that at tree level the mass m_h of the lightest Higgs boson is lower than the mass of the Z boson. If radiative corrections are included, m_h increases to about 130 GeV/c^2. The main corrections to m_h come from the top and stop loops. At the one loop order, the mass m_h is given by [38]:

$$m_h^2 \approx m_Z^2 cos^2 2\beta + \frac{3g_1^2 m_t^4}{16\pi^2 m_W^2} log\left(\frac{\tilde{m}_{t_1}^2 \tilde{m}_{t_2}^2}{m_t^4}\right) \quad , \tag{6.27}$$

where $\tilde{m}_{t_1}$, $\tilde{m}_{t_2}$ are the stop mass eigenvalues, m_t is the top-qark mass and g_1 the SU(2) gauge coupling.

In Figure 6.3, the masses of the MSSM Higgs bosons including radiative corrections are shown as a function of the pseudoscalar Higgs boson mass m_A, for two values of $tan\beta$ and for MSSM parameters settings which maximize m_h ($m_h - max$ scenario; see next section). For values of m_A higher than 130 GeV one also sees that $m_H = m_A$. This region is called the decoupling regime, where m_h reaches its maximum value of about 130 GeV

To reduce the number of free parameters of the MSSM, one can use the universality hypothesis, that at a high energy scale all spin 0 and all spin 1/2 particle masses should converge to two universal mass values, m_0 and $m_{1/2}$, respectively. In this case, the free MSSM parameters are reduced to the following five:

$$\mu, \quad m_0, \quad m_{1/2}, \quad A \quad and\ tan\beta = \frac{v_2}{v_1} \quad . \tag{6.28}$$

where μ is the Higgs doublet mixing parameter and A the trilinear Higgs-sfermion-sfermion coupling [38].

6.6 Production and Decays of Neutral MSSM Higgs Bosons

The production of neutral MSSM Higgs bosons at LHC can be characterized by the following four mechanisms:

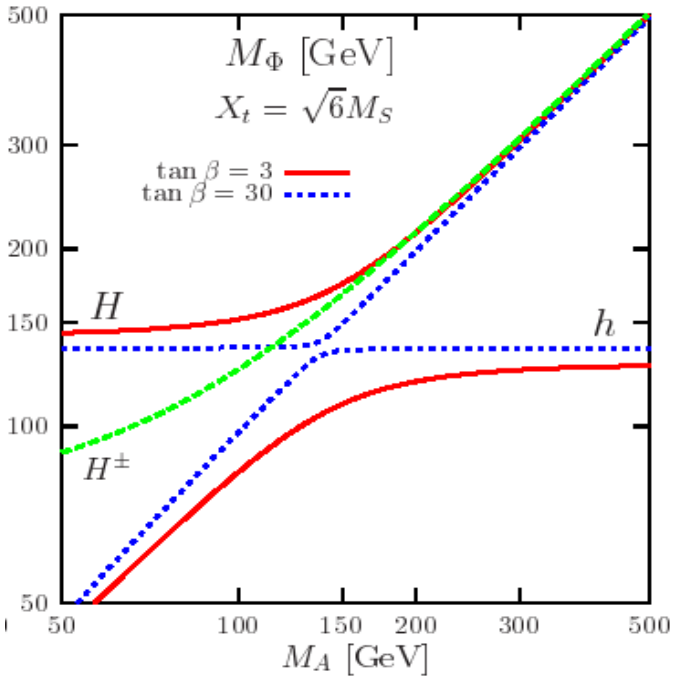

Fig. 6.3: The masses of the MSSM Higgs bosons as a function of the pseudoscalar Higgs boson mass m_A, for two values of $tan\beta$ in the $m_h - max$ scenario (see text) [48].

1. Gluon - gluon fusion: $gg \to h/H/A$
2. Associated production with heavy quarks (Q=t,b): $gg,\ q\bar{q} \to Q\bar{Q} + h/H/A$
3. Vector boson (V) fusion for h and H production: $qq \to V^*V^* \to qq + h/H$
4. Associated h and H production (with V=W/Z): $q\bar{q} \to V + h/H$.

The Feynmann diagrams for the production mechanisms mentioned above are shown in Figure 6.4. The CP-odd Higgs boson A cannot be produced in association with the gauge bosons or via vector boson fusion at the tree level, since the direct coupling of A to gauge bosons is supppressed in the MSSM.

There exist also higher order mechanisms which allow for the production of two Higgs particles ($q\bar{q},\ gg \to \Phi_i\Phi_j$), the production in association with a gluon ($gg \to g\Phi$) and the production of the CP-odd Higgs boson in association with a Z boson ($gg \to AZ$), where Φ is a general notation for the three neutral Higgs bosons.

The production cross sections for the different mechanisms at the LHC are summarized in Figure 6.5. For low values of tanβ (≈ 3), the Higgs coupling to up-type quarks are enhanced. In this region, the dominant production process is the gluon-gluon fusion, especially via the top quark loop. On the other hand, for high $tan\beta$ values ($\gtrsim 30$), couplings to b-quarks are enhanced and associated production with b-quarks is the dominant process, while gluon-gluon fusion via b quark loops gives a lower, but still significant contribution.

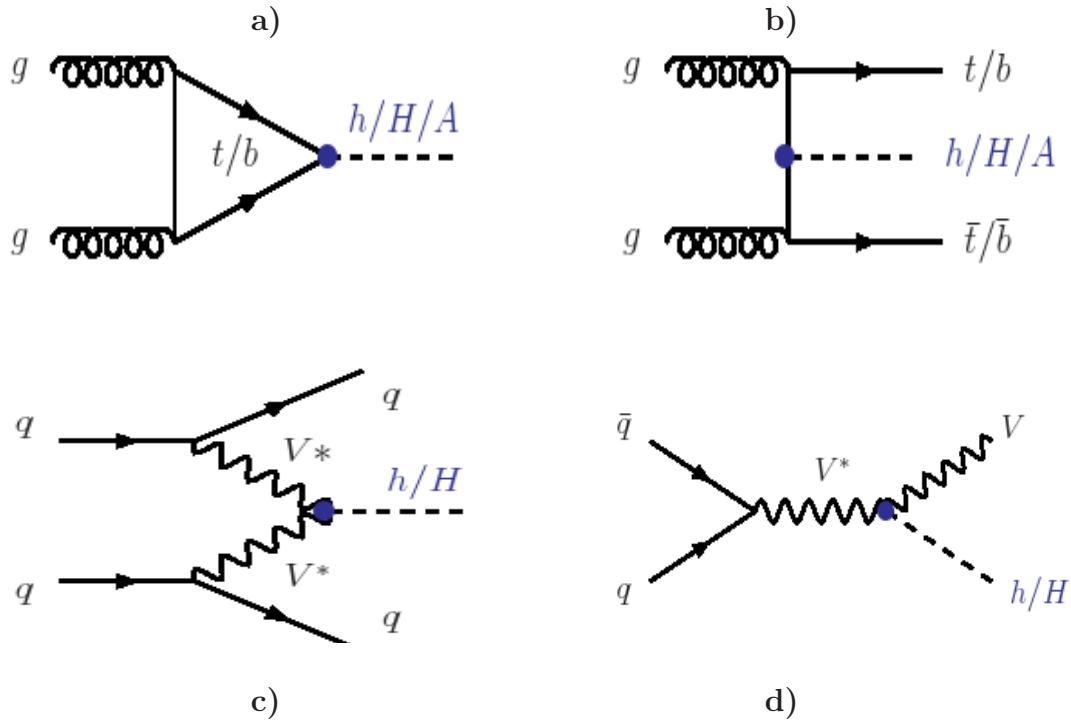

Fig. 6.4: The dominant production mechanisms of the neutral MSSM Higgs bosons at the LHC [48]. a) Gluon-gluon fusion, b) associated production with heavy quarks, c) vector boson fusion, d) associated production with V=W/Z.

The branching ratios of the MSSM Higgs bosons decays to fermions, gauge bosons and other Higgs particles are shown in Figure 6.6 for two different values of tanβ in the $m_h - max$ scenario [48].

The light h boson has SM-like couplings and a mass $\lesssim$130 GeV. It decays dominantly to $b\bar{b}$. WW^* gives an important contribution for masses higher than 120 GeV while the decay to $\tau^+\tau^-$ is more important for lower masses (Figure 6.6 a, b). Other decays have branching ratios of a few percent and lower. The decay rates of the heavy neutral Higgs bosons (H,A) depend strongly on $tan\beta$. For values of $tan\beta \gg 1$ (Figure 6.6 d, f), couplings to down type fermions are strongly enhanced. Therefore H/A decay almost exclusively to $b\bar{b}$ (BR$\simeq$ 90%) and $\tau^+\tau^-$ ($\simeq$ 10%). Experimentally relevant is also the decay into $\mu^+\mu^-$. It is governed by the same couplings as for the $\tau^+\tau^-$ final state, but is suppressed by a factor of $(m_\mu/m_\tau)^2$. For low values of tanβ (Figure 6.6 c, e) couplings to up type fermions are enhanced and the decays to $t\bar{t}$, when kinematicaly allowed, are dominating.

At both the LEP (e^+e^-) and the Tevatron ($p\bar{p}$) collider, searches for the neutral MSSM Higgs bosons have been performed. No discovery has been claimed so far, but both experimenta have set exclusion limits in the $tan\beta - m_A$ parameter plane. At LEP [39], the searches concentrated on the $b\bar{b}$ and $\tau^+\tau^-$ final states. Limits of

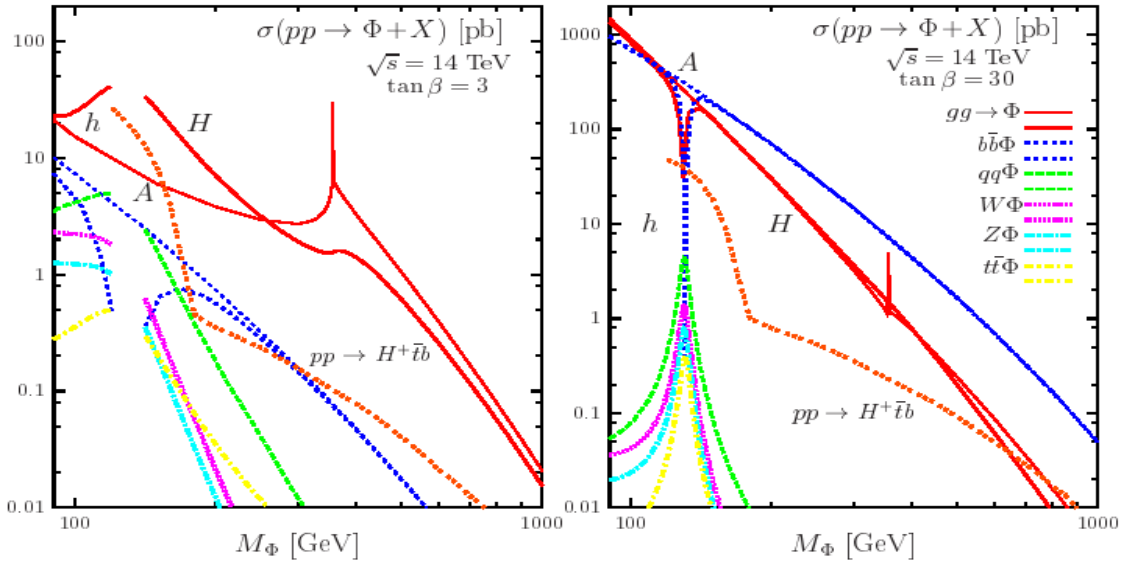

Fig. 6.5: Production cross sections of neutral MSSM Higgs bosons $\phi = h,\ H,\ A$ at the LHC for tanβ=3 and tanβ=30 [48].

m_h >114 GeV at tanβ <5 and $m_{h/A}$ >93 GeV for higher tanβ have been set at 95% confidence level. Tevatron searches mainly focused on $\tau^+\tau^-$ final states. The combined excluded areas from LEP and Tevatron are shown in Figure 6.7, for the $m_h - max$ scenario and scenario without stop quark mixing. The results show that the intermediate tanβ region between 5 and 60 is still uncovered. This region will be accessible by the LHC experiments.

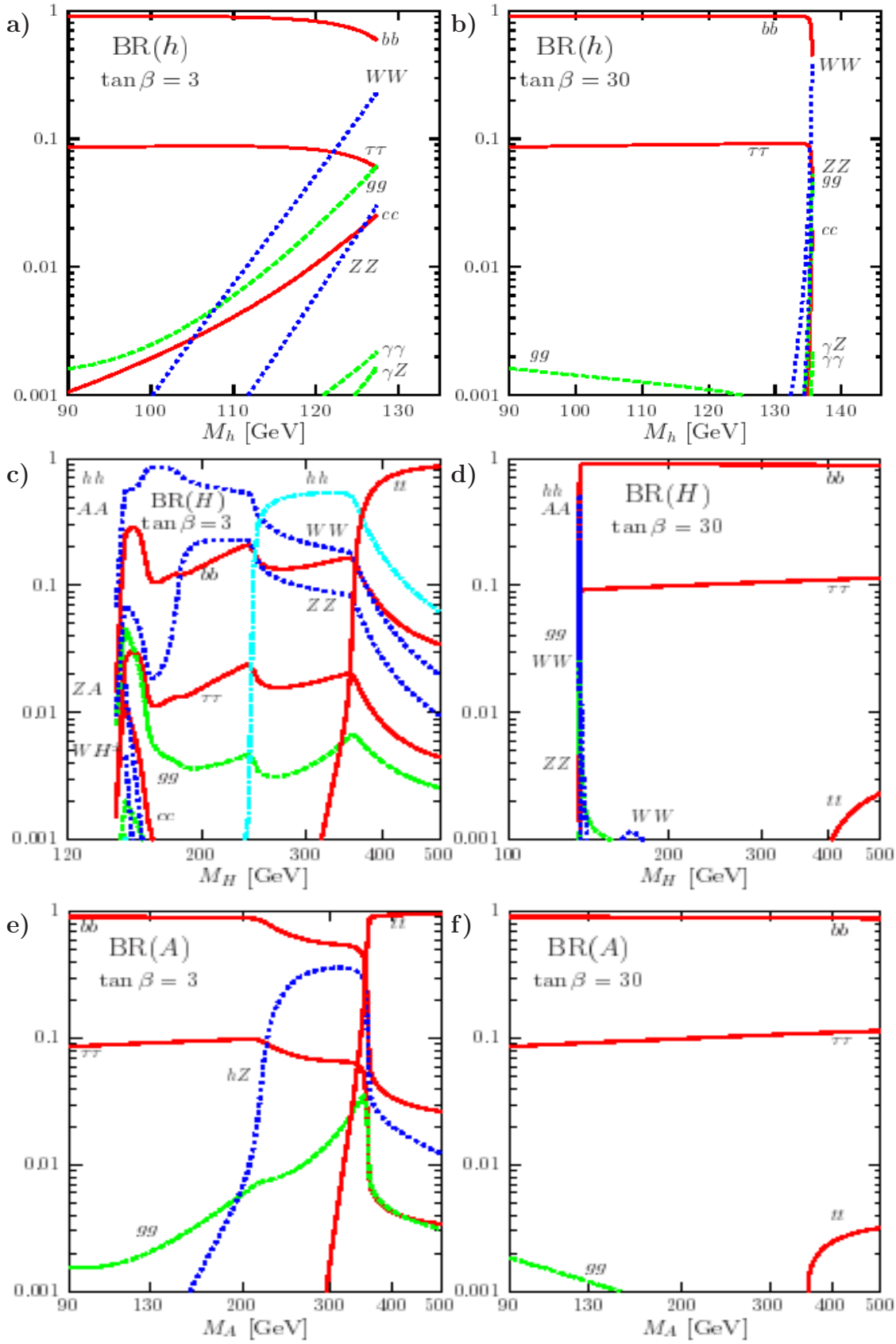

Fig. 6.6: The branching ratios of neutral MSSM Higgs boson decays for small and large $tan\beta$ values [48]: a), b) for the h boson, c), d) for the H boson and e), f) for the A boson.

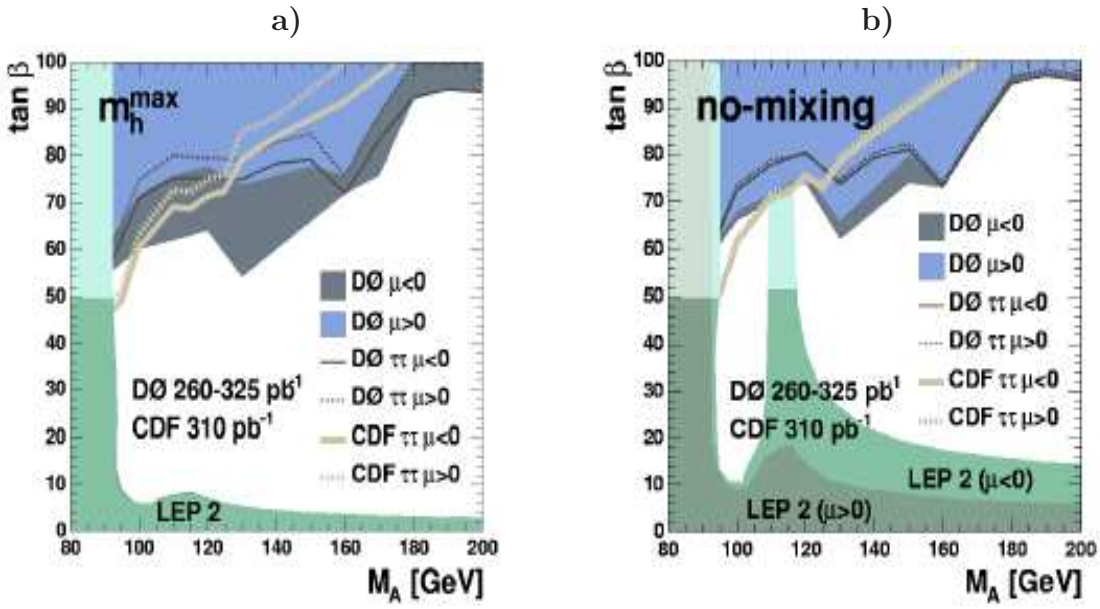

Fig. 6.7: The 95% exclusion limits from direct searches at LEP and Tevatron in the m_A-tanβ plane. The results were obtained for two benchmark scenarios, $m_h - max$ (a) and $no - mixing$ (b) (see text) [49].

7

MSSM Higgs Boson Search in the $pp \rightarrow (b\bar{b})H/A \rightarrow (b\bar{b})\tau^+\tau^-$ Channel

In this chapter the analysis of the MSSM channel $b\bar{b}H/A$, $H/A \rightarrow \tau^+\tau^-$ will be presented, where one of the two τ-leptons decays leptonically and the other one hadronically. The signal final state and the important background processes will be introduced in Sections 7.1, 7.2. Subsequently, the programs for the event generation and simulation will be discussed in Section 7.3. In Sections 7.4, 7.5 and 7.6, the detector performance and the event selection criteria are described. Finally, the analysis results are presented in Section 7.7.

7.1 Signal Production Mechanisms and Cross Sections

The MSSM $H/A \rightarrow \tau^+\tau^-$ decay rates are strongly enhanced with respect to the standard model over a large region of the $tan\beta$-m_A parameter space.

There are two dominant production mechanisms of H and A bosons. The first one is the direct production via the gluon-gluon fusion ($gg \rightarrow H/A$), which is mostly significant for small values of $\tan\beta$ (< 10) and for low masses ($m_{H/A} < 200$ GeV/c^2). For large values of $\tan\beta$, the dominant production mechanism is the associated production ($gg \rightarrow b\bar{b}H/A$), in which in addition to the Higgs boson two b-quarks are produced in the final state. Figures 6.4 a) and b) in the previous chapter show the corresponding Feynmann diagrams for the above processes.

For Higgs masses above 150 GeV/c^2, the two heavy neutral Higgs bosons are degenerate in mass and their signal rates can therefore be summed up. In the lower mass regions, the analysis procedure depends on the mass difference between A and H bosons, as well as on the experimental resolution. The analysis presented in this chapter will be performed in the range of candidate signal masses between 150 GeV/c^2 and 600 GeV/c^2.

The two τ-leptons produced in the decay of the A or H boson can decay hadronically or leptonically. Table 7.1 shows all possible decay modes and corresponding decay rates [40]. Therefore, three possible final states in the $H/A \rightarrow \tau^+\tau^-$ channel can be studied. The lepton-lepton decay mode ($\simeq 12\%$), where both τ-leptons decay leptonically, the hadron-hadron decay mode ($\simeq 42\%$) with both τ-leptons decaying

	τ^- decay mode	decay rate (%)
leptonic decays	$\mu^-\bar{\nu}_\mu\nu_\tau$	17.36±0.05
	$e^-\bar{\nu}_e\nu_\tau$	17.84±0.05
hadronic decays	$\pi^-\nu_\tau$	10.90±0.07
	$\pi^-\pi^0\nu_\tau$	25.50±0.10
	$\pi^-\pi^+\pi^-\nu_\tau$	8.99±0.08
	$\pi^-2\pi^0\nu_\tau$	9.25±0.12
	25 additional modes	10.16

Tab. 7.1: Table summarizing τ-lepton decay modes and branching ratios. Approximately 90% is attributed to six main decay modes while other twenty five modes (combinations of decays in K, π, η, ω, ρ) account for the remaining 10% [40].

hadronically, and finally the lepton-hadron decay mode ($\simeq 46\%$) [40] which will be studied in this chapter. The latter offers the best sensitivity to the signal, since the higher rate compared to the lepton-lepton mode is combined with a good triggering efficiency. It also has a lower contribution of the background processes compared to the hadron-hadron mode, which is sensitive to the rather abundant rate of the multijet events at LHC. Following the present exclusion limits, we concentrate our study to the region with large tanβ(>10), where the associated $b\bar{b}H/A$ production dominates. The lepton-hadron decay of the H/A bosons produced in the associated production mode, will contain one high energetic muon or electron, one jet identified as a τ-jet, two b-jets from the two accompanying b-quarks and the missing energy due to the presence of neutrinos from the τ-decays. In addition, more jets from initial and final state radiation, as well as the products from the underlying event and the pile-up events are expected. For illustration see Figure 7.1 [50].

The calculation of the H/A production cross sections and branching ratios into $\tau^+\tau^-$ pairs has been performed with the FEYNHIGGS program (version 2.5.1 - R. Harlander, W. Kilgore) [51],[52],[53],[54]. Cross sections are calculated at the next-to-leading order (NLO), for both direct and $b\bar{b}$-associated production mode, assuming the $m_h - max$ scenario of MSSM (see Section 6.4). More details about the input parameters and the results for various points in the m_A - $tan\beta$ parameter space can be found in Appendix C. Figures 7.2, 7.3 and 7.4 show the cross section for the two production mechanisms and the branching ratio in dependence on different masses and $tan\beta$ values.

7.2 Background Processes and Cross Sections

The search for the $pp \to (b\bar{b})H/A \to (b\bar{b})\tau^+\tau^-$ decay channel suffers from potential backgrounds with large cross sections which have jets and an energetic lepton in the final state. The most important of these background processes are the following (see Figures 7.5):

- $\boldsymbol{t\bar{t}}$: This process accounts for one of the dominant backgrounds in almost entire

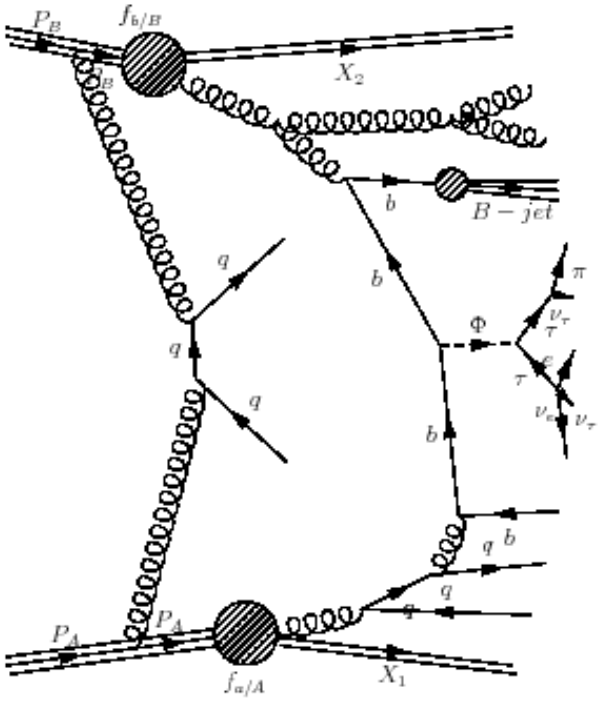

Fig. 7.1: Illustration of the Higgs boson production (Φ) in a proton-proton collision $p + p \to \Phi + X$. Each proton ($f_{a/A}$,$f_{b/B}$) emits a gluon. The upper gluon splits here into a $b\bar{b}$, the lower gluon into a $q\bar{q}$ pair, where one quark subsequently emits another gluon. This gluon then splits to a $b\bar{b}$. Two of the b quarks fuse to give a Higgs boson (Φ). Finally, Φ may decay into two τ-leptons which decay into $e^- + \bar{\nu}_e + \nu_\tau$ and $\pi^+ + \bar{\nu}_\tau$. Before or after the hard interaction, electrically charged or coloured particles might undergo radiation and emit additional particles. Such proccesses are called the initial state or final state radiation. Additional activity originating from the proton remnants represents the underlying event.

Higgs mass range under study. Each top quark decays to a W boson and a b quark (with a branching ratio of almost 100%) [40]. Subsequently, each W decays either hadronically ($\simeq$ 68%) or leptonically ($\simeq$ 32%). Therefore, two b-quarks, one high energy lepton and one or more neutrinos from the leptonic W decay are present in the final state. Neutrinos are accounted for by the missing energy measured in the detector.

- **Z+jets**: Despite of the small branching ratio of a Z-boson decay into a τ-pair (3.37% [40]), the large Z-boson production rate and additional jets which can fake the b-jets, make this process contribute significantly to the reducible background. In addition, there is a small fraction of irreducible background

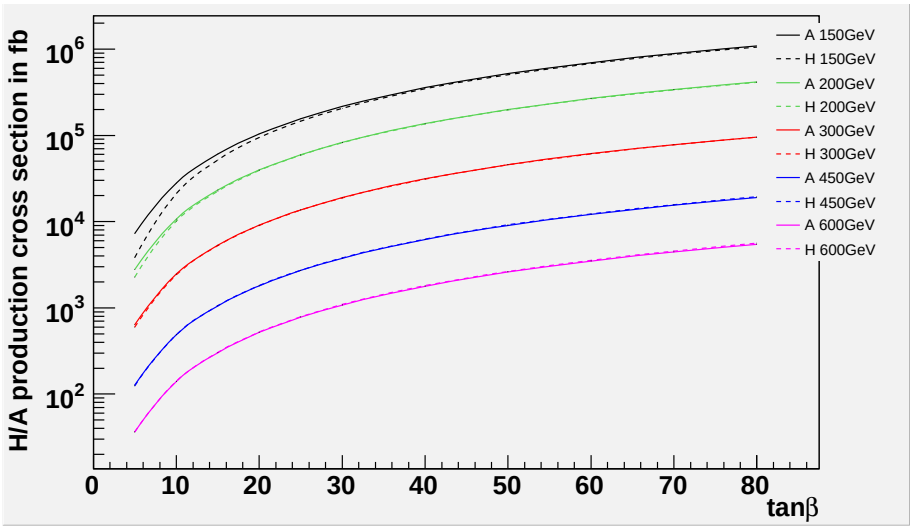

Fig. 7.2: Cross-sections for the associated production $gg \to b\bar{b}H/A$, in dependence on tanβ, shown for different H/A masses.

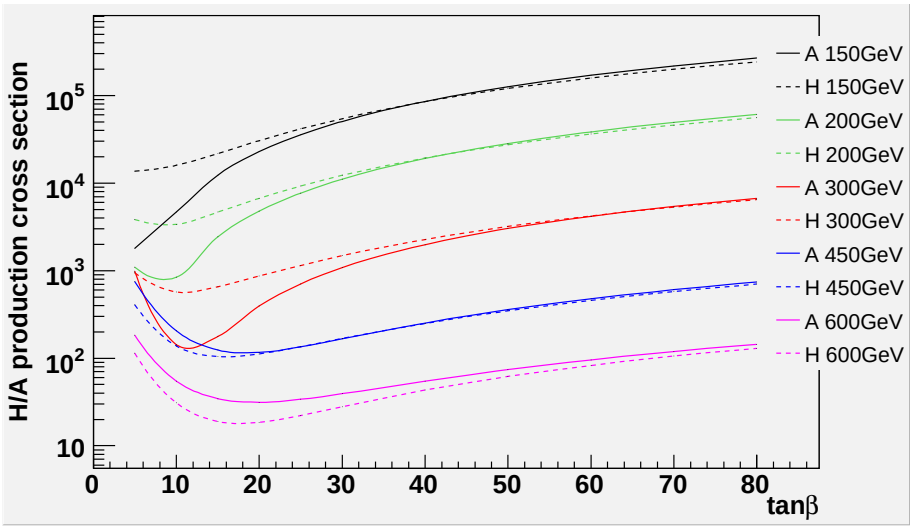

Fig. 7.3: Cross-sections for the direct production $gg \to H/A$, in dependence on tanβ, shown for different H/A masses.

events in which the Z boson is produced in association with two b-quarks.

- **$W^{\pm}$+jets**: W-boson decays leptonicaly into an e, μ or a τ-lepton with branching ratio of approximately 10% [40] for each lepton. Thus, an energetic lepton and additional jets that can fake a τ-jet or a real τ-jet and a lepton from the underlying event can be reconstructed, leading to final state similar to the signal.

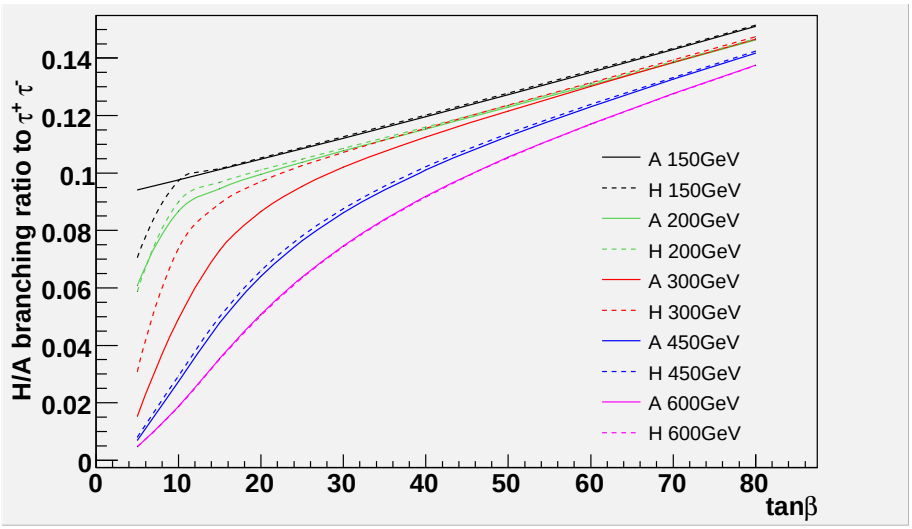

Fig. 7.4: Branching ratio of the $H/A \rightarrow \tau^+\tau^-$ decay in dependence on tanβ, shown for different H/A masses.

- **QCD-background**: QCD multijet events rarely contain high energy leptons. Nevertheless, such an event can have missing energy coming from neutrinos produced in decays of c and b quarks, while the jets can be mistagged as τ-jets or b-jets. Taking into account the large inclusive QCD production cross section at the LHC, this process can have a significant contribution to the total background.

The cross sections for all background processes (see Table 7.3) are calculated at the next-to-leading order (NLO). Differential distributions of the leading-order generators are scaled by the corresponding scale factors.

7.3 Event Simulation

Four signal mass points (150, 300, 450 and 600 GeV/c^2) were generated with the PYTHIA event generator [56],[57],[58]. For all samples, only events with A bosons were produced. Since the H and A bosons are degenerate in mass and the event topologies for the H and A boson are almost identical, their cross sections can be summed up. For the production of the different background processes various event generators were used. The MC@NLO generator interfaced to JIMMY/HERWIG [59],[60],[61],[62] has been used for the $t\bar{t}$ background, ACERMC with PYTHIA for Zbb background, PYTHIA for W+jets processes and ALPGEN [64] with JIMMY/HERWIG for the Z+jets background. The decays of the τ leptons were handled by the TAUOLA [65] package for all generated samples. In addition, the events that contain two b-quarks were removed from the Z+jets background sample in order to avoid the overlap with the events from the Zbb sample. A number of dedicated generator filters (see Table 7.3) were used in order to select only the

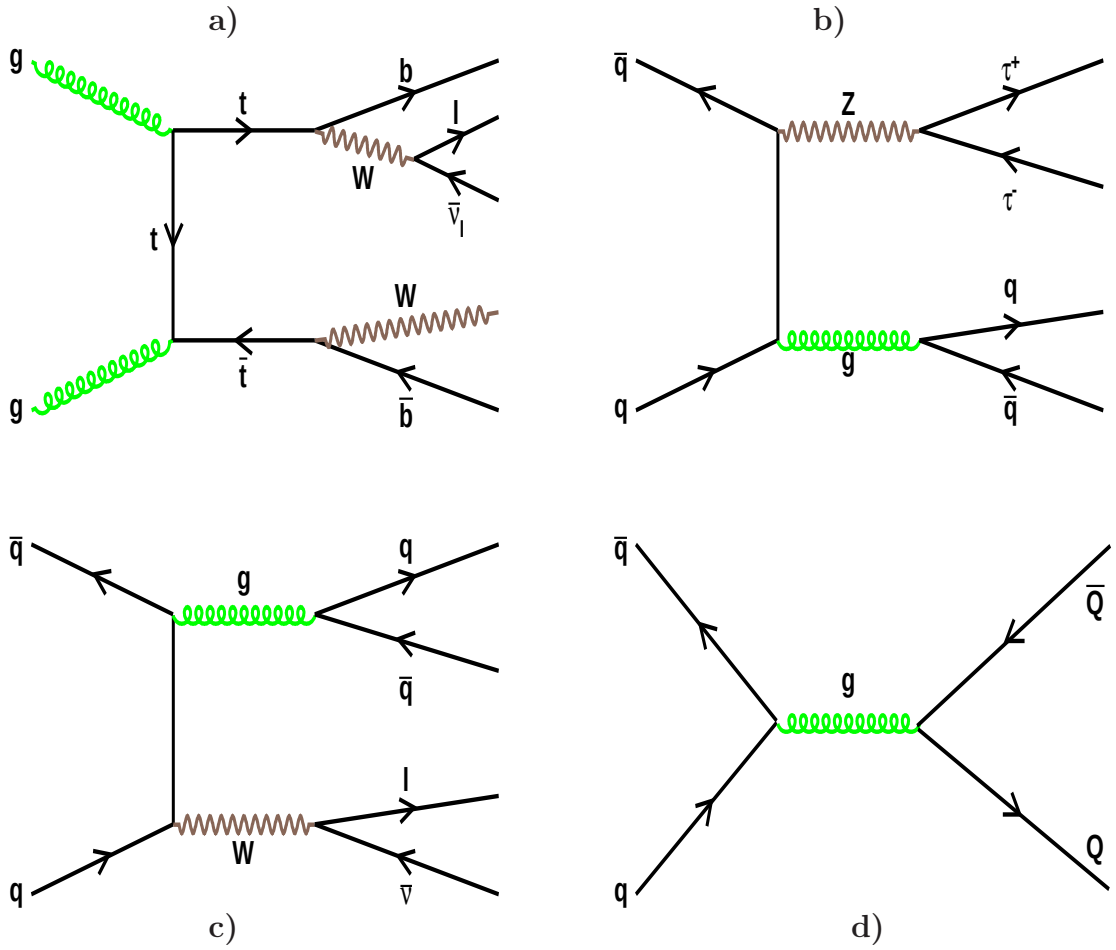

Fig. 7.5: Feynmann diagrams of the background processes: a) $t\bar{t}$ with at least one W-boson decaying hadronicaly, b) Z+jets with the Z-boson decaying into a τ-pair, c) W+jets with the W-boson decaying into a lepton and a neutrino and d) QCD jet events.

interesting events and thus to decrease the needed Monte Carlo statistics. "ATAU-FILTER" applies a p_T-cut and in addition a cut on the transverse angular distance between the visible decay products of the two τ-leptons. "TTbarLeptonFilter" selects only the interesting $t\bar{t}$ events with at least one leptonically decaying W-boson. "MultiLeptonFilter" and "TruthJetFilter" apply cuts on the minimal number, p_T and η of leptons and jets respectively. Detailed description of each filter can be found in Appendix B, while the resulting filter efficiencies are summarized in Table 7.3. The efficiencies for the Z+jets samples include the factor obtained from the overlap removal with the Zbb sample.

Two different approaches are available for the event simulation in ATLAS. The first approach is a detailed Geant4-based [17],[18] detector simulation, which is conventionally called the full simulation. Particles are propagated through the detector

volume and interact with all active detector elements and passive material on their way. This information is then used by the ATLAS reconstruction algorithms. The full simulation provides a detailed and realistic detector response. However, since the CPU resources needed for the full simulation are high while a very large number of events is needed for the analysis, an alternative approach was developed. The fast detector simulation, so called ATLFAST [55] simulation replaces the detailed simulation and reconstruction steps with a parametrized description of the detector. Momentum vectors of particles produced by the Monte Carlo generators are directly smeared with given momentum resolutions. The reconstruction efficiencies and rejection of misidentified objects are parametrized based on the studies performed with full simulation. ATLFAST includes no description of the inner detector and uses a homogeneous magnetic field. The calorimeter description consists of a longitudinal layer with a segmentation of $\Delta R = 0.1 \times 0.1$ for the barrel sector and $\Delta R = 0.2 \times 0.2$ for the end-cap sectors. Stable particles deposit all their energy in the cells they hit, no noise is taken into account. The jet reconstruction is based on these energy depositions.

In the study presented in this chapter the following strategy was used: The fully simulated data (so called CSC data samples) [66] have been compared with -in general larger- ATLFAST samples. These comparisons of the detector performance serve for the evaluation of the systematic uncertainties in the analysis. Subsequently, the large ATLFAST samples were used for the fully optimized analysis since only with these is it feasible to perform a detailed study of this channel. Both ATLAS simulation chains were running within the ATHENA framework version 12.0.6. Full list of the samples used, as well as further relevant information is summarized in Tables 7.3 and 7.3.

7.4 Comparison of Full and Fast Simulation

In the current analysis of $pp \to (b\bar{b})H/A \to (b\bar{b})\tau^+\tau^-$ via the lepton-hadron decay mode, one looks for the muons, electrons, b-jets and τ-jets in the final state. Neutrinos are not directly observed in the detector, but their summed contribution is measured as the missing energy in the plane transverse to the beam direction. The description of the missing energy reconstruction in full and fast simulation will be given in Section 7.4.5. The basic kinematic and identification cuts applied to select the reconstructed particles in ATLFAST samples are the following:

- **Muons**: Isolated[1] muons, in the kinematical range of $p_T > 25$ GeV/c and $|n| < 2.5$.
- **Electrons**: Isolated electrons, in the kinematical range of $p_T > 25$ GeV/c and $|n| < 2.5$.

[1] If the sum of the transverse energy of all calorimeter cells within a $\Delta R < 0.4$ around the true lepton does not exceed the energy of the true lepton by more than 10 GeV, then the lepton is considered as isolated

Process	σ x BR	Generator /Filter	Filter Efficiency
$bbH/A \to \tau^+\tau^-$ $m_{H/A} = 150$ GeV/c^2	4792.90fb	Pythia /ATauFilter	0.425
$bbH/A \to \tau^+\tau^-$ $m_{H/A} = 300$ GeV/c^2	299.67fb	Pythia /ATauFilter	0.45
$bbH/A \to \tau^+\tau^-$ $m_{H/A} = 450$ GeV/c^2	27.73fb	Pythia /ATauFilter	0.218
$bbH/A \to \tau^+\tau^-$ $m_{H/A} = 600$ GeV/c^2	5.27fb	Pythia /ATauFilter	0.192
$gg \to H/A \to \tau^+\tau^-$ $m_{H/A} = 150$ GeV/c^2	2005.92fb	Pythia	1.
$gg \to H/A \to \tau^+\tau^-$ $m_{H/A} = 300$ GeV/c^2	49.04fb	Pythia	1.
$gg \to H/A \to \tau^+\tau^-$ $m_{H/A} = 450$ GeV/c^2	9.66fb	Pythia	1.
$gg \to H/A \to \tau^+\tau^-$ $m_{H/A} = 600$ GeV/c^2	1.60fb	Pythia	1.
$t\bar{t}$	833pb	MC@NLO - JIMMY/HERWIG /TTbarLeptonFilter	0.54
$Z \to \tau^+\tau^-$ + 1parton	215.97pb	ALPGEN - JIMMY/HERWIG /MultiLeptonFilter-TruthJetFilter	0.18
$Z \to \tau^+\tau^-$ + 2partons	76.0pb	ALPGEN - JIMMY/HERWIG /MultiLeptonFilter-TruthJetFilter	0.19
$Z \to \tau^+\tau^-$ + 3partons	23.8pb	ALPGEN - JIMMY/HERWIG /MultiLeptonFilter-TruthJetFilter	0.18
$Zbb, Z \to \tau^+\tau^-$ →lepton-hadron	39.3pb	ACERMC - PYTHIA /ATauFilter	0.112
$W + jets, W \to \mu\bar{\nu_\mu}$ P_T^W >30 GeV	3010.5pb	PYTHIA /MultiLeptonFilter-TruthJetFilter	0.56
$W + jets, W \to e\bar{\nu_e}$ P_T^W >30 GeV	3010.5pb	PYTHIA /MultiLeptonFilter-TruthJetFilter	0.23
$W + jets, W \to \tau\bar{\nu_\tau}$ P_T^W >30 GeV	3009.4pb	PYTHIA /MultiLeptonFilter-TruthJetFilter	0.55

Tab. 7.2: Signal and background samples simulated with ATLFAST program. In second column, the NLO cross sections without the filter efficiencies are shown. Third column shows the generator and the filter used and in the fourth column the filter efficiencies are listed (for the Z+1,2,3 partons including the factor corresponding to the overlap removal with the Zbb sample). The signal cross section is evaluated at tanβ=10.

- **τ-jets**: ATLFAST jets tagged as τ-jets, with additional energy corrections applied to account for the different energy scale of the τ-jets. The kinematical

Process	σ x BR	Generator /Filter	Filter Efficiency
$bbH/A \rightarrow \tau^+\tau^-$ $m_{H/A} = 150$ GeV/c^2 data sample 5354	4792.9fb	Pythia /ATauFilter	0.425
$bbH/A \rightarrow \tau^+\tau^-$ $m_{H/A} = 300$ GeV/c^2 data sample 5353	299.67fb	Pythia /ATauFilter	0.45
$bbH/A \rightarrow \tau^+\tau^-$ $m_{H/A} = 450$ GeV/c^2 data sample 6345	27.73fb	Pythia /ATauFilter	0.218
$bbH/A \rightarrow \tau^+\tau^-$ $m_{H/A} = 600$ GeV/c^2 data sample 6346	5.27fb	Pythia /ATauFilter	0.192
$t\bar{t}$ data sample 5200	833pb	MC@NLO - JIMMY/HERWIG /TTbarLeptonFilter	0.54

Tab. 7.3: Fully simulated signal and background samples. In the first column we mention also the official dataset number. In second column, the NLO cross sections without the filter are mentioned. The third column shows the generator and the filter used and in the fourth column the filter efficiencies are listed. Here tanβ=10 was used for the signal cross section.

cuts applied on the τ-jets are $p_T > 15$ GeV/c and $|n| < 2.7$.

- **b-jets**: ATLFAST jets tagged as b-jets and not tagged as τ-jets, with additional energy corrections applied to account for the different energy scale of the b-jets. The kinematical cuts applied on the b-jets are $p_T > 15$ GeV/c and $|n| < 2.7$.

In Full Simulation the following preselection is done:

- **Muons:** Isolated muons reconstructed with the MUID algorithm [2] (see Section 7.4.1). Isolation criteria require that the sum of transverse energy of the calorimeter cells in a cone $\Delta R = \sqrt{\Delta\eta^2 + \Delta\phi^2} = 0.4$ around the muon be less than 9 GeV. Only the reconstructed muons with $p_T > 25$ GeV/c and $|n| < 2.5$ are selected.

- **Electrons:** Standard ATLAS reconstruction algorithm EGAMMA [68], [69], [8] (see also Section 7.4.2) and the medium identification criteria are used for the electrons, meaning the use of only the calorimeter identification variables and not the inner detector information as explained in Section 7.4.2. In addition, reconstructed electrons should be in the kinematical range of $p_T > 25$ GeV/c and $|n| < 2.5$. For the electron isolation the sum of transverse energy in the calorimeter in a cone $\Delta R = 0.2$ should be less than 6 GeV.

- **τ-jets:** TAUREC [70] package (see Section 7.4.3) is used for the reconstruction of hadronicaly decaying τ-leptons. τ-dentification is performed by requiring the value of the τ-likelihood (see Section 7.4.3) variable to be greater than 4 in the kinematical range of $p_T > 15$ GeV/c and $|n| < 2.7$. Also the ratio of the transverse energy in the hadronic calorimeter to the transverse momentum of the leading track is required to be greater than 0.1, since this hadronic energy should originate from the pion emmited in the τ-decay.

- **b-jets:** b-jets are reconstructed in the range of $p_T > 15$ GeV/c and $|n| < 2.7$. The b-tagging weight from the standard ATLAS b-tagging algorithms is required to be higher than 5 (Section 7.4.4). The jet reconstruction algorithm used is the Cone4, meaning that energy depositions in various cells of the calorimeter are being clusterized in jets with a cone size of $\Delta R = 0.4$.

Since in full simulation a particular object can be identified simultaneously as several different kind of particles from more than one reconstruction algorithms, an overlap removal is applied in the following order: Electrons that are overlapping with muons (in $\Delta R = 0.1$) are removed. τ-jets matching muons or electrons (in $\Delta R = 0.4$) are removed. b-jets that are matching muons, electrons or τ-jets (in $\Delta R = 0.4$) are removed.

Already at this preselection step, the comparison between ATLFAST and full simulation is of great importance. The difference in detector performance given by the two simulations affects all following analysis steps. The basic comparison is performed for the identification and reconstruction efficiencies and fake rates of single particles. Efficiency is defined as the probability for a truth Monte Carlo particle to be identified and reconstructed by a reconstruction algorithm. Its value depends on the type of the particle and its kinematical properties. The efficiencies are calculated by matching the reconstructed particle to the Monte Carlo truth particle in the given angular range (see Equation 7.1). The cone size between the reconstructed and the truth particle for the matching is defined by $\Delta R = \sqrt{\Delta n^2 + \Delta\phi^2}$ and it is 0.1 for muons and electrons and 0.4 for τ-jets and b-jets. Fake (misidentified) particle is a reconstructed particle (Equation 7.1) that fails this matching procedure.

$$\epsilon = \frac{Number\ of\ truth\ particles\ which\ are\ matched\ to\ reconstructed\ (in\ cone\ \Delta R)}{Number\ of\ truth\ particles}$$
$$f = \frac{Number\ of\ reconstructed\ particles\ which\ are\ not\ matched\ to\ truth\ (in\ cone\ \Delta R)}{Number\ of\ reconstructed\ particles} \quad (7.1)$$

7.4.1 Muon Reconstruction

Muon reconstruction in fully simulated events can be performed by using either STACO [67] or MUID [2] packages. In the current analysis muons reconstructed with MUID algorithm were used. Nevertheless, the differences in performance of the two algorithms are small and do not significantly affect the presented results.

The MUID package combines the information from the muon spectrometer and the inner detector. Tracks inside the muon spectrometer are reconstructed starting with the segments within a single muon chamber, which can be assumed to be straight lines. These segments are determined from the drift time information in the MDT chambers. Combining the second coordinate information of all trigger chambers and the precision measurement from MDT chambers, a muon track is fitted, taking into account the energy loss and the Coulomb scattering effects. As a subsequent step, tracks reconstructed in the muon spectrometer are associated with the tracks reconstructed in the inner detector and a combined fit is performed. Final track objects are stored with track parameters at the interaction point.

In ATLFAST [55] muon reconstruction and identification is parametrized in the following way. The true momenta of each muon are smeared by a gaussian function whose width depends on the transverse momentum, the pseudorapidiy η and the azimuthal angle ϕ. In addition, the muon isolation is required, i.e. the energy deposited in a cone $\Delta R = 0.4$ around the true muon should not exceed the energy of the reconstructed muon by more than 10 GeV. Isolation criteria provide for the rejection of muons which originate from the jets.

In Figures 7.6 and 7.7, the muon reconstruction efficiencies and the fake rates are shown as a function of p_T, η and ϕ, for the $t\bar{t}$ process. No significant systematic discrepancies can be seen. Nevertheless, one can point out that ATLFAST does not reproduce the small inefficiency due to the crack region around $\eta = 0$ in the muon spectrometer (see Figure 7.6 b). In addition, inefficiencies that are expected in the transition region between barrel and endcap of the muon spectrometer at $|\eta| \simeq 1.5$ and in the feet region at $\phi \simeq -2.5$ and -1.5 are also not decribed by ATLFAST. The overall (average) efficiency is 88%, while fake rate is rather small, less than 2%.

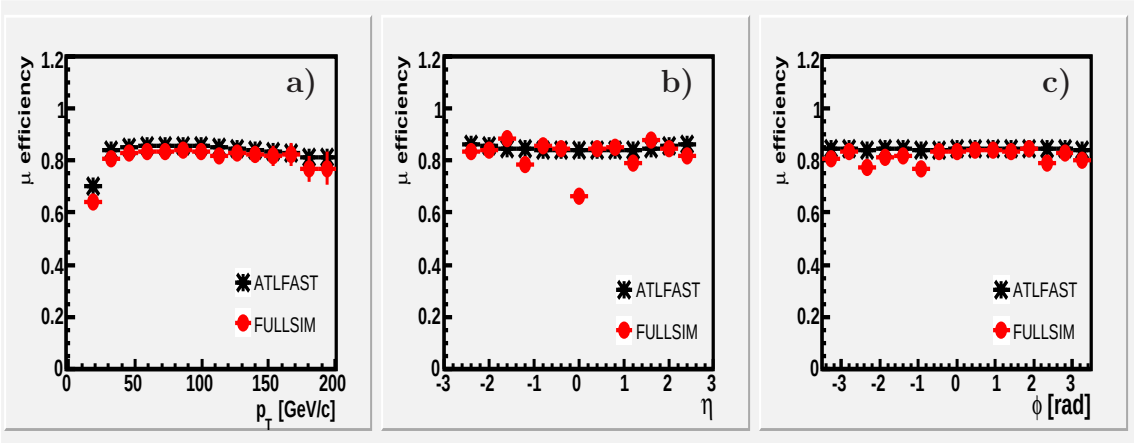

Fig. 7.6: Muon reconstruction efficiency as a function of p_T , η and ϕ for the $t\bar{t}$ process. Results of the full simulation are shown in red (circles), while the ATLFAST results are given in black (stars).

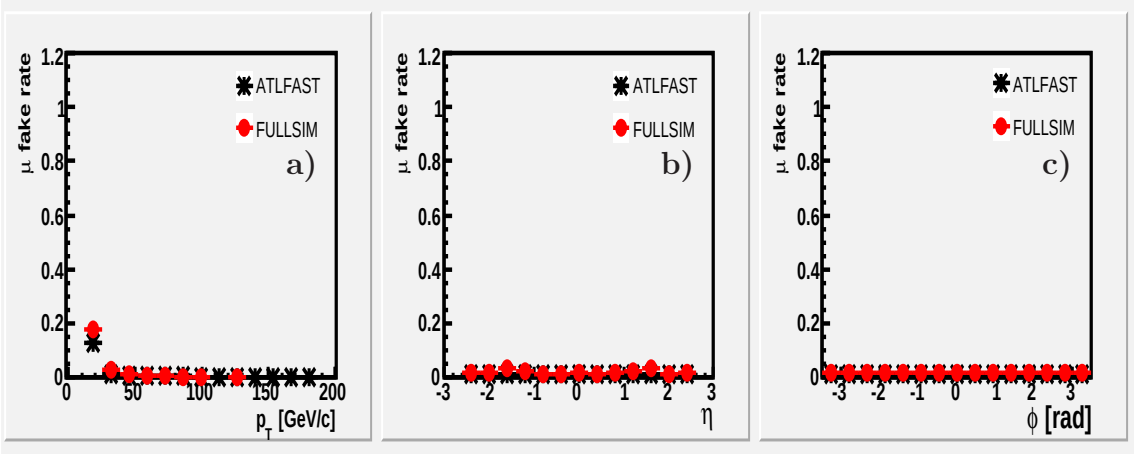

Fig. 7.7: Muon fake rate as a function of p_T , η and ϕ for the $t\bar{t}$ process. Results of the full simulation are shown in red (circles), while the ATLFAST results are given in black (stars).

7.4.2 Electron Reconstruction

As a first step for the electron identification [68], [69], [8] in full simulation, electron candidates are reconstructed. This mainly involves the matching of calorimeter clusters (grouped energy depositions in the calorimeters) to the inner detector tracks with transverse momentum higher than 5 GeV/c. Since the jets also deposit energy in the calorimeters, they can fake an electron signal. Therefore, a strong supression of jets is needed. This is possible by means of the following discriminant properties:

- The hadronic leakage is the ratio of the transverse energy in the first compartment of the hadronic calorimeter and the transverse energy reconstructed in the electromagnetic calorimeter. Since the electrons deposit most of their energy in the electromagnetic calorimeter, this ratio is relatively small (2%) as compared to the jet signals.

- Electromagnetic shower shape: Electromagnetic showers deposit the most of their energy in the second compartment of the electromagnetic calorimeter. Therefore, the energy deposit in the first and the second compartment of the electromagnetic calorimeters are compared to reject jets. After this selection, the remaining fake electrons originate mostly from photon conversion and low multiplicity jets containing a high transverse momentum pion.

- Inner detector information: Track quality cuts require at least nine precision hits in the inner detector (SCT and Pixel) yielding a track with a transverse impact parameter (minimum distance of the track from the beam axis, projected in the transverse plane) less than 0.1 cm. The ratio E/p of the energy (E) in the calorimeter and the track momentum (p) in the inner detector should be approximatelly equal to the unit for electrons, while it is in general lower

for the jets and thus rejects the heavier pions. Finally, a further reduction of the charged hadron contamination is obtained by requiring the large energy depositions in the transition radiation tracker, due to the transition radiation (proportional to E/mc^2).

Electrons in ATLFAST [55] are obtained from the generated true momentum vectors which point to a calorimeter cluster within $\Delta R<0.15$. The truth electron energy is smeared in dependence on the transverse momentum and the pseudorapidity η. Similar as for the muons, the isolation criteria are applied.

In Figures 7.8 and 7.9, the reconstruction efficiencies and the fake rates are shown as a function of p_T, η and ϕ for the $t\bar{t}$ process. When comparing ATLFAST and full simulation, some differences can be seen. ATLFAST overestimates the reconstruction efficiency (Figures 7.8 a), b), c) and 7.9 b), especially in the transition regions between the barrel and endcaps ($\eta = \pm 1.6$) and the in the forward regions ($|\eta| > 1.8$).

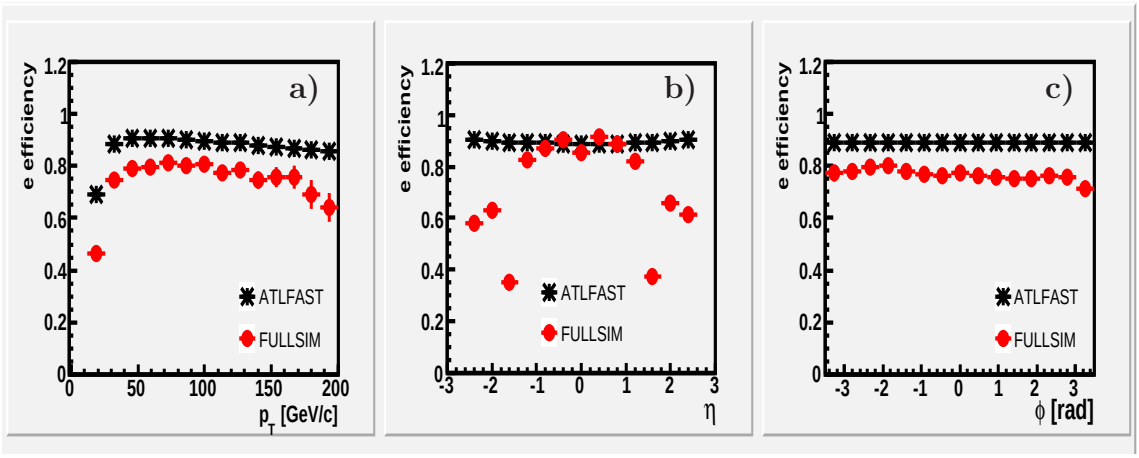

Fig. 7.8: Electron reconstruction efficiency as a function of p_T , η and ϕ for $t\bar{t}$ proccess. Results of the full simulation are shown in red (circles), while the ATLFAST results are given in black (stars).

7.4.3 τ-jet Reconstruction

In full simulation, the TAUREC package [70] was used for the τ-reconstruction and identification. The τ-candidates are defined by the calorimeter cluster. The τ-identification is performed on the τ-candidates based on the likelihood value constructed from the following eight variables:

- Number of charged tracks (N_{tr}) associated with the τ-candidates. One expects ideally one or three tracks, corresponding to the one prong or three prong hadronic τ decays (decays into one or into three charged pions).

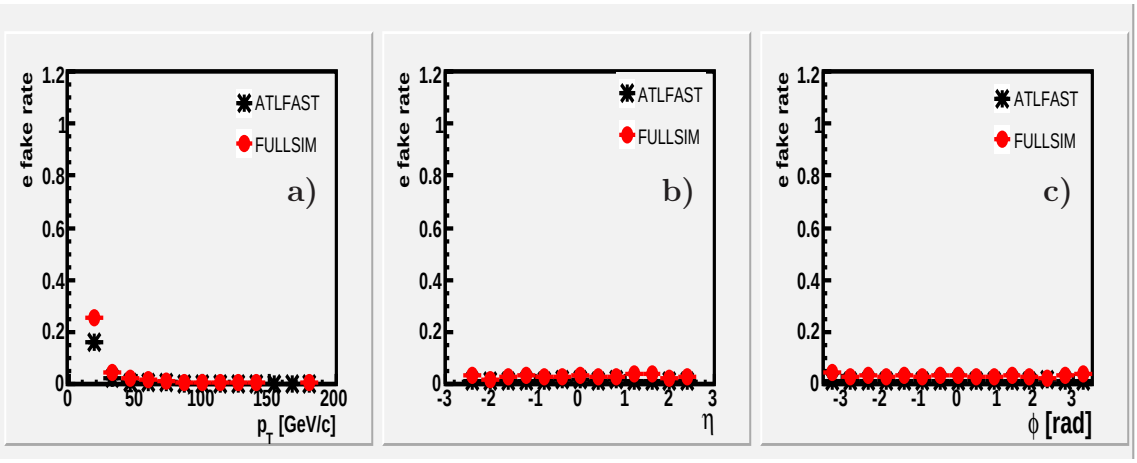

Fig. 7.9: Electron fake rate as a function of p_T , η and ϕ for $t\bar{t}$ proccess. Results of the full simulation are shown in red (circles), while the ATLFAST results are given in black (stars).

- Number of hits (N_{hits}) in the η-strip layer of the EM calorimeter. Hadronically decaying τ-leptons tend to have a lower hit multiplicity than QCD jets.
- The charge (Q_τ) of the hadronicaly decaying τ should be ± 1. It is calculated by summing the charge of all associated tracks.
- The shower profile in the transverse plane in the EM calorimeter:

$$\mathrm{R}_{EM} = \frac{\sum_{i=1}^{j} E_{T_i} \sqrt{(\eta_i - \eta_{cluster})^2 + (\phi_i - \phi_{cluster})^2}}{\sum_{i=1}^{j} E_{T_i}} \quad , \tag{7.2}$$

  were i is the index of all cells of the electromagnetic calorimeter within a cluster of $\Delta R < 0.4$, j denotes the total number of the cells in the cluster, E_{T_i} the tranverse energy in cell i and η and ϕ the pseudorapidity and the azimuthal angle of a cell or a cluster respectively. R_{EM} is narrower for τ-jets which are well-collimated compared to the QCD jets.
- Electromagnetic calorimeter isolation variable (ΔE_T^{12}). For similar arguments related to the narrowness of the jet, the energy deposited in a ring area of $0.1 < \Delta\mathrm{R} < 0.2$ around the τ-candidate is required to be small.
- Transverse energy width in the η-strip layer of the EM calorimeter $\Delta\eta$:

$$\Delta\eta = \sqrt{\frac{\sum_{i=1}^{j} E_{T_i} (\eta_i - \eta_{cluster})^2}{\sum_{i=1}^{j} E_{T_i}}} \quad , \tag{7.3}$$

were i is the index of all cells of the electromagnetic calorimeter within a cluster of $\Delta R < 0.4$, j denotes the total number of the cells in the cluster, E_{T_i} the tranverse energy in cell i and η and ϕ the pseudorapidity of a cell or a cluster respectively. At low energy scale $\Delta\eta$ is smaller for the τ-candidates than for QCD jets.

- The vertex position of the τ-jet (σ_{IP}). The τ-jet vertex is displaced from the primary interaction vertex, due to the relatively high τ-lifetime of 2.9×10^{13} sec.

- The ratio of transverse energy of the τ-candidate measured in the hadronic calorimeter and the transverse momentum of the leading track associated to the τ candidate (E_T/p_T^{1st}). This ratio is smaller for τ-jets than for other jets, since τ-jets are expected to have a high fraction of their energy in the leading track. QCD jets, on the other hand, have more tracks with uniform p_T distribution. Also, they have more additional neutral particles.

The ATLFAST τ-identification is parametrized in the following way: All clusters that have not been asigned to a true electron or photon are considered as jets. All muons that are within a cone $\Delta\mathrm{R} = 0.4$ close to a jet are included into the jet. The τ-jets are tagged by association of the candidate jet to the true hadronically decaying τ-lepton within a cone of $\Delta\mathrm{R} = 0.3$. The ratio of the transverse momentum of the sum of all visible decay products of hadronically decaying τ-leptons ($p_T^{\tau-had}$) and the jet transverse momentum ($p_T^{\tau-jet}$) should be $p_T^{\tau-had}/p_T^{\tau-jet} > (1 - 2\sigma(p_T^{jet})/p_T^{jet})$, where $\sigma(p_T^{jet})$ is the expected τ-jet momentum resolution. It indicates the dominance of the jet energy by the hadronic τ-decay products. The identification efficiency and the energy correction of the selected true τ-jets is parametrized in accordance with results from the full simulation studies.

Detailed description of the τ-identification with the TAUREC package as well as the corresponding ATLFAST parametrization can be found in [50],[55].

By comparing τ-jet reconstruction performance for the two simulations (Figures 7.10 and 7.11 a) to c), some differences are observed. The efficiency as a function of p_T (Figure 7.10 a) in full simulation reaches a maximum in the regin between 30 to 50 GeV/c, while it is almost constant for higher momenta. On the contrary, ATLFAST parametrization yields an almost constant efficiency for momenta above 30 GeV/c. In addition, the large inefficiency (Figure 7.10 b) due to worse track reconstruction is observed in the transition region between barrel and end-cap of inner detector ($|\eta| = 1$), while this is not taken into account in ATLFAST. The fake τ-jets originate from the light jets (u-, d-, s-quarks) and the electrons in full simulation, while mostly in ATLFAST the mistagged τ-jets originate from b-quarks, as can be seen in the Figure 7.12. In the signal sample, this rate is significantly lower, since no contribution from the light jets is present.

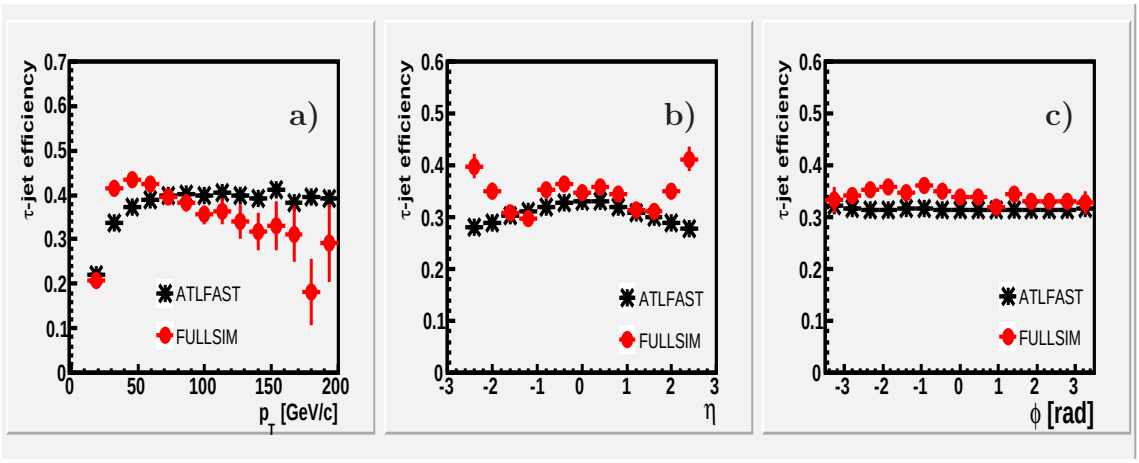

Fig. 7.10: τ-jet efficiency as a function of p_T , η and ϕ for $t\bar{t}$ proccess. Results of the full simulation are shown in red (circles), while the ATLFAST results are given in black (stars).

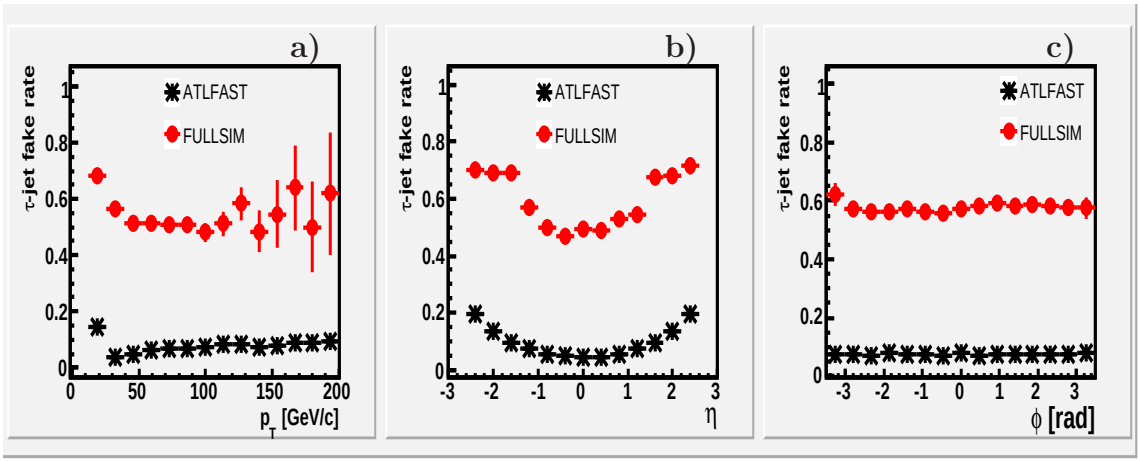

Fig. 7.11: τ-jet fake rate as a function of p_T , η and ϕ for $t\bar{t}$ proccess. Results of the full simulation are shown in red (circles), while the ATLFAST results are given in black (stars).

7.4.4 b-jet Reconstruction

In full simulation, the b-jet candidates are given by the jets reconstructed using the cone algorithms with $\Delta R = 0.4$ cone size. The b-tagging is then performed using the selected the associated tracks and the secondary vertex position. In order to select only the well measured tracks, at least seven precision track hits are required in the inner detector, assigned to a track of transverse momentum higher than 1 GeV/c. Additional constraints for the transverse and longitudinal impact parameters of each track at the perigee are required.

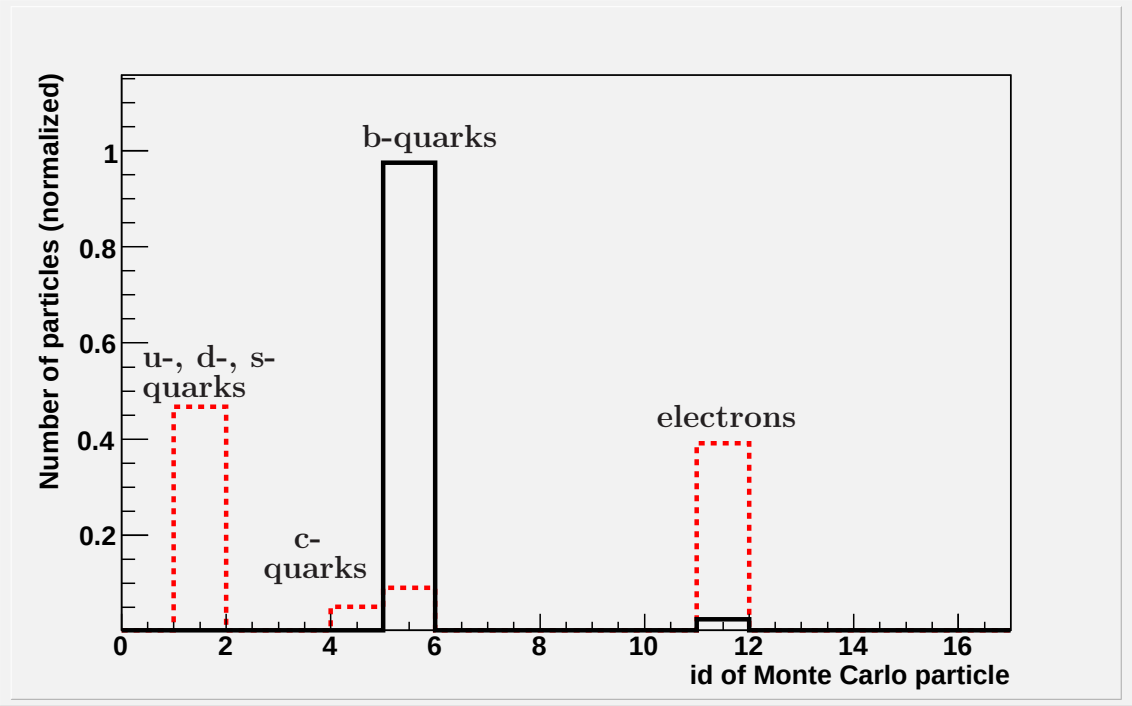

Fig. 7.12: Contribution of different particles to the τ-jet fake rate in the case of $t\bar{t}$ background. Results of the full simulation are shown in red (dashed), while the ATLFAST results are given in black (full).

Both impact-parameter tagging based on track information and the secondary vertex tagging information are combined through the likelihood method into a single output variable, the so called b-tagging weight.

The b-tagging in ATLFAST [55] is performed in a similar way as for the τ-jets. The b-jet candidate is a reconstructed jet which matches a true b-quark within a cone of $\Delta R = 0.3$ after the final state radiation. The identification (b-tagging) efficiency and energy corrections are then applied on these true b-jets candidates, parametrized as a function of the p_T and η of the true b-quarks. Similarly, the reconstructed jets which do not match the b-quarks contributr to the misidentified b-jets, with the fake rate according to the parametrized rejection curves.

ATLFAST parametrization yields similar average efficiencies and fake rates as in the full simulation (Figures 7.13 and 7.14 a) and c). However, there are differencies in the p_T- and η-dependence. Full simulation is less efficient for the b-jets with p_T below 50 GeV/c (Figure 7.13 a), as well as in the forward η-region (Figure 7.13 b). This η-dependance is corellated with the tracking performance of the inner detector, which plays a vital role for the reconstruction of secondary vertices.

Average efficiencies and fake rates of all reconstructed objects are summarized in Table 7.4 for both full and fast simulation of the $t\bar{t}$ events.

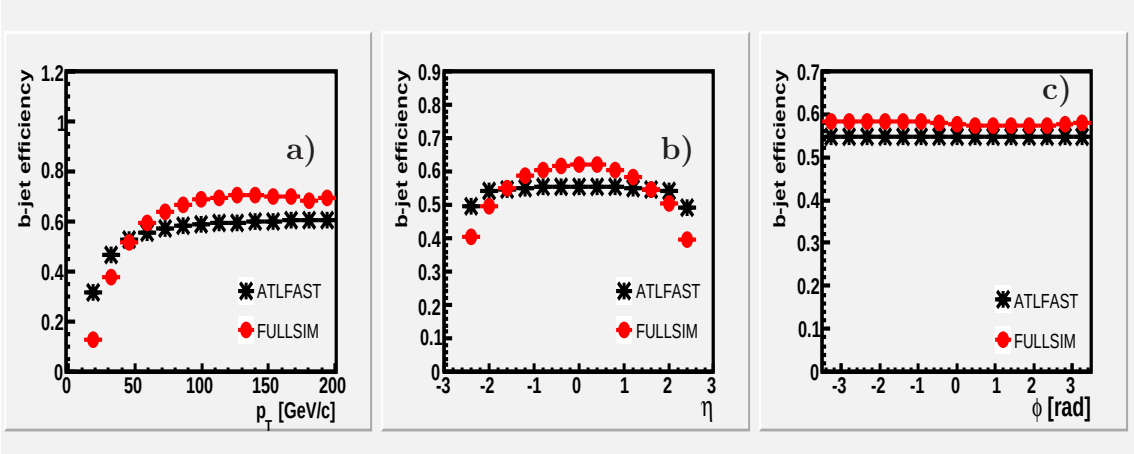

Fig. 7.13: b-jet efficiency (jet reconstruction efficiency multiplied by the b-tagging efficiency) as a function of p_T , η and ϕ for $t\bar{t}$ proccess. Results of the full simulation are shown in red (circles), while the ATLFAST results are given in black (stars).

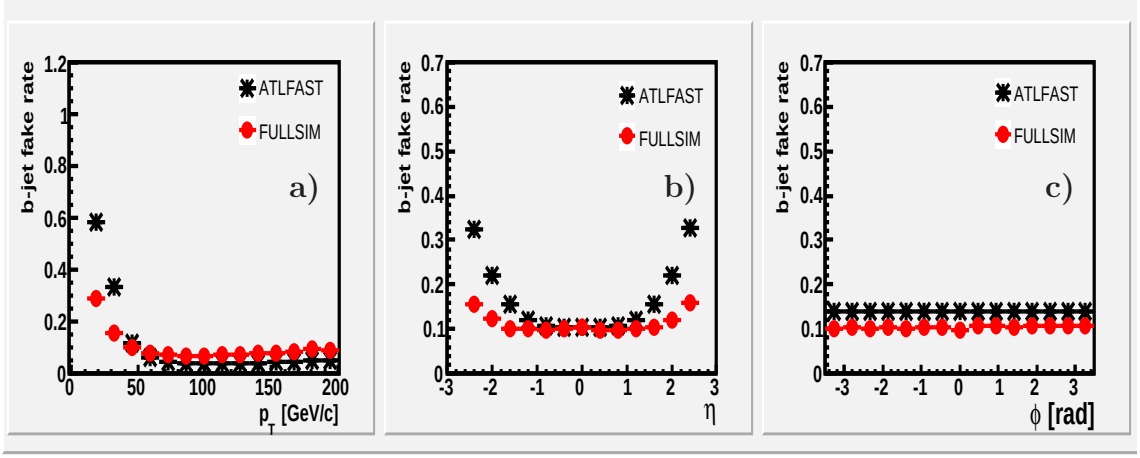

Fig. 7.14: b-jet fake rate as a function of p_T , η and ϕ for $t\bar{t}$ proccess. Results of the full simulation are shown in red (circles), while the ATLFAST results are given in black (stars).

While the muon, τ-jet and b-jet reconstruction efficiencies are in good agreement between the two simulations, the electron efficiency is overestimated by ATLFAST.

It can also be observed that the rate of fake particles is somewhat lower in ATLFAST, in particular for the τ-jets, as explained in Section 7.4.3.

In order to investigate how the detector performance depends on the event topology, we extend our performance study also on the signal data sample. In Figure 7.15 the reconstruction efficiency is shown for muons, electrons, b-jets and τ-jets and the fake rate for b-jets and τ-jets evaluated for bbA signal at 450 GeV/c^2. While the conclusions for muons, electrons and b-jets are similar to those for the $t\bar{t}$ sample,

	Fast		Full	
	ϵ	fake	ϵ	fake
μ	85%	<<1%	84%	1%
e	89%	<<1%	78%	4%
τ-jet	33%	8%	35%	57%
b-jet	55%	14%	58%	11%

Tab. 7.4: $t\bar{t}$ sample: efficiencies and fake rates in full and fast simulation, after applying the preselection discribed in Section 7.4.

the τ-jet fake rate shows smaller discrepancies between full and fast simulation, as explained above. It is approximatelly ten times higher in full simulation. These τ-jets mostly come from the b-jets, light jets and electrons. The large number of fake τ-jets in the $t\bar{t}$ sample will result in additional background events which have not been considered in the final analysis, which was performed on ATLFAST data.

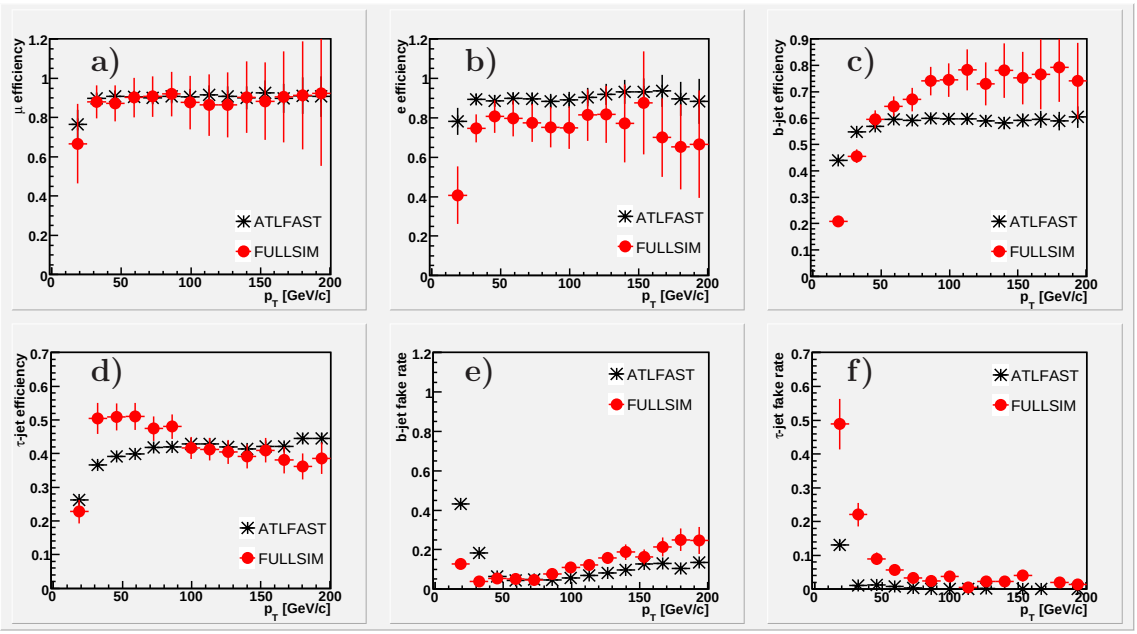

Fig. 7.15: Muon, electron, b-jet and τ-jet reconstruction efficiency (a, b, c, d), as well as b-jet and τ-jet fake rates (e, f) for the $b\bar{b}A$ proccess. Results of the full simulation are shown in red (circles), while the ATLFAST results are given in black (stars).

7.4.5 Missing Energy Reconstruction

The total transverse energy of all non- or weakly-interacting particles is measured as a transverse missing energy. It is calculated by summing the momentum vectors of all visible particles and taking the negative transverse projection of this sum. Due to energy conservation, the total transverse energy of all particles produced in pp-collisions should be equal to 0, so that the contribution of all non-detected particles (neutrinos) is balanced by the contributions from the visible particles.

In full simulation, the calculation of the transverse missing energy is performed by summing up the energy of all calorimeter cells which contain energies above a given noise level. The momenta of all reconstructed muons (without the energy lost in the calorimeter) is also taken into account.

In ATLFAST, the calculation is performed by adding the momenta of isolated leptons (e and μ), photons, jets, non-isolated muons which are not associated to a jet, clusters not accepted as jets and cells not inlcuded in clusterization.

Comparison of the transverse missing energy reconstruction in full and fast simulation is shown in Figures 7.16 and 7.17, for the Higgs mass of 300 GeV/c^2. Figure 7.16 shows the difference between the true and the reconstructed transverse missing energy. The width of the two distributions is a measure of the resolution. A fit of the gaussian curve to the distribution from the full simulation yields a mean at -3.5% with standard deviation (i.e. resolution) of 23.6%. In ATLFAST, the mean is 0.05% and the resolution 15.3%. The observed difference in the resolution does not affect significatly the overall distribution of the transverse missing energy as can be seen in Figure 7.17.

In Figures 7.18 the transverse momentum resolutions for muons, electrons, τ-jets and the missing energy resolution for ATLFAST are shown. Missing energy resolution is in the order of 15%. Momentum resolution for muons and electrons is 2.3% and 1.6% respectively, better than for the τ-jets with a resolution of 5.3%.

7.5 Reconstruction of the Higgs Mass

Weakly interacting particles like neutrinos cannot be directly measured in the detector. In the case of more than one neutrino in an event, the missing energy accounts for the total contribution of all neutrinos, no seperate detection is possible.

In the $H/A \rightarrow \tau\tau \rightarrow (\ell\nu_\ell\nu_\tau)(\tau_{jet}\nu_\tau)$ decays, there are three neutrinos present in the event. This makes the direct reconstruction of the invariant mass of two τ-leptons and therefore of the Higgs mass impossible. Nevertheless, the Higgs mass peak can still be reconstructed by means of the assumption that the τ decay products are collinear to the τ-lepton. This assumption, also known as the collinear approximation, is quite accurate (see Figure 7.19) since the mass of the τ-lepton (1.777 GeV/c^2) is much lower than the Higgs mass, which results in a strong boost of τ-leptons from the Higgs decay.

By means of collinear approximation, it is possible to project the vector of transverse missing energy into two components whose directions are defined by the vectors

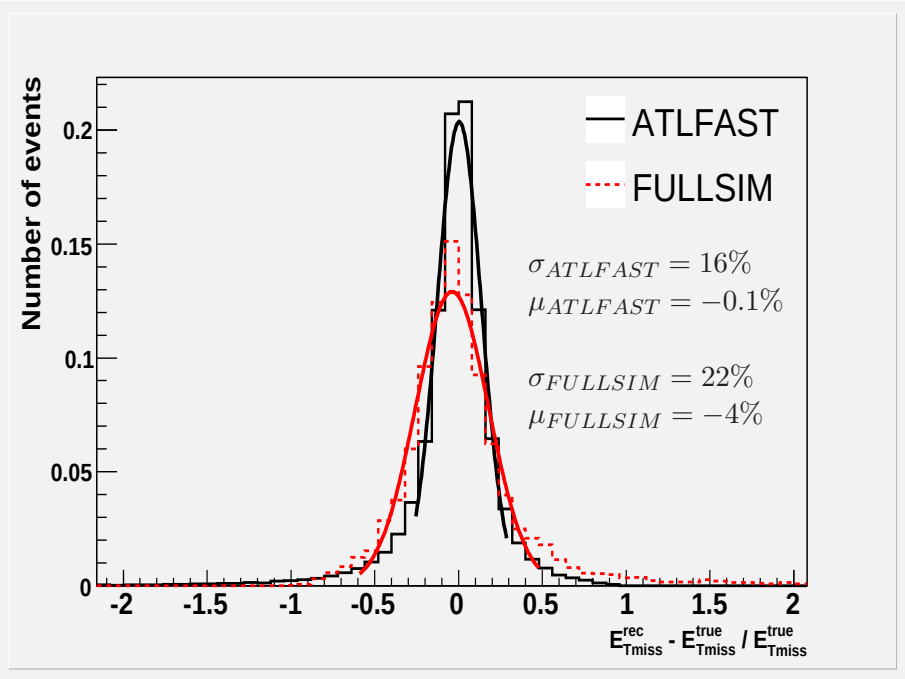

Fig. 7.16: Resolution of the transverse missing energy measurement. Red (dashed) line shows the results of the full simulation and the black (full) line the fast simulation. The distributions are obtained for the bbA signal sample with $m_A = 300$ GeV/c^2.

of the two visible τ decay products (see Figure 7.20). In this way, the four-momenta of the Higgs decay products are unambiguously determined.

Assuming the massles τ particles, the invariant mass of the Higgs system is given by:

$$M_{H/A} = M_{\tau\tau} = \sqrt{2 \cdot p_{\tau_1} p_{\tau_2}(1 - cos\theta)} = \sqrt{2 \cdot (p_1 + p_{\nu_1})(p_2 + p_{\nu_2})(1 - cos\theta)} \quad (7.4)$$

where $p_{\tau_{1(2)}}$ is the momenta of the τ-leptons, the momenta of the visible τ decay products are $p_{1(2)}$, while the energy from the neutrino momenta are given by $p_{\nu_{1(2)}}$. θ is the angle between the two visible τ decay products. Collinear approximation implies that the visible τ-decay products cary a fraction $\chi_{1(2)}$ of the whole $\tau_{1(2)}$ momentum:

$$\begin{aligned} \frac{p_1^x}{p_{\tau_1}^x} &= \frac{p_1^x}{p_1^x + p_{\nu_1}^x} = \chi_1 \quad , \quad \frac{p_1^y}{p_{\tau_1}^y} = \frac{p_1^y}{p_1^y + p_{\nu_1}^y} = \chi_1 \\ \frac{p_2^y}{p_{\tau_2}^y} &= \frac{p_2^x}{p_2^x + p_{\nu_2}^x} = \chi_2 \quad , \quad \frac{p_2^y}{p_{\tau_2}^y} = \frac{p_2^y}{p_2^y + p_{\nu_2}^y} = \chi_2 \end{aligned} \quad (7.5)$$

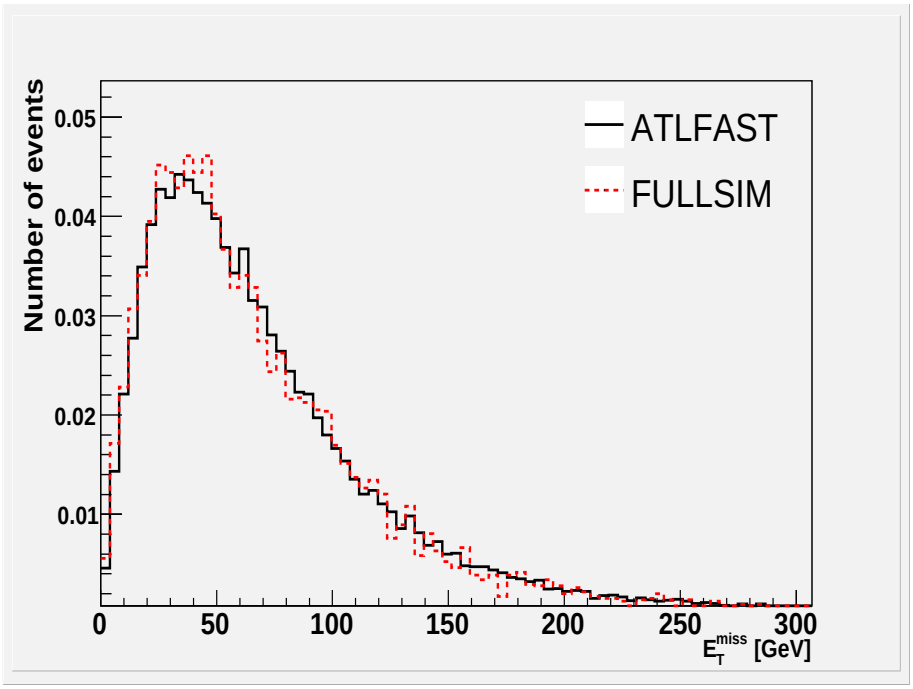

Fig. 7.17: Transverse missing energy distributions for full (full line) and fast (dashed line) simulation, obtained for the bbA signal sample with the Higgs mass of 300 GeV/c^2.

Indices x and y indicate the two components of the momentum vectors.

Making use of the measured missing transverse energy $E^{x,y}_{miss}$, following constraint is applied:

$$\begin{aligned} p^x_{\nu_1} + p^x_{\nu_2} &= E^x_{miss} \quad , \\ p^y_{\nu_1} + p^y_{\nu_2} &= E^y_{miss} \quad . \end{aligned} \tag{7.6}$$

Combining equations 7.5 and 7.6, one obtains:

$$\begin{aligned} \frac{1-\chi_1}{\chi_1} p^x_1 + \frac{1-\chi_2}{\chi_2} p^x_2 &= E^x_{miss} \quad , \\ \frac{1-\chi_1}{\chi_1} p^y_1 + \frac{1-\chi_2}{\chi_2} p^y_2 &= E^y_{miss} \quad . \end{aligned} \tag{7.7}$$

Solving the system of equations 7.8, the momentum fractions χ_1 and χ_2 are obtained:

$$\begin{aligned} \chi_1 &= \frac{p^y_1 p^x_2 - p^x_1 E^y_2}{p^y_1 p^x_2 - p^x_1 p^y_2 + E^y_{miss} p^x_2 - E^x_{miss} p^y_2} \quad , \\ \chi_2 &= \frac{p^y_1 p^x_2 - p^x_1 E^y_2}{p^y_1 p^x_2 - p^x_1 p^y_2 + E^x_{miss} p^y_1 - E^y_{miss} p^y_1} \quad . \end{aligned} \tag{7.8}$$

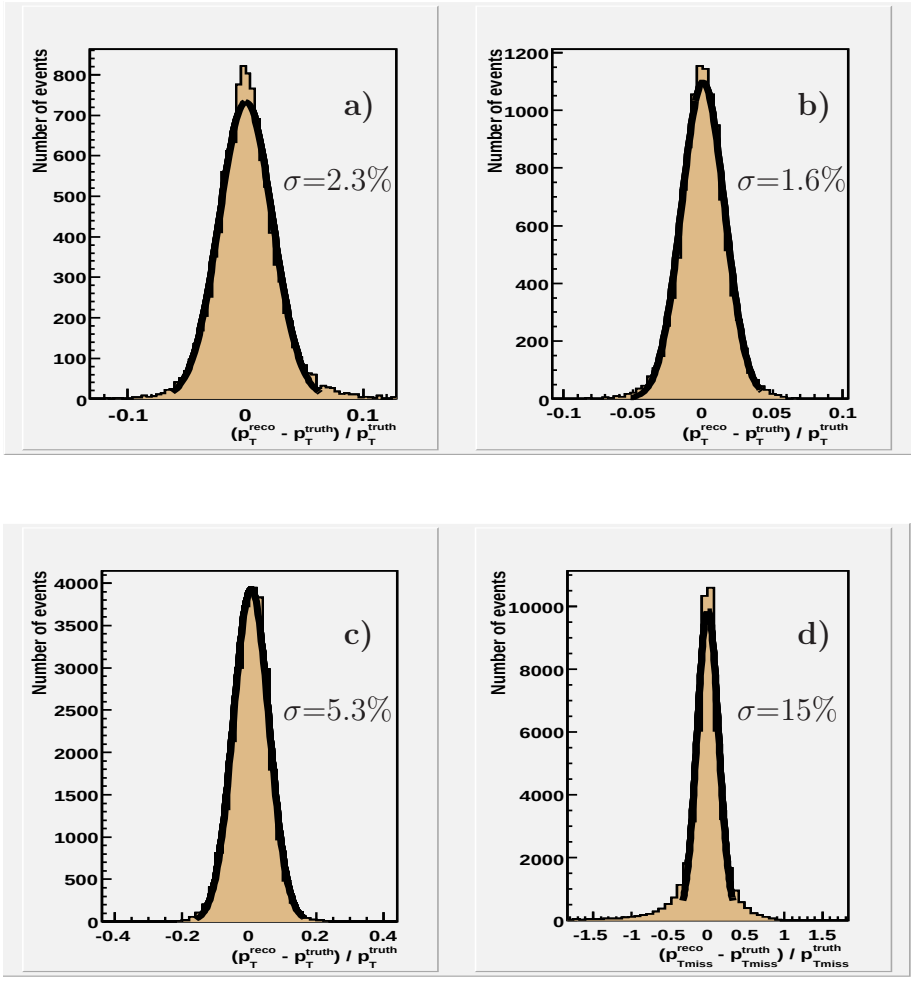

Fig. 7.18: Transverse momentum resolution for muons (a), electrons (b), τ-jets (c) and the missing energy (d).

By means of χ_1 and χ_2, the τ-momenta are determined ($p_{\tau_1} = p_1/\chi_1$) and therefore the mass of the Higgs boson can be calculated, the assumption of the collinear approximation is limited by the angle between the visible decay products. In events where the two τ's are emmitted back-to-back, at an azimuthal angle of 180^o degrees (see Figure 7.21). The transverse missing energy is equal to zero and the solutions of the equations mentioned above are completely arbitrary, creating large tails in the $M_{\tau\tau}$-spectrum (Figure 7.22).

The impact of the collinear approximation on the Higgs mass reconstruction is shown in Figure 7.23. The narrow peak indicated by the black (doted) line shows the generated Higgs resonance, including only the physical width of the particle. The collinear approximation applied on the true momenta of visible τ-decay products results in a wider peak indicated by the blue (full) line. Additional effect of the finite detector resolution results in a mass peak indicated be the red (dashed)

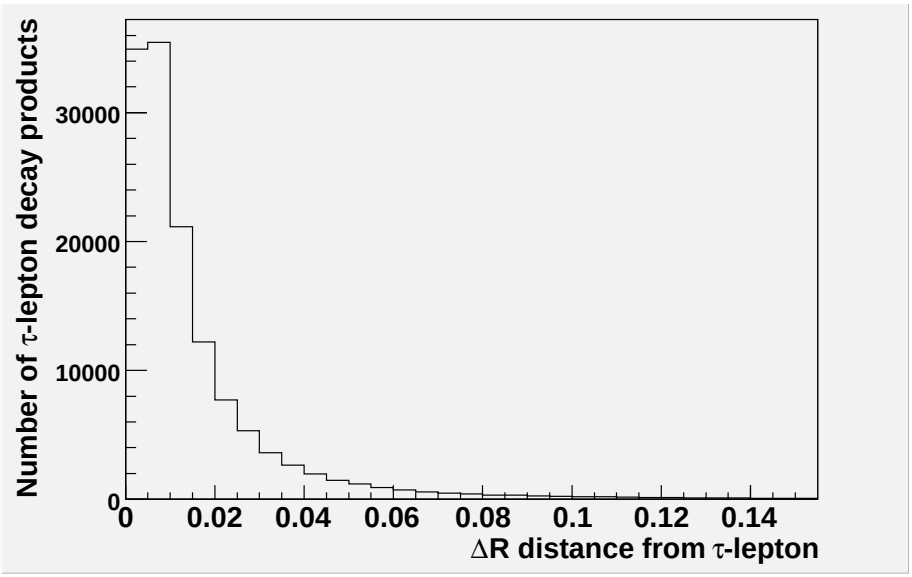

Fig. 7.19: Distance between the τ-lepton and its decay products, defined as $\Delta R = \sqrt{(\Delta\phi)^2 + (\Delta\eta)^2}$.

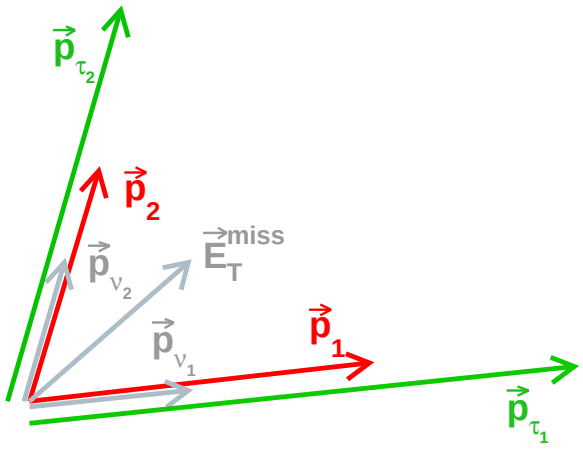

Fig. 7.20: A schematic view of the collinear approximation concept. The measured vector of the missing transverse energy ($\vec{E}_T^{miss}$) can be projected in the direction of the visible τ-decay products ($\vec{p}_1, \vec{p}_2$). This procedure assumes that all τ-decay products are collinear with the parent τ-particle. The two projections ($\vec{p}_{\nu_1}, \vec{p}_{\nu_2}$) represent the energy of neutrinos coming from the decay of two τ-leptons. Therefore, the τ-momenta can be fully reconstructed as $\vec{p}_{\tau_{1(2)}} = \vec{p}_{1(2)} + \vec{p}_{\nu_{1(2)}}$.

line. Detector resolution affects very slightly the mass resolution much less than the collinear approximation itself. The $\chi_{1(2)}$ distributions will be affetced by the momentum resolution of the corresponding visible τ-decay products. Since the electron and

muon resolution is better than τ-jet resolution (see Section 7.4), the corresponding χ-distribution will also be broader and shifted out of the physical range between 0 and 1 for τ-jets (see Figure 7.24). For the Higgs mass reconstruction, only the physical solutions with $\chi_{1(2)}\ \epsilon$ (0,1) are selected (see Figure 7.25).

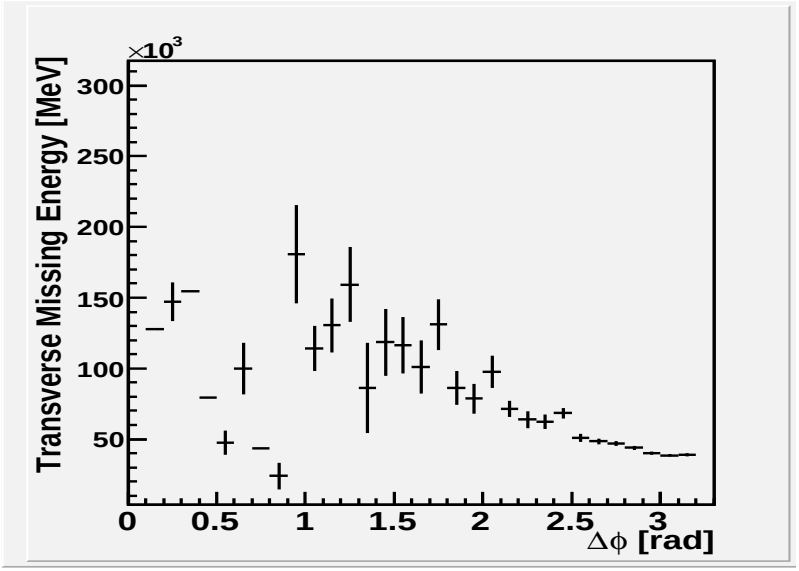

Fig. 7.21: Transverse missing energy in dependence on the azimuthal angle $\Delta\phi$ between the visible τ decay products. For events with back-to-back Higgs decay products the transverse missing energy tends to zero.

7.6 Event Selection Criteria

As mentioned in section 7.1, dominant production mode of the neutral MSSM Higgs bosons at high tanβ values is the associated production with two b-quarks. Therefore, the selection criteria are optimized for the signatures with at least one b-jet in the final state. The set of discriminating variables which have been used to discriminate signal from the background are:

- **lepton - τ-jet pair**: At least one lepton and one τ-jet, oppositely charged and with a lepton transverse momentum $p_T^l > 25$ GeV and a τ-jet transverse momentum $p_T^h > 40$ GeV are required (see Figures 7.26 and 7.27). If more than one combination exists, the selected pair is the one with the highest lepton and τ-jet transverse momenta.

- **angular azimuthal distance $\Delta\phi$ between the lepton and τ-jet**: Events with back-to-back Higgs decay products do not have a unique solution for the collinear approximation, as explained in the previous section. Therefore, the upper bound on $\Delta\phi$ should be set. In addition, significant suppresion of the Z

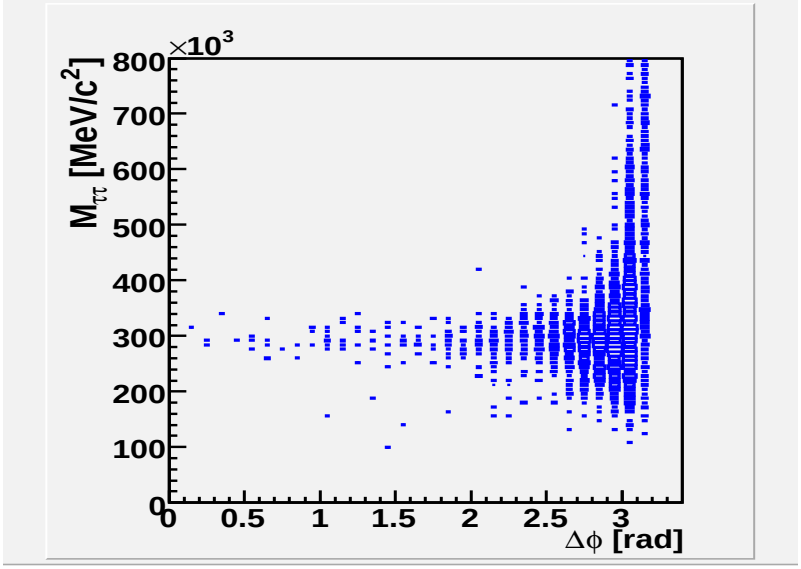

Fig. 7.22: Azimuthal angle $\Delta\phi$ between the visible τ decay products in dependence on the reconstructed Higgs mass $M_{\tau\tau}$. For the back-to-back topologies with $\Delta\phi \simeq 180^o$, the collinear approximation does not work, causing the tails in the Higgs mass distribution.

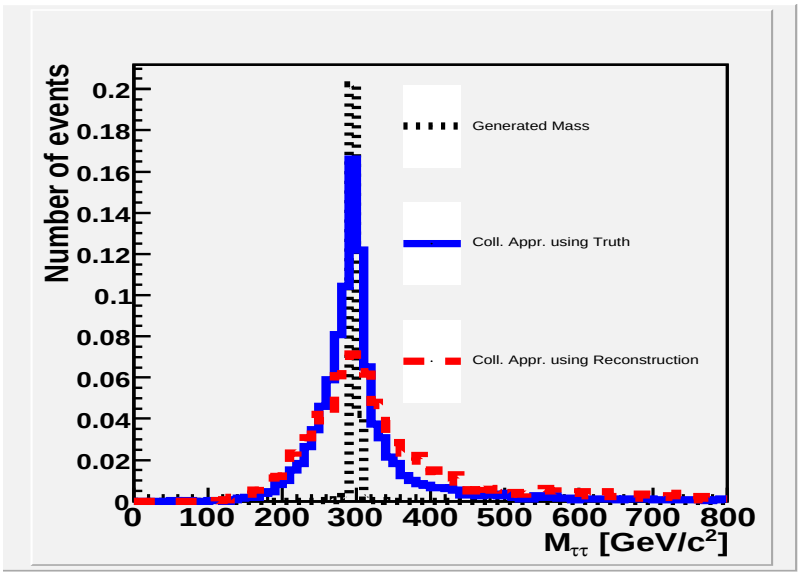

Fig. 7.23: Higgs mass reconstruction. Black (dotted) line shows the the narrow Higgs resonance obtained directly from the generator. Collinear approximation applied on the true momenta of visible paticles and true E_T^{miss} results in broader mass distribution, as shown by the blue (full) line. Finally, the red (dashed) line illustrates the reconstructed mass obtained from the collinear approximation applied on the reconstructed objects.

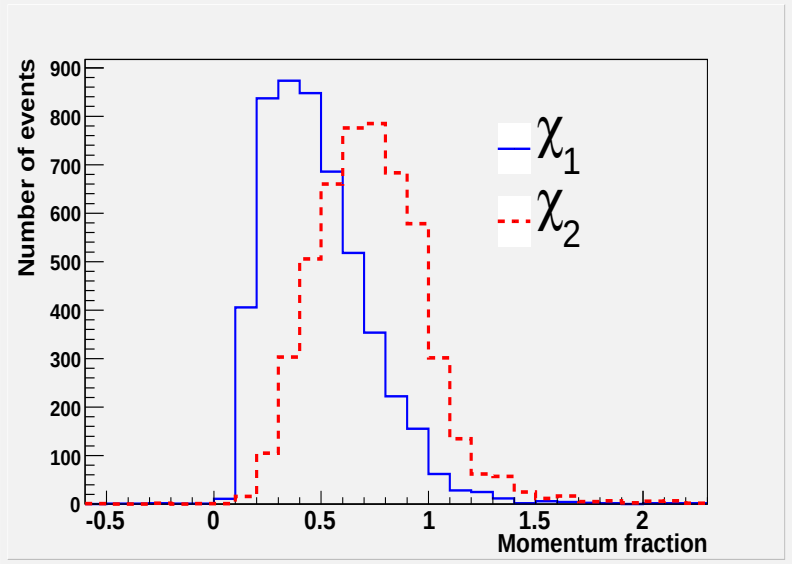

Fig. 7.24: Momentum fractions χ_1 and χ_2. The χ_2 which corresponds to the momentum fraction carried by τ-jets (dashed red line) is broader and shifted out of the physical range between 0 and 1, with respect to χ_1 (blue full line) which corresponds to the momentum fraction carried by the electrons or the muons.

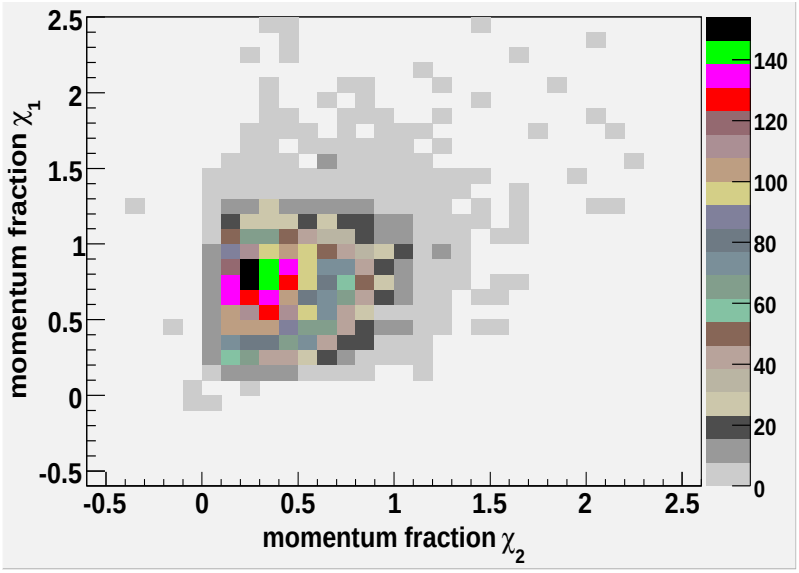

Fig. 7.25: Two-dimensional plot showing the χ_1 versus χ_2 momentum fraction distribution for the signal process. χ_2 corresponds to the mimentum fraction carried by τ-jets and χ_1 corresponds to the momentum fraction carried by the electrons or the muons. Only the physical solutions with $\chi_{1(2)}$ ϵ (0,1) are selected for the analysis.

background by the lower bound on $\Delta\phi$ can be achieved. The Z boson is lighter than the H/A bosons considered in the present study, thus having less boosted decay products. Therefore, $\Delta\phi$ tends to be lower for the Z background. Events with 1.8< $\Delta\phi$ <2.85 are selected in the analysis (Figure 7.28).

- **Collinear approximation**: Events are required to have physical solutions of equations 7.5, 7.6. Therefore, the momentum fractions χ_1 and χ_2 should be between 0 and 1 (Figures 7.29 and 7.30). This selection is mostly effective against the $t\bar{t}$ background.

- **Transverse mass (M_T)**: Transverse mass is defined as $M_T = \sqrt{2 \cdot p_T^l \cdot E_T^{miss}(1 - cos\Delta\theta)}$, where $\Delta\theta$ is the azimuthal angle between the vectors of $\vec{p}_T^{\,l}$ and $\vec{E}_T^{miss}$, $\vec{p}_T^{\,l}$ is the lepton transverse momentum. Events with W decays give a higher a higher transverse mass than the Higgs signal, with an end point close to the W mass. Thus we require $M_T < 35$ GeV (Figure 7.31), mainly aiming to reduce the W background.

- **Missing energy (E_T^{miss})**: Due to the presence of neutrinos from the τ decays, high missing energy is a characteristic signature of this channel. $E_T^{miss} > 25$ GeV is required (Figure 7.32) to supresses the Z background. Since the Z boson is lighter than the Higgs boson, the neutrinos from the τ-leptons in Z-decays will have a lower energy.

- **Number of b-jets (N_b)**: In the associated Higgs production mode, the b-jets are expected in the final state. Taking into account a relatively low b-jet reconstruction efficiency of 40% to 50%, at least one reconstructed b-jet ($N_b \geq 1$) is required in the event (Figure 7.33). Requiring the presence of both b-jets would substantially decrease the signal. This selection criteria is in particular effective against the Z production, with no b-jets in the final state.

- **Mass window ($\Delta M_{\tau\tau}$)**: Events that pass the previous selection criteria succesfully should give a reconstructed mass within a certain mass window around the generated signal mass. The mass window is defined as the region of 1.5 standard deviations around the mean value of a gaussian curve fitting the reconstructed Higgs resonance, after the collinear approximation and before any other cuts. The range of the mass window depends on the Higgs mass, see Table 7.5. For low Higgs masses the detector resolution gives the dominant contribution to size of the mass window. For higher masses the dominant contribution comes from the natural width of the Higgs resonance.

All cuts mentioned above have been optimized for the maximum signal significance, for each cut separately. The signal significance σ is defined as the number of signal events divided by the square root of the sum of signal and background events:

$$\sigma = S/\sqrt{S+B} \quad . \tag{7.9}$$

	Mass window ΔM
150 GeV/c^2	$\pm$25 GeV/c^2
300 GeV/c^2	$\pm$55 GeV/c^2
450 GeV/c^2	$\pm$75 GeV/c^2
600 GeV/c^2	$\pm$120 GeV/c^2

Tab. 7.5: Mass window for the four different signal mass points.

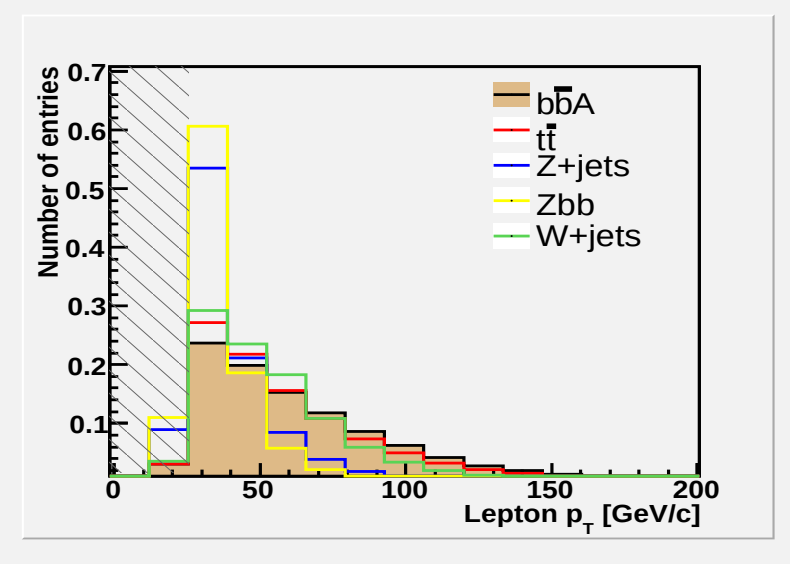

Fig. 7.26: Distribution of the lepton (e,μ) transverse momentum, shown for the bbA signal at 300 GeV/c^2 and for the dominant backgrounds. Cut at 25 GeV/c (indicated by the shaded area) is effective mostly against the Z background where the τ-leptons are less boosted than in the signal process.

An example of the optimization procedure is illustrated in Figure 7.34 for the lower bound on the $\Delta\phi$ azimuthal angle between the τ-visible decay products. Significance curves, showing the dependance of the signal significance on the particular cut value of a given discriminating variable, have been produced for each discriminating variable. The optimal cut values have been extracted from these curves.

7.7 Analysis Results

We apply the selection criteria mentioned in the previous section on the signal and the background processes mentioned in Table 7.3. The results are summarized in Tables 7.6 and for the signal and in Table 7.8 for the background processes. The signal production rates processes are evaluated at tanβ=10 and the rates for H and A vosons have been added together. The first row shows the total number of events expected for an integrated luminosity of 30 fb^{-1}. The impact of the

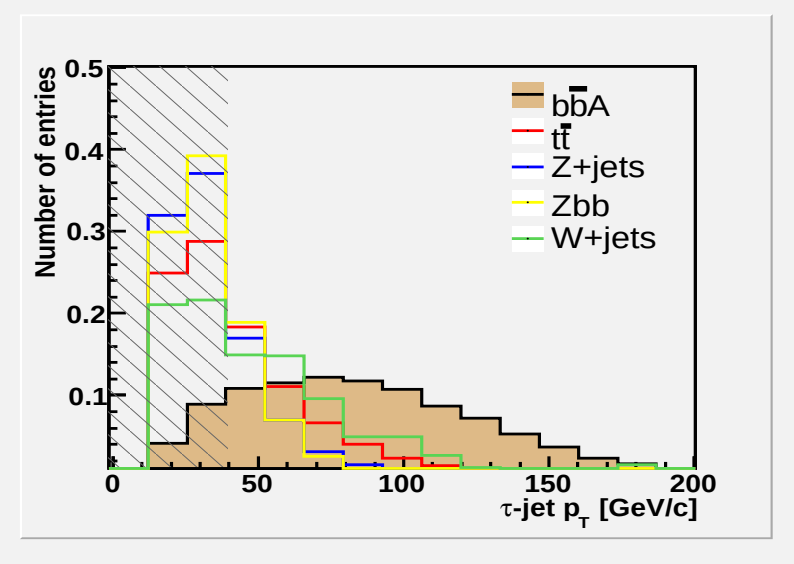

Fig. 7.27: Distribution of the τ-jet transverse momentum, shown for the bbA signal at 300 GeV/c^2 and for the dominant backgrounds. The cut at 40 GeV/c (indicated by the shaded area) is effective mostly against the Z background where the τ-leptons are less boosted compared to the signal process.

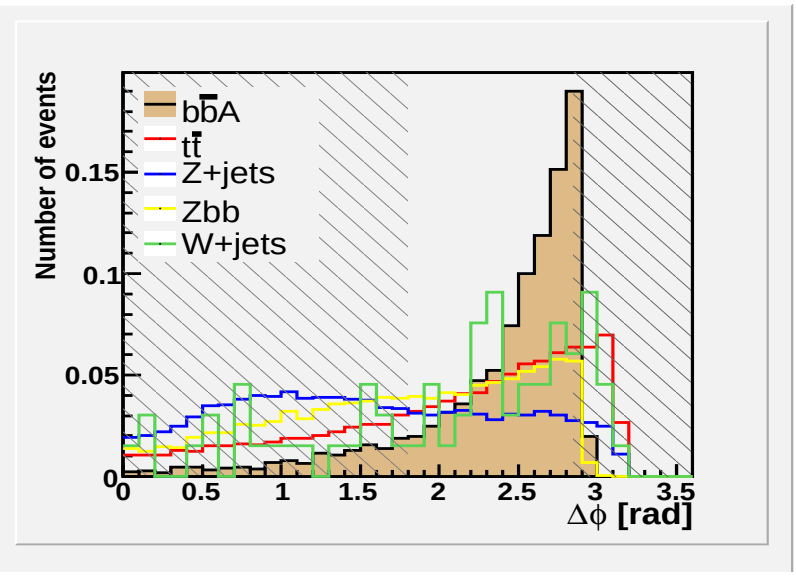

Fig. 7.28: Angular separation $\Delta\phi$ between lepton and a τ-jet in the transverse plane. The cut at $1.8 < \Delta\phi < 2.85$ (indicated by the shaded area) is effective against the Z background.

selection cuts is shown in the subsequent rows in terms of relative efficiencies with respect to the previous selection cut. The last two rows show the number of events

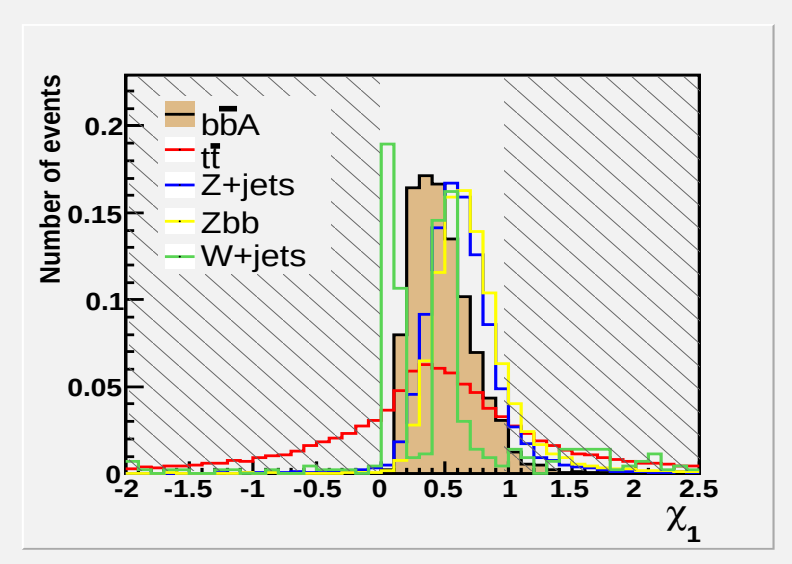

Fig. 7.29: τ-momentum fraction χ_1 carried by an electron or a muon. The cut $\chi_1 \epsilon (0,1)$ (indicated by the shaded area) is effective against the $t\bar{t}$ background.

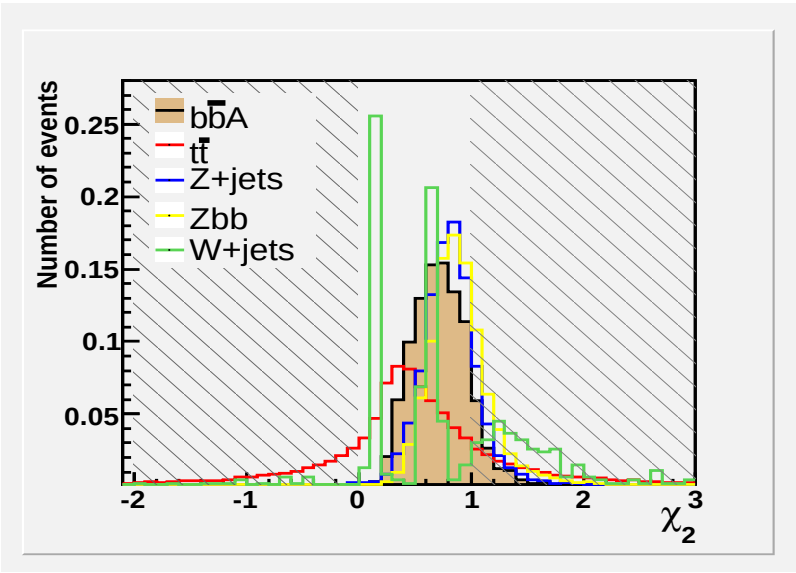

Fig. 7.30: τ-momentum fraction χ_2 carried by an electron or a muon. The cut $\chi_2 \epsilon (0,1)$ (indicated by the shaded area) is effective against the $t\bar{t}$ background.

remaining after all selection cuts, with the corresponding statistical error. For the signal data samples, where many events remain after the selection, the statistical error is obtained from the standard deviation of the gaussian distribution (68% confidence level). For the background, where only a few events remain after all cuts, the upper and lower limit was defined with a confidence level of 68% assuming a

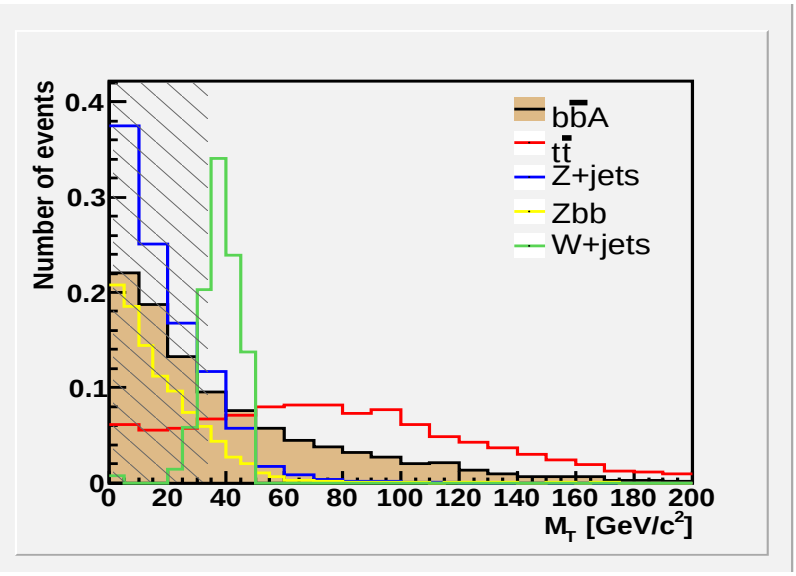

Fig. 7.31: Transverse mass M_T as defined in the text. The cut at 35 GeV/c^2 (indicated by the shaded area) mostly rejects the W background.

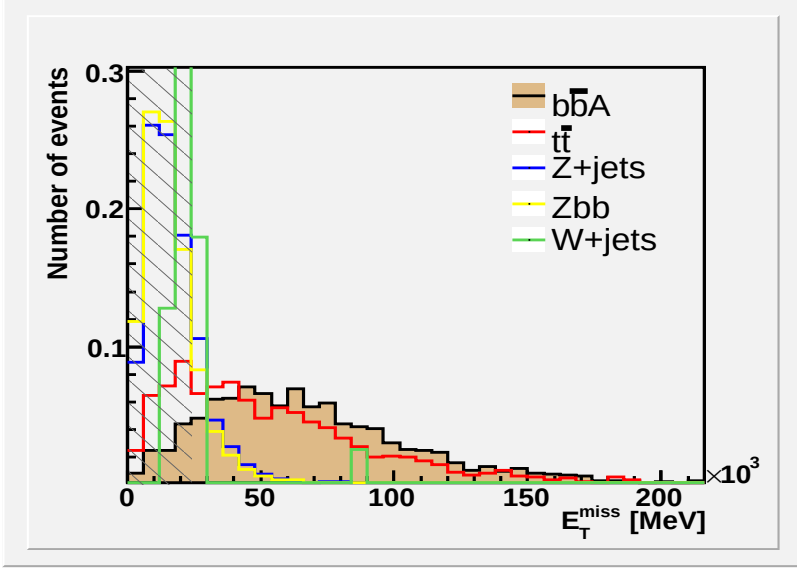

Fig. 7.32: Transverse missing energy E_T^{miss}. The cut at 25 GeV (indicated by the shaded area) is effective against the Z background.

Poisson distribution. The mass windows used are listed in Table 7.5.

As can be seen from Table 7.6-7.8, selection cuts are mass dependent. Selection efficiency for the large Higgs masses is higher due to the higher momenta of leptons and τ-jets. The heavier Higgs bosons also provide for a higher boost of their decay products and therefore a higher efficiency of the $\Delta\phi$ cut and a better collinear

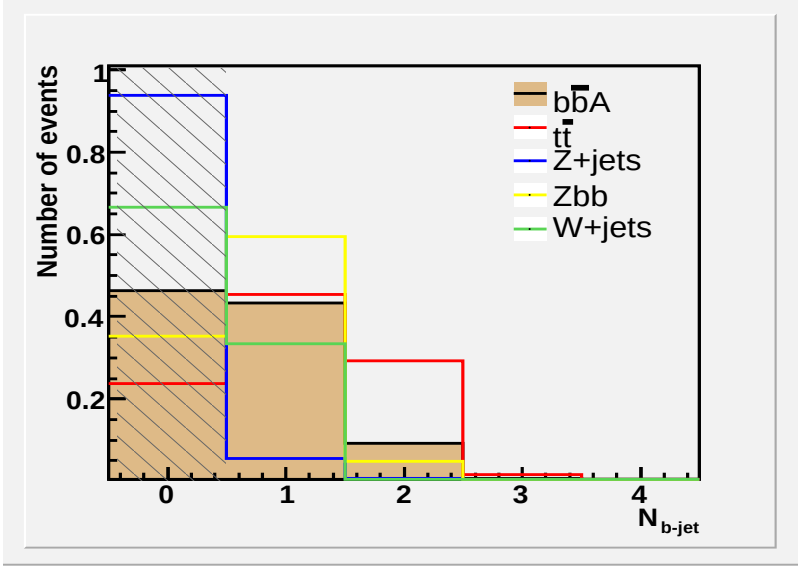

Fig. 7.33: Number of b-jets. Requirement of at least one b-jet in an event is effective against the Z background.

approximation. Similarly, the higher available energy for the neutrinos from the heavier Higgs bosons results in higher values of the missing energy. In addition, the b-jets from the associated production tend to counter-balance the Higgs mass. Thus, for higher Higgs masses, the b-jets will acquire higher momenta and will be more efficiently reconstructed.

In the mass range investigated in the present study, $t\bar{t}$ is the dominant background (see Table 7.8). Z background is heavily reduced by requiring high momentum lepton and τ-jet pair, and due to the absence of b-jets. Finally, no events from the W background remain after all cuts. Nevertheless one should remark the limited available statistics for W- and partialy also for the Z-background. For those backgrounds, the higher mass range where no events survive the selection chain, the Poissonian upper limits are used.

In Figure 7.36 the invariant mass ($M_{\tau\tau}$) distributions normalized to 30 fb^{-1} are shown. For tanβ=10, only the mass peak of 150 GeV/c^2 and a small excess of events at 300 GeV/c^2 can be observed on top of the major backgrounds. The same distributions are shown also for tanβ=30. Due to the scaling of the signal cross section proportional to $(tan\beta)^2$, the Higgs signal is here approximately ten times enhanced and the 5σ-discovery can be achieved for 150 GeV/c^2 and 300 GeV/c^2, while only hints for 450 GeV/c^2 and 600 GeV/c^2 exist.

Summarizing the analysis results in Table 7.9, one can calculate the signal significance by counting the number of signal and background events inside the given mass window (Table 7.5). As a discovery threshold, a signal significance of at least 5σ is required. For tanβ = 10, discovery is achieved only for the Higgs boson with mass of 150 GeV/c^2. Higher masses could be observed more easily at larger tanβ

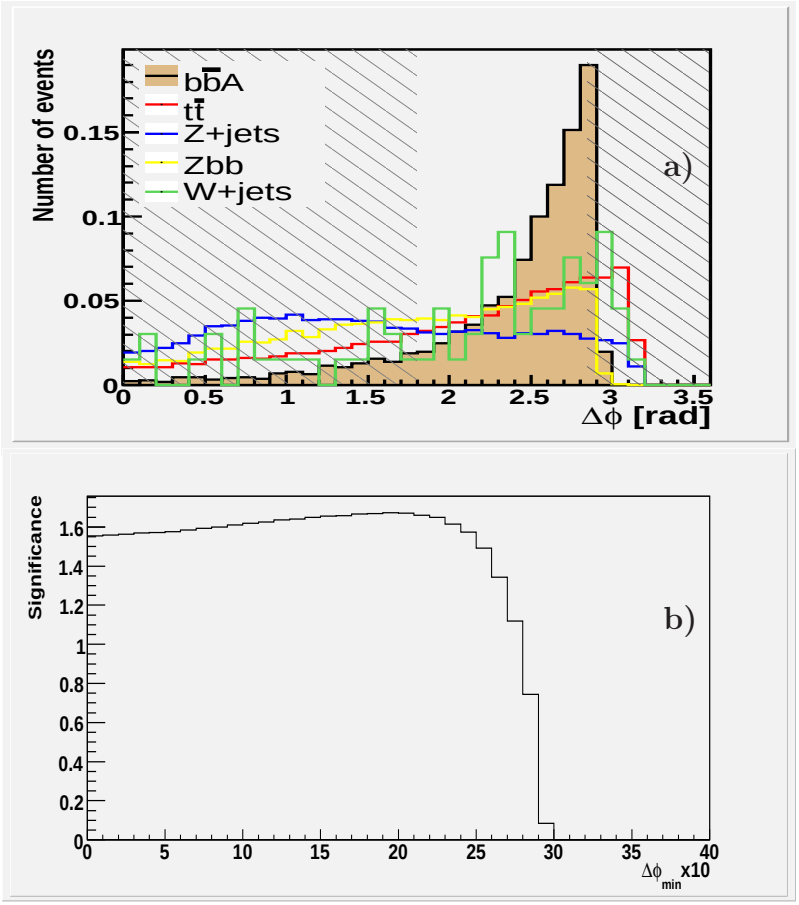

Fig. 7.34: An example of the cut optimization procedure for the lower bound on the angular separation $\Delta\phi$ between the lepton and the τ-jet in the transverse plane, for a Higgs mass of 300 GeV/c^2. a) shows the $\Delta\phi$ distibution for the signal and the different background processes. b) signal significance ($S/\sqrt{S+B}$) in dependance on the cut value $\Delta\phi_{min}$ ($\Delta\phi > \Delta\phi_{min}$). Optimal cut value ($\Delta\phi_{min} = 1.9$ for a Higgs mass of 300 GeV/c^2) is selected at the maximum value of signal significance. Due to the mass dependence of the distribution, the optimal cut values are averaged for all masses leading to the value of $\Delta\phi_{min} = 1.8$ for the whole mass region in study.

values whith enhanced signal production rates.

For the mass range studied (150 GeV/c^2 - 600 GeV/c^2), one can determine the required tanβ value in order to achieve the 5σ-significance for each mass point. Important to mention is that, different tanβ values affect also (apart from the production rates) the physical width of the Higgs resonance. The width increases with

Process	bbH/A 150GeV/c^2	bbH/A 300GeV/c^2	bbH/A 450GeV/c^2	bbH/A 600GeV/c^2
Nevents @ 30 fb^{-1}	143787	89901	832	158
Filter [%]	42.5	45.0	21.8	19.2
lepton-τ-jets [%]	4.7	10.1	12.3	12.9
$\Delta\phi$ [%]	67.8	75.6	76.4	75.7
$0 < \chi_1, \chi_2 < 1$ [%]	74.9	84.5	81.6	82.3
M_T [%]	75.6	59.0	55.0	47.8
P_T^{miss} [%]	53.0	88.9	92.4	96.0
N b-jet [%]	49.8	53.6	60.3	64.8
Mass window [%]	70.6	84.1	80.2	84.9
Nevents @ 30 fb^{-1} in mass window	205.3	62.2	3.4	0.61
Statistical error	$\pm$15.8	$\pm$2.2	$\pm$0.1	$\pm$0.02

Tab. 7.6: Number of signal events expected at 30 fb^{-1} and tanβ=10 for the associated production mode, taking into account both H and A bosons. First row shows the number of unfiltered events, before any selection criteria. In the following rows the relative efficiency for the filter and each selection cut is shown (see section 7.6). Finally, the number of events after all selection cuts and the corresponding statistical errors are summarized in the last two rows.

Process	H/A 150GeV/c^2	H/A 300GeV/c^2	H/A 450GeV/c^2	H/A 600GeV/c^2
Nevents @ 30 fb^{-1}	60178	1471	290	48
lepton-hadron pair [%]	3.2	8.9	11.4	12.7
$\Delta\phi$ [%]	30.9	25.8	21.7	18.4
$0 < \chi_1, \chi_2 < 1$ [%]	67.3	79.6	82.6	85.8
M_T [%]	80.3	64.0	53.5	46.6
P_T^{miss} [%]	40.6	83.8	92.9	97.3
N b-jet [%]	34.5	45.3	50.4	54.9
Mass window [%]	77.9	88.8	83.5	84.0
Nevents @ 30 fb^{-1} in mass window	39.8	5.7	1.16	0.20
Statistical error	$\pm$5.5	$\pm$0.3	$\pm$0.06	$\pm$0.02

Tab. 7.7: Number of signal events expected at 30 fb^{-1} and tanβ=10 for the direct production mode, taking into account both H and A bosons. First row shows the number of events, before any selection criteria are applied. In the following rows, the relative efficiency for the filter and each selection cut is shown (see section 7.6). Finally the number of events after all the selection cuts and the corresponding statistical errors are summarized in the last two rows.

the tanβ (see Appendix C and Figure 7.35 for the 150 GeV/c^2 mass explicitly).

Process		$t\bar{t}$	Z+jets	Zbb	W+jets
Nevents @ 30 fb^{-1}		$24.8 \cdot 10^6$	$9.3 \cdot 10^6$	$1.18 \cdot 10^6$	$270.9 \cdot 10^6$
Filter [%]		54.0	18.6	11.1	44.7
lepton-hadron pair [%]		0.44	2.2	2.5	0.4
$\Delta\phi$ [%]		30.2	43.7	51.3	37.4
$0 < \chi_1, \chi_2 < 1$ [%]		36.1	67.4	57.8	84.3
M_T [%]		19.2	87.1	88.2	27.6
P_T^{miss} [%]		74.0	16.2	15.6	7.6
N b-jet [%]		76.2	5.4	49.2	33.2
Nevents	(150±25)GeV/c^2	227.4	14.5	9.4	0.
@ 30 fb^{-1}	(300±55)GeV/c^2	349.4	0.	3.8	0.
in mass window	(450±75)GeV/c^2	183.5	0.	0.7	0.
for H/A mass of	(600±120)GeV/c^2	95.6	1.3	0.4	0.
	150 GeV/c^2	$^{+16.6}_{-15.6}$	$^{+12.7}_{-6.3}$	$^{+1.3}_{-1.1}$	$^{+33.8}_{-0.}$
Statistical error	300 GeV/c^2	$^{+20.5}_{-19.5}$	$^{+15.2}_{-0.}$	$^{+0.9}_{-0.7}$	$^{+33.8}_{-0.}$
for H/A mass of	450 GeV/c^2	$^{+15.6}_{-14.6}$	$^{+15.2}_{-0.}$	$^{+0.4}_{-0.3}$	$^{+33.8}_{-0.}$
	600 GeV/c^2	$^{+11.7}_{-10.7}$	$^{+15.0}_{-1.1}$	$^{+0.4}_{-0.3}$	$^{+33.8}_{-0.}$

Tab. 7.8: Number of background events expected at 30 fb^{-1}. The first row shows the number of events expected before any selection cuts are applied. The following rows refer to the relative efficiency for each cut applied in the analysis. In the last two rows we refer to the number of events expected at 30 fb^{-1} after all cuts. Finally, the statistical errors (Poissonian lower and upper limits with 68% confidence level) are given.

Nevertheless, for the tanβ values relevant for the analysis, the physical width of the Higgs resonance is still smaller than the achieved experimental mass resolution. Therefore, no significant change in the already defined mass windows is needed for different tanβ values. All other distributions are expected to remain unchanged with tanβ. Therefore, the same kinematical cuts can be used for a wide tanβ range. The dependence of the signal significance on the tanβ value is shown for all four studied mass points in Figure 7.36. The significanc eis obtained by scaling the final nuumber of events in Tables 7.6 - 7.9 to the cross-sections which correspond to a particular tanβ value.

In Figure 7.38 the minimum tanβ value for which the 5σ can be achieved is ploted for each of the four masses studied. The shaded area above the curve represents the parameter space in which the Higgs boson can be discovered by the current analysis, after 30 fb^{-1} of integrated luminosity.

The discussed discrepancies between fast and full simulation (see section 7.4) have a significant impact on the analysis results. Although these discrepancies are relatively small in the case of the Higgs samples, in the $t\bar{t}$ background the fully simulated sample yields a much higher τ-jet fake rate compared to ATLFAST. These fake τ-jets result in lower acceptance of $t\bar{t}$ events compared to the fully simulated $t\bar{t}$ sample. In Table 7.10 the relative efficiencies of the selection cuts for the signal

Process		bbH/A	H/A	$t\bar{t}$	Z+jets	Zbb	W+jets
Nevents	150 GeV/c^2	205.3	39.8	227.4	14.5	9.4	0.
@ 30 fb^{-1}	300 GeV/c^2	62.2	5.7	349.4	0.	3.8	0.
in mass window	450 GeV/c^2	3.4	1.16	183.5	0.	0.7	0.
for H/A mass of	600 GeV/c^2	0.61	0.20	95.6	1.3	0.4	0.
Total Nevents	150 GeV/c^2	245.1		255.6			
@ 30 fb^{-1}	300 GeV/c^2	67.9		360.7			
in mass window	450 GeV/c^2	4.56		188.5			
for H/A mass of	600 GeV/c^2	0.81		99.4			
	150 GeV/c^2	$11.0\ ^{+0.6}_{-0.7}$					
Signal significance	300 GeV/c^2	$3.3\ ^{+0.1}_{-0.2}$					
for H/A mass of	450 GeV/c^2	$0.33\ ^{+0.01}_{-0.03}$					
	600 GeV/c^2	$0.08\ ^{+0.01}_{-0.01}$					

Tab. 7.9: Signal significance at 30 fb^{-1} and tanβ=10. In the first row each process is mentioned seperately. In the second row the numbers of signal and background events after all sellection cuts are shown. Finally, the signal significance achieved for each mass point and the corresponding statistical error can be found in the last row.

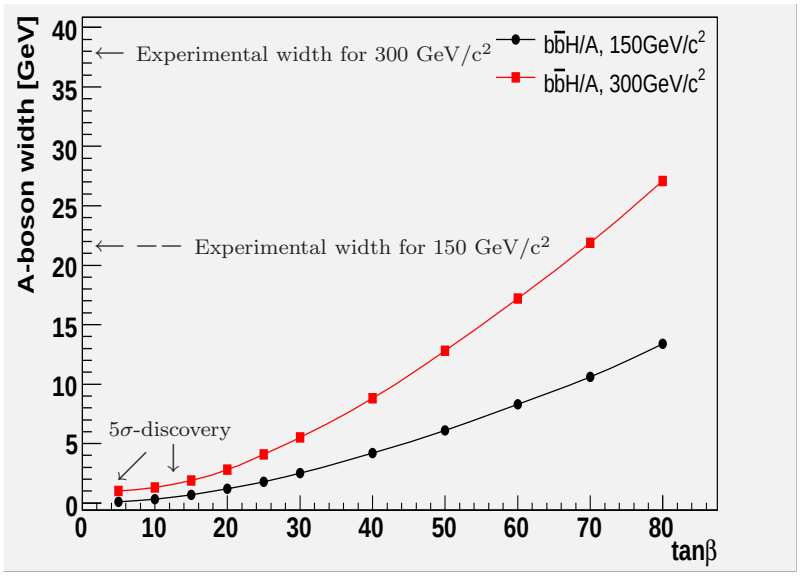

Fig. 7.35: Natural width of the A boson as a function of tanβ for the Higgs mass of 150 and 300 GeV/c^2. The tanβ values for which the 5σ-discovery is achieved are indicated on the plot. For the whole tanβ range the natural width is well below the experimental resolution.

sample of 300 GeV/c^2 mass and for the $t\bar{t}$ background are compared. As it can be observed, approximatelly twice as many $t\bar{t}$ events are found in full simulation

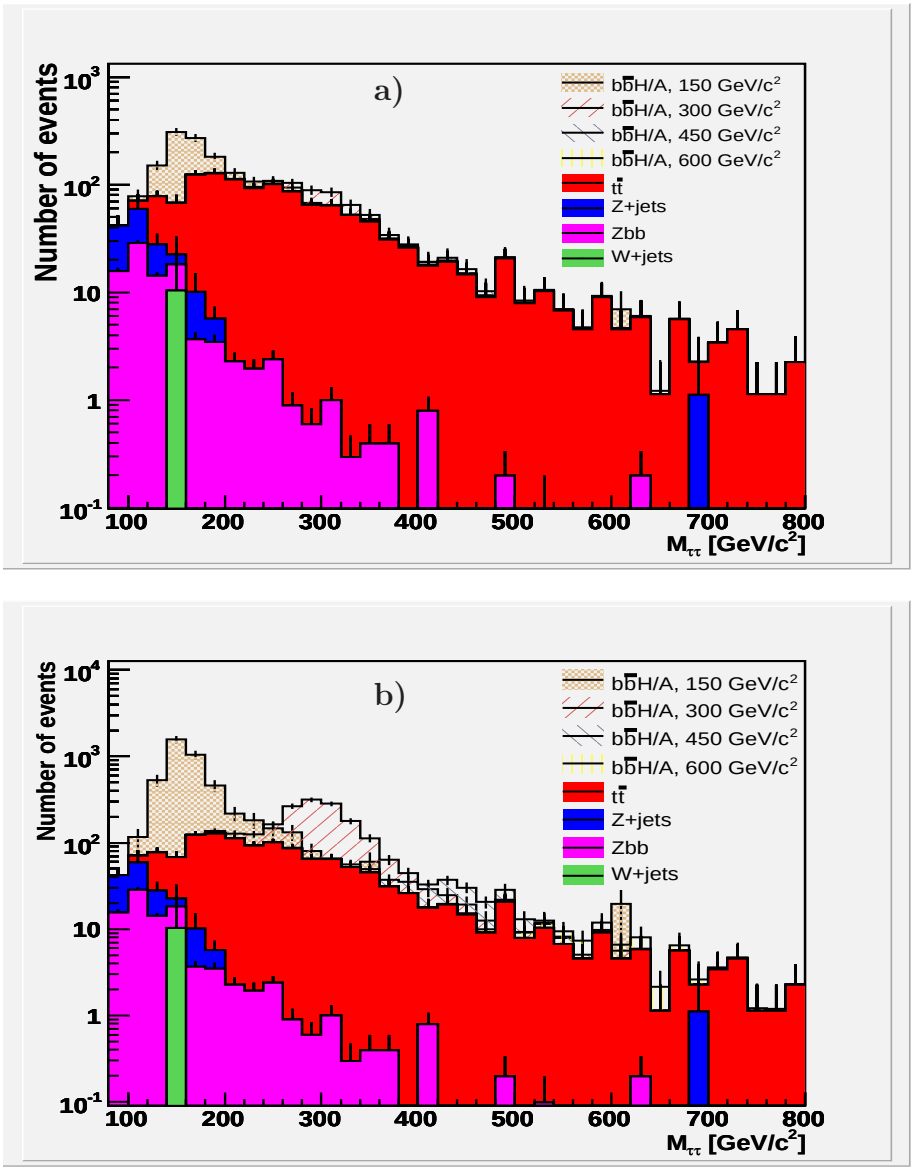

Fig. 7.36: Invariant mass distribution ($M_{\tau\tau}$) expected at an integrated luminosity of 30 fb^{-1}, after applying all kinematical cuts, (a) for tanβ=10 and (b) for tanβ=30.

compared to the fast simulation. The total acceptance (selection efficiency after all cuts) is about about 3 times higher for the $t\bar{t}$ background (see lepton-hadron pair selection efficiency in Table 7.10), compared to fast simulation. Also, the signal selection efficiency is about 30% lower in full simulation, due the worse momentum resolution of electrons and τ-jets, which leads to lower acceptance in the collinear approximation ($chi_{1,2}$ momentum fractions cut) and also in more events outside the mass window. Therefore, the presented difference in the performance of the two

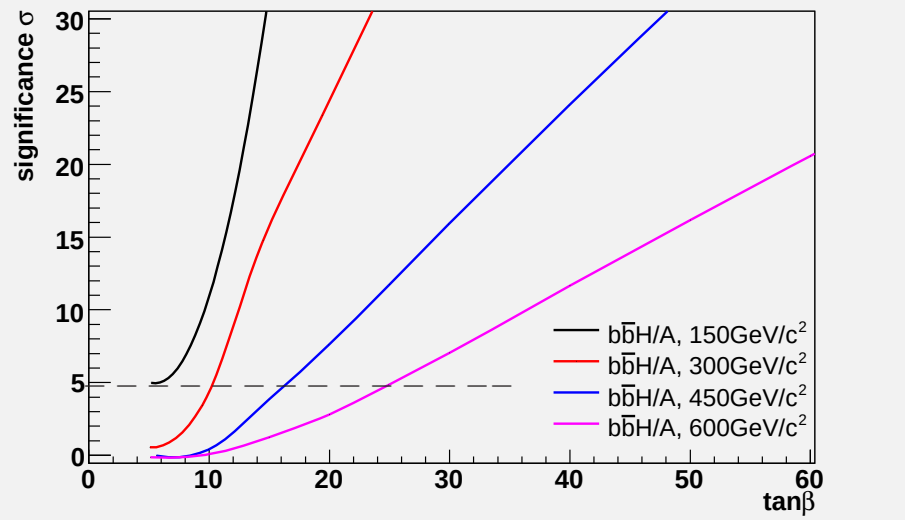

Fig. 7.37: Signal significance as a function of tanβ for the four mass points studied, for an integrated luminosity of 30 fb^{-1}

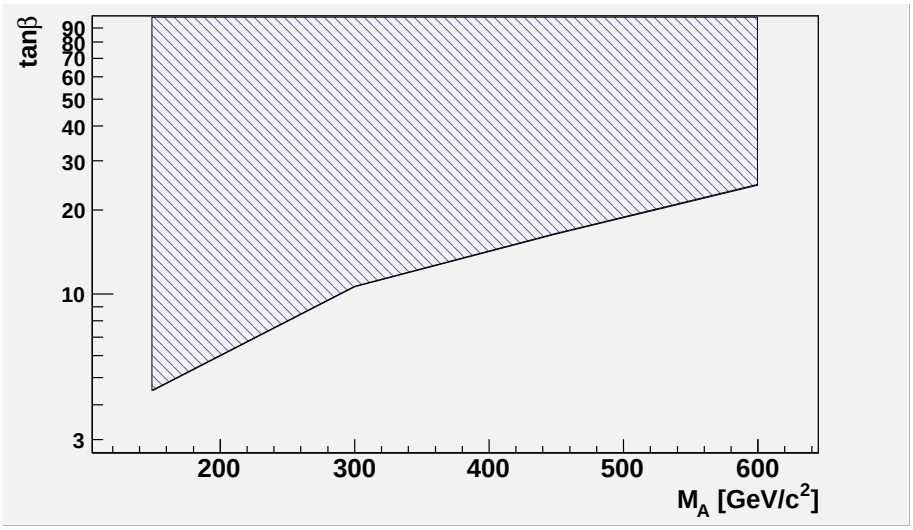

Fig. 7.38: 5σ-discovery curve. In the shaded area of the tanβ-M_A parameter space, the H/A bosons can be observed at an integrated luminosity up to 30 fb^{-1} the current analysis with a 5σ significance.

simulations results to a decrease up to a factor of 2 of the signal significance in the case of full simulation. Recent work on the identification of hadronicaly decaying

τ-leptons leads to a significant rejection of electrons misidentified as τ-jets and therefore decreasing the number of fake τ-jets to rates similar to the ones showed from ATLFAST.

Process	$b\bar{b}H/A$ fast	$b\bar{b}H/A$ full	$t\bar{t}$ fast	$t\bar{t}$ full
Nevents @ 30 fb^{-1}	$89.9 \cdot 10^3$	$89.9 \cdot 10^3$	$24.8 \cdot 10^6$	$24.8 \cdot 10^6$
Filter [%]	45.0	45.0	54.0	54.0
lepton-hadron pair [%]	10.1	9.6	0.44	0.82
$\Delta\phi$ [%]	75.6	78.1	30.2	40.9
$0 < \chi_1, \chi_2 < 1$ [%]	84.5	76.3	36.1	32.6
M_T [%]	59.0	52.5	19.2	25.9
P_T^{miss} [%]	88.9	91.5	74.0	70.7
N b-jet [%]	53.6	48.6	76.2	77.4
Mass window [%]	84.1	74.7	50.2	48.4
Total acceptance	0.69	0.45	$1.4 \cdot 10^{-3}$	$4.0 \cdot 10^{-3}$

Tab. 7.10: Relative efficiency for each cut applied in the analysis and total acceptance of the analysis, shown for a signal sample of 300 GeV/c^2 Higgs boson mass and for the $t\bar{t}$ background.

8

MSSM Higgs Boson Search in the $pp \rightarrow (b\bar{b})H/A \rightarrow (b\bar{b})\mu^+\mu^-$ Channel

In this chapter the analysis of the MSSM channel $pp \rightarrow (b\bar{b})H/A \rightarrow (b\bar{b})\mu^+\mu^-$ will be presented. First the signal and the important background processes will be introduced in Sections 8.1 and 8.2. Subsequently, the event generation and simulation programs will be discussed in Section 8.3. In Section 8.3.1 a description of the event selection is given. Finally, the analysis results and the side-bands method for extraction of the Higgs signal are presented in Sections 8.3.2 and 8.3.3.

8.1 Signal Production Mechanisms

The observability of the $pp \rightarrow (b\bar{b})H/A \rightarrow (b\bar{b})\mu^+\mu^-$ decay channel in the standard model is low due to the predicted low Higgs branching ratio into two muons and the high backgrounds with two muons in the final state. The corresponding rates are largely enhanced in the case of MSSM, allowing for the detection of the heavy neutral Higgs bosons decaying into two muons.

Compared to the $H/A \rightarrow \tau^+\tau^-$ channel, the decay rates of the $H/A \rightarrow \mu^+\mu^-$ process are governed by the same couplings (refer to Sections 7.1 and 6.4), but the branching ratio, which scales as $(m_\mu/m_\tau)^2$ is 280 times lower than for the decays into τ-leptons. Even though the two-muon channel is highly supressed with respect to the $H/A \rightarrow \tau^+\tau^-$, this channel offers a clean experimental signature with two high energetic muons. By exploiting the excellent muon identification and energy resolution of the ATLAS muon spectrometer, it is possible to distinguish the signal from the large contribution of the background. Of great importance in this channel is the possibility of the direct Higgs mass reconstruction with a very good resolution. Thus, the $H/A \rightarrow \mu^+\mu^-$ channel can serve, after the observation of the heavy neutral MSSM Higgs in the $H/A \rightarrow \tau^+\tau^-$ channel, for an accurate Higgs mass measurement.

The analysis presented in this chapter is performed in the range of candidate signal masses between 200 GeV/c^2 and 450 GeV/c^2, concentrating on the similar area of the M_A-tanβ parameter plane as in the case for the $H/A \rightarrow \tau^+\tau^-$ analysis presented in Chapter 7.

As in Section 7.1, the FEYNHIGGS [51],[52],[53],[54] program has been used for the calculation of the production cross sections for the H and A bosons, as well as

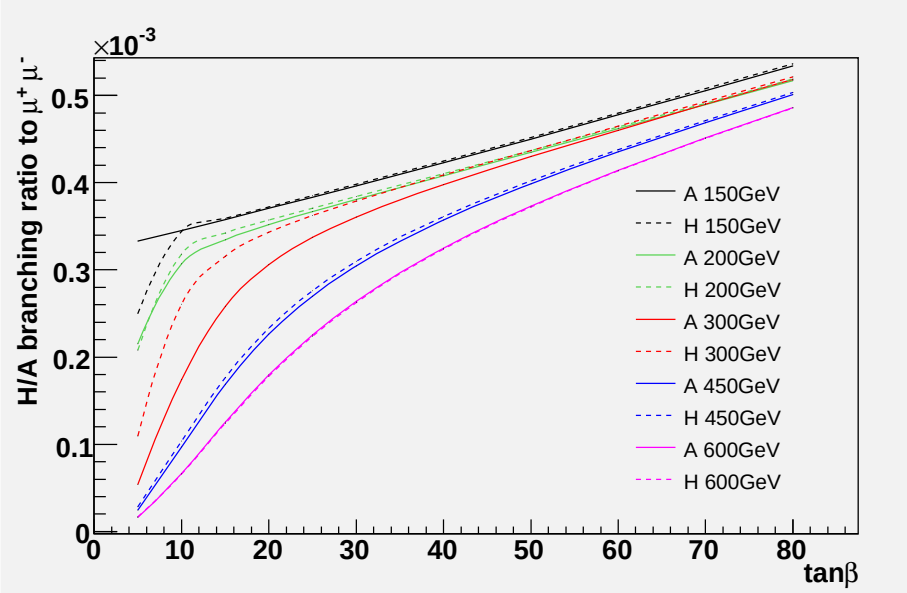

Fig. 8.1: Branching ratio for the decay $H/A \rightarrow \mu^+\mu^-$ in dependence on tanβ, for different H and A-boson masses.

for their branching ratios. Cross sections are calculated at the next-to-leading order (NLO), taking into account both direct and $b\bar{b}$-associated associated production mode for the $m_h - max$ scenario (see Section 6.6). More details about the input parameters and the results for various points in the M_A - $tan\beta$ parameter space can be found in Appendix D. Figure 8.1 shows the branching ratio for different A and H masses as function of tanβ. Figures 7.2 and 7.3 show the production cross section for the two mentioned production processes.

8.2 Background Processes

For the study presented in this chapter, the following major background proccesses have been taken into account (for the corresponding Feynmann diagrams see Section 7.2):

- ***$t\bar{t}$***: Similarly as for the $H/A \rightarrow \tau^+\tau^-$, for the high mass region (m_A >150 GeV) the dominant background is $t\bar{t}$. Each top quark decays to a W-boson and a b-quark (with a branching ratio of almost 100%). W-bosons subsequently decay to a muon with a branching ratio of 11%. Therefore, there are two b-quarks and two muons present in the final state as in the signal. Neutrinos from the W decays result in a finite missing energy, which allows for the discrimination of this process against the signal where the missing transverse energy is small.

- **Z(+jets)**: The branching ratio of the Z-boson decaying into a muon pair is only 3.4%. Nevertheless, the enormous production cross section and the

possibility of mistagging the light jets as b-jets can provide a large background with a signal-like topology.

For all background processes the cross section is calculated to the next-to-leading order (NLO). All signal and background processes, together with the corresponding cross sections, are shown in Table 8.1.

8.3 Event Simulation

In the current study, the signal and background proccesses were simulated using full detector simulation and the ideal detector layout without misallignment effects. The ATLAS ATHENA software version used was 10.0.4.

For the evaluation of the observability of this channel, as well as for the Higgs mass determination, three different signal mass points were generated (200, 300 and 450 GeV/c^2). For all three signal samples the PYTHIA [56], [57], [58] event generator was used. It should be mentioned that for the signal, only events with the A boson were generated, since the event topologies for the H and A boson are very similar. Both $t\bar{t}$ and Z background were also produced using PYTHIA generator. The HiggsMultiLeptonFilter (for details refer to Appendix C) was used in order to select only interesting event topologies and thus decrease the needed Monte Carlo statistics. Filter cuts were appled on the p_T, η and number of muons in an event. In addition, only events with dimuon invariant mass above a given value are selected by the filter, since the study is concentrated on the mass range above 200 GeV/c^2.

8.3.1 Event Selection

The particle selection criteria as well as the reconstruction algorithms used for the analysis of this channel have already been described in detail in Section 7.4, for the case of full simulation.

As mentioned in Table 8.1, the dominant signal production mode at high tanβ values is the associated production with two b-quarks. Therefore, the selection criteria are optimized for the dimuon final state with at least one b-jet. The selection criteria used to discriminate signal from the background are the following:

- **$\mu^+\mu^-$ pair:** Events with oppositely charged muon pair in the final state are selected. As shown in Figure 8.2, muon p_T-distribution is dependent on Higgs mass. For a mass-independent high signal acceptance, we require a rather loose muon p_T-threshold of 20-GeV/c. In addition the muons are required to be isolated, i.e. we reject the muons surrounded by a jet.

- **Missing transverse energy (E_T^{miss}) :** $t\bar{t}$ events are characterized by a large missing transverse energy due to the presence of the neutrinos from the $W^{\pm}$ leptonic decays. Opposite to that, low missing energy is expected in the signal events. Thus, we require that events have $E_T^{miss} < 36$ GeV (see Figure 8.3).

Process	σ x BR	Generator /Filter	Filter Eff
$bbH/A \to \mu^+\mu^-$ $m_{H/A} = 200$ GeV	63.03fb	Pythia	1.0
$bbH/A \to \mu^+\mu^-$ $m_{H/A} = 300$ GeV	14.01fb	Pythia	1.0
$bbH/A \to \mu^+\mu^-$ $m_{H/A} = 450$ GeV	2.32fb	Pythia	1.0
$H/A \to \mu^+\mu^-$ $m_{H/A} = 200$ GeV	8.92fb	Pythia	1.0
$H/A \to \mu^+\mu^-$ $m_{H/A} = 300$ GeV	0.95fb	Pythia	1.0
$H/A \to \mu^+\mu^-$ $m_{H/A} = 450$ GeV	0.10fb	Pythia	1.0
$t\bar{t}$	833pb	Pythia /HiggsMultiLeptonFilter	0.01
$Z \to \mu^+\mu^-$	2026.4pb	Pythia /HiggsMultiLeptonFilter	0.0066
$Z + q/g \to \mu^+\mu^-$ + jets p_T^{jet} >10 GeV	1148.0pb	Pythia /HiggsMultiLeptonFilter	0.0049

Tab. 8.1: Fully simulated signal and background processes. In the second column, the NLO cross sections without the filter are listed for tanβ = 30. In the third column the generator and the filter used and in the fourth column the filter efficiency are shown.

- **Higgs transverse momentum ($p_T^{2\mu}$) :** Higgs particles are expected to be produced almost at rest and have relatively low transverse momenta. Opposite to that, in $t\bar{t}$ process, the two muons originate from the two top quarks, yielding a higher transverse momentum of the dimuon system. Therefore, $p_T^{2\mu} < 50$ GeV/c is required (see Figure 8.4).

- **Angular distance between muons in the transverse plane ($\Delta\phi$) :** The muons originating from a low-p_T Higgs boson are emmited mostly back-to-back in the transverse plane. Muons from $t\bar{t}$ decays originate from two different particles and thus have lower angular separation. Therefore, a cut is applied on the angular distance $\Delta\phi$ between muons in the transverse plane, $\Delta\phi > 2.8$ radians (see Figure 8.5).

- **Number of b-jets (N_b)** : In the associated Higgs production proccess, two b-jets are expected in the final state. Similarly as in the case of $H/A \to \tau\tau$ final state, we require at least one reconstructed b-jet ($N_b \geq 1$) to be present in the event. This is in particular effective against a large fraction of the Z background, where no b-jets are present (see Figure 8.6).

- **b-jet transverse momentum (p_T^{b-jet}) :** b-jets originating from the top-quark decays are more energetic and central than those from the signal. Thus the p_T of the b-jet can be used as a discriminant between the signal and $t\bar{t}$ background. We require $p_T^{b-jet} < 50$ GeV/c (see Figure 8.7).

- **Mass window :** Finally, events that pass the previous selection criteria should give a reconstructed dimuon mass within a certain mass window. The width of the mass window depends on the Higgs mass. It is defined as the mass range of one standard deviation around the mean value of a gaussian curve fitted to the reconstructed Higgs mass distribution (before any cuts). For low masses, the detector resolution gives the dominant contribution to the Higgs width. For higher masses, the intrinsinc width of the Higgs-boson gives the major contribution. The same window defines the final number of background and signal events, which are used for the calculation of the signal significance. The mass windows for the three Higgs mass points investigated in the analysis are shown in Table 8.2

The cuts have been optimized using the same procedure as described in 7.6

	Mass window ΔM
200 GeV/c^2	$\pm$5 GeV/c^2
300 GeV/c^2	$\pm$10 GeV/c^2
450 GeV/c^2	$\pm$15 GeV/c^2

Tab. 8.2: Mass windows for the three different signal mass points.

8.3.2 Analysis Results

The event selection criteria described in the previous section, have been applied in the simulated data samples listed in Table 8.1. The analysis results are summarized in Tables 8.3-8.5. In the first row, the total number of events expected at an integrated luminosity of 30 fb^{-1} and before any analysis cuts are presented. For the signal, the value of tanβ=30 was used for the calculations. The impact of the lepton filter and of all selection cuts is shown in the subsequent rows as a relative efficiency with respect to the previous cut. The last two rows show the number of events and the statistical error, after all cuts have been applied. The error is calculated as a standard deviation (68% confidence level) of the gaussian distribution. For the background (especially for the Z background, where only a few events pass the complete event selection), the upper and lower limit have been determined with a confidence level of 68% assuming a Poisson distribution of the events. The mass window as already described is $\pm$7 GeV/c^2, $\pm$10 GeV/c^2 and $\pm$15 GeV/c^2 for the signal masses of 200 GeV/c^2, 300 GeV/c^2 and 450 GeV/c^2 respectively.

From the number of events passing the selection, one can calculate the signal significance σ, defined as the number of signal events divided by the square root of

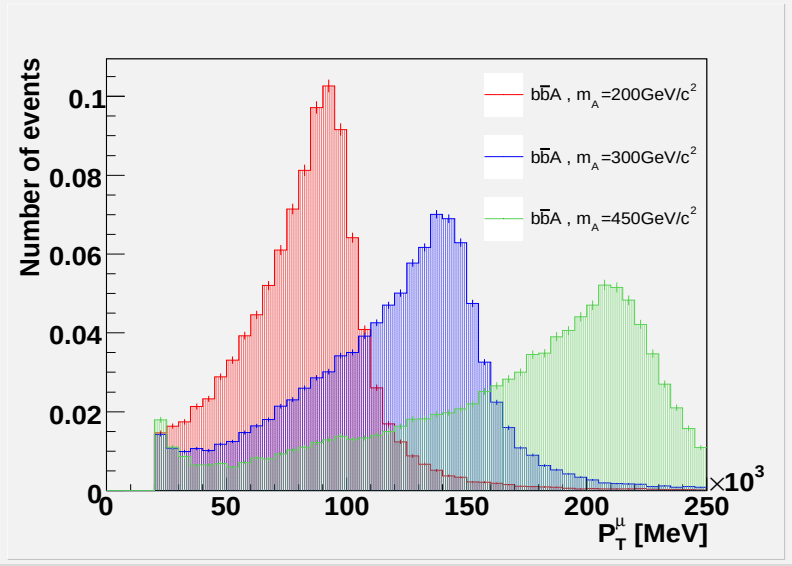

Fig. 8.2: Muon p_T-distribution for three different Higgs masses. A loose threshold of $p_T > 20$ GeV/c was chosen for the muon selection, in order to have a high mass-independent signal acceptance.

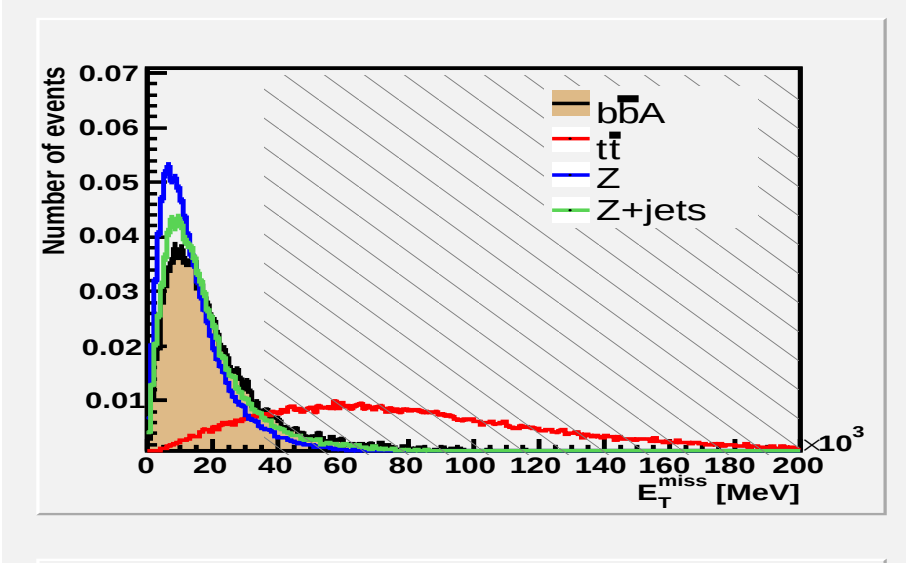

Fig. 8.3: Transverse missing energy distribution, shown for the signal at the Higgs mass of 300 GeV/c^2 and for the dominant background processes. The cut at 36 GeV (indicated by the shaded area) rejects the $t\bar{t}$ background.

the sum of signal and background events, inside the given mass window (Equation 7.9). As a discovery threshold, a signal significance of at least 5σ is required. Final numbers for the signal and the background, as well as the obtained signal significance

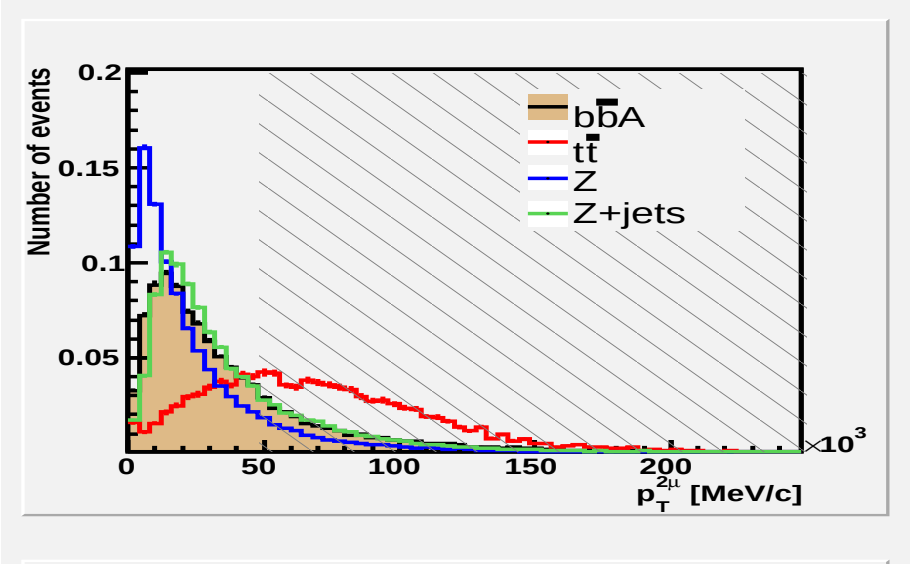

Fig. 8.4: Higgs transverse momentum distribution, shown for the signal at the Higgs mass of 300 GeV/c^2 and for the dominant background processes. The cut at 50 GeV/c (indicated by the shaded area) is mostly effective against the $t\bar{t}$ background.

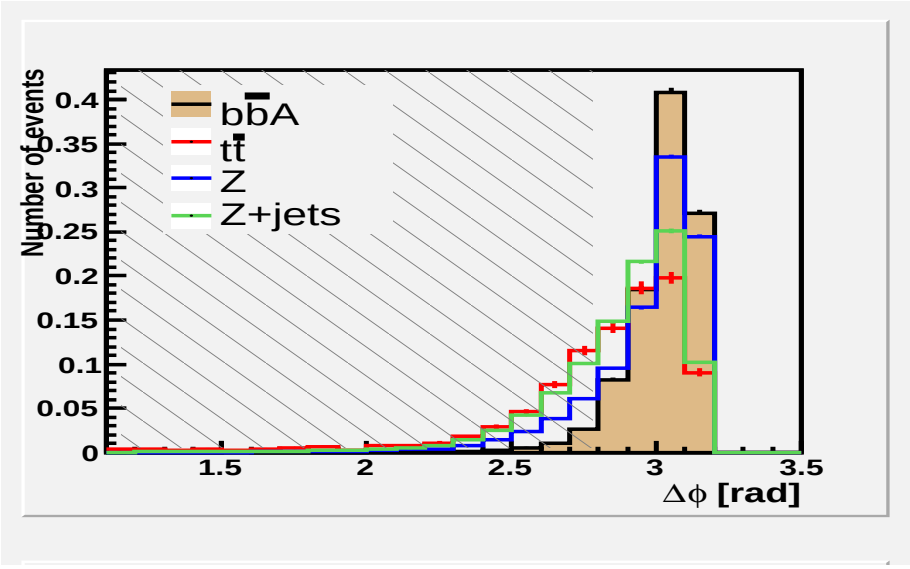

Fig. 8.5: Angular distance between the muons in the transverse plane, shown for the signal at the Higgs mass of 300 GeV/c^2 and for the dominant background processes. The cut at 2.8 radians (indicated by the shaded area) reduces the $t\bar{t}$ background.

are shown in Table 8.6 together with the corresponding statistical errors.

Figure 8.8 shows the distribution of the dimuon invariant mass after applying the selection cuts and for tanβ=30, normalized to an integrated luminosity of 30 fb^{-1}.

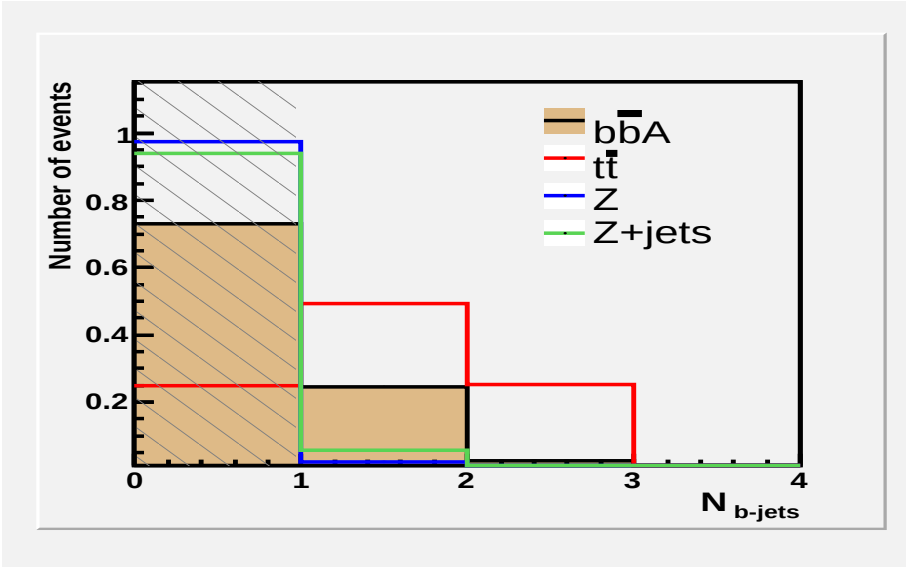

Fig. 8.6: Number of b-jets per event, shown for the signal at the Higgs mass of 300 GeV/c^2 and for the dominant background processes. The cut (indicated by the shaded area) strongly supresses the Z background. The b-jet multiplicity is lower for the signal than for the $t\bar{t}$ process due to the lower transverse momentum of b-jets produced in the bbH/A associated production. The b-jet reconstruction efficiency is lower at lower p_T-values.

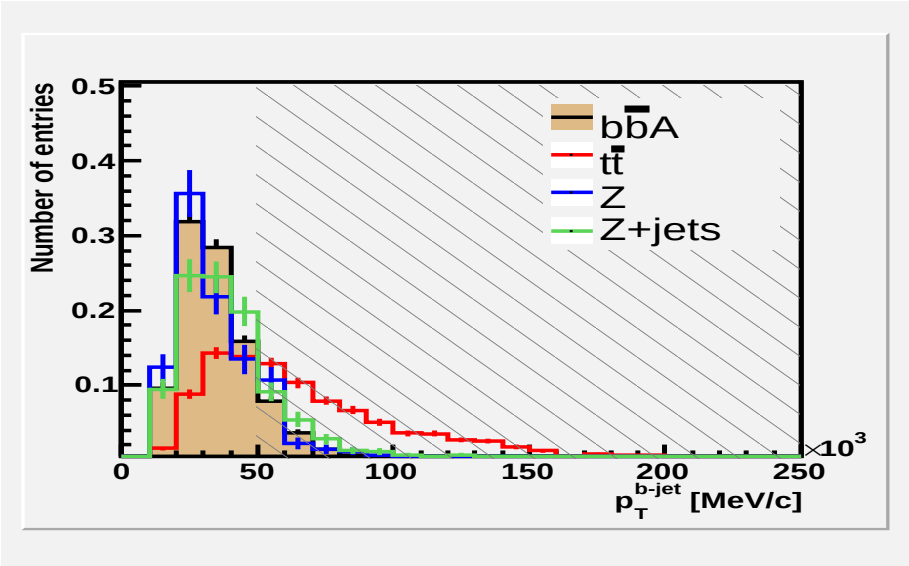

Fig. 8.7: Transverse momentum of reconstructed b-jets, shown for the signal at the Higgs mass of 300 GeV/c^2 and for the dominant background processes. The cut at 50 GeV/c (indicated by the shaded area) rejects the $t\bar{t}$ background.

Process	bbH/A 200GeV/c^2	bbH/A 300GeV/c^2	bbH/A 450GeV/c^2
Nevents @ $30fb^{-1}$	1890	419	71
Filter [%]	100	100	100
$\mu^+\mu^-$ [%]	87	83	83
E_T^{miss}	86	80	70
$P_T^{2\mu}$	82	76	68
$\Delta\phi$ [%]	87	95	98
N_b [%]	26	27	30
P_T^{b-jet} [%]	88	85	82
Mass window [%]	68	66	63
Nevents @ $30fb^{-1}$ in mass window	154.7	29.3	4.3
Statistical error	± 3.8	± 0.6	± 0.1

Tab. 8.3: Number of signal events for both H and A boson expected at 30 fb^{-1} and tanβ=30 for the associated production mode. The relative efficiency of each cut is shown, together with the final number of events expected after all selection cuts. The corresponding statistical error is also indicated.

Process	H/A 200GeV/c^2	H/A 300GeV/c^2	H/A 450GeV/c^2
Nevents @ $30fb^{-1}$	266	29	3
Filter [%]	100	100	100
$\mu^+\mu^-$ [%]	87	85	83
E_T^{miss}	80	71	61
$P_T^{2\mu}$	74	65	52
$\Delta\phi$ [%]	86	94	99
N_b [%]	3	3	4
P_T^{b-jet} [%]	85	63	75
Mass window [%]	73	50	38
Nevents @ $30fb^{-1}$ in mass window	2.0	0.1	0.01
Statistical error	$^{+0.3}_{-0.2}$	$^{+0.1}_{-0}$	$^{+0.01}_{-0}$

Tab. 8.4: Number of signal events for both H and A boson expected at 30 fb^{-1} and tanβ=30 from the direct production mode. The relative efficiency of each cut is shown, together with the final number of events expected after all selection cuts. The corresponding statistical error is also indicated.

8.3.3 Higgs Mass Masurement

The analysis described above yields the dimuon mass spectrum shown in Figure 8.8, for three different Higgs boson masses. Although a discovery of an MSSM heavy

Process		$t\bar{t}$	Z, $Z \to \mu^+\mu^-$	Z+jets, $Z \to \mu^+\mu^-$
Nevents @ $30fb^{-1}$		$24.8 \cdot 10^6$	$60.8 \cdot 10^6$	$34.4 \cdot 10^6$
Filter [%]		0.01	6.6	4.9
$\mu^+\mu^-$ [%]		87	83	81
E_T^{miss}		14	90	84
$P_T^{2\mu}$		37	87	76
$\Delta\phi$ [%]		67	84	72
N_b [%]		75	3	6
P_T^{b-jet} [%]		35	83	79
Nevents @ $30fb^{-1}$ in mass window for H/A mass of	(200±5)GeV/c^2	27.9	96.3	76.2
	(300±10)GeV/c^2	5.4	9.6	34.6
	(450±15)GeV/c^2	2.7	9.6	0
Statistical error for H/A mass of	200 GeV/c^2	$^{+3.0}_{-2.8}$	$^{+23.1}_{-18.9}$	$^{+15.7}_{-13.2}$
	300 GeV/c^2	$^{+1.5}_{-1.2}$	$^{+11.2}_{-6.2}$	$^{+11.3}_{-8.8}$
	450 GeV/c^2	$^{+1.2}_{-0.9}$	$^{+11.2}_{-6.2}$	$^{+6.9}_{-0}$

Tab. 8.5: Number of background events expected at 30 fb^{-1}. The relative efficiency of each cut is shown, together with the final number of events expected after all selection cuts. The corresponding statistical error is also indicated.

Process		$b\bar{b}H/A$	H/A	$t\bar{t}$	Z	Z+jets
Nevents @ $30fb^{-1}$ in mass window for H/A mass of	200 GeV/c^2	154.7	2.0	27.9	96.3	76.2
	300 GeV/c^2	29.3	0.1	5.4	9.6	34.6
	450 GeV/c^2	4.3	0.01	2.7	9.6	0.
Total Nevents @ $30fb^{-1}$ in mass window for H/A mass of	200 GeV/c^2	156.7		200.4		
	300 GeV/c^2	29.4		49.6		
	450 GeV/c^2	4.3		12.3		
Signal significance for H/A mass of	200 GeV/c^2	$8.3\ ^{+0.3}_{-0.4}$				
	300 GeV/c^2	$3.3\ ^{+0.2}_{-0.3}$				
	450 GeV/c^2	$1.1\ ^{+0.2}_{-0.4}$				

Tab. 8.6: Signal significancies for 30 fb^{-1} and tanβ=30. In the second row the number of signal and total number of background events are shown. Signal significance for each mass point and the corresponding statistical error can be found in the last row.

neutral Higgs boson is less likely in the $\mu^+\mu^-$ decay mode, as compared to the $\tau^+\tau^-$ decay channel, the dimuon mass resolution is about four times better and allows for a more accurate mass determination. The mass resolution obtained from the two different decay modes is shown in Table 8.7.

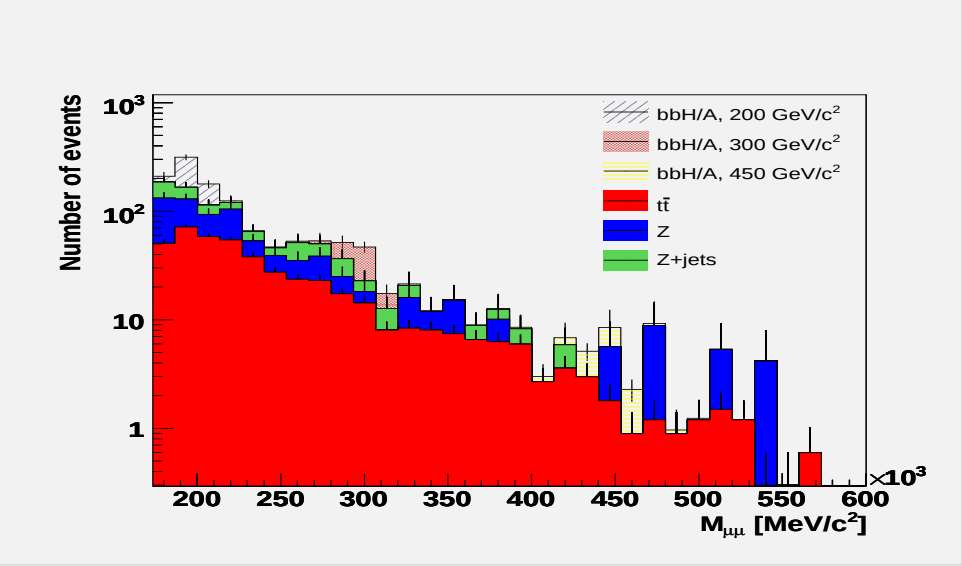

Fig. 8.8: Invariant dimuon mass distributions for three studied signal mass points and for all background processes (stacked histogram). The distributions are normalized to an integrated luminosity of 30 fb^{-1} at tanβ=30.

The Higgs mass resonance can be extracted if one estimates the background from the side-bands. The procedure requires that a prominent mass peak is observed in the $\mu^+\mu^-$ channel. If this is not the case, either because of insufficient background suppression, large background fluctuations, or low signal rates, the alternative information can be obtained from the $\tau^+\tau^-$ decay mode. Once the Higgs mass is roughly identified in the $\tau^+\tau^-$ channel, a signal region of three standard deviations around the candidate signal is defined. Two side-bands regions three standard deviations below and above the mass peaks are defined and the fit of the exponential function ($f_L = exp(p_o x - p_1)$) is performed seperately in these two regions ($f_L = exp(8.9x - 2.0 \cdot 10^{-5})$, $f_R = exp(9.7x - 2.0 \cdot 10^{-5})$ for the left and right side-bands of the 300 GeV/c^2 mass spectrum and $f_L = exp(10.6x - 3.2 \cdot 10^{-5})$, $f_R = exp(8.4x - 1.8 \cdot 10^{-5})$ for the left and right side-bands of the 200 GeV/c^2 mass spectrum). The fits of the side-bands are used for a common fit of the whole mass spectrum. In this way, the background inside the signal region can be estimated. After subtracting the estimated background contribution in the signal region one is left with the signal mass distribution. The results of this method are shown in Figure 8.9, for an integrated luminosity of 30 fb^{-1} and for tanβ=30, for two different mass points 300 GeV/c^2 and $m_{H/A}$ = 200 GeV/c^2. The functions used to fit the whole mass spectrum are the $f = exp(7.5x - 1.7 \cdot 10^{-5})$ and $f = exp(8.4x - 1.8 \cdot 10^{-5})$ for the $m_{H/A}$ = 300 and 200 GeV/c^2 correspondingly.

For the tanβ=30, the signal at 450 GeV/c^2 cannot be discriminated from the background. Higher value of tanβ is needed for the observability of this mass point. The results of the background subtraction method applied for the 300 and

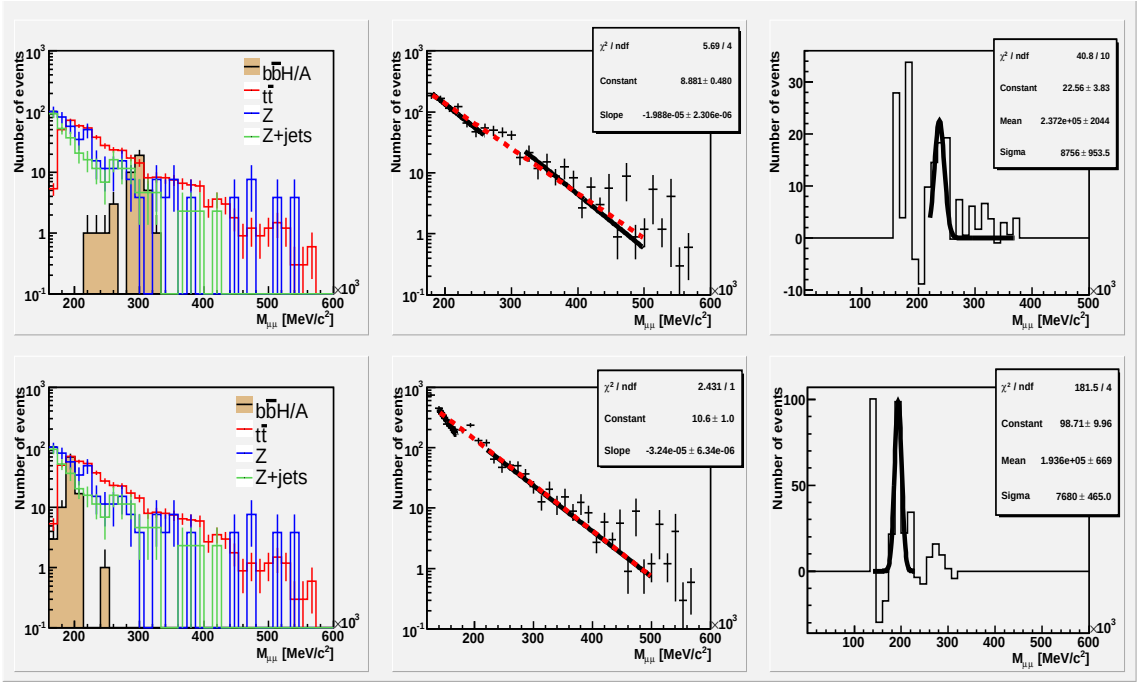

Fig. 8.9: *Left column*: Mass distributions for the signal and the background processes at 30 fb^{-1} and tanβ=30. *Middle column*: Total mass spectrum for 30 fb^{-1} and tanβ=30. Black lines represent the fit in the side-band regions, used for background estimation. Red dashed line represents the common fit using the side-band fit parameters. *Right column*: The signal shape after subtraction of the background function obtained from the side-band fit. Two cases are shown, for the Higgs masses of 300 (upper row) and 200 GeV/c^2 (bottom row).

200 GeV/c^2 are summarized in Table 8.7. In the case of 200 GeV/c^2 signal where the mass peak is more prominent, the results are comparable to the ones obtained by a simple gauss fit of the signal mass distribution alone (second row). At 300 GeV/c^2 the available statistics is still too low. Signal extraction is still possible but yields a mass considerably shifted compared to the mean value obtained from the gauss fit on the signal sample. The shift on the mass measurement is 2.5% for the 200 GeV/c^2 Higgs boson and 20% for the 300 GeV/c^2 Higgs boson.

8.3.4 Discovery potential

As presented in Table 8.6, observability of an MSSM heavy neutral Higgs boson at 30 fb^{-1} and tanβ=30 can be achieved for Higgs masses up to 300 GeV/c^2. For higher Higgs masses a higher integrated luminosity or a higher tanβ value is needed.

For the studied mass range between 200 GeV/c^2 and 450 GeV/c^2 one can determine the tanβ value needed for the 5σ-significance at 30 fb^{-1} for each mass point. Different tanβ values affect the signal rates, but distributions of all discriminating variables are expected to remain very similar. Therefore, the same kinematical cuts

	$M_{H/A}$ =200 GeV/c^2		$M_{H/A}$ =300 GeV/c^2		$M_{H/A}$ =450 GeV/c^2	
	mean [GeV/c^2]	σ [GeV/c^2]	mean [GeV/c^2]	σ [GeV/c^2]	mean [GeV/c^2]	σ [GeV/c^2]
$b\bar{b}H/A, H/A \to \tau^+\tau^-$	-	-	289	34	430	50
$b\bar{b}H/A, H/A \to \mu^+\mu^-$	197	6	296	9	442	15
$b\bar{b}H/A, H/A \to \mu^+\mu^-$ from side-bands	194	8	237	8	-	-

Tab. 8.7: Mean mass value and the mass resolution of the reconstructed Higgs resonance. The numbers in first two rows are obtained from a fit of a gaussian curve to the Higgs resonance after applying all but the mass window cut. Mass resolution is 3-4 times better in the $\mu\mu$-channel. Last row shows the values obtained after the signal extraction by means of the side-band background subtraction, as explained in the text.

can be used in a wide tanβ range.

Discovery potential in terms of a 5σ-discovery curve is shown in Figure 8.11. The minimum tanβ value at which the 5σ-significance can be achieved is ploted in dependance of the Higgs mass. The shaded area above the curve represents the tanβ-M_A parameter space in which the H/A bosons can be discovered at an integrated luminosity of up to 30 fb^{-1}.

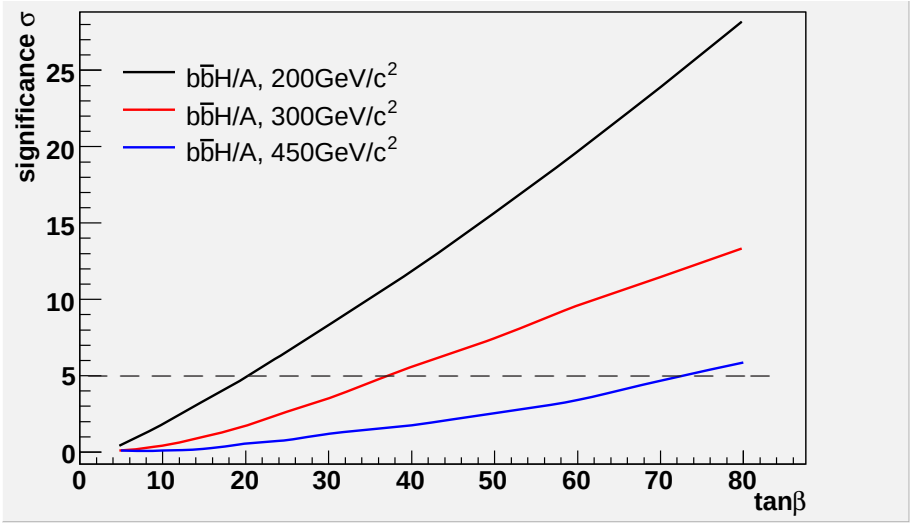

Fig. 8.10: Signal significance as a function of tanβ for the three mass points studied, for an integrated luminosity of 30 fb^{-1}

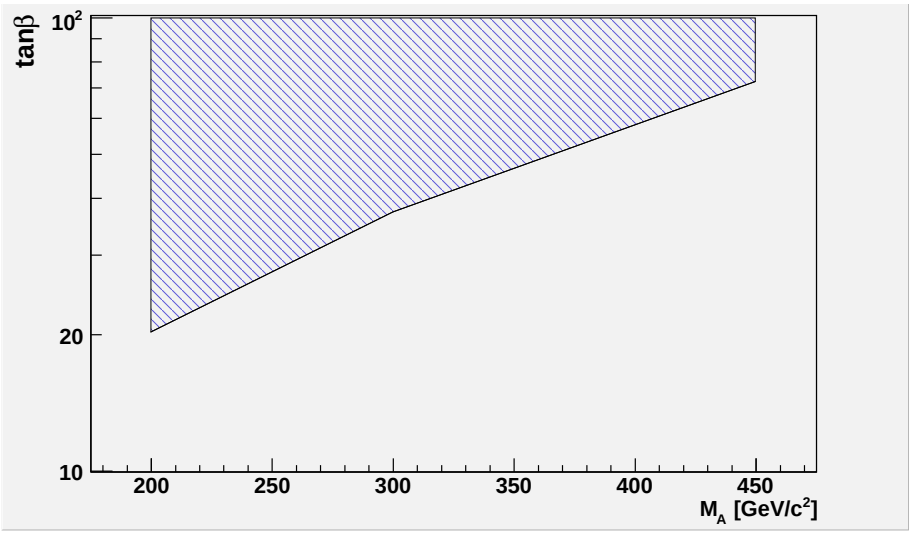

Fig. 8.11: 5σ-discovery curve. The shaded area represents the $\tan\beta$-M_A parameter space in which the Higgs signal significance is higher than 5σ at an integrated luminosity of 30 fb^{-1}.

9

Conclusions

The ATLAS detector, one of the two general purpose experiments at the Large Hadron Collider (LHC), is designed to explore particle physics up to the TeV energy scale. Its main purpose is to shed light onto the spontaneous electroweak symmetry breaking mechanism, either by discovering the postulated Higgs boson and determining its mass, or by excluding its existence. The ATLAS muon spectrometer is designed to achieve high precision muon momentum measurement, allowing for detection of important physics processes as the decays $H/A \rightarrow \mu^+\mu^-$ and $H/A \rightarrow \tau^+\tau^-$ of heavy Higgs bosons in supersymmetric extensions of Standard Model studied in this thesis.

For the largest part of the muon system, the precision measurements on the muon tracks are obtained from the Monitored Drift Tube (MDT) chambers. Ensuring the expected performance of MDT chambers is a vital part for the ATLAS operation. In this thesis the performance of the MDT chambers has been studied in different steps, from the validation of the detector in simulation, to data quality monitoring and calibration of the chambers using cosmic muons.

The ATLAS muon detector simulation incorporates the detector material and geometry description as well as the description of the processes occuring when particles move through the detector and of the detector response. In this thesis, dedicated software tools for the validation of the detector geometry implementation in the simulation program were developed. Therefore, allowe for the detection and correction of faulty detector description and for the constant monitoring of it, ensuring current simulation of the muon system. The application of the developed software on two different detector geometry layouts (ideal and misalligned) showed the satisfactory status of the ATLAS muon spectrometer simulation software.

As a subsequent step, with data of cosmic ray muons collected during the past year with the ATLAS detector, the performance of the muon data quality monitoring software have been tested. The outcome of this effort was the verification of the data from a large number of chambers and the separation of high and low quality data runs. High quality data were used for the callibration of the space-to-drift-time (r(t)) relationship of the MDT chambers. A new calibration method called analytical autocalibration was tested on the collected data by using different parametrizations of the r(t)-relationship, different number of tracks and different number of iterations in the calibration algorithm indicating the robustness and speed of the method. The

proposed method is proved to achieve the required accuracy of 20 μm in 5 iterations using not more than 2000 muon tracks per MDT chamber.

The studies of the ATLAS muon spectrometer allow for a reliable and accurate simulation of the physics processes involving high-momentum muons, like the decays $H/A \to \tau^+\tau^- \to e/\mu + X$ and $H/A \to \mu^+\mu^-$ studied in detail in this thesis.

The first study was carried out in the CP conserving scenario m_h-max of the Minimal Supersymmetric extension of the Standard Model (MSSM). Exploiting the dominant leptonic decay of the H/A bosons into a τ-lepton pair (BR$\simeq$ 10%) and the excellent muon momentum resolution of the ATLAS detector, the search for the heavy neutral MSSM Higgs bosons has been studied in the mass range of 150 to 600 GeV/c^2 for the initial low-luminosity stage of the LHC operation with an expected luminosity of 10^{33} cm^{-2}s^{-1}. The neutral MSSM Higgs bosons H/A decays to a τ-lepton pair are expected to be discovered with 5σ-significance e.g. for tan$\beta \gtrsim 5$ and $m_A = 150$ GeV/c^2 or for tan$\beta \gtrsim 25$ and $m_A = 600$ GeV/c^2 with an integrated luminosity of 30 fb^{-1}.

The H/A boson decays into a muon pair are governed by the same couplings as the decays into a τ-pair but the branching ratio, which scales as $(m_\mu/m_\tau)^2$, is 280 times lower. Nevertheless, this channel can be used for the measurement of the Higgs mass, utilizing the high momentum resolution of the ATLAS muon spectrometer. Decays of the neutral MSSM Higgs bosons H/A into a muon pair can be discovered with 5σ-significance e.g. for tan$\beta \gtrsim 20$ and $m_A = 200$ GeV/c^2 or for tan$\beta \gtrsim 60$ and $m_A = 450$ GeV/c^2 with an integrated luminosity of 30 fb^{-1}. Furthermore, the Higgs mass determination using the side-bands method for background subtraction has been studied. A nominal H/A mass of 200 GeV/c^2 can be determined with an accuracy of approximately 2% at tan$\beta = 30$ with an integrated luminosity of 30 fb^{-1}.

Appendix A

Muon Chamber Position Identifiers

A.1 Scope

The scope of this section is to provide more detailed information about the correspondence between the physical location of Muon chambers and the Software identifier values for each chamber type. We present here, in a detailed way, the mapping needed in order to interpret the output of the validation software as the location of the chambers. For each subdetector technology we summarize in a table the possible values of η and φ identifiers/locations. The ultimate purpose of this appendix is to give the connection between identifier/location for all chamber types and explain the relevant identifier schemes for special cases of chambers. All the pictures of the Muon Spectrometer elements presented in this section are produced by using the PERSINT 3D visualization programm, developed by the Saclay Muon Software Group.

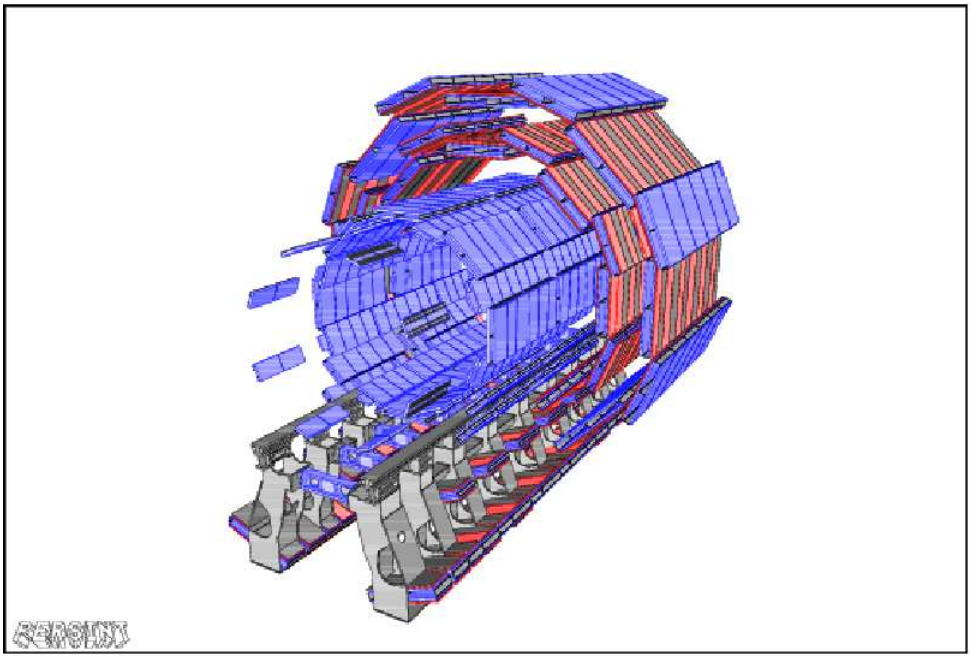

Fig. A.1: Part of MDT-RPC chambers in the Barrel

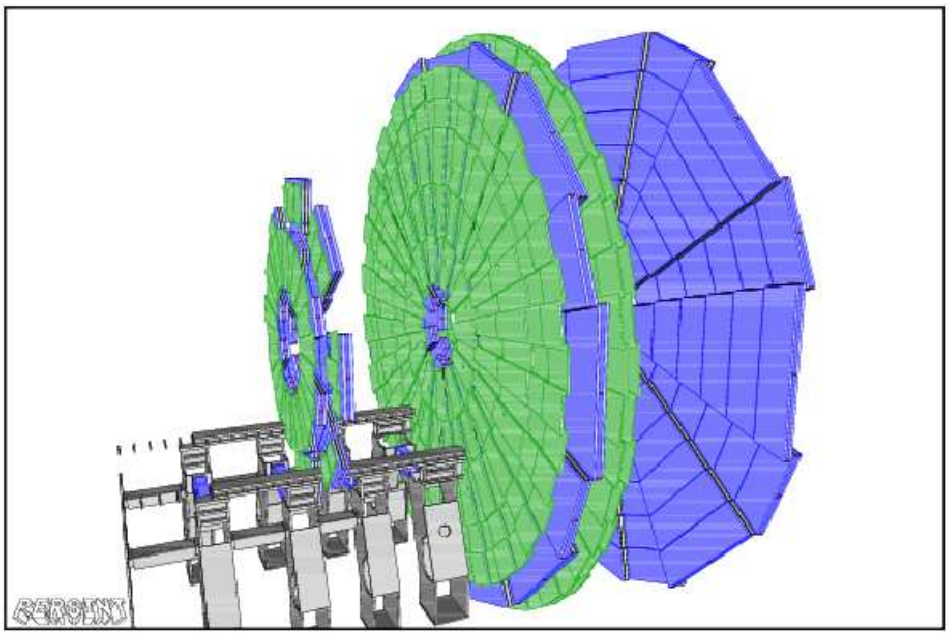

Fig. A.2: Part of MDT-TGC chambers in the Endcap

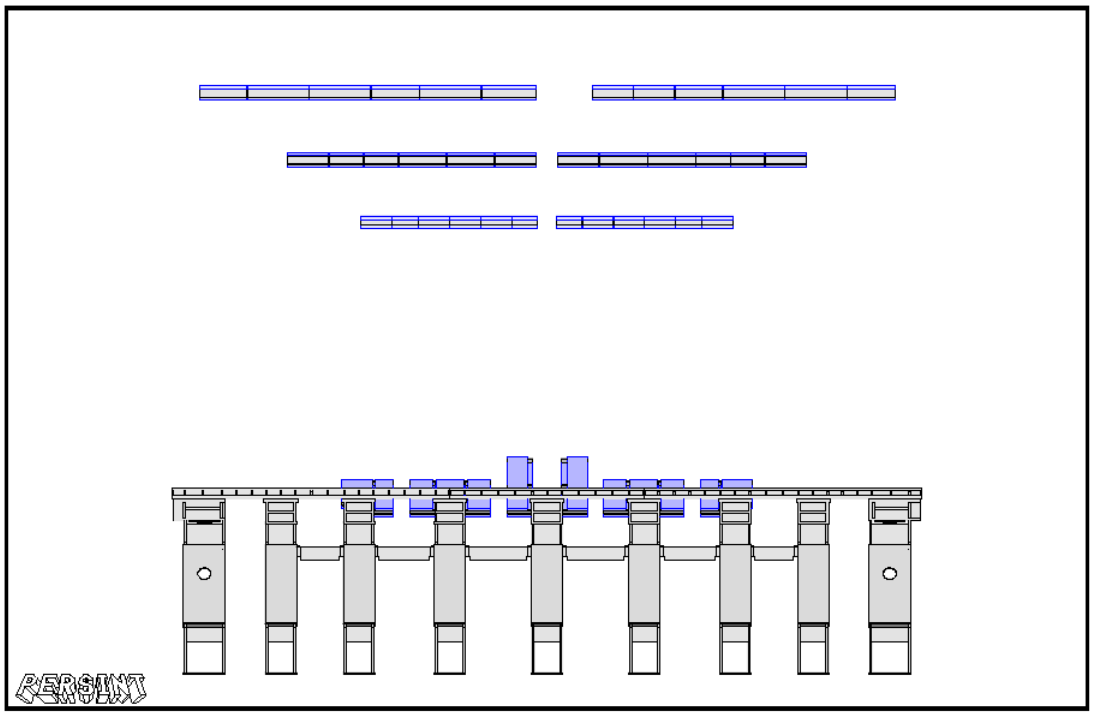

Fig. A.3: MDT Barrel η sectors

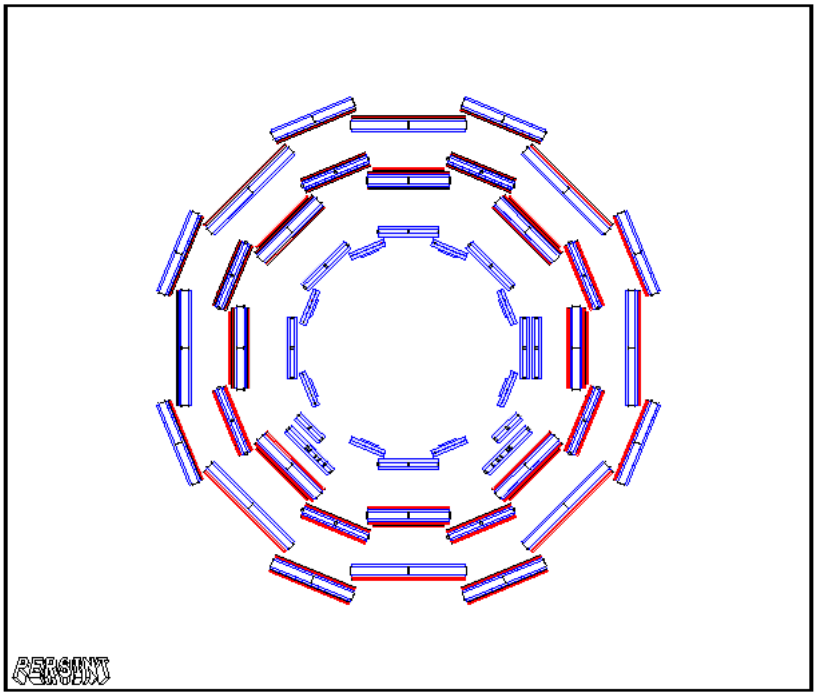

Fig. A.4: MDT Barrel φ sectors, view from C side

A.2 MDT

The most of the Barrel MDT chambers, as explained in section B.1, are located mainly in twelve different η sectors. There are six sectors in each side of the detector, starting with -6 in side C and ending with 6 in side A. In the middle there is a gap in sector 0. Each η sector represents a physical chamber. As listed in table A.1 chambers following this layout in η are the BMS, BOS, BIL, BML, BOL and BIR. An example of such a layout can be seen in figure A.3. In addition there are cases where we have a different nuber of η sectors than six. These cases are: BIS where eight sectors in each side exist, BIM with five η sectors in each side (see figure A.5), BMF with three η sectors in each side, BEE with two η sectors in each side and the BOF and BOG chambers where there are four sectors of each type alternating in each side plus one BOG in the sector 0 (see figure A.6).

Again in the Barrel but concerning φ there are eight sectors as explained in section B.1. Each of the software φ sectors icorporates two physical φ sectors (see figure A.4). In the cases of BIS, BML, BOL and BEE, the chambers are located in all eight sectors. Special cases are: BMS don't exist in the feet sectors 6 and 7 but instead there are BMF, BOS that are substituted with BOF and BOG in feet sectors 6 and 7, BIL that don't exist in sectors 6 and 8 and instead there are BIR and BIM.

For the Endcap, as noted in section B.1, the MDT chambers are located in η sectors that represent a physical chamber. The numbering is negative for side

C, positive for side A and is increases with cylindrical R. The number of physical chambers (and so the identifiers range) in η varies, depending on the type of the chamber. For example it is six for EOS and EOL chambers (see figure A.7) and two for EIS chambers. Note the detail (see figure A.8) that there are in general four EIL chambers (three trapezoid and one rectangular) but five in φ sectors 1 and 5 (three trapezoid and two rectangular).

Concerning the φ sectors in the Endcap, for all chamber types there are eight software sectors which include one small and one large physical chambers (see figure A.7). The numbering of the sectors follows the same way as for the Barrel.

MDT Chamber Type	Eta Sector (Identifier)	Phi Sector (Identifier)
BIS	[-8,-1] , [1,8]	[1,8]
BMS	[-6,-1] , [1,6]	[1,5] , 8
BOS	[-6,-1] , [1,6]	[1,5] , 8
BIL	[-6,-1] , [1,6]	[1,5] , 7
BML	[-6,-1] , [1,6]	[1,8]
BOL	[-6,-1] , [1,6]	[1,8]
BIR	[-6,-1] , [1,6]	6 , 8
BIM	[-5,-1] , [1,5]	6 , 8
BMF	[-3,-1] , [1,3]	[6,7]
BOF	[-4,-1] , [1,4]	[6,7]
BOG	[-4,4]	[6,7]
BEE	[-2,1] , [1,2]	[1,8]
EIS	[-2,1] , [1,2]	[1,8]
EMS	[-5,1] , [1,5]	[1,8]
EOS	[-6,1] , [1,6]	[1,8]
EIL	[-5,1] , [1,5]	[1,8]
EML	[-5,1] , [1,5]	[1,8]
EOL	[-6,1] , [1,6]	[1,8]
EES	[-2,1] , [1,2]	[1,8]
EEL	[-2,1] , [1,2]	[1,8]

Tab. A.1: MDT software identifiers table

A.3 RPC

The RPC chambers layout in η sectors is the same as for the MDT Barrel chambers.There are six sectors in each side of the detector, starting with -6 in side C and ending with 6 in side A. These are the cases of BMS, BOS and BOL. Special cases are BMF and BOF/BOG (see figure A.9) which follow the cases of the respective MDT chambers. Note that in ... RPCs in both sides of the MDT are installed. Note that for the BML chambers there are six MDTs in each side but six pairs of RPCs (above and below MDT) plus an extra RPC in high η in each side, offering an extended η coverage (see figure A.10).

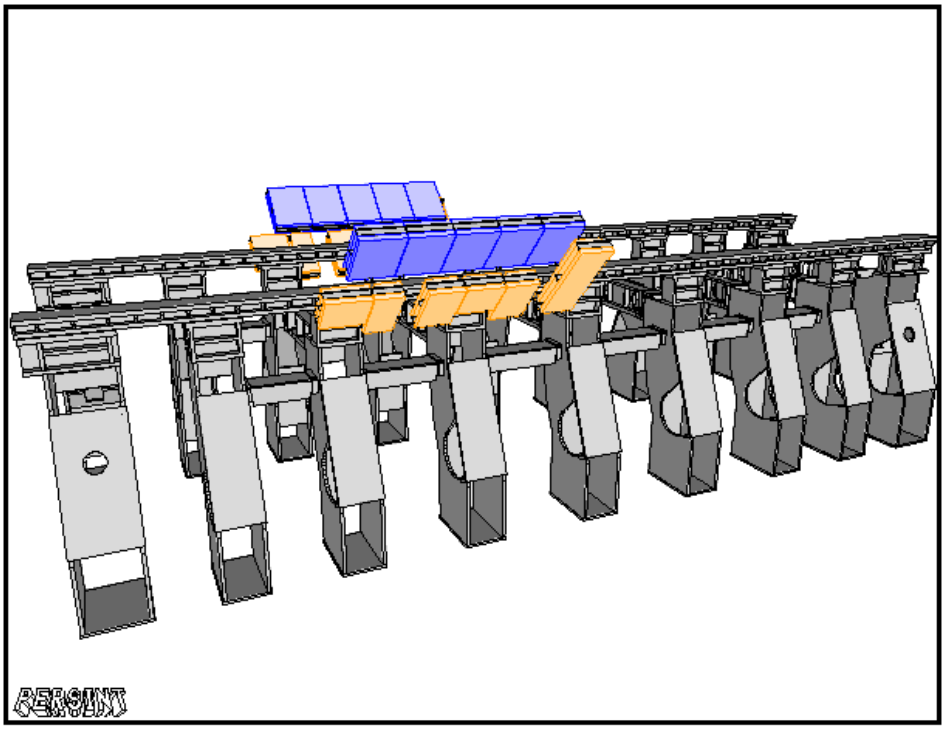

Fig. A.5: BIM (blue) and BIR (yellow) chambers

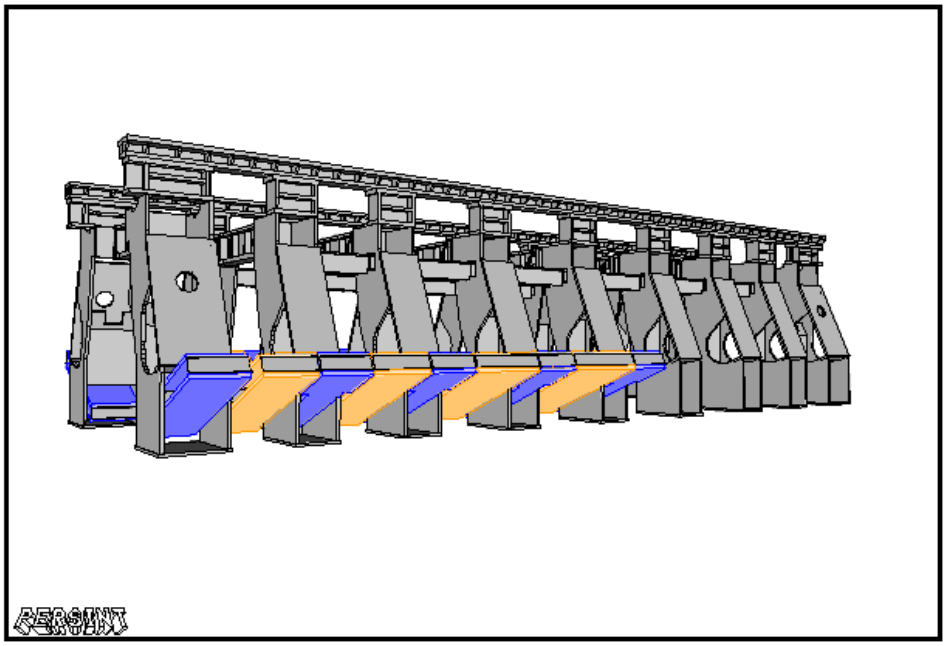

Fig. A.6: BOG (blue) and BOF (yellow) chambers

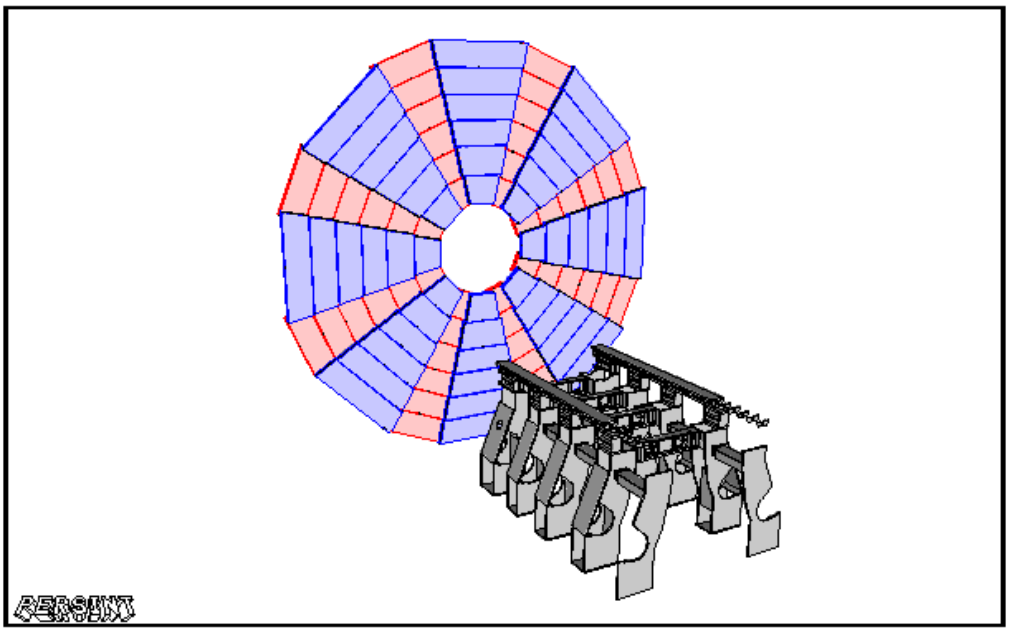

Fig. A.7: EOL (blue) and EOS (red) chambers

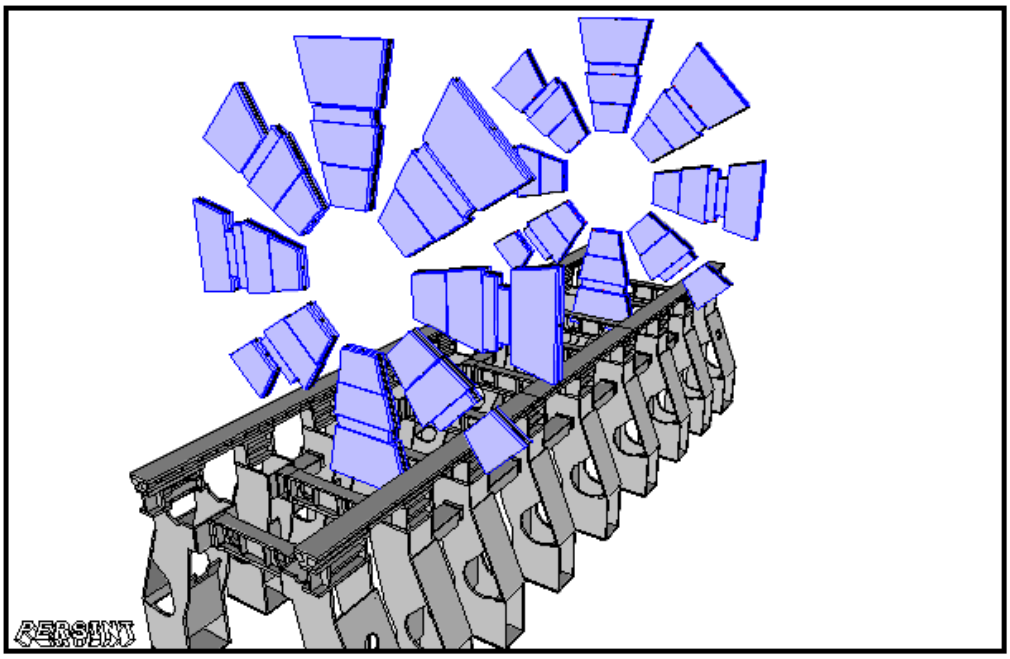

Fig. A.8: EIL chambers

In φ sectors RPC chambers follow again the scheme of the MDTs. That means BMS and BOS RPCs exist only in sectors 1 to 5 and 8, and are substituted with BMF and BOF/BOG.

RPC Chamber Type	Eta Sector (Identifier)	Phi Sector (Identifier)
BMS	[-6,-1] , [1,6]	[1,5] , 8
BOS	[-6,-1] , [1,6]	[1,5] , 8
BML	[-7,-1] , [1,7]	[1,8]
BOL	[-6,-1] , [1,6]	[1,8]
BMF	[-3,-1] , [1,3]	[6,7]
BOF	[-4,-1] , [1,4]	[6,7]
BOG	[-4,4]	[6,7]

Tab. A.2: RPC table

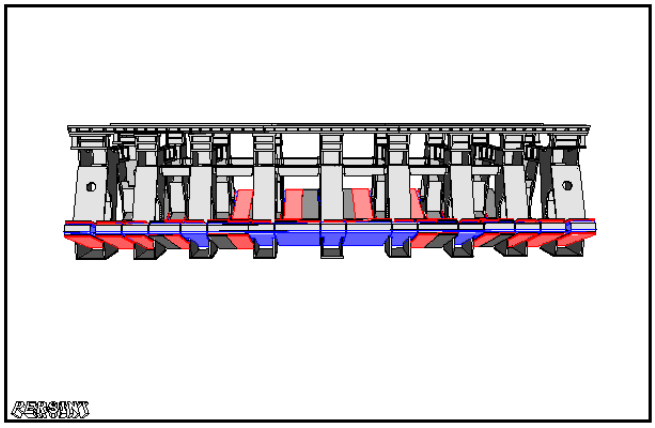

Fig. A.9: BOG and BOF chambers (Blue MDT / Red RPC)

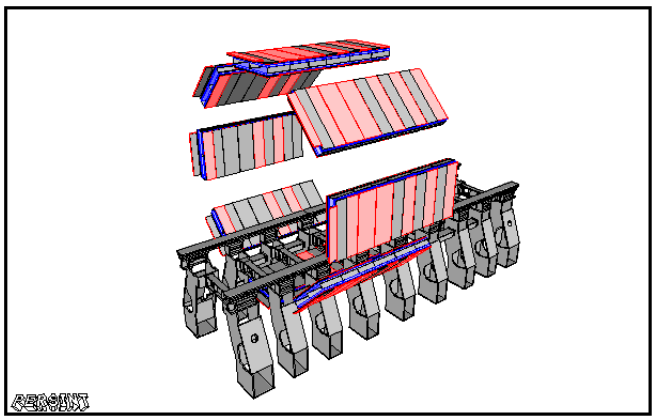

Fig. A.10: BML chambers (Blue MDT / Red RPC)

A.4 CSC

CSC chambers are mounted in two discs in the two sides of the Muon Spectrometer. Counting with cylindrical R there is one chamber so η identifier is -1 for the C side and 1 for the A side. The two sizes of CSC chambers, CSS and CSL are alternating in φ sectors (see figure A.11) and the identifier range is from -8 to 8, follows the same scheme as for Barrel MDTs where each identifier sector consists of one large and one small chamber.

CSC Chamber Type	Eta Sector (Identifier)	Phi Sector (Identifier)
CSS	-1 , 1	[1,8]
CSL	-1 , 1	[1,8]

Tab. A.3: CSC table

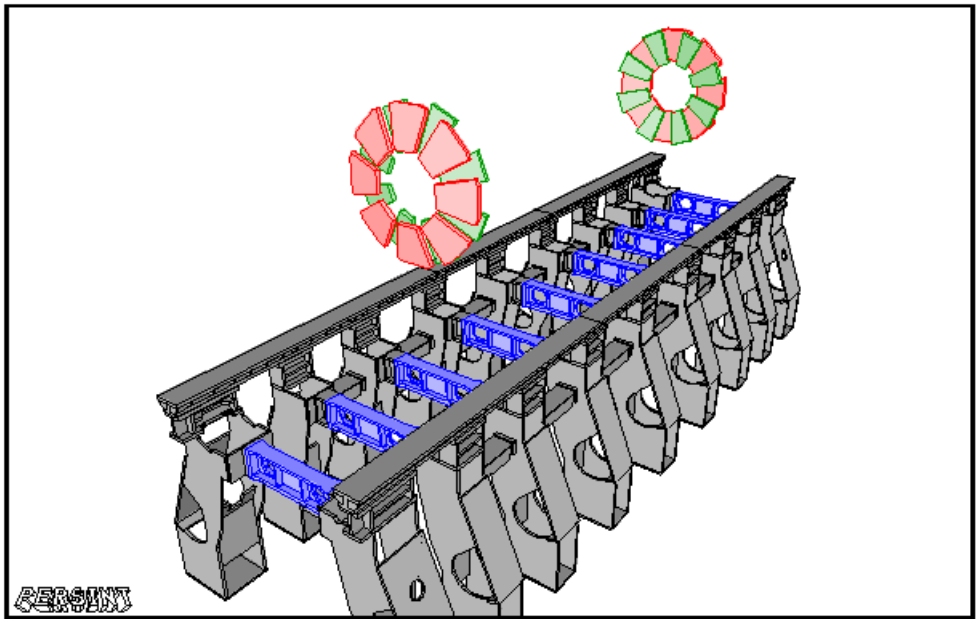

Fig. A.11: CSC chambers (Green CSS / Red CSL)

A.5 TGC

The TGC chambers layout follows closely that of MDT Endcap chambers (see figure A.2). This means that in η sectors TGC chambers are numbered adcoording to their cylindrical R. So η identifier is negative for side C and positive for side A. For T4F, T1F, T2F, T3F and T4E we the range of the identifier is either -1 or 1 depending on the side of the Muon Spectrometer. For T1E we have 4 chambers in the cylindrical R direction while five for T2E and T3E. In more detail the layout of

TGCs can be seen in figure A.12. Note the difference between F and E chambers. F chambers are located in the forward regions (higher η) of each discs and there is always one as counted in cylindrical R.

As far as it concerns φ sectors, F chambers are mounted in twenty four sectors and E chambers in forty eight sectors (see figure A.12). The identifier is increasing clockwise as seen form side C. A special case is T4E chambers which occupy twenty one φ sectors (see figure A.13).

A last important detail is that the numbering of TGC discs with increasing $|Z|$ is done in the following way: 4, 1, 2 and 3.

TGC Chamber Type	Eta Sector (Identifier)	Phi Sector (Identifier)
T4F	-1 , 1	[1,24]
T1F	-1 , 1	[1,24]
T2F	-1 , 1	[1,24]
T3F	-1 , 1	[1,24]
T4E	-1 , 1	[1,21]
T1E	[-4,-1] , [1,4]	[1,48]
T2E	[-5,-1] , [1,5]	[1,48]
T3E	[-5,-1] , [1,5]	[1,48]

Tab. A.4: TGC table

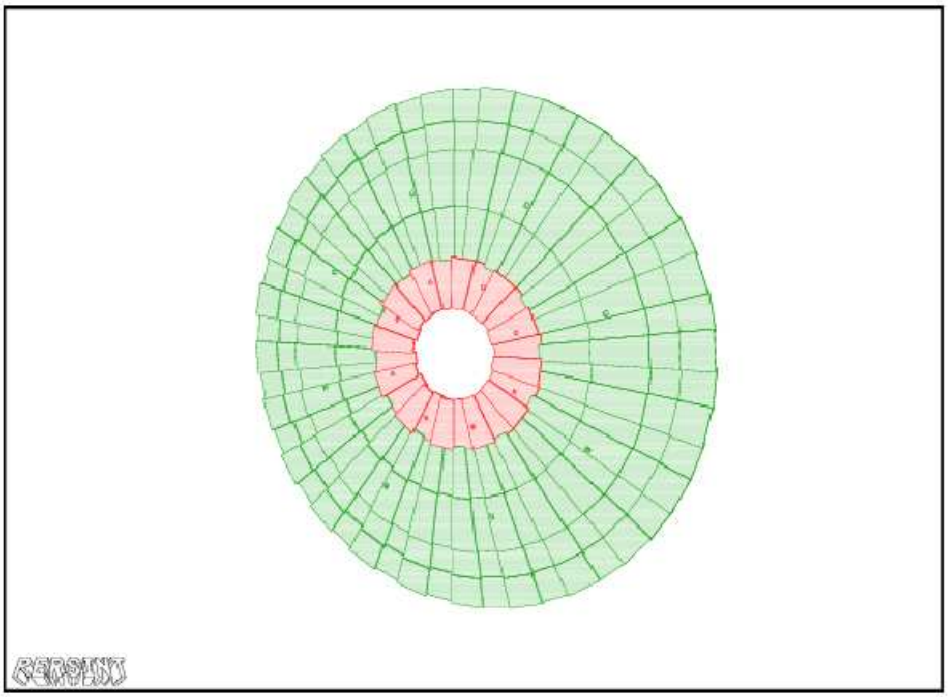

Fig. A.12: TGC chambers (Green T1E / Red T1F)

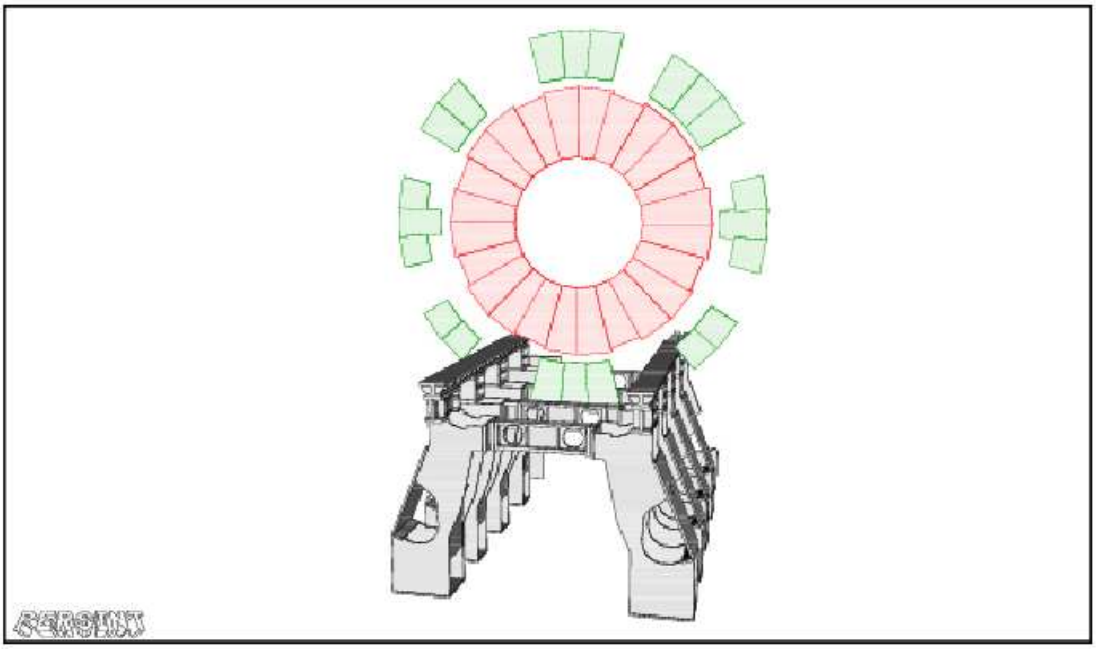

Fig. A.13: TGC chambers (Green T4E / Red T4F)

Appendix B

Full Set of Muon Chamber Identifiers

B.1 Muon Simulation Identifier Scheme

The current ATLAS Detector Description is based on a geometrical model (called GeoModel) that describes the basic geometry in terms of volumes, solids and materials and the logical structure of the detector in terms of a hierarchy of detector elements. The ATLAS Detector Description DataBase (DDDB) provides the parameters used by GeoModel to construct a model in which the subsystems are described in terms of detector nodes. For example the MuonSpectrometer has a set of MDT nodes (stations) with tubes corresponding to read-out channels. The link between the event and the detector description is an identification scheme which follows the hierarchical structure of the detectors. For each-subsystem, the hierarchy of the corresponding identifier is represented as a series of fields with the level of detail increasing. For example, for the Muon System the upper level element of the hierarchy is the muon station represented by the field

- MuonSpectrometer/StationName/StationEta/StationPhi

The StationName represents the muon station, StationEta and StationPhi represent the η-ϕ sector. For the specific subdetector subsystems there are more detailed value range; for an MDT the identifier is:

- Technology/Multilayer/TubeLayer/Tube

in which the Technology fields in the string 'MDT', the MultiLayer is an integer denoting the stack of tube layers. The TubeLayer field numbers the single layer of tubes and finally the Tube field identifies the single tube.

The ATHENA architecture aims to shield the application from the details of the persistent detector description database. The job of the conversion services is to populate the Transient Detector Store with a representation of the detector description.

The detector description data depends on time-varying conditions; an interval of validity service (IOVSvc) can be used to handle the changes when a time boundary of the data condition validity is crossed. For the needs of the Muon Simulation Validation, the ATLAS Muon Spectrometer offline identifier scheme [28] has been adopted here, in addition to the Simulation Identifier. It is intented to provide

a unique identification of the active components of the muon spectrometer and consists of a sequence of integers and character strings that are described in the current document in an order of increasing detail. Some of the identifier fields are common among the different subsystem technologies (MDT, RPC, CSC or TGC). In addition a number of subsystem specific identifiers are available in order to fully cover the fundamental components or the readout channels of the subdetectors.

Except for a few cases where the identifier refers to subdetector local coordinates, identifier values range corresponds to the global coordinate system of the ATLAS Detector.

Coordinate	Description - Orientation
X	Cartesian X, pointing to center of LHC ring (perpendicular to beam)
Y	Cartesian Y, pointing upwards (perpendicular to beam)
Z	Cartesian Z, pointing along beam (direction defined from X and Y for a right handed system)
R	Cylindrical radius, pointing out radialy from interaction point
φ	Cylindrical azimuth angle (defined by R and Z for a right handed system)

Tab. B.1: ATLAS global coordinate system as defined in the Muon Spectrometer TDR.

In the following sections the muon identifiers used for each subdetector technology are explained. For each identifier the range of its values and a short explanation is given. Furthermore the AANtuple variable name in which each identifier's value is being stored and the range of the identifier are summarized in Table **??**. This information is given for all four subdetector technologies. The Simulation Identifiers and the Offline Identifiers are treated separately.

MDT Simulation Description

- The field **m_Validation_MDT_StationName** denotes the conventional ATLAS nomenclature, in which a MDT chamber name is given according to its location in $|\eta|$ (Barrel/Endcap), to the corresponding station radius (Inner/Middle/Outer/Extension) and to its size within a station (Large/Small /Rib/Feet).

- The **m_Validation_MDT_StationEta** field denotes the position of the chambers in different η slices. For the Barrel ($|\eta| < 1$) the identifier range is [-8,8], from side C(negative) to side A(positive) and icreases with Z. For the Endcap ($|\eta| > 1$) the identifier range is [-6,-1] or [1,6] (again negative in side C and positive in side A), with -1 and 1 starting from the lowest cylindrical R values and the absolute value increases with cylindrical R.

- Field **m_Validation_MDT_StationPhi** denotes the different φ sectors in a cross section of the Muon Spectrometer. MDT chambers belong to sixteen physical φ sectors with their index incrementing clockwise as seen from side

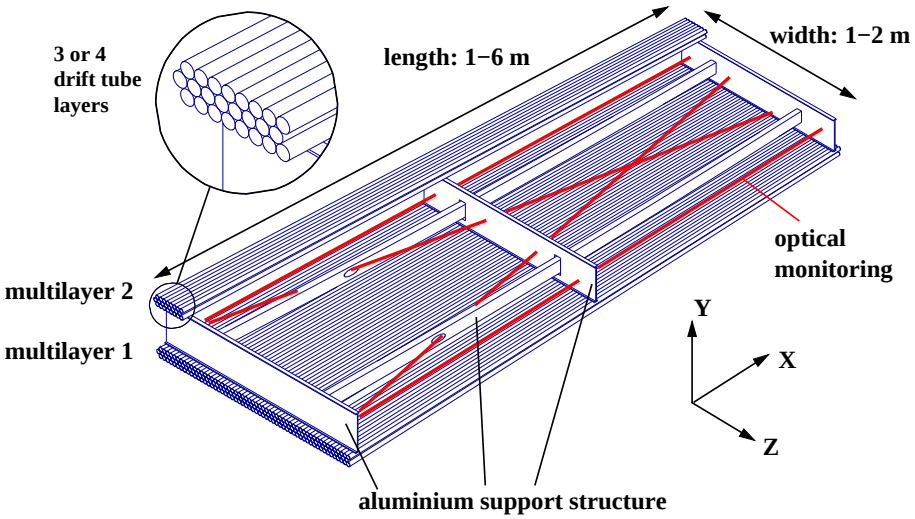

Fig. B.1: Schematic representation of an MDT chamber. In detail the three or four layer of tubes that make each of the two multilayers are illustrated.

C. In the case of the software identifier the value range is [1,8], that means that each software φ sector includes two physical φ sectors (one Small and one Large), starts counting from the same sector as the physical (sector1) and incrementing the same way.

- Fields **m_Validation_MDT_IDMultiLayer**, **m_Validation_MDT_IDLayer** and **m_Validation_MDT_IDTube** correspond to the following information respectively. Two multilayers [1,2] which for the Barrel increment with cylindrical R and for the Endcap with $|Z|$. Each multilayer consists of four tube layers for inner stations and three tube layers for middle and outer stations. So the range of the identifier is [1,4] and it increases with cylindrical R for the Barrel and with $|Z|$ for the Endcap. Each layer consist of a stack of tubes of variable size [1,72] and the identifier increases with $|Z|$ in the Barrel and with cylindrical R in the Endcap region.

- Finally the fields **m_Validation_MDT_HitX/Y/Z/R** and **m_Validation_MDT_LocalX/Y/Z/R** correspond to the X, Y, Z and cylindrical R of the hit in the global system (MDT active volumes positions in the Muon Spectrometer) and in the local system (wrt to the middle of the wire - tube dimensions).

More details about the correspondence between software identifier values for name, η, φ and the physical location of each chamber type, can be found in the Appendix A.2.

Level/AANtuple variable	Value Range	Meaning
m_Validation_MDT_EventNumber	[1,n_{event}]	Number of events processed
m_Validation_MDT_RunNumber	Run Number	Run Number
m_Validation_MDT_NumberOfHits	[1,n_{hits}]	Total number of hits
m_Validation_MDT_Type	[1,3]	1=Hits, 2=Digits, 3=Prepraw
m_Validation_MDT_StationName	BIL, BIR, BIM, BIS BEE BML, BMS, BMF BOL, BOS, BOF BOG EIL, EIS EES, EEL EML, EMS EOL, EOS	Barrel Inner Radius (Large, Rib, Small) Barrel Extension (mounted on endcap toroid) Barrel Middle Radius (Large, Small, Feet) Barrel Outer Radius (Large, Small, Feet) Barrel Outer Radius (between BOFs) Endcap Inner Radius (Large, Small) Endcap Extension (next to barrel toroid) Endcap Middle Radius (Large, Small) Endcap Outer Radius (Large, Small)
m_Validation_MDT_StationEta	[-6,-1] [-8,8] [1,6]	Backward Endcap (η < -1): -1 at lowest R Barrel ($\|\eta\|$ < 1): Increases with Z Forward Endcap (η > 1): 1 at lowest R
m_Validation_MDT_StationPhi	[1,8]	Incrases with φ (clockwise as seen from C side)
m_Validation_MDT_IDMultiLayer	[1,2]	Barrel: Increases with R Endcap: Increases with |Z|
m_Validation_MDT_IDLayer	[1,4]	Barrel: Increases with R Endcap: Increases with |Z|
m_Validation_MDT_IDTube	[1,72]	Barrel: Increases with |Z| Endcap: Increases with R
m_Validation_MDT_HitX	[,]	Global X wrt the interaction point
m_Validation_MDT_HitY	[,]	Global Y wrt the interaction point
m_Validation_MDT_HitZ	[,]	Global Z wrt the interaction point
m_Validation_MDT_HitR	[,]	Global cylindrical R wrt the interaction point
m_Validation_MDT_LocalX	[,]	Local X wrt the middle of the wire
m_Validation_MDT_LocalY	[,]	Local Y wrt the middle of the wire
m_Validation_MDT_LocalZ	[,]	Local Z wrt the middle of the wire
m_Validation_MDT_LocalR	[,]	Local cylindrical R wrt the wire axis

Tab. B.2: Set of value ranges for the MDT software identifier levels.

RPC Identifier Description

- The field **m_Validation_RPC_StationName** follows the conventional ATLAS nomenclature, according to which a RPC chamber name is given by its location in $|\eta|$ (Barrel only), in the corresponding station radius (Middle/Outer) and to its size within a station (Large/Small Feet). The name of the RPC chamber for the software identifier follows the name of the MDT chamber on wich the RPC is mounted.

- The **m_Validation_RPC_StationEta** field denotes the position of the chambers in different η slices. The identifier range is [-7,7], from side C(negative) to side A(positive) and increases with Z.

- Field **m_Validation_RPC_StationPhi** denotes the different φ sectors in a cross section of the Muon Spectrometer. RPC chambers follow in φ sectors the same scheme as the MDT Barrel chambers.

- Field **m_Validation_RPC_DoubletR** denotes the number of RPC chambers attached to a MDT chamber. It increases with cylindrical R and its range is [1,2] (two for all Middle chambers and one for all Outer chambers with the exeption of a few BOF/BOG chambers).

- Fields **m_Validation_RPC_DoubletZ** and **m_Validation_RPC_DoubletPhi** denote the two Z units and two φ units of an RPC chamber. The Z modules have a physical overlap and the identifier value has a range [1,2] which increases with $|Z|$. The φ modules are adjacent, the identifier range is [1,2] and increases with φ.

- The field **m_Validation_RPC_DoubletGasGap** corresponds to the gas volume between the bacelite plates within a RPC chambers. Each chamber consists of two such gas volumes so the range of the identifier is [1,2] and it increases with cylindrical R.

- Field **m_Validation_RPC_MeasuresPhi** denotes the orientation of the strip that registers the hit. The range is [0,1], 0 in the case of strips that measure Z (parallel to the MDT wires) and 1 in the case of strips that measure φ (orthogonal to the MDT wires).

- Finally the fields **m_Validation_MDT_HitX/Y/Z/R** correspond to the X, Y, Z and cylindrical R of the hit in the global system (RPC active volumes positions in the Muon Spectrometer).

More details about the correspondence between software identifier values for name, η, φ and the physical location of each chamber type, can be found in the Appendix A.3.

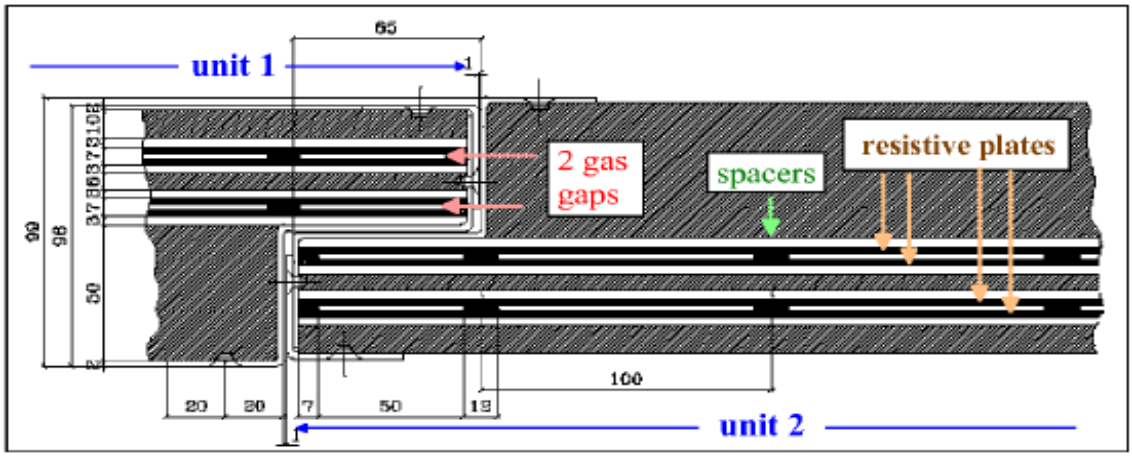

Fig. B.2: Schematic representation of an RPC chamber. The cross section on the y-z plane shows the two units with an overlap in Z and the two gas gaps in each unit. In the perpenticular to the drawing direction (x), the units are also segmented in two DoubletPhi contigious parts.

Level/AANtuple variable	Value Range	Meaning
m_Validation_RPC_EventNumber	[1,n_{event}]	Number of events processed
m_Validation_RPC_RunNumber	Run Number	Run Number
m_Validation_RPC_NumberOfHits	[1,n_{hit}]	Total Number of hits
m_Validation_RPC_Type	[1,3]	1=Hits, 2=Digits, 3=Prepraw
m_Validation_RPC_StationName	BML, BMS, BMF BOL, BOS, BOF BOG	Barrel Middle Radius (Large, Small, Feet) Barrel Outer Radius (Large, Small, Feet) Barrel Outer Radius (between BOFs)
m_Validation_RPC_StationEta	[-7,7]	Increases with Z
m_Validation_RPC_StationPhi	[1,8]	Incrases with φ (clockwise as seen from C side)
m_Validation_RPC_DoubletR	[1,2]	Number of RPC chamber in the station
m_Validation_RPC_DoubletZ	[1,2]	Increases with cylindrical R
m_Validation_RPC_DoubletPhi	[1,2]	Incrases with φ (clockwise as seen from C side)
m_Validation_RPC_DoubletGasGap	[1,2]	Increases with cylindrical R
m_Validation_RPC_MeasuresPhi	[0,1]	
m_Validation_RPC_HitX	[,]	Global X wrt the interaction point
m_Validation_RPC_HitY	[,]	Global Y wrt the interaction point
m_Validation_RPC_HitZ	[,]	Global Z wrt the interaction point
m_Validation_RPC_HitR	[,]	Global cylindrical R wrt the interaction point

Tab. B.3: Set of value ranges for the RPC software identifier levels.

CSC Identifier Description

- The field **m_Validation_CSC_StationName** refers to the two kinds of CSC chambers mounted on each disc with sixteen chambers in total. The two kinds are the CSS (Small) and the CSL (Large) which alternate in φ sectors.
- Field **m_Validation_CSC_StationEta** denotes the η sector of the chambers. The identifiers range is [-1,1] which means a chamber mounted either on the disc located in the Backward Endcap (side C) or on the disc located in the Forward Endcap (side A).
- Field **m_Validation_CSC_StationPhi** corresponds to the different φ sectors in a cross section of the Muon Spectrometer. For CSC chambers each φ sector includes one CSS and one CSL. The value range for this identifier is [-8,8] and it icreases with φ in the same way as for MDTs and RPCs.
- Field **m_Validation_CSC_ChamberLayer** corresponds to the chamber modules that form a complete CSC chamber. The identifier values range is [1,2], it increases with $|Z|$ and indicates the two identical modules that form the chamber (if you understand why, please tell me too).
- Field **m_Validation_CSC_WireLayer** indicates the gas gaps with the anode wires used to form a CSC module. Since a CSC module consists of four such elements, the identifier value range is [1,4] and it increases with $|Z|$.
- Finally the fields **m_Validation_CSC_HitX/Y/Z/R** correspond to the X, Y, Z and cylindrical R of the hit in the global system (CSC active volumes positions in the Muon Spectrometer).

More details about the correspondence between software identifier values for name, η, φ and the physical location of each chamber type, can be found in the Appendix A.4.

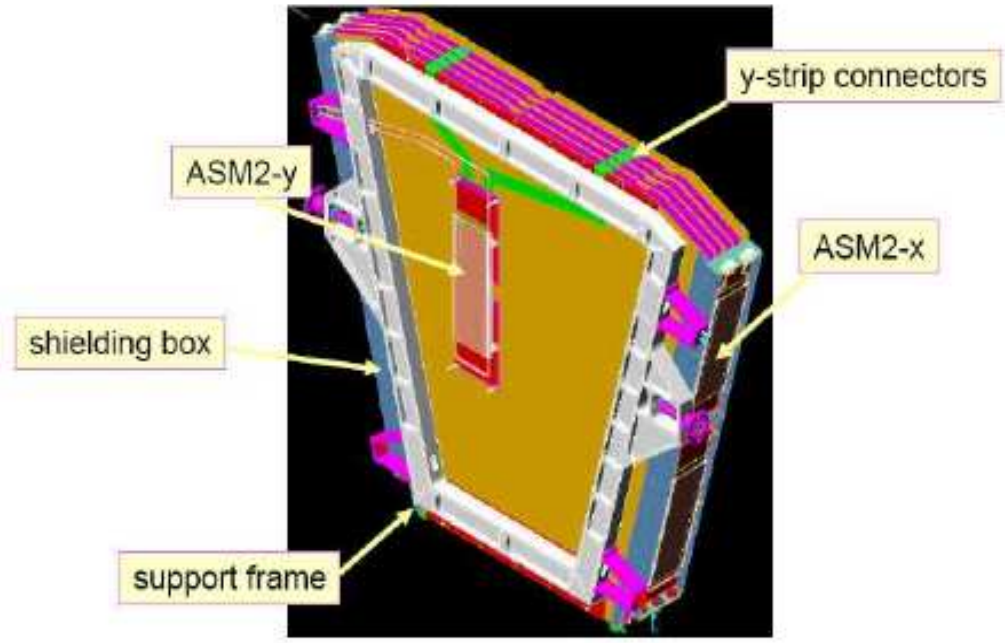

Fig. B.3: Schematic representation of a CSC chamber. In the picture, the four wire layers, almost parallel to the x-y plane and the read out and support structures are indicated.

TGC Identifier Description

- The field **m_Validation_TGC_StationName** refers to the chamber name according to the Z plane where it is located. There are four planes in increasing $|Z|$ order. One innermost plane (before EI MDTs) and three on the middle endcap chamber stations (one before and two after EM MDTs). Note that the naming sequence with order of increasing $|Z|$ is T4E/F, T1E/F, T2E/F, T3E/F.

- Field **m_Validation_TGC_StationEta** denotes the η sector of the chambers. The identifiers range is [-5,1] for the Backward Endcap (side C) and [1,5] for the Forward Endcap (side A). Both -1 and 1 refer to the lowest cylindrical R and the the absolute value increases with cylindrical R.

- Field **m_Validation_TGC_StationPhi** corresponds to the different φ sectors in a cross section of the Muon Spectrometer. Two TE chambers correspond to each φ sector of a TF chamber. Thus the identifier values range is [1,24] for TF chambers and [1,48] for TE chambers. The φ increases the same way as for the MDTs.

Level/AANtuple variable	Value Range	Meaning
m_Validation_CSC_EventNumber	[1,n_{event}]	Number of events processed
m_Validation_CSC_RunNumber	Run Number	Run Number
m_Validation_CSC_NumberOfHits	[1,n_{hit}]	Total Number of hits
m_Validation_CSC_Type	[1,3]	1=Hits, 2=Digits, 3=Prepraw
m_Validation_CSC_StationName	CSS, CSL	Short and Long phi sectors
m_Validation_CSC_StationEta	-1 or 1	Backward Endcap (η < -1): -1 at lowest R
m_Validation_CSC_StationPhi	[1,8]	Incrases with φ (clockwise as seen from C side)
m_Validation_CSC_WireLayer	[1,4]	Increases with $\|Z\|$
m_Validation_CSC_HitX	[,]	Global X wrt the interaction point
m_Validation_CSC_HitY	[,]	Global Y wrt the interaction point
m_Validation_CSC_HitZ	[,]	Global Z wrt the interaction point
m_Validation_CSC_HitR	[,]	Global cylindrical R wrt the interaction point

Tab. B.4: Set of value ranges for the CSC software identifier levels.

- Field **m_Validation_TGC_GasGap** denotes the physical gas volumes that form a TGC chamber. TGCs are either doublets or triples so the rate of the software identifier is either [1,2] or [1,3]. The identifier value increases with $|Z|$.

More details about the correspondence between software identifier values for name, η, φ and the physical location of each chamber type, can be found in the Appendix A.5.

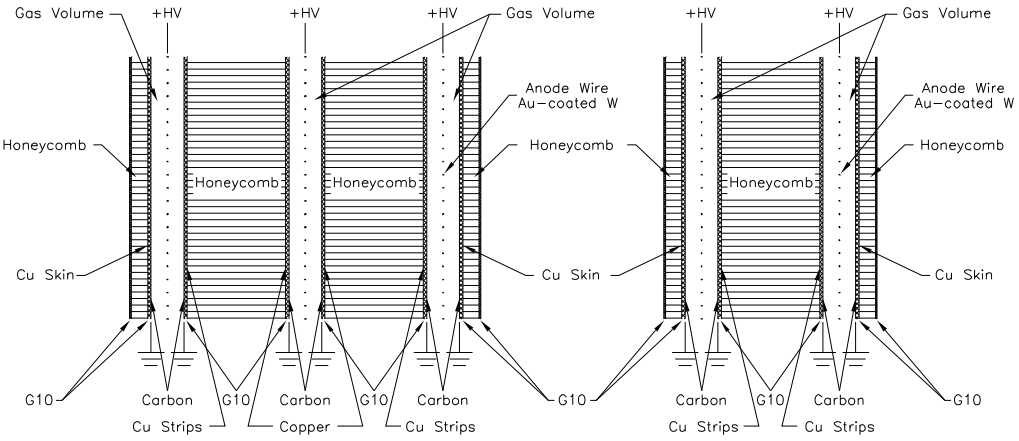

Fig. B.4: A schematic representation of a TGC chamber. In the picture a cross section on the y-z plane is illustrated. In the two drawings the case of the triplet and the doublet with two and three gas volumes respectively is depicted.

Level/AANtuple variable	Value Range	Meaning
m_Validation_TGC_EventNumber	[1,n$_{event}$]	Number of events processed
m_Validation_TGC_RunNumber	Run Number	Run Number
m_Validation_TGC_NumberOfHits	[1,n$_{hit}$]	Total number of hits
m_Validation_TGC_Type	[1,3]	1=Hits, 2=Digits, 3=Prepraw
m_Validation_TGC_StationName	T1E, T2E, T3E, T4E T1F, T2F, T3F, T4F	Endcap ($1.0 < \|\eta\| < 1.4$) approximately Forward ($1.4 < \|\eta\| < 2.0$) approximately For increasing $\|Z\|$ the name sequence is T4E/F, T1E/F, T2E/F, T3E/F
m_Validation_TGC_StationEta	[-5,-1] [1,5]	Backward Endcap: -1 at lowest R Forward Endcap: 1 at lowest R
m_Validation_TGC_StationPhi	[1,48] [1,24]	Endcap: Incrases with φ Forward: Incrases with φ (clockwise as seen from C side)
m_Validation_TGC_GasGap	[1,2] [1,3]	Doublet: Increases with $\|Z\|$ Triplet: Increases with $\|Z\|$
m_Validation_TGC_HitX	[,]	Global X wrt the interaction point
m_Validation_TGC_HitY	[,]	Global Y wrt the interaction point
m_Validation_TGC_HitZ	[,]	Global Z wrt the interaction point
m_Validation_TGC_HitR	[,]	Global cylindrical R wrt the interaction point

Tab. B.5: Set of value ranges for the TGC software identifier levels.

Appendix C

Filter settings

C.1 Scope

As mentioned in chapters **??** and **??** several different filters were used in order to simulate the required data samples. In this section we present the settings used for each sample and the corresponding filter.

C.2 Filter settings for $b\bar{b}H/A \rightarrow \tau\tau$ samples

For all signal samples and Zbb process used in the $b\bar{b}H/A \rightarrow \tau\tau$ analysis the ATauFilter was used. It applies P_T cut in the tau decay products depending on the decay mode, and in addition a cut in the transverse angular distance between the visible tau decay products. The setting used are the following:

```
//--------------------
// ATauFilter
//--------------------
theApp.Dlls += [ "GeneratorFilters" ]
theApp.TopAlg += [ "ATauFilter" ]
ATauFilter = Algorithm( "ATauFilter" )
ATauFilter.Etacut = 2.7 // lepton and hadron |n| cut
ATauFilter.llPtcute = 13000.0 // P_T^e cut in l-l decays
ATauFilter.llPtcutmu = 8000.0 // P_T^mu cut in l-l decays
ATauFilter.lhPtcute = 13000.0 // P_T^e cut in l-h decays
ATauFilter.lhPtcutmu = 8000.0 // P_T^mu cut in l-h decays
ATauFilter.lhPtcuth = 12000.0 // P_T^h cut in l-h decays
ATauFilter.hhPtcut = 12000.0 // P_T^h cut in h-h decays
ATauFilter.maxdphi = 2.9 // Δφ cut
ATauFilter.OutputLevel = INFO
```

For the $t\bar{t}$ background the TTbarLeptonFilter was utilized. It selects only event with at least one top quark giving a leptonically decaying W.

```
//---------------------
// TTbarLeptonFilter
//---------------------
theApp.Dlls += [ "GeneratorFilters" ]
theApp.TopAlg += [ "TTbarLeptonFilter" ]
TTbarLeptonFilter = Algorithm( "TTbarLeptonFilter" )
TTbarLeptonFilter.Ptcut = 1. // P_T^l cut
```

For the W events produced the MultiLeptonFilter and the TruthJetFilter were used. The combination of two ensures that at least one lepton within a P_T and $|n|$ range and at least two jets within a P_T and $|n|$ range are present in the event.

```
//---------------------
// MultiLeptonFilter
//---------------------
theApp.TopAlg += [ "MultiLeptonFilter" ]
MultiLeptonFilter = Algorithm( "MultiLeptonFilter" )
MultiLeptonFilter.Ptcut = 20000. // P_T^l cut
MultiLeptonFilter.Etacut = 2.7 // lepton |n| cut
MultiLeptonFilter.NLeptons = 1 // minimum number of leptons
```

```
//---------------------
// TruthJetFilter
//---------------------
theApp.TopAlg += ["TruthJetFilter"]
TruthJetFilter = Algorithm( "TruthJetFilter" )
TruthJetFilter.Njet=2; // minimum number of jets
TruthJetFilter.NjetMinPt=10000.; // P_T^jet cut
TruthJetFilter.NjetMaxEta=3; // jet |n| cut
TruthJetFilter.jetpt1=10000.; // hardest jet P_T cut
TruthJetFilter.TruthJetContainer="Cone4TruthJets"; // jet algorithm
```

C.3 Filter settings for $b\bar{b}H/A \to \mu\mu$ samples

The HiggsMultiLeptonFilter was used in all background processes for the $b\bar{b}H/A \to \mu$ analysis. The aim was to have dimuon final state in certain kinematical range and in addition, to keep events whose dimuon invariant mass is close to the studied signal invariant masses.

```
//−−−−−−−−−−−−−−−−−−−−−−−−−−
// HiggsMultiLeptonFilter
//−−−−−−−−−−−−−−−−−−−−−−−−−−
HiggsMultiLeptonFilter = Algorithm( "HiggsMultiLeptonFilter" )
HiggsMultiLeptonFilter.NLeptons = 2 // minimum number of leptons
HiggsMultiLeptonFilter.Etacut = 2.7 // lepton |n| cut
HiggsMultiLeptonFilter.Ptcut = 5000. // P_T^l cut
HiggsMultiLeptonFilter.Zbbbar = TRUE; // switching on mass cut
HiggsMultiLeptonFilter.bbMassCut = 180000. // mass cut value (120000. for Z
bkg)
```

Appendix D

Feynhiggs 2.5.1 output

M_A [GeV/c^2]	tanβ	Γ [GeV]
150	5	h : $2.4{\cdot}10^{-2}$ H : $8.1{\cdot}10^{-2}$ A : $8.3{\cdot}10^{-2}$
150	10	h : $5.2{\cdot}10^{-2}$ H : $2.7{\cdot}10^{-1}$ A : $3.2{\cdot}10^{-1}$
150	20	h : $7.4{\cdot}10^{-2}$ H : 1.1 A : 1.2
150	30	h : $7.8{\cdot}10^{-2}$ H : 2.4 A : 2.5
150	50	h : $7.7{\cdot}10^{-2}$ H : 6.0 A : 6.1
150	80	h : $7.1{\cdot}10^{-2}$ H : 1.3 A : 1.3
200	5	h : $1.1{\cdot}10^{-2}$ H : $1.6{\cdot}10^{-1}$ A : $1.7{\cdot}10^{-1}$
200	10	h : $1.3{\cdot}10^{-2}$ H : $4.5{\cdot}10^{-1}$ A : $4.8{\cdot}10^{-1}$
200	20	h : $1.4{\cdot}10^{-2}$ H : $9.6{\cdot}10^{-1}$ A : $9.9{\cdot}10^{-1}$
200	30	h : $1.4{\cdot}10^{-2}$ H : 3.4 A : 3.5
200	50	h : $1.3{\cdot}10^{-2}$ H : 8.4 A : 8.4
200	80	h : $1.3{\cdot}10^{-2}$ H : 17.8 A : 18.1

M_A [GeV/c^2]	tanβ	Γ [GeV]
300	5	h : $6.2{\cdot}10^{-3}$ H : $4.0{\cdot}10^{-1}$ A : 1.0
300	10	h : $7.1{\cdot}10^{-3}$ H : $8.4{\cdot}10^{-1}$ A : 1.3
300	20	h : $7.3{\cdot}10^{-3}$ H : 2.6 A : 2.9
300	30	h : $7.3{\cdot}10^{-3}$ H : 5.2 A : 5.5
300	50	h : $7.2{\cdot}10^{-3}$ H : 12.6 A : 12.8
300	80	h : $7.2{\cdot}10^{-3}$ H : 26.8 A : 27.1
450	5	h : $5.0{\cdot}10^{-3}$ H : 2.9 A : 3.4
450	10	h : $5.7{\cdot}10^{-3}$ H : 3.2 A : 3.4
450	20	h : $5.9{\cdot}10^{-3}$ H : 5.7 A : 5.8
450	30	h : $5.9{\cdot}10^{-3}$ H : 9.6 A : 9.7
450	50	h : $5.9{\cdot}10^{-3}$ H : 20.6 A : 20.7
450	80	h : $6.0{\cdot}10^{-3}$ H : 42.2 A : 42.1

M_A [GeV/c^2]	tanβ	Γ [GeV]
600	5	h : $4.7{\cdot}10^{-3}$ H : 6.7 A : 6.7
600	10	h : $5.3{\cdot}10^{-3}$ H : 6.7 A : 6.7
600	20	h : $5.5{\cdot}10^{-3}$ H : 9.9 A : 9.8
600	30	h : $5.6{\cdot}10^{-3}$ H : 15.2 A : 14.9
600	50	h : $5.6{\cdot}10^{-3}$ H : 30.0 A : 29.5
600	80	h : $5.6{\cdot}10^{-3}$ H : 59.2 A : 57.9

M_A [GeV/c^2]	tanβ	$\sigma\times$BR$_{\tau\tau}$ [fb] direct	$\sigma\times$BR$_{\tau\tau}$ [fb] associated	$\sigma\times$BR$_{\mu\mu}$ [fb] direct	$\sigma\times$BR$_{\mu\mu}$ [fb] associated
150	5	h : $2.3\cdot10^3$ H : $9.6\cdot10^2$ A : $1.6\cdot10^2$	h : $5.2\cdot10^2$ H : $2.7\cdot10^2$ A : $6.9\cdot10^2$	h : 8.3 H : 3.4 A : $5.9\cdot10^{-1}$	h: 1.8 H : $9.5\cdot10^{-1}$ A : 2.4
150	10	h : $2.5\cdot10^3$ H : $1.5\cdot10^3$ A : $4.5\cdot10^2$	h : $8.5\cdot10^2$ H : $2.1\cdot10^3$ A : $2.7\cdot10^3$	h : 8.8 H : 5.4 A : 1.6	h : 3.1 H : 7.2 A : 9.6
150	20	h : $2.8\cdot10^3$ H : $3.2\cdot10^3$ A : $2.3\cdot10^3$	h : $1.1\cdot10^3$ H : $9.9\cdot10^3$ A : $1.0\cdot10^4$	h : 9.9 H : $1.1\cdot10^1$ A : 8.4	h : 4.1 H : $3.5\cdot10^1$ A : $3.8\cdot10^1$
150	30	h : $3.0\cdot10^3$ H : $6.1\cdot10^3$ A : $5.6\cdot10^3$	h : $1.2\cdot10^3$ H : $2.3\cdot10^4$ A : $2.4\cdot10^4$	h : $1.1\cdot10^1$ H : $2.1\cdot10^1$ A : $2.0\cdot10^1$	h : 4.3 H : $8.2\cdot10^1$ A : $8.5\cdot10^1$
150	50	h : $3.3\cdot10^3$ H : $1.5\cdot10^4$ A : $1.6\cdot10^4$	h : $1.3\cdot10^3$ H : $6.4\cdot10^4$ A : $6.6\cdot10^4$	h : $1.2\cdot10^1$ H : $5.4\cdot10^1$ A : $5.6\cdot10^1$	h : 5.3 H : $2.6\cdot10^2$ A : $2.7\cdot10^2$
150	80	h : $3.6\cdot10^3$ H : $3.6\cdot10^4$ A : $4.0\cdot10^4$	h : $1.3\cdot10^3$ H : $1.6\cdot10^5$ A : $1.6\cdot10^5$	h : $1.2\cdot10^1$ H : $1.2\cdot10^2$ A : $1.4\cdot10^2$	h : 5.4 H : $6.5\cdot10^2$ A : $6.7\cdot10^2$
200	5	h : $2.9\cdot10^3$ H : $2.2\cdot10^2$ A : $6.6\cdot10^1$	h : $1.5\cdot10^2$ H : $1.3\cdot10^2$ A : $1.6\cdot10^2$	h : $1.0\cdot10^1$ H : $7.9\cdot10^{-1}$ A : $2.3\cdot10^{-1}$	h : $5.6\cdot10^{-1}$ H : $4.7\cdot10^{-1}$ A : $5.9\cdot10^{-1}$
200	10	h : $2.8\cdot10^3$ H : $3.0\cdot10^2$ A : $7.2\cdot10^1$	h : $1.5\cdot10^2$ H : $9.1\cdot10^2$ A : $9.3\cdot10^2$	h : $1.0\cdot10^1$ H : 1.1 A : $2.5\cdot10^{-1}$	h : $5.6\cdot10^{-1}$ H : 3.2 A : 3.3
200	20	h : $2.9\cdot10^3$ H : $6.7\cdot10^2$ A : $4.7\cdot10^2$	h : $1.5\cdot10^2$ H : $3.9\cdot10^3$ A : $3.9\cdot10^3$	h : $1.0\cdot10^1$ H : 2.4 A : 1.7	h : $5.6\cdot10^{-1}$ H : $1.3\cdot10^1$ A : $1.3\cdot10^1$
200	30	h : $3.0\cdot10^3$ H : $1.3\cdot10^3$ A : $1.1\cdot10^3$	h : $1.5\cdot10^2$ H : $8.9\cdot10^3$ A : $8.9\cdot10^3$	h : $1.1\cdot10^1$ H : 4.6 A : 4.2	h : $5.5\cdot10^{-1}$ H : $3.1\cdot10^1$ A : $3.1\cdot10^1$
200	50	h : $3.1\cdot10^3$ H : $3.3\cdot10^3$ A :$3.4\cdot10^3$	h : $1.5\cdot10^2$ H : $2.4\cdot10^4$ A : $2.4\cdot10^4$	h : $1.1\cdot10^1$ H : $1.1\cdot10^1$ A : $1.2\cdot10^1$	h : $5.4\cdot10^{-1}$ H : $8.6\cdot10^1$ A : $8.6\cdot10^1$
200	80	h : $3.3\cdot10^3$ H : $8.1\cdot10^3$ A : $8.8\cdot10^3$	h : $1.5\cdot10^2$ H : $6.0\cdot10^4$ A : $6.1\cdot10^4$	h : $1.1\cdot10^1$ H : $2.8\cdot10^1$ A : $3.1\cdot10^1$	h : $5.3\cdot10^{-1}$ H : $2.1\cdot10^2$ A : $2.1\cdot10^2$

M_A [GeV/c^2]	tanβ	$\sigma\times$BR$_{\tau\tau}$ [fb] direct	$\sigma\times$BR$_{\tau\tau}$ [fb] associated	$\sigma\times$BR$_{\mu\mu}$ [fb] direct	$\sigma\times$BR$_{\mu\mu}$ [fb] associated
300	5	h : $2.7\cdot10^{3}$ H : $2.9\cdot10^{1}$ A : $1.5\cdot10^{1}$	h : $6.5\cdot10^{1}$ H : $1.8\cdot10^{1}$ A : 9.7	h : 9.7 H : $1.0\cdot10^{-1}$ A : $5.3\cdot10^{-2}$	h : $2.3\cdot10^{-1}$ H : $6.5\cdot10^{-2}$ A : $3.4\cdot10^{-2}$
300	10	h : $2.5\cdot10^{3}$ H : $4.1\cdot10^{1}$ A : $7.0\cdot10^{1}$	h : $5.7\cdot10^{1}$ H : $1.7\cdot10^{2}$ A : $1.2\cdot10^{2}$	h : 8.9 H : $1.4\cdot10^{-1}$ A : $2.4\cdot10^{-2}$	h : $2.0\cdot10^{-1}$ H : $6.3\cdot10^{-1}$ A : $4.2\cdot10^{-1}$
300	20	h : $2.4\cdot10^{3}$ H : $8.3\cdot10^{1}$ A : $3.4\cdot10^{1}$	h : $5.5\cdot10^{1}$ H : $8.7\cdot10^{2}$ A : $7.8\cdot10^{2}$	h : 8.7 H : $2.9\cdot10^{-1}$ A : $1.2\cdot10^{-1}$	h : $1.9\cdot10^{-1}$ H : 3.1 A : 2.7
300	30	h : $2.4\cdot10^{3}$ H : $1.5\cdot10^{2}$ A : $1.1\cdot10^{2}$	h : $5.4\cdot10^{1}$ H : $2.0\cdot10^{3}$ A : $1.9\cdot10^{3}$	h : 8.7 H : $5.6\cdot10^{-1}$ A : $3.9\cdot10^{-1}$	h : $1.9\cdot10^{-1}$ H : 7.1 A : 6.8
300	50	h : $2.5\cdot10^{3}$ H : $3.9\cdot10^{2}$ A : $3.6\cdot10^{2}$	h : $5.3\cdot10^{1}$ H : $5.6\cdot10^{3}$ A : $5.5\cdot10^{3}$	h : 8.9 H : 1.3 A : 1.3	h : $1.8\cdot10^{-1}$ H : $1.9\cdot10^{1}$ A : $1.9\cdot10^{1}$
300	80	h : $2.5\cdot10^{3}$ H : $9.5\cdot10^{2}$ A : $9.8\cdot10^{2}$	h : $5.1\cdot10^{1}$ H : $1.4\cdot10^{4}$ A : $1.4\cdot10^{4}$	h : 9.0 H : 3.3 A : 3.4	h : $1.8\cdot10^{-1}$ H : $4.9\cdot10^{1}$ A : $4.9\cdot10^{1}$
450	5	h : $2.5\cdot10^{3}$ H : 3.2 A : 5.2	h : $4.3\cdot10^{1}$ H : $9.9\cdot10^{-1}$ A : $8.8\cdot10^{-1}$	h : 9.1 H : $1.1\cdot10^{-2}$ A : $1.8\cdot10^{-2}$	h : $1.5\cdot10^{-1}$ H : $3.5\cdot10^{-3}$ A : $3.1\cdot10^{-3}$
450	10	h : $2.2\cdot10^{3}$ H : 4.0 A : 5.6	h : $3.7\cdot10^{1}$ H : $1.4\cdot10^{1}$ A : $1.3\cdot10^{1}$	h : 8.1 H : $1.4\cdot10^{-2}$ A : $1.9\cdot10^{-2}$	h : $1.3\cdot10^{-1}$ H : $5.1\cdot10^{-2}$ A : $4.7\cdot10^{-2}$
450	20	h : $2.2\cdot10^{3}$ H : 7.4 A : 7.4	h : $3.5\cdot10^{1}$ H : $1.2\cdot10^{2}$ A : $1.1\cdot10^{2}$	h : 7.8 H : $2.6\cdot10^{-2}$ A : $2.6\cdot10^{-2}$	h : $1.2\cdot10^{-1}$ H : $4.2\cdot10^{-1}$ A : $4.1\cdot10^{-1}$
450	30	h : $2.2\cdot10^{3}$ H : $1.4\cdot10^{1}$ A : $1.4\cdot10^{1}$	h : $3.5\cdot10^{1}$ H : $3.3\cdot10^{2}$ A : $3.2\cdot10^{2}$	h : 7.8 H : $5.1\cdot10^{-2}$ A : $5.0\cdot10^{-2}$	h : $1.2\cdot10^{-1}$ H : 1.1 A : 1.1
450	50	h : $2.2\cdot10^{3}$ H : $3.9\cdot10^{1}$ A : $4.0\cdot10^{1}$	h : $3.4\cdot10^{-1}$ H : $1.0\cdot10^{3}$ A : $1.0\cdot10^{3}$	h : 7.8 H : $1.3\cdot10^{-1}$ A : $1.4\cdot10^{-1}$	h : $1.2\cdot10^{-1}$ H : 3.6 A : 3.6
450	80	h : $2.2\cdot10^{3}$ H : $9.9\cdot10^{1}$ A : $1.0\cdot10^{2}$	h : $3.3\cdot10^{1}$ H : $2.7\cdot10^{3}$ A : $2.6\cdot10^{3}$	h : 7.7 H : $3.5\cdot10^{-1}$ A : $3.7\cdot10^{-1}$	h : $1.1\cdot10^{-1}$ H : 9.7 A : 9.5

M_A [GeV/c^2]	tanβ	$\sigma\times$BR$_{\tau\tau}$ [fb] direct	$\sigma\times$BR$_{\tau\tau}$ [fb] associated	$\sigma\times$BR$_{\mu\mu}$ [fb] direct	$\sigma\times$BR$_{\mu\mu}$ [fb] associated
600	5	h : $2.5{\cdot}10^{3}$ H : $5.3{\cdot}10^{-1}$ A : $8.5{\cdot}10^{-1}$	h : $3.7{\cdot}10^{1}$ H : $1.7{\cdot}10^{-1}$ A : $1.7{\cdot}10^{-1}$	h : 8.8 H : $1.8{\cdot}10^{-3}$ A : $3.0{\cdot}10^{-3}$	h : $1.3{\cdot}10^{-1}$ H : $6.0{\cdot}10^{-4}$ A : $6.0{\cdot}10^{-4}$
600	10	h : $2.2{\cdot}10^{3}$ H : $5.7{\cdot}10^{-1}$ A : 1.0	h : $3.2{\cdot}10^{1}$ H : 2.6 A : 2.6	h : 7.7 H : $2.0{\cdot}10^{-3}$ A : $3.6{\cdot}10^{-3}$	h : $1.1{\cdot}10^{-1}$ H : $9.3{\cdot}10^{-3}$ A : $9.3{\cdot}10^{-3}$
600	20	h : $2.1{\cdot}10^{3}$ H : $9.3{\cdot}10^{-1}$ A : 1.5	h : $3.0{\cdot}10^{1}$ H : $2.6{\cdot}10^{1}$ A : $2.6{\cdot}10^{1}$	h : 7.5 H : $3.3{\cdot}10^{-3}$ A : $5.6{\cdot}10^{-3}$	h : $1.0{\cdot}10^{-1}$ H : $9.3{\cdot}10^{-2}$ A : $9.2{\cdot}10^{-2}$
600	30	h : $2.1{\cdot}10^{3}$ H : 2.0 A : 2.9	h : $3.0{\cdot}10^{1}$ H : $8.1{\cdot}10^{1}$ A : $8.0{\cdot}10^{1}$	h : 7.4 H : $7.3{\cdot}10^{-3}$ A : $1.0{\cdot}10^{-2}$	h:$1.1{\cdot}10^{-1}$ H : $2.8{\cdot}10^{-1}$ A : $2.8{\cdot}10^{-1}$
600	50	h : $2.1{\cdot}10^{3}$ H : 6.5 A : 7.7	h : $2.9{\cdot}10^{1}$ H : $2.7{\cdot}10^{2}$ A : $2.7{\cdot}10^{2}$	h : 7.4 H : $2.3{\cdot}10^{-2}$ A : $2.7{\cdot}10^{-2}$	h:$1.0{\cdot}10^{-1}$ H : $9.8{\cdot}10^{-1}$ A : $9.6{\cdot}10^{-1}$
600	80	h : $2.0{\cdot}10^{3}$ H : $1.7{\cdot}10^{1}$ A : $1.9{\cdot}10^{1}$	h : $2.9{\cdot}10^{1}$ H : $7.7{\cdot}10^{2}$ A : $7.4{\cdot}10^{2}$	h : 7.3 H : $6.3{\cdot}10^{-2}$ A : $7.0{\cdot}10^{-2}$	h : $1.0{\cdot}10^{-1}$ H : 2.7 A : 2.6

List of Figures

List of Tables

Bibliography

[1] LHC Study Group, The Large Hadron Collider: Conceptual Design, CERN-AC-95-5 (1995)

[2] ATLAS Collaboration, ATLAS Technical Proposal for a General-Purpose pp Experimenr at the Large Hadron Collider at CERN, CERN/LHCC/94-43 (1994)

[3] CMS Collaboration, CMS The Compact Muon Solenoid Technical Proposal, CERN/LHCC/94-38 (1994)

[4] ALICE Collaboration, ALICE Technical Proposal for A Large Ion Collider Experiment at the LHC, CERN/LHCC/95-71 (1995)

[5] LHCb Collaboration, LHCb Technical Proposal A Large Hadron Collider Beauty Experiment for Precision Measurements of a CP Violation and rare Decays, CERN/LHCC/98-4 (1998)

[6] TOTEM Collaboration, TOTEM Technical Design Report, CERN/LHCC/2004-002 (2004)

[7] LHCF Collaboration, Technical Design Report of the LHCf experiment, CERN/LHCC/2006-004 (2006)

[8] ATLAS Collaboration, The ATLAS Experiment at the CERN Large Hadron Collider, to be published (2008)

[9] ATLAS Collaboration, ATLAS Magnet System Technical Design Report, CERN/LHCC/97-18 (1997)

[10] ATLAS Inner Detector Community, ATLAS Inner Detector Technical Design Report, CERN/LHCC/97-16 (1997)

[11] A.Poppleton, N.Ch.Benekos, R.Clifft, S.Dallison, G.Gorfine, ATLAS Inner Detector Performance with the Rome-Initial Layout, ATL-INDET-PUB-2007-008 (2007)

[12] ATLAS Collaboration, ATLAS Calorimeter Performance Technical Design Report, CERN/LHCC/96-40 (1996)

[13] V.Giangiobbe, P.Johansson, K.Jon-And, C.Santoni, Hadronic calorimeter performance in the ATLAS combined testbeam 2004, ATL-TILECAL-PUB-2005-008 (2005)

[14] ATLAS Collaboration, ATLAS Muon Spectrometer Technical Design Report, CERN/LHCC/97-22 (1996)

[15] ATLAS Collaboration, ATLAS First Level Trigger Technical Design Report, CERN/LHCC/98-14 (1998)

[16] A.Rimoldi, A.Dell'Acqua, M.Gallas, A.Nairz, J.Boudreau, V.Tsulaia, D.Costanzo, The Simulation of the ATLAS Experiment: present Status and Outlook, ATL-SOFT-2004-006 (2004)

[17] GEANT4 Collaboration, GEANT4-a simulation toolkit, doi:10.1016/S0168-9002(03)01368-8 (2003)

[18] GEANT4 Collaboration, Geant4 developments and applications, Nuclear Science, IEEE Transactions, Volume 53, Issue 1, Feb. 2006 Page(s): 270 - 278 (2006)

[19] J.Boudreau, V.Tsulaia, The GeoModel Toolkit for Detector Description, Proceedings for the CHEP04 Conference, Interlaken, Switzerland (2004)

[20] ATHENA Developer Guide, http://atlas.web.cern.ch/Atlas/GROUPS/SOFTWARE/OO/architecture/General/Tech.Doc/Manual/2.0.0 Draft/AthenaUserGuide.pdf

[21] AMDB Web Page, http://atlas.web.cern.ch/Atlas/GROUPS/MUON/AMDB_SIMREC/amdb_simrec.html

[22] ORACLE, Application's Developers Guide-Object relations features, 9.2 edition (2002)

[23] D.M.Rebuzzi, N.C.Benekos, S.Baranov, L.Chevalier, S.Goldfarb, J.-F.Laporte, T.Moore, A.Ouraou, D.Pomarede, M.Schott, S.Spagnolo, I.Trigger, Muon Detector-Description as Built and Its Simulation for the ATLAS Experiment, proceedings of the 2006 IEEE Nuclear Science Symposium, San Diego, California (2006)

[24] Web Page http://boudreau.home.cern.ch/boudreau/v-atlas-hepvis.htm

[25] ATLAS Wiki Page for the muon geometry in the Data Challenge 3: https://twiki.cern.ch/twiki/bin/view/Atlas/MuonGeometryDC3

[26] ATLAS CVS Repository, http://atlas-sw.cern.ch/cgi-bin/viewcvs-atlas.cgi/offline/MuonSpectrometer/MuonSimEvent

[27] D.Rebuzzi, K.A.Assamagan, A.Di Simone, N.Van Eldik, Y.Hasegawa, Geant4 Muon Digitization in the ATHENA Framework, ATL-SOFT-PUB-2007-001 (2007)

[28] K.A.Assamagan et al, A Hierarchical Software Identifier Scheme for the ATLAS Muon Spectrometer ; updated version, ATL-MUON-2004-003 (2004)

[29] Information about the ATHENA-Aware Ntuple, https://twiki.cern.ch/twiki/bin/view/Atlas/AthenaAwareNTuple

[30] RunTimeTest Web Page, http://www.hep.ucl.ac.uk/atlas/AtlasTesting/TRRUserGuide/RTTUserGuide.html

[31] A.Corso-Radu, S.Kolos, H.Hadavand, R.Kehoe, Data Quality Monitoring Framework for the ATLAS Experiment at the LHC, ATLAS-COM-DAQ-2007-033 (2007)

[32] R.Brun, F.Rademakers, ROOT - An Object Oriented Data Analysis Framework, Proceedings AIHENP'96 Workshop, Lausanne, Sep. 1996, Nucl. Inst. Meth. in Phys. Res. A 389 (1997) 81-86. See also http://root.cern.ch/

[33] Muon Offline DQA Web Page, https://twiki.cern.ch/twiki/bin/view/Atlas/MuonOfflineDQAM4OfflineMonitoring

[34] M.Virchaux,D.Pomarède,PERSINT MANUAL version 3.00, Saclay Muon Software Group, CEA/DSM/DAPNIA/SEDI+SPP

[35] M.Deile, Optimization and Calibration of the Drift-Tube Chambers for the ATLAS Muon Spectrometer, Doctoral Thesis, Ludwig-Maximilians-Universität München (2000)

[36] M.Deile, N.Hessey, O.Kortner, H.Kroha, J.v.Loeben, A.Staude, An efficient method to determine the space-to-drift-time relationship of the ATLAS monitored drift tube chambers Nuclear Science Symposium Conference Record, 2007. NSS '07. IEEE Volume 1, Oct. 26 2007-Nov. 3 2007 Page(s):685 - 688

[37] A.Pich, The Standard Model of Electroweak Interactions, arXiv:0705.4264v1 [hep-ph]

[38] S.P.Martin, A Supersymmetry Primer, hep-ph/9709356, version 4

[39] ALEPH, DELPHI, L3 and OPAL Collaborations, The LEP Working Group for Higgs Boson Searches, Search for Neutral MSSM Higgs Bosons at LEP, CERN-PH-EP/2006-001 (2006)

[40] W-M Yao et al 2006 J.Phys. G: Nucl. Part. Phys. **33** 1

[41] The UA1 collaboration (G.Arnison et al), Experimental observation of isolated large transverse energy electrons with associated missing energy at $\sqrt{s}$=540 GeV, Phys. Lett. **B 122** (1983) 103

[42] UA2 Collaboration (P.Bagnaia et al), Observation Of Single Isolated Electrons Of High Transverse Momentum In Events With Missing Transverse Energy At The Cern $p\bar{p}$ Collider, Phys. Lett. **B 122** (1983) 476

[43] The UA1 collaboration (G.Arnison et al), Experimental Observation Of Lepton Pairs Of Invariant Mass Around 95 GeV/c^2 At The CERN SPS Collider, Phys. Lett. **B 126** (1983) 398

[44] UA2 Collaboration (P.Bagnaia et al), Evidence For $Z^0 \rightarrow e^+e_-$ At The Cern $p\bar{p}$ Collider, Phys. Lett. **B 129** (1983) 130

[45] A.V.Gladyshev, D.I.Kazakov, SUPERSYMMETRY AND LHC, hep-ph/0606288v1

[46] S.Dimopoulos, S.Raby, F.Wilczek (1981), "Supersymmetry and the Scale of Unification". Phys. Rev. D **24**: 1681-1683.

[47] S. Dimopoulos, H. Georgi (1981). "Softly Broken Supersymmetry and SU(5)". Nucl. Phys B **193**: 150.

[48] A.Djouadi, The Anatomy of Electro-Weak Symmetry Breaking, Tome II: The Higgs bosons in the Minimal Supersymmetric Model, arXiv:hep-ph/0503172 (2005)

[49] Tevatron Searches for Higgs Bosons Beyond the Standard Model J. Nielsen, The CDF and D0 Collaborations, FERMILAB-CONF-07-415-E. Published Proceedings Hadron Collider Physics Symposium 2007 (HCP 2007), La Biodola, Isola d'Elba, Italy, May 20-26, 2007.

[50] M.Heldmann, The Identification of Hadronically Decaying τ Leptons in the ATLAS Experiment and Investigation of the Discovery Potential for MSSM Higgs Bosons in τ Final States, Doctoral Thesis (2007)

[51] M.Frank, T.Hahn, S.Heinemeyer, W.Hollik, H.Rzehak, G.Weiglein, The Higgs Boson Masses and Mixings of the Complex MSSM in the Feynman-Diagrammatic Approach, arXiv:hep-ph/0611326v2 (2007)

[52] G.Degrassi, S.Heinemeyer, W.Hollik, P. Slavich, G.Weiglein, Towards High-Precision Predictions for the MSSM Higgs Sector, arXiv:hep-ph/0212020v2 (2003)

[53] S.Heinemeyer, W.Hollik, G.Weiglein, The Masses of the Neutral CP-even Higgs Bosons in the MSSM: Accurate Analysis at the Two-Loop Level, arXiv:hep-ph/9812472v1 (1998)

[54] S.Heinemeyer, W.Hollik, G.Weiglein, FeynHiggs: a program for the calculation of the masses of the neutral CP-even Higgs bosons in the MSSM, arXiv:hep-ph/9812320v1 (1998)

[55] The ATLFAST Validation Task Force, Performance of the ATLAS fast simulation ATLFAST (2007)

[56] T.Sjöstrand, P.Edén, C.Friberg, L.Lönnblad, G.Miu, S.Mrenna, E.Norrbin, PYTHIA, Computer Physics Commun. 135 238 (2001)

[57] T.Sjöstrand, P.Z.Skands, Transverse-momentum-ordered showers and interleaved multiple interactions, Eur. Phys. J. C 39, 129 (2005)

[58] T.Sjöstrand, S.Mrenna, P.Z.Skands, PYTHIA 6.4 physics and manual, JHEP 0605, 026 (2006)

[59] S.Frixione, B.R.Webber, Matching NLO QCD computations and parton shower simulations, JHEP 0206 (2002) 029 [hep-ph/0204244]

[60] S.Frixione, P.Nason, B.R Webber, Matching NLO QCD and parton showers in heavy flavour production, JHEP 0308 (2003) 007 [hep-ph/0305252]

[61] G.Marchesini, B.R.Webber, G.Abbiendi, I.G.Knowles, M.H.Seymour, L.Stanco, Computer Phys. Commun. 67 (1992) 465

[62] S.Moretti, K.Odagiri, P.Richardson, M.H.Seymour, B.R.Webber, JHEP 0204 (2002) 028 [hep-ph/0204123]

[63] B.P.Kersevan, E.Richter-Was, The Monte Carlo Event Generator AcerMC 2.0 with Interfaces to PYTHIA 6.2 and HERWIG 6.5, arXiv.org:hep-ph/0405247 (2004)

[64] M.L.Mangano et al, ALPGEN, a generator for hard multiparton processes in hadronic collisions, JHEP07(2003) 001, doi:10.1088/1126-6708/2003/07/001

[65] Z.Was, P.Golonka, TAUOLA as tau Monte Carlo for future applications, arXiv:hep-ph/0411377 v1 (2004)

[66] ATLAS Web Page for CSC-DC3 simulated Data Samples, https://twiki.cern.ch/twiki/bin/view/Atlas/HiggsWGMCSamples

[67] S. Hassani et al., A muon identification and combined reconstruction procedure for the ATLAS detector at the LHC using the MUONBOY, STACO and MuTag reconstruction packages; NIM A , 572, 77 (2007)

[68] ATLAS Web Page, https://twiki.cern.ch/twiki/bin/view/Atlas/ElectronReconstruction

[69] ATLAS Web Page, https://twiki.cern.ch/twiki/bin/view/Atlas/ElectronGammaIsEM

[70] ATLAS Web Page, https://twiki.cern.ch/twiki/bin/view/Atlas/TauRec